System Level Drop-Impact Simulation and Validation of Handheld Radio Devices

Edward Barclay

2014

A thesis submitted in partial fulfillment of the requirements

for the Degree of Master of Engineering

in the Department of Mechanical Engineering

at the University of Canterbury

Executive Summary

The aim of this project was to develop a finite element model capable of simulating the drop-impact event of handheld radio devices in support of Tait Communications (Tait).

The handheld radios developed by Tait call for exceptional robustness and reliability due to their deployment in critical applications. One key design requirement of the radios is that they must survive a 1.8 m drop; this is currently assessed using a build and test approach. The development of a drop-impact finite element model in this project will aid in reducing product development time and make it easier to identify weaknesses in existing designs. Virtual optimisation could be performed to minimise prototyping. The understanding of finite element methods for modelling impact events, of setup parameters for the finite element solver and of the accuracy of simulation results are required before finite element analysis can be successfully implemented at Tait.

A literature review was conducted on the impact testing methods for handheld electronic devices. As a result of this review a drop-impact test rig was developed. The experimental results were used throughout the project to validate the finite elements models developed.

The drop-impact modelling of a radio is exceptionally challenging because of the complex interaction of the contacting surfaces, the complex stress-strain and damping characteristics of the materials, and the excitation of the high frequency modes. For this reason, the finite element model was developed in two stages: a simplified radio was used to develop the understanding of the above complexities and then the understandings implemented in a more detailed radio model.

The mesh size of the finite elements, the elastic and the damping characteristics of the materials and the contact conditions for the simplified radio model were varied to understand their influence on the simulation results. The finite element input settings and parameters were then altered to give better agreement with the experimental results.

A detailed radio that closely matched the Tait design was subsequently modelled. The geometry was “smoothed out” so as to minimise the degrees of freedom of the numerical model. The lessons learnt from the simplified radio model were applied to the analysis of the detailed radio assembly. Despite the general agreement, there were disagreements between the finite element and experimental results, which is attributed to the high complexity of the model. Further improvement of the model is required to improve the agreement with the experimental results and these improvements could include:

- a better definition of the contacts, which requires better understanding of friction coefficients between parts and the clamping forces and restrictions provided at screw connections
- a better definition of the material properties
- further refinement of the finite element mesh
- remodelling of the radio assembly for better integration into the finite element model

This project has delivered a workable finite element model capable of analysing the drop-impact event of handheld radio devices. Suggestions have been provided that would further improve the quality of the model. Such a model provides a powerful analytical tool that minimises the engineering effort and reduces the cycle time for product development.

Acknowledgements

I would like to thank my supervisors Dr. Ee-Hua Wong and Dr. John Pearse for their guidance and support over the course of the project.

I would also like to recognize the support provided Tait Communications, in particular Daniel Foster and the entire Mechanical Design Team and Testing Laboratory. The resources they provided in both equipment and technical expertise was invaluable.

I would also like to acknowledge the support of the Ministry of Science and Innovation who provided funding for this project through their Technology for Industry Fellowship program.

I would also like to recognize the Acoustics Research Group for providing a weekly forum to present my work and also the daily discussions both work related and not.

Finally I would like to thank my family and friends for supporting me throughout this project without them this would not have been possible.

Contents

List of Figures

List of Tables

1. Introduction

The objectives and aims of the project are presented together with the purpose of the investigation, including relevant background information. The approach taken to achieve the project goals are described.

1.1. Project Objective

The primary objective of this project was to create a finite element model of a Tait handheld radio subject to a drop-impact event. The finite element model was to be ultimately used in evaluating and optimising handheld radio designs, leading to a more robust and commercially competitive product. The secondary objective of this project was to develop a test rig and perform drop-impact tests to validate the finite element models.

1.2. Project Background

Tait Communications (Tait) is a large Christchurch-based business which specialises in the design and manufacture of communication systems. Portable handheld radios from Tait (Figure 1.1) are deployed extensively in critical field applications that demand exceptionally high reliability. One of the critical requirements of the handheld radios is to be able to survive a 1.8 meter drop. This requirement has become challenging due to the miniaturisation of their products as well as the recent adoption of lead-free solder. Lead-free solder joints have been found to be more susceptible to brittle fracture [1], as compared to the eutectic tin-lead solder joints, under the high strain rate loading experienced by handheld radios during a drop-impact. The magnitudes of stress and strain experienced by the solder joints are dependent on the mechanical structure of the entire handheld radio. A mechanical design that provides adequate protection of the solder joints has become increasingly critical.

Figure 1.1 - Tait handheld radios, current model (left) and previous model (right)

The existing product development methodology is based on a build-and-test methodology which is time and resource intensive. A development methodology that incorporates virtual prototyping using computer simulation opens up the possibility to test a wider range of designs and streamline the design evaluation and optimisation stages of the product cycle. Developing a computational modelling methodology for system level product drop-impact is extremely challenging in view of the relatively short duration and high force of the event, especially if the subject of interest is, for example, a minute ball grid array (BGA) connection. The aim of this project was to develop an impact model at a system level that could be used to evaluate different radio designs.

1.3. Project Approach

Due to the complex nature of the handheld radio a progressive approach was taken to develop the drop-impact finite element model, a flow chart of the project is shown in Figure 1.2.

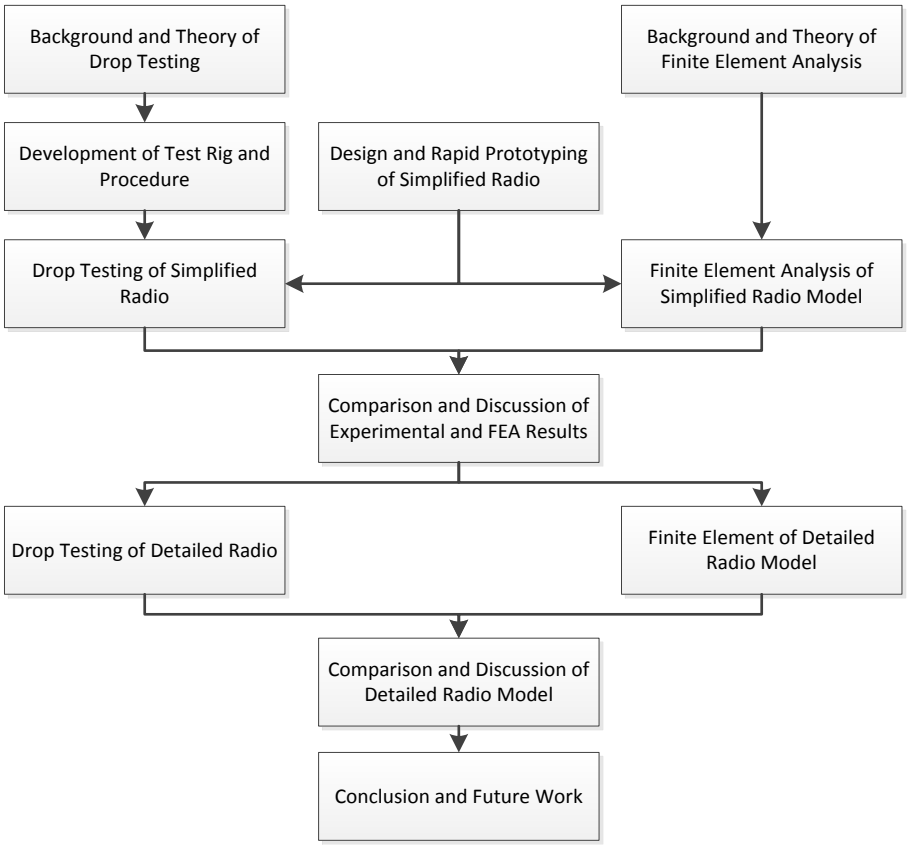

Figure 1.2 - Flow chart of project approach

A background investigation was undertaken to understand the previous work that has been carried out in this area. This background research provided a basic understanding of the fundamental concepts and capabilities of finite element impact modelling and the various test methods. A test procedure and a test rig were designed and constructed. A simplified radio was developed for use in

both drop-impact testing and the initial finite element simulations. Once a good correlation between the simplified radio drop tests and simulation were achieved, the findings were applied to the more complex handheld radio from Tait. The outcomes from the tests and simulations were discussed and possible future work presented.

1.4. Report Overview

The work is presented in six chapters. The following chapter (Chapter 2) describes the importance of drop testing, the current methods employed for evaluating the performance of portable electronics under impact, and the testing procedures used at Tait. The test rig developed for this project is presented.

Key concepts of finite element analysis related to the simulation of highly transient events and examples of previous works completed on portable electronic impacts are presented in the third chapter.

The fourth chapter outlines the initial impact tests on a simplified radio assembly. This chapter discusses how the finite element model of the simplified radio is set up and tuned to get improved correlation to the experimental tests performed. The conclusion of the chapter presents the finite element model for simulating a drop-impact event of a simplified radio, comparing and contrasting the results to physical tests.

The fifth chapter presents the experimental and simulation results for the detailed model of the handheld radio. Drop-impact test were performed on the detailed radio and the results discussed, including a comparison to the simulation results. Several critical behaviours of the detailed radio were investigated to show the use of the finite element model developed.

The final chapter summarises the work completed on the project highlighting the key findings, discusses the effectiveness of finite element analysis as a design and development tool and outlines future work.

2. Drop Testing

This chapter explains the fundamentals of the drop-impact testing used for the evaluation of handheld electronics. A literature review of drop testing was performed, detailing the importance of drop-impact testing for handheld electronics, the commonly used test conditions and procedures. An overview of the testing procedures implemented at Tait; including a discussion on the strengths and weaknesses of their test program are presented. Finally, drop testing requirements and procedures for this project are discussed.

2.1. Overview of Drop Testing

Drop testing is commonly performed to evaluate a device's susceptibility to being dropped. Drop testing is widely performed on handheld electronic devices because the ability of the device to survive an impact is very important due to the high probability of a drop occurring during use. Test methods range from simple hand-drops to the use of equipment and instruments that give control of the impact conditions. Testing is performed on the assembled system (system level) as well as on the printed circuit board assemblies within the product (board level). Most commercial drop-impact tests are performed in accordance to industry standards and/or internally developed test criteria.

2.2. Importance of Drop Testing

Drop-testing is carried out for the following reasons:

- Identify failure regions
- Test and justify design modifications
- Quality control of products (check for loose components, poor solder connections etc.)
- Meet relevant standards designed to minimise in-field failure, either internal or industry accepted
- For validation of finite element/analytical models

System level drop testing is necessary during the development stage of a handheld product to ensure that the product meets the design intent. Board level drop testing is performed during the development stage to evaluate and qualify the design of the subassembly. A product that cannot survive being dropped can be expected to incur replacement and repair costs; as well as a dissatisfied customer base.

2.3. Testing States

Handheld products are commonly tested at packaging level, system level and subassembly level.

2.3.1. Packaging level

Drop tests of packaged products are performed to ensure that the packaging of the product is capable of protecting it during transportation and handling. A wide range of products are tested in this state because any damage to the product during transportation results in replacement costs. A number of test standards are available. Design guidelines are well established, such as those provided by Westpak Packaging [2-4].

2.3.2. System level

System level testing consists of drop testing the fully assembled product to simulate conditions experienced by the end consumer. These tests are used to validate the robustness of the product as a whole. System level tests are commonly performed on a live product where its functionality is checked after each test. Alternatively a product can have monitoring instrumentation mounted as a substitute for a live test. To pass an instrumented test the measured values would have to meet predetermined criteria. For example, the strain (deflection) of a circuit board during impact would have to be below a certain value to ensure no circuit board failures occur. A live test will provide more complete results for validating products as measurement instrumentation cannot be placed at all locations on the product. However during the initial design stage, measured results provide quantitative data that can be used for design comparisons. The drop height of system level tests generally ranges from 1-2 meters depending on how the product is normally used and what level of robustness is required for the product. Drops are normally onto rigid surfaces as this is a worst case.

2.3.3. Board level

Components critical to the functionality of the product can be tested at a subassembly level. For handheld electronic products this type of testing is generally performed on printed circuit board assemblies to check the robustness of the solder interconnection and the microelectronic packaging. Subassembly testing allows the designer to focus on certain crucial components and parameters without having to deal with the complexity of an entire assembled product. These tests are not performed as a final validation of the product; but are often used to investigate different (printed circuit) board, solders, and component arrangements as a way of finding the most suitable and robust board assembly method.

The number of published works on subassembly testing and simulations is larger than work performed at a system level. There are good reasons for this: the subassembly test is used for evaluation of a number of design decisions - the selection of solders materials, the dimensions of solder joints, the design of the component and the layout of the components on a board which means they apply to a broader range of electronic products. The commercial sensitivity of providing details of final assembled products usually prohibits their publication.

2.4.Testing Methods

Testing procedures for both system and subassembly are outlined below. Packaging level impact testing is not addressed further in this project.

2.4.1. Hand drop

Hand drop testing consists of a drop from normal operating height (or higher) by hand. The impact orientations of such tests are difficult to control for the following reasons:

- Experimenter will often induce rotation on the product during release
- Release orientation is not precisely controlled
- Objects have the tendency to rotate during freefall due to their centre of gravity not being aligned with their aerodynamic centre

These three mechanisms affecting the final impact orientation makes repeatability of such tests very challenging. Due to the low accuracy and repeatability of this test, hand drops are uncommon in commercial product design environments.

2.4.2. Tumble testing

Tumble testing is a random orientation impact testing method. The tumble tester often consists of a rotating drum with a geometry that provides for a free fall component (Figure 2.1). The tumble tests are used to ensure the product can handle the more frequent knocks and lower level drops, meaning drop heights are generally lower than other drop-impact tests. Tumble testing can be considered as a form of highly accelerated life testing (HALT). Tumble testing will give an approximation of how many impacts a product can handle before failure occurs. The random nature of the testing makes it difficult to determine what impact orientations are causing damage to the product meaning this form of testing would only be realistically used as a product validation test and not used during the initial design evaluation stages. Tumble testing is likely to highlight failures due to fatigue rather than stress-overload in a high-shock loading.

The tumble testing method is mentioned in the IEC standard on Environmental testing [5] as an example of performing repeated free fall impact testing (Figure 2.1 b). The IEC standard requires a fall height of 500 mm and the number of falls can be 50, 100, 200, 500 or 1000.

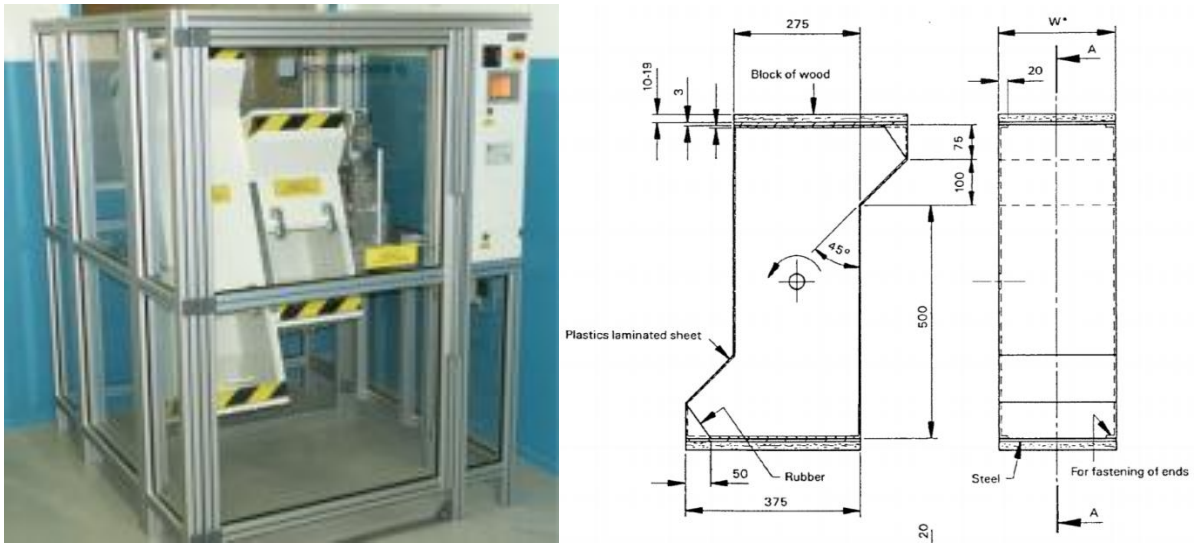

Figure 2.1 - a) Commercially available tumble tester (large and small drop heights), b) general schematic of a tumble tester from IEC 60068 [5]

2.4.3. Board level

Board level testing is a method designed for component testing, predominantly used to test the different solder and component layout techniques of printed circuit boards. The Joint Electron Devices Engineering Council (JEDEC) is an independent semiconductor engineering trade organisation and standardisation body, which has developed a number of industry standards for the testing of microelectronic devices. The JEDEC board level test consists of securing a test board to a drop table, the table is then dropped (Figure 2.2), inducing a shock pulse to the test board. Lai et al. [6] completed a series of board-level drop tests based around JEDEC testing standards. They carried out experiments investigating the effect of solder joint compositions, fluxes and mounting surface treatments (electroless Ni/Au surface finish or organic solderability preservative) on the drop-impact reliability of printed circuit boards. This type of testing demonstrated the ability of board level tests to easily generate data on different mounting technologies and materials. This data is very beneficial when developing a circuit board design that is less susceptible to shock impact failures.

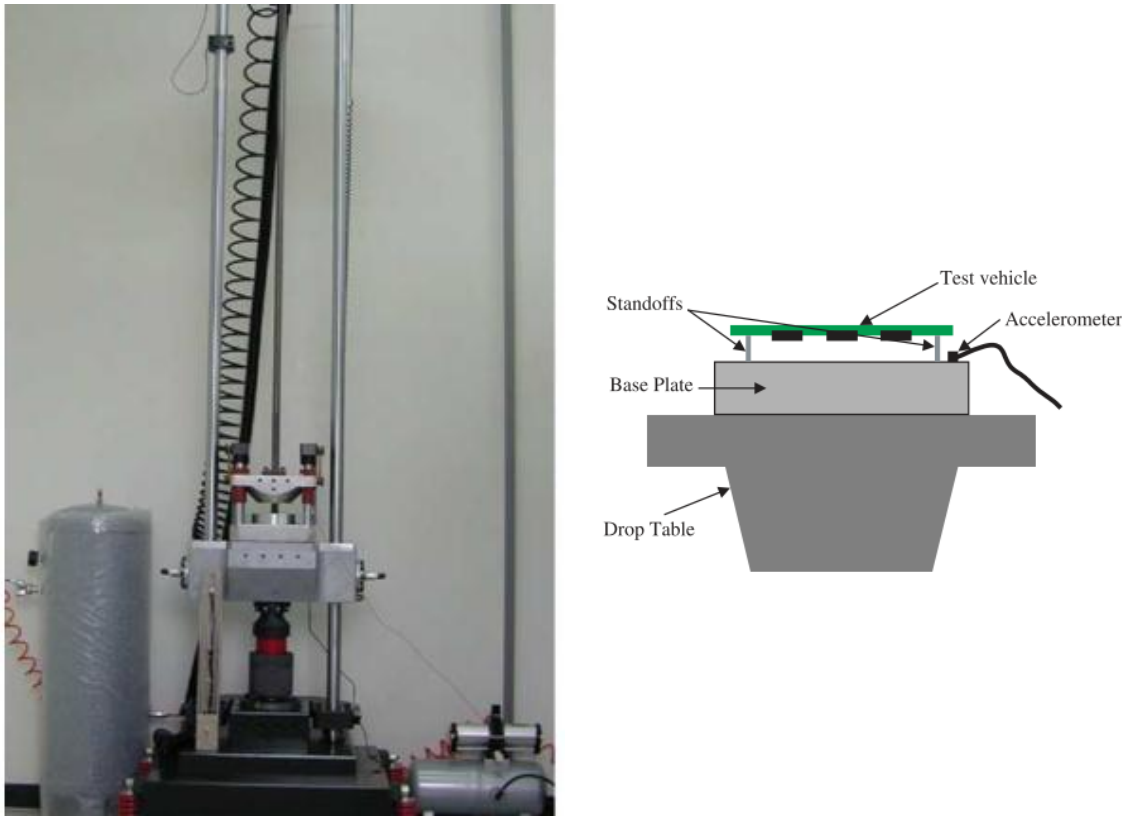

Figure 2.2 - Schematic of a board level drop test rig

JEDEC has produced two standards relevant to board level/subassembly testing, JESD22-B110A[7] and JESD22-B111[8]. JESD22-B110A describes a method to evaluate a subassembly's (i.e. a printed circuit board) capability to withstand a moderately severe shock. The standard calls for a test rig that is capable of providing shock pulses up to a peak of 2900 g and impact durations between 0.3 and 8.0 milliseconds. Two different test conditions are described, a free condition where the subassembly is not attached to a connecting member and a mounted condition where the subassembly is attach by means of an assembly method to a connecting member. Each test condition has a range of test severities (service conditions) which are dependent on the level of shock resilience the assembly requires. Each service condition defines the required peak acceleration, velocity change and pulse duration for the tests (Table 2.1 for free-condition tests and Table 2.2 for mounted state tests). Each condition also includes an equivalent drop height which describes the free-fall height needed to attain a velocity equal to the specified velocity change if impact with zero rebound occurs; the equivalent drop height is intended as a reference value only.

Table 2.1 - Subassembly free state test levels

Service condition	*Equivalent drop height [cm]*	*Velocity change [cm/s]*	*Peak acceleration [g]*	*Pulse duration [ms]*
H	150	534	2900	0.3
G	130	505	2000	0.4
B	112	467	1500	0.5
F	76.2	386	900	0.7
A	50.8	316	500	1.0

Table 2.2 - Portable subassembly service condition test levels

Service condition	*Equivalent drop height [cm]*	*Velocity change [cm/]*	*Peak acceleration [g]*	*Pulse duration [ms]*
P1	150	543	235	3.7
P2	130	505	225	3.6
P3	112	467	214	3.5
P4	91.4	424	199	3.4
P5	76.2	386	188	3.3

Ng et al. [9] developed a finite element model which aided in tuning the board level drop testing apparatus so that the appropriate shock pulse amplitude and duration could be achieved. It was found that the peak acceleration and pulse duration are strongly affected by the density and thickness of the drop table as well as the modulus and thickness of the absorbing surface. The drop height was found to effect the peak acceleration but had little effect on the pulse duration. A flow chart (Figure 2.3) was developed to aid in calibrating a board level drop tester to achieve the desired impact peak and duration.

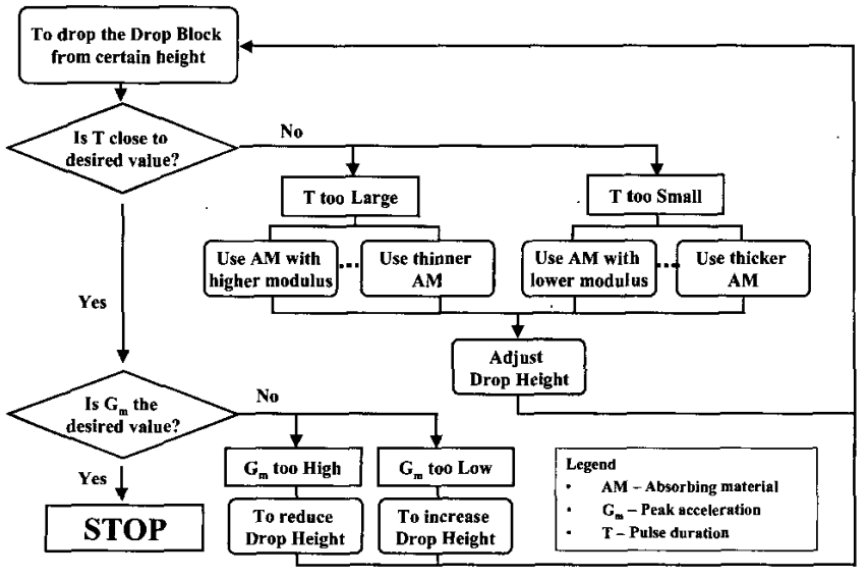

Figure 2.3 - Design flowchart to calibrate and characterize a drop tester to obtain the desired impact pulse [9]

JESD22 B111 was developed to evaluate and compare the performance of surface mounted electronic components for handheld electronic applications. A standardised test board and methodology is explained to provide reproducible assessment of surface mounted components. This test standard was developed to provide relative component performances for evaluation purposes, not to replace system level pass/fail based testing. The standard explains the composition and construction of a test board which the components are mounted to. This test becomes useful when trying to investigate which designs are going to be the most robust in terms of shock behaviour by trailing different mounting techniques, solder compositions and package arrangements.

2.4.4. Fixed product drop

Fixed product testing involves fixing the test product onto a drop table and then the entire system is dropped. This form of testing allows for more consistent measurement data over unconstrained product impact tests, but does not sufficiently recreate real life events due to the added rigidity of the fixation to the drop table. This method would be good for corroborating a finite element model but falls short for product validation.

Askari Farahani et.al [10] investigated the transient response of a portable electronic device and associated subassemblies using a fixed product drop testing procedure. Firstly a drop test was performed using a clamped printed circuit board (Figure 2.4), the drop table was setup to experience a 1500 g peak acceleration on the drop-table fixture (measured at locations A and C). The acceleration experienced on the printed circuit board (location B) was found to be magnified by around a factor of 1.5 to that measured on the drop table. The repeatability of these tests showed that although the acceleration experienced by the drop fixture varied by only 1.5%, the magnified acceleration experienced on the printed circuit board ranged between a factor of 1.2 and 1.5. For the same test the strain measured on the board only varied by 0.2%, showing strain measurements provided a more consistent measurement than acceleration.

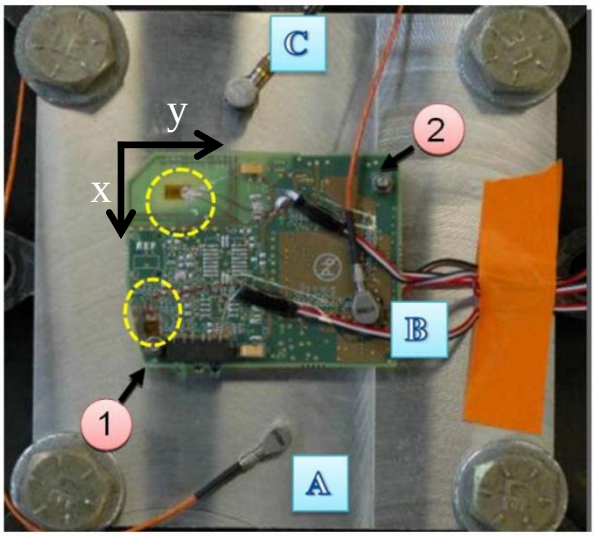

Figure 2.4 - Test setup of board level test from Askari et al. [10]. Letters indicate accelerometer locations, the numbers indicate clamping locations and the two yellow circles indicate strain gauge locations

The drop behaviour of a fixed, fully assembled product (Figure 2.5) was investigated using a 1600 g peak acceleration on the drop table (location A). The printed circuit board was attached to the housing at the same two points as it was during the board level tests. Figure 2.6 shows good repeatability of strain and acceleration measurements, the peak acceleration on the board was found to be a factor 1.8 higher than that on the drop-table. The difference in acceleration between the board and the product tests suggested that board level testing does not accurately recreate the behaviour of the board within the assembly, even if test boards both are fixed at identical locations.

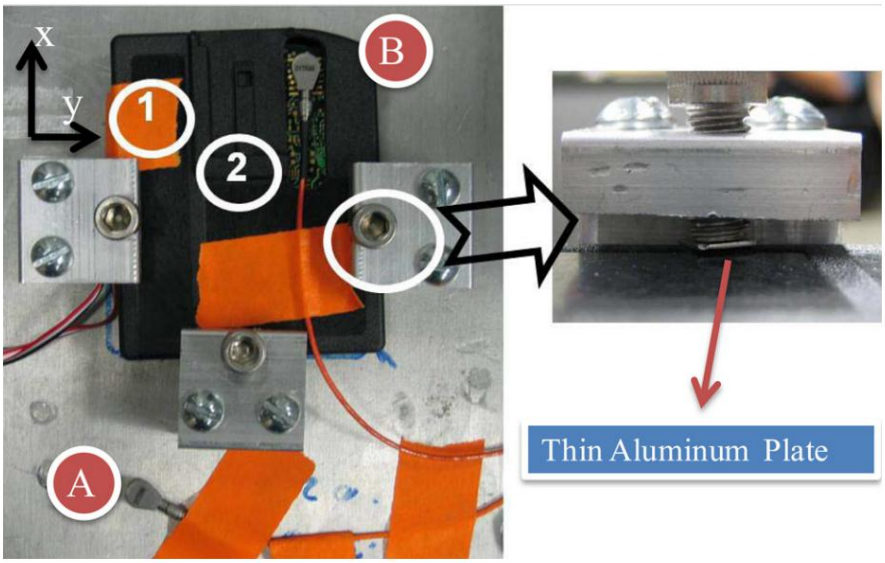

Figure 2.5 - Test setup of fully assembled product, lettering indicating accelerometer locations and numbering indicating strain gauge locations [10]

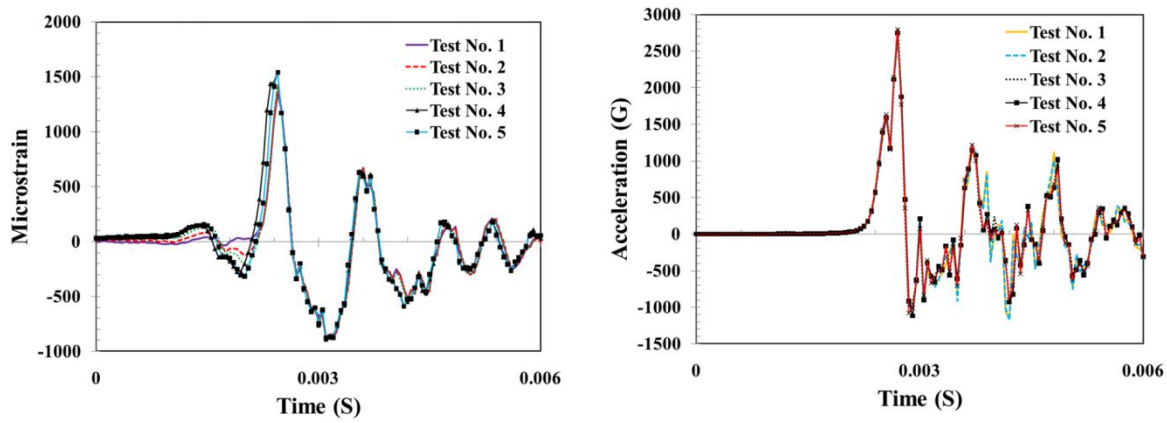

Figure 2.6 - a) stain measured in the x direction at point 2 of the assembled product during a drop testing which induced a 1600 g shock impulse on the drop table b) acceleration at point B during the same test as described in a) [10]

2.4.5. Swinging pendulum

Zhou et al. [11] used a swinging pendulum as a substitute for a drop tower to perform impact analysis of system level handheld electronic devices. The test rig (Figure 2.7) consisted of a pendulum which had an air gripper to hold the test specimen in place; designed to release the product prior to impacting with a PVC bar. To verify the impact orientation, high speed video was used; additionally, red ink was spread over the impact surface to mark the contact area on of the product. The test vehicle (Figure 2.8) consisted of a printed circuit board, instrumented with strain gauges, within a PVC housing. The developed test rig was capable of achieving a point contact impact, with the impact velocity and angles easily adjustable. Measurements of both impact force and board strain (Figure 2.9) showed good repeatability between tests.

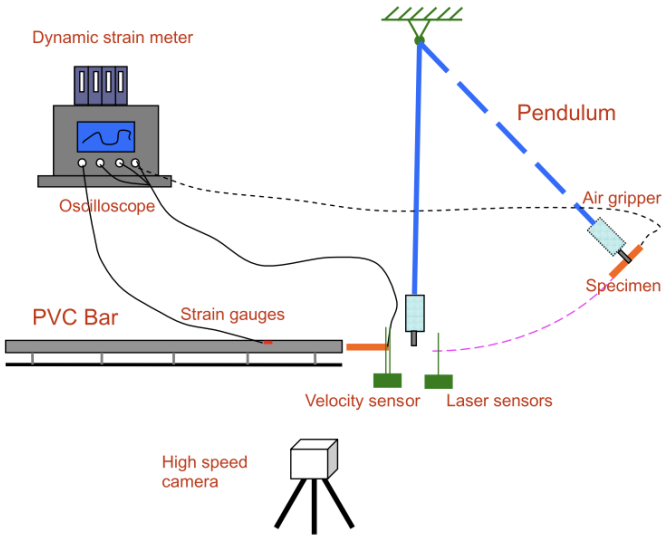

Figure 2.7 - Pendulum impact test and test vehicle used by Zhou et al. [11]

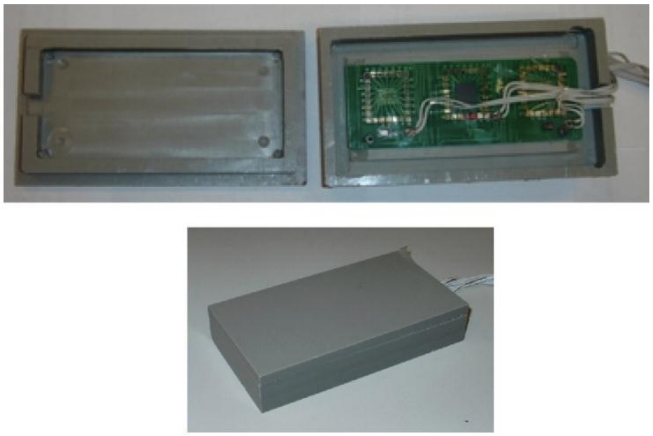

Figure 2.8 - Test specimen used during the swinging pendulum drop testing [11]

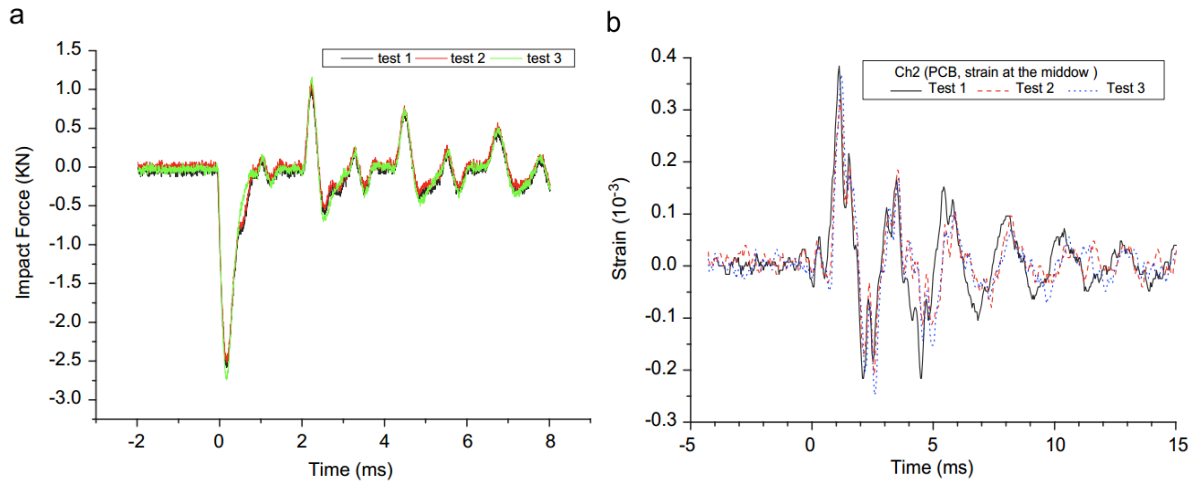

Figure 2.9 - a) Impact force for swinging pendulum tests, b) strain measurement on PCB experience during swinging pendulum impact testing [11]

2.4.6. Controlled impact drop test

Controlled drop testing is a system level test designed to closely control the impact orientation and velocity. Several testing methods have been developed to control the impact orientation, most consist of a fixture which holds the test vehicle at the desired orientation until just prior to impact. At this point the fixture releases the product to ensure it is completely unconstrained in order to replicate a real life impact event.

An example of a controlled impact test rig was developed by Chen et al. [12]. The test rig (Figure 2.10) has a falling fixture with 'U-arms' which clamped the product in place; photoelectric sensors were used to release the product at the appropriate time. A CCD camera was used in conjunction with a mirror and grid system to determine the impact angle of the product. Four different impact orientations were tested with 50 tests performed at each impact orientation. The results showed that 97.2% of the drops impacted within ±5° of the desired impact orientation.

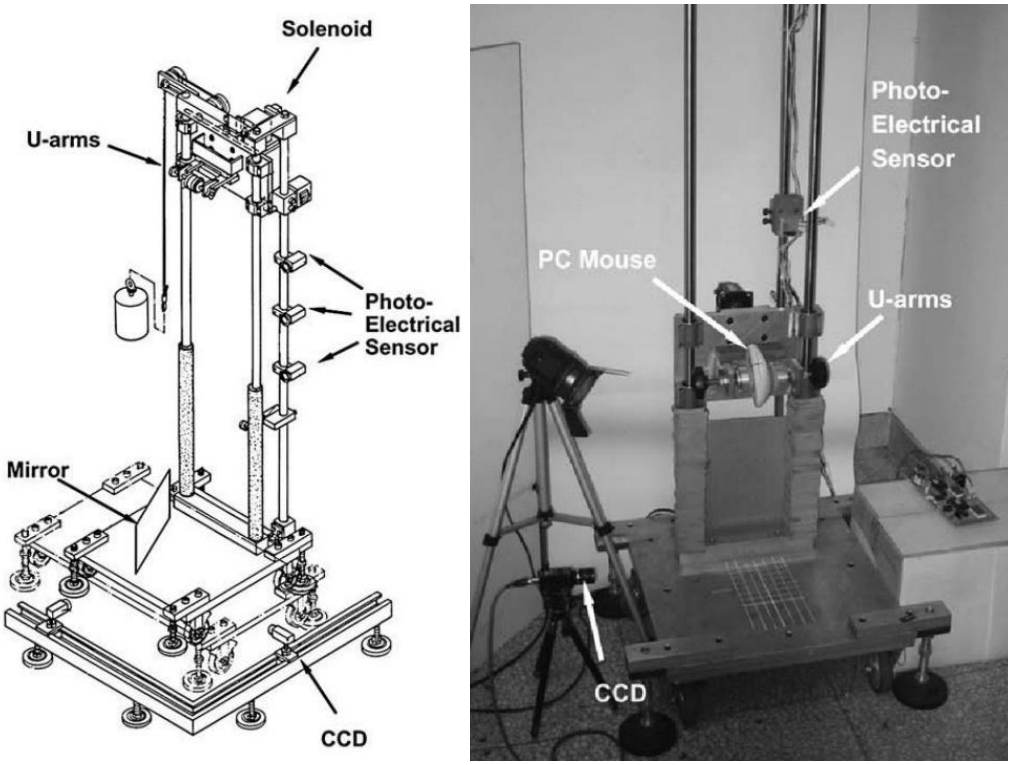

Figure 2.10 - Controlled drop-impact orientation test rig developed by Chen et al. [12]

Lim et al.[13] developed a similar drop-impact testing device (Figure 2.11). The release mechanism had a similar two point clamping method that opened to release the test product. Measurement equipment included an accelerometer and strain gauges mounted on the PCB's of the test product; a load cell was used to capture the impact force. High speed photography was used to help visualise the deformation of the housing and to verify the impact orientation.

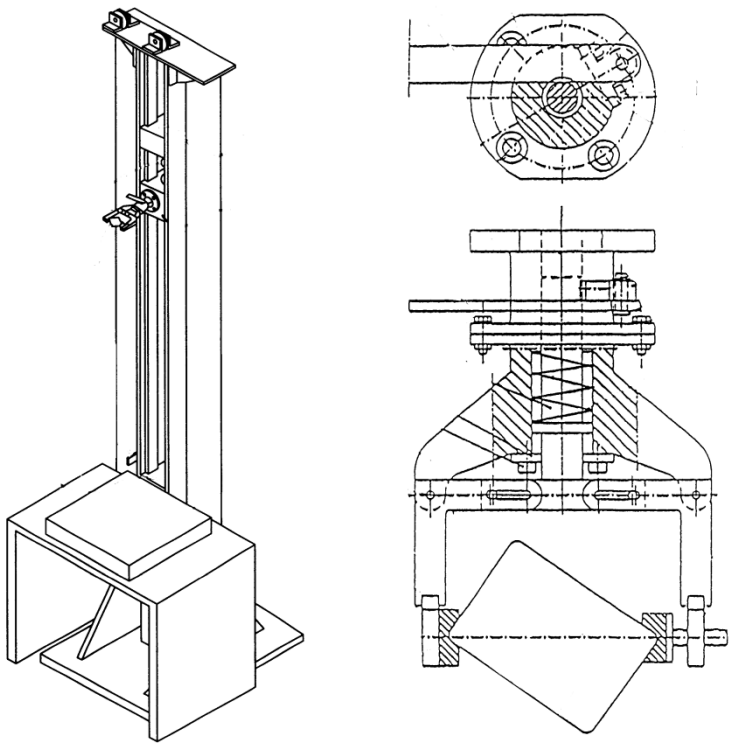

Figure 2.11 - Controlled drop test rig developed and used by Shim and Lim [14]

Tan et al. [15], using the testing rig developed by Lim et al., investigated the performance of 9 handheld electronic products. Ten different impact orientations (Figure 2.12) were investigated with strain, acceleration and impact forces measured.

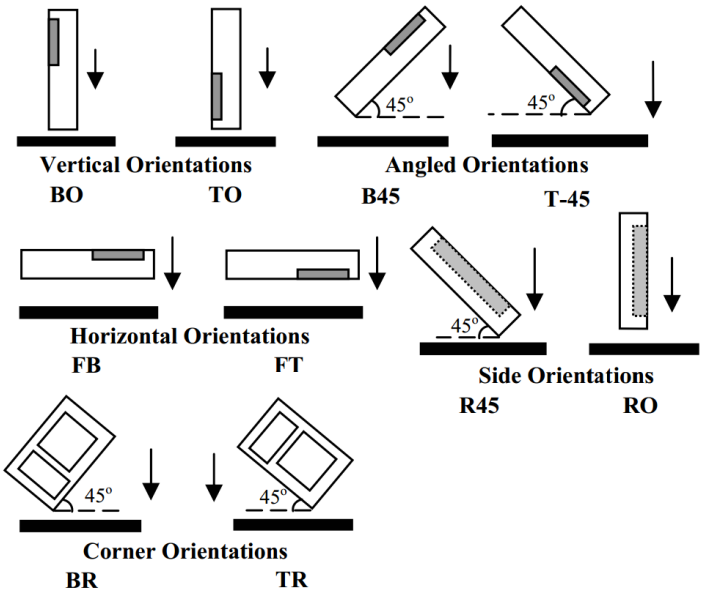

Figure 2.12 - Impact orientations used by Tan et al. for testing various handheld electronic devices [12]

Results from the drop tests show that the peak impact forces were most severe during the vertical impact orientations, followed by horizontal impacts (Figure 2.13). The vertical impacts had a higher

impact force than the horizontal impact due to the impact face exposed during the vertical impact being more rigid than the equivalent horizontal impact face.

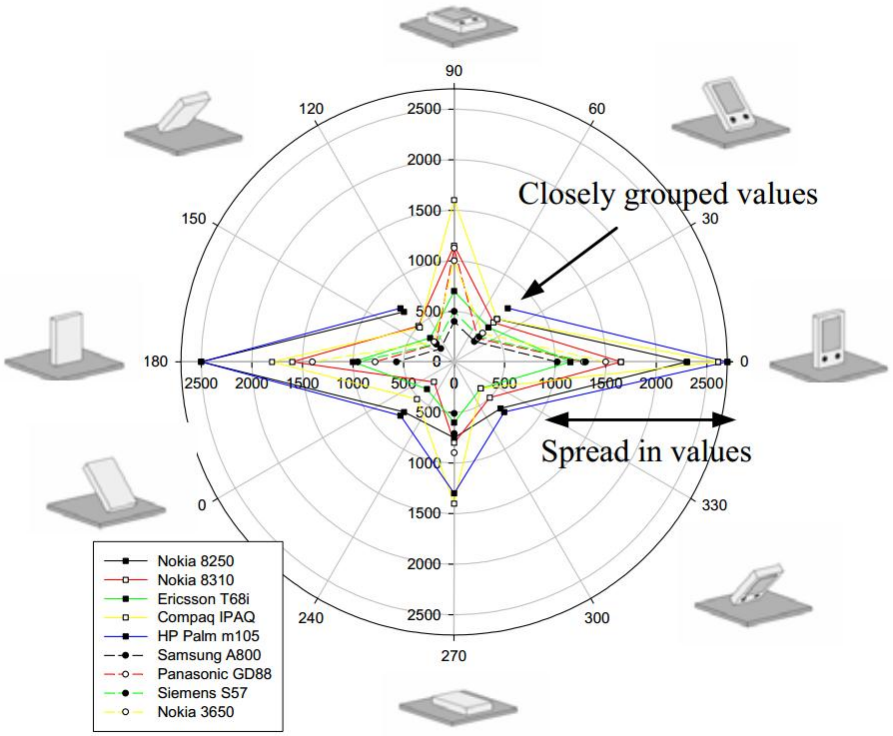

Figure 2.13 - Peak impact force of handheld electronic devices at various impact orientations[15]

Impact testing of more impact angles showed that some secondary impacts (clattering) could result in higher impact loads, particularly at impact angles close to horizontal (Figure 2.14).

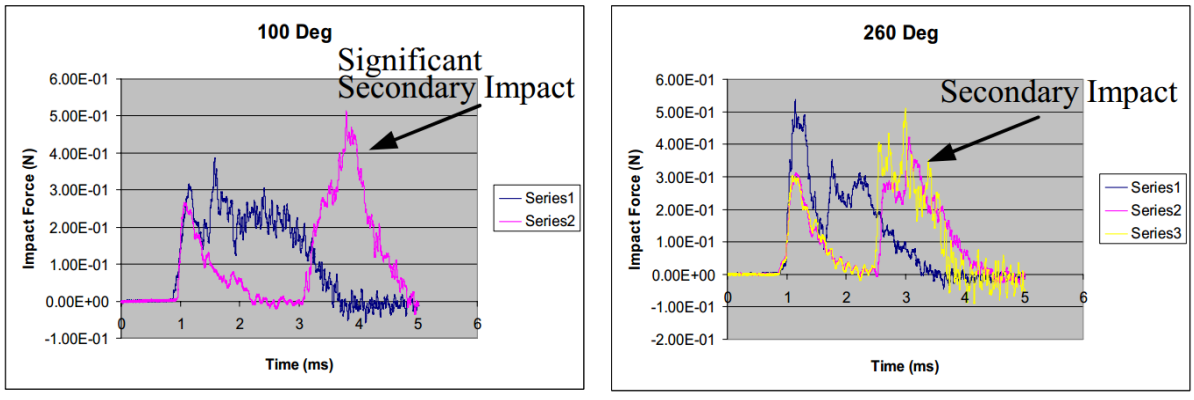

Figure 2.14 - Impact force at two impact angles demonstrating the occurrence of high secondary impacts (clattering) [15]

Measurements of strain on the PCB showed the horizontal impact generated the highest peak strain values (Figure 2.15). The large strain experienced by the horizontal impacts was attributed to the inertial direction being aligned with a low bending stiffness direction of the PCB assembly.

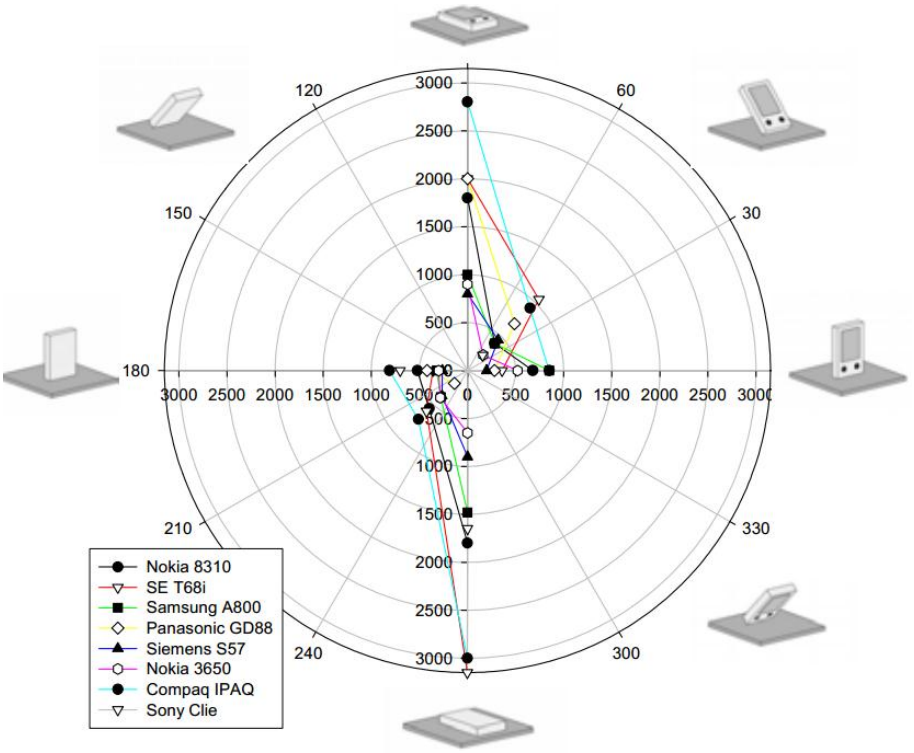

Figure 2.15 - Peak strain of handheld electronic PCBs at various impact orientations [15]

Knocking between PCBs and adjacent components was also observed during the testing by Tan et al. One example was identified by testing a Siemens phone with and without the battery; tests showed an increase in peak strain when the battery was removed (Figure 2.16). The increase in strain was likely due to the loss of rigidity of the case causing the case to bend more which meant that the PCB no longer came into contact with the outer case as they deformed in unison.

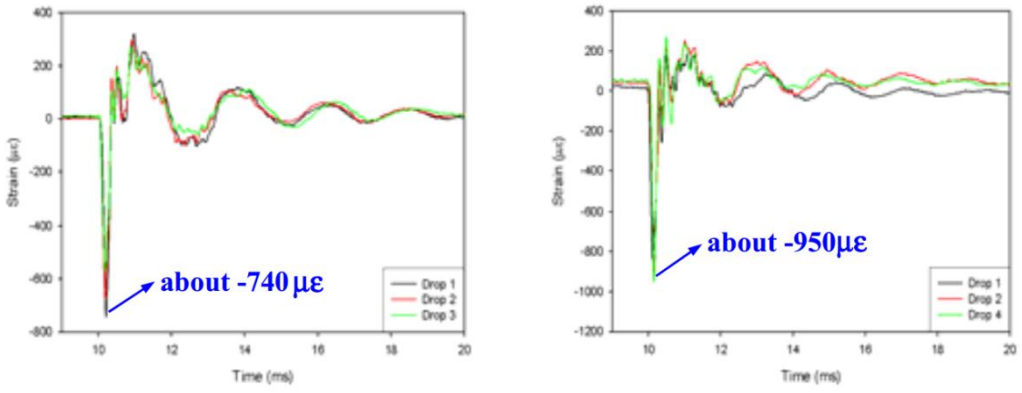

Figure 2.16 - Longitudinal strain of a Siemens with (left) and without (right) battery [15]

Another interesting phenomenon observed was that a longer battery significantly increased the overall rigidity of the test product, restricting bending. A Siemens S57 and Nokia 3650 (Figure 2.17) gave similar impact forces of 1300 and 1500 N respectively, but the Siemen S57, which has a longer

battery, attained a significantly lower longitudinal strain value of -500 microstrain (με) compared with -1700 με for the Nokia 3650

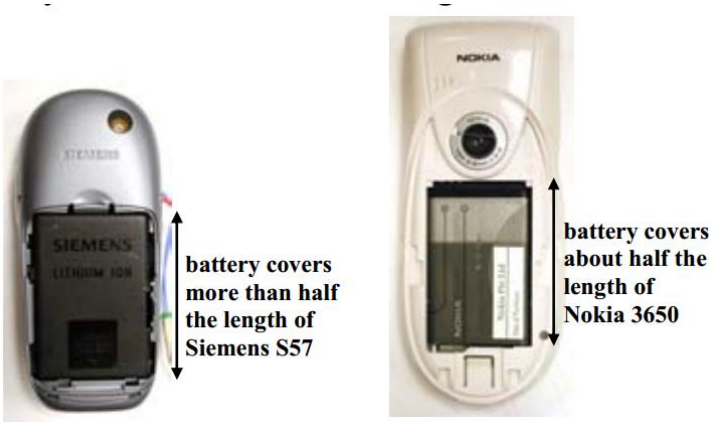

Figure 2.17 - Comparison in battery size between the Siemens S57 (left) and Nokia 3650 (right) phones [15]

The effects of secondary impacts, knocking and the size of the battery on measured PCB strains can only be observed on an unconstrained system level drop test.

2.5. Board Level Tests vs. System Level

Board level tests provide useful information on the impact resilience of electronic components; however it is important to understand that passing a board level test does not guarantee the survival of the components within a system level environment. Ong et.al [16] compared the mechanical response of printed circuit boards subjected to board level and system level impacts. They showed differences in loading dynamics between the board level and the system level tests, namely:

- The rigid mounting of the board to the test table does not allow the board to rotate, making it unable to execute its natural dynamics
- Interaction between the board and other parts are not considered during board level tests
- Impact against the edges and vertices are difficult to achieve in board level tests due to the column mounting scheme
- The support columns of the board level test provide different support materials (metal vs. plastic) and surfaces to that found in the system level tests

The results from measuring the acceleration and strain of a board from a Nokia Model 3210 in both system level and board level tests (Figure 2.18) generated some interesting results.

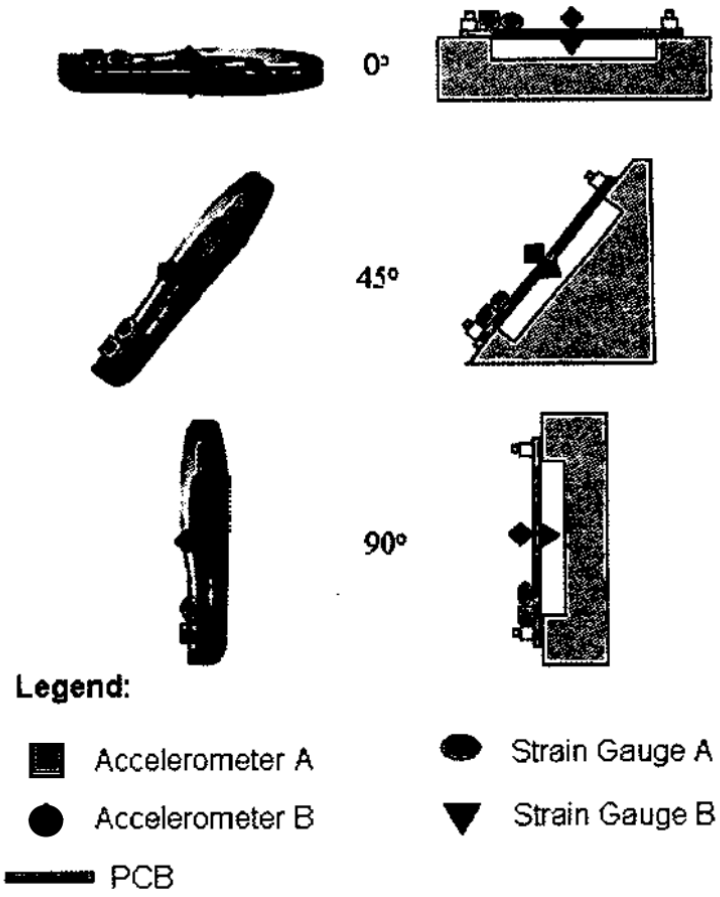

Figure 2.18 - Schematic of system level and board level tests from Ong et al.[16]

The measured PCB strain of the respective 90° impact tests (Figure 2.19 and Figure 2.20) shows a large disparity between equivalent board and system level tests. One reason for the difference is that the 90° impact subjects the circuit board to a direct impact against its edge in the system level tests which is not present for the board level test. The printed circuit board in the system level tests flexes and deforms in tandem with the casing whereas the deformation of the board level tests in normally controlled by its downward inertia. The damping in the board level test is significantly lower than the equivalent system level test.

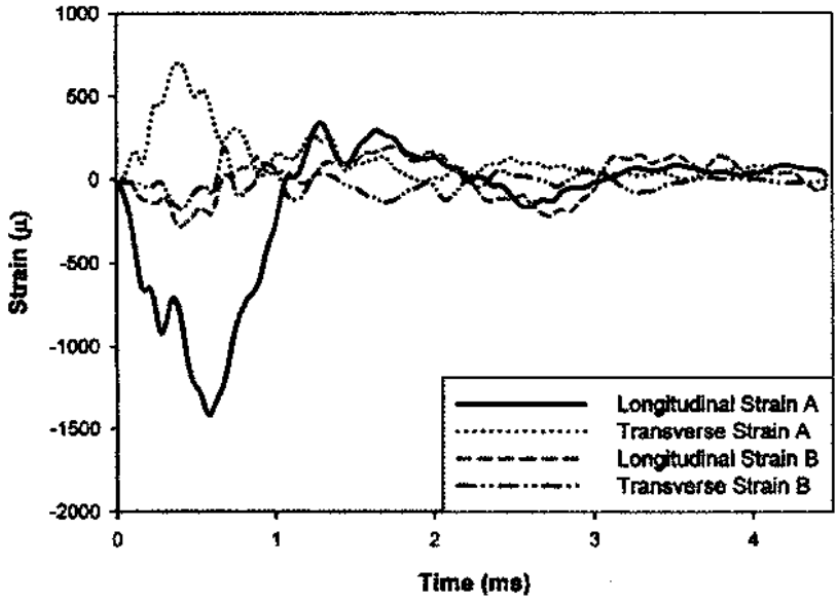

Figure 2.19 - Strain measurements from Ong et al. of a 90° system level impact test [16]

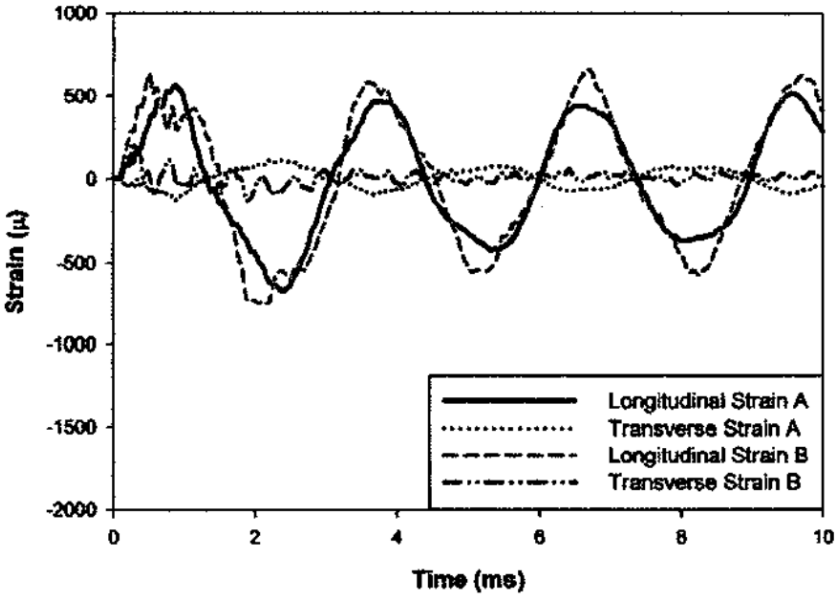

Figure 2.20 - Strain measurements from Ong et.al of a 90° board level impact test. [16] NB: The time scale is different to that found in Figure 2.19

Goyal et al. [17] also discussed the difference in dynamics between board and the system level tests. He states the advantages of performing board level/rigidly attached drop testing which include:

- Shock pulse amplitude and duration can be controlled well by varying drop height and the shock absorption surface
- The impact orientation is predetermined and easily controllable
- The tests are repeatable and easy to instrument

Yu et al. [18] investigated the dynamic response of PCBs within a system level test (Figure 2.21) under different impact heights, PCB supports (Figure 2.22), casing shapes (Figure 2.23) and battery placement (Figure 2.24).

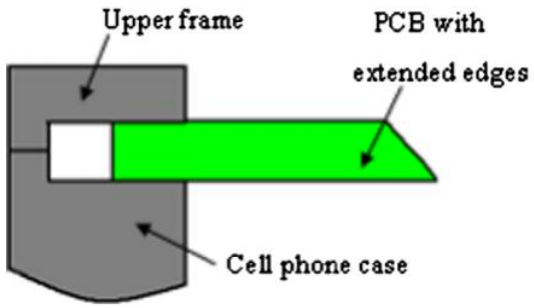

Figure 2.21 - Construction of system level test by Yu et al. [18]

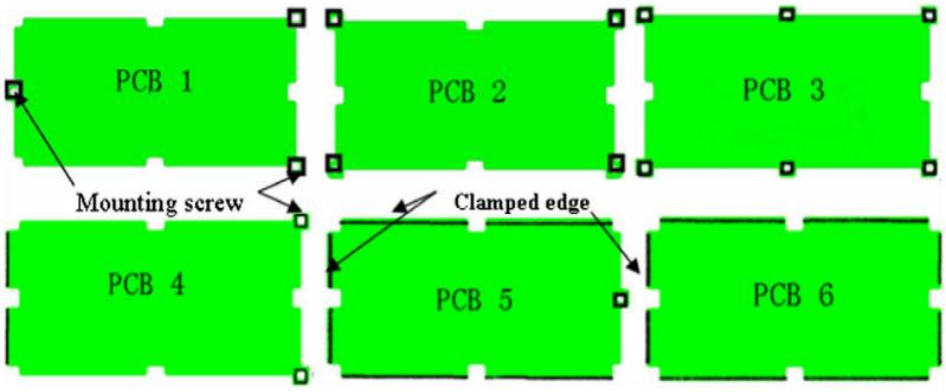

Figure 2.22 - Different clamping arrangements of PCB [18]

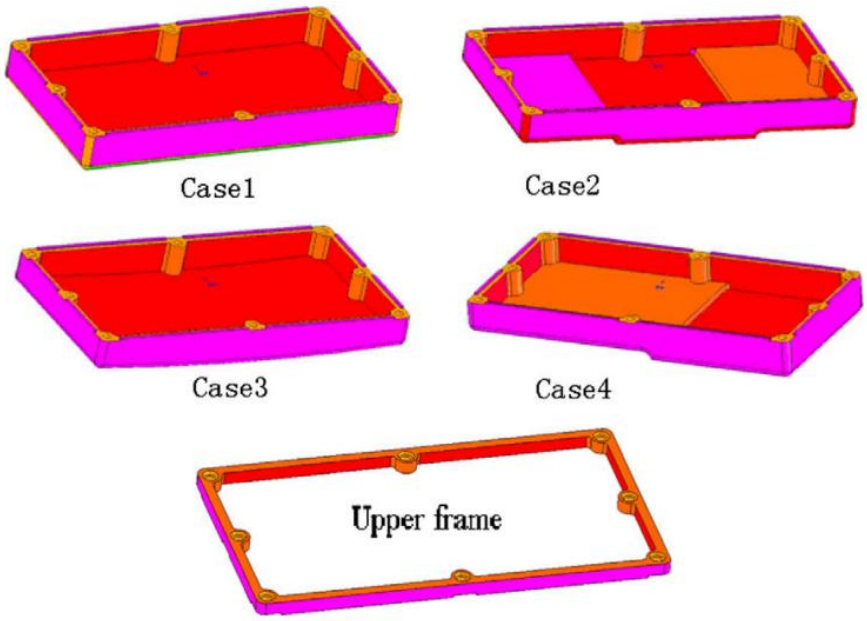

Figure 2.23 - Different case designs and upper frame investigated by Yu et al. [18]

Figure 2.24 - Battery placements used by Yu et al. [18]

Yu et al. showed that all four parameters tested (drop height, PCB clamping, case design and battery placement) had an effect on the observed displacement of the PCB. By increasing the drop height from 12 inches (304.8 mm) to 20 inches (508 mm) the PCB increased its peak displacement from 1.6 mm to 2 mm (Figure 2.25).

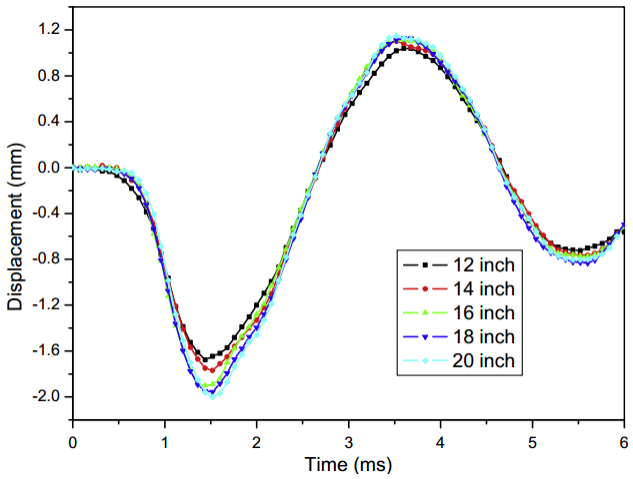

Figure 2.25 - Displacement of PCB at different drop heights [18]

The different PCB clamping methods were found to greatly alter the behaviour of the PCB. The more constrained test sample, PCB3 (6 screws), had a much smaller peak displacement of 0.5 mm when compared against PCB1 and PCB2 (3 and 4 screws respectably) which had peak displacements of just over 2 mm (Figure 2.26).

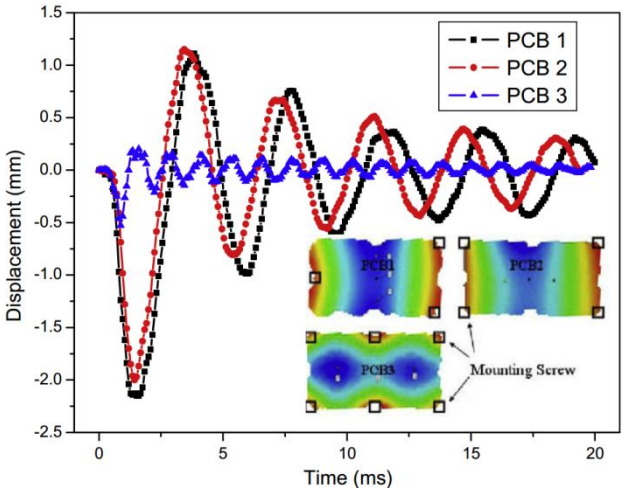

Figure 2.26 - Displacement of PCB for different screw placements [18]

Clamping along an edge in place of two corner screws had minimal effect on the maximum displacement of the PCB, although the natural frequency differed marginally (Figure 2.27).

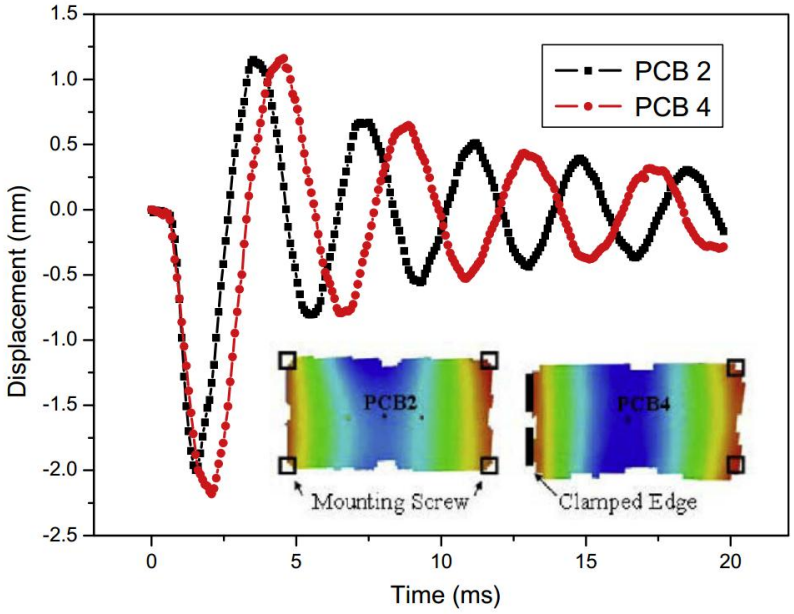

Figure 2.27 - Displacement of PCB for screw vs. clamped/screwed mounting [18]

A smaller magnitude of displacement was registered the clamped PCB's and it damped out the excitation quicker than screwed connections (Figure 2.28). This shows that a clamped constraint can be more effective at dissipating energy when compared to a screw connection.

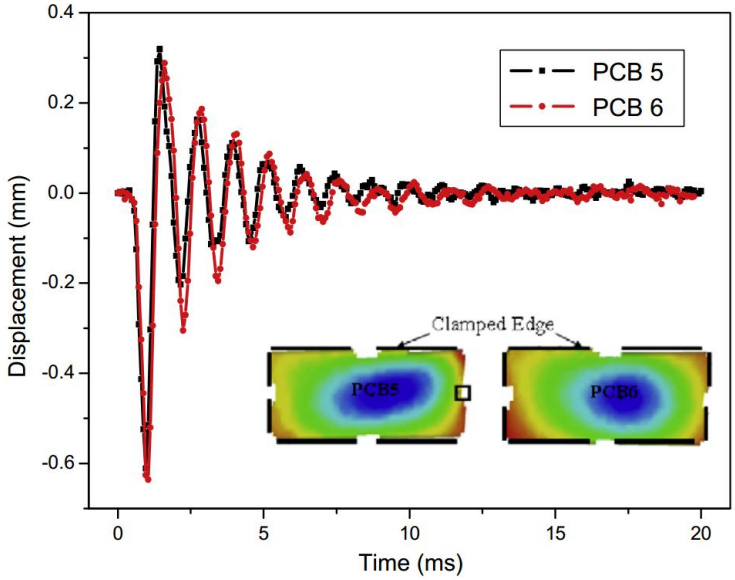

Figure 2.28 - PCB displacement of clamped PCBs [18], PCB 6 has all edges clamped whereas PCB 5 has three edges clamped, the right hand edge is secured by a screw

Testing of different cases showed that the shape of the outer case will also influence the PCB behaviour (Figure 2.29). The curved bottom (Case 3) generated the highest PCB out of plane displacement followed by the stepped case (Case 2) and the flat case (Case 1). The asymmetric case (Case 4) produced the lowest deflection, as a secondary impact occurred, which reduced the force impulse because the impact energy was spread over two impact events.

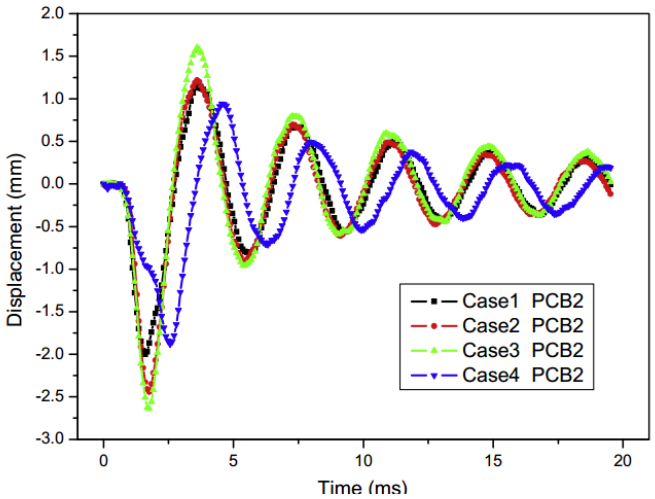

Figure 2.29 - PCB displacement for different case designs [18]

The final case schematic investigated involved looking at the effect of the placement of the battery. The battery often contributes a high portion of the stiffness and mass to a handheld electronic device, so it is important it is considered. Three battery placements were investigated: at the longitudinal centre of mass, off to the left, and no battery. The test results (Figure 2.30) showed only minor variance in the PCB displacement, which could be attributed to the fact that the battery was small (40 x 36 x 6 mm, 18.6 g) compared to the overall test assembly (106 mm x 56 mm, 25 g).

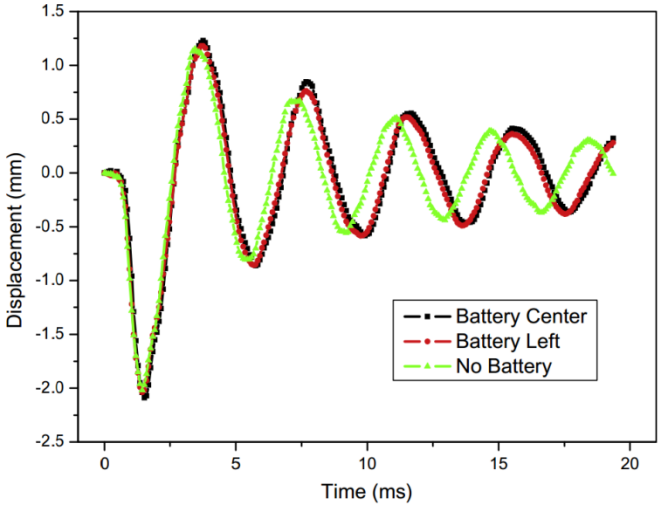

Figure 2.30 - Variation in PCB displacement for different battery placements [18]

The work by Yu et al. demonstrated the importance of understating the effects that case design has on the behaviour of internally mounted components. This level of understanding can only be generated through extensive system level impact testing and/or finite element simulation. Many of the effects are not intuitive.

2.6. Test Methods Performed at Tait

The majority of environmental tests performed on Tait handheld radios are based upon Military Standards. As well as complying with the Military Standards [19] in regard to shock impact, Tait also employs further, more stringent impact testing. This ensures that their radios are robust enough for the field conditions they commonly experience.

Tait perform a 1.8 m drop onto concrete using 26 impact orientations (Figure 2.31), repeating the test set four times. The functionality of the radio is tested every four impacts, ensuring the radio continues to transmit and receive at acceptable levels. After each set of 26 drops the radio is vacuum and pressure tested to ensure the radio is still sealed. When the four sets of drops have been completed a detailed inspection follows. This inspection includes evaluating critical components visually using a microscope, inspection for cracks using die penetrant and sectioning of components (predominately on solder connection regions).

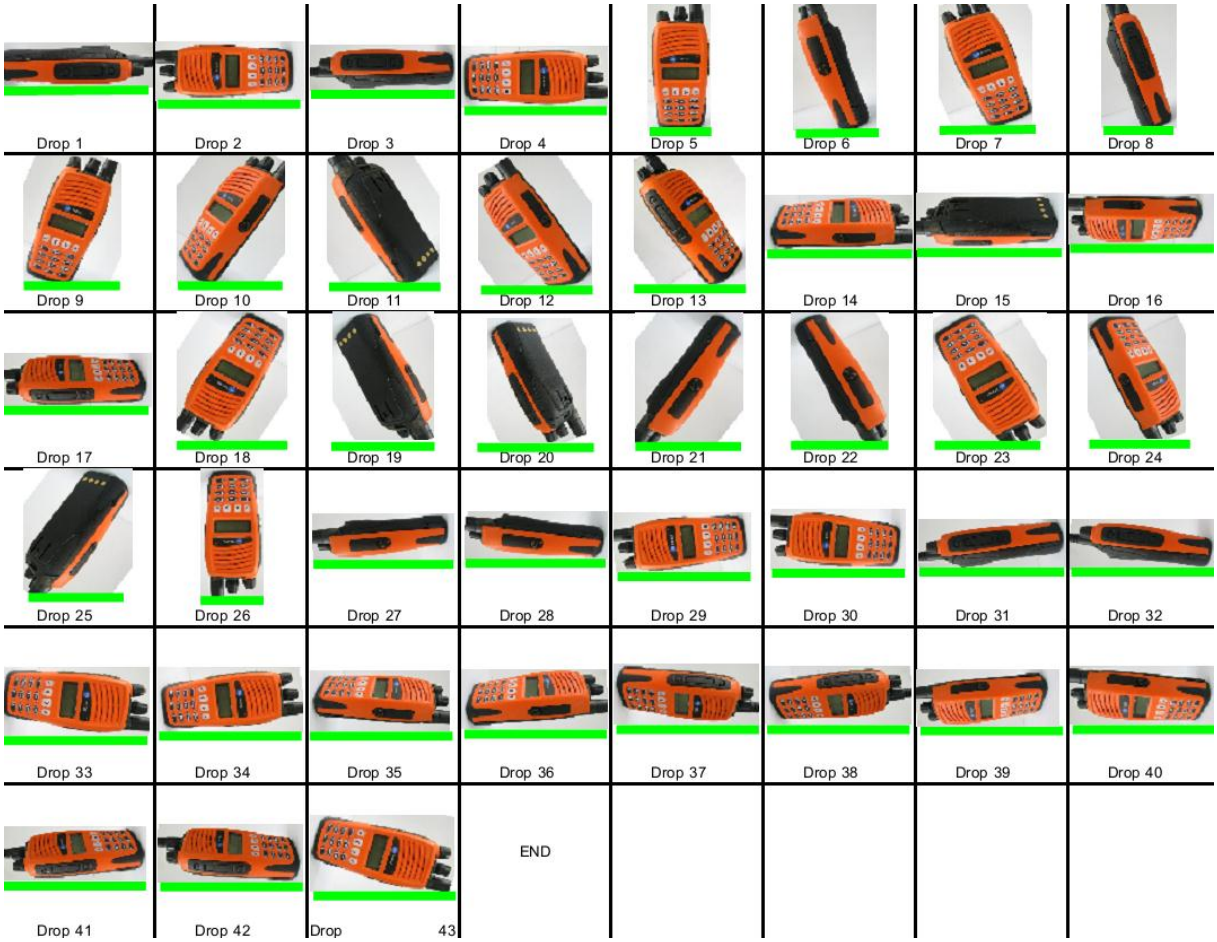

Figure 2.31 - Impact orientations tested at Tait (green line indicates ground)

Transducers such as accelerometers and strain gauges are rarely included in the drop tests performed at Tait. The test rig used at Tait uses a hook to hold the radio in place which is then pulled to release the radio. Tape is placed on the radio to create a cradle that is placed onto the hook. The release orientation is controlled, however the radio is free to rotate during free-fall making the impact orientation somewhat uncontrollable.

As well as the 1.8 m drop test, Tait also perform the falling-dart impact tests (Figure 2.32) where a rounded weight is dropped onto the radio. The dart weighs at approximately 1 kg, has an impact radius of 25 mm and is commonly dropped from a height of 1 m. This test is used to ensure the radio can survive point impact events, experienced when an object is dropped onto the radio or the radio is dropped onto an uneven surface.

Figure 2.32 - Falling dart test fixture

2.6.1. Limitations of tests

The free-air rotation infers that it is difficult to control the orientation at impact. The absence of instrumentation also makes it challenging to quantify any improvements made via modifications apart from visually inspecting at the extent of damage. For this project it was important to have reliable and repeatable measurements of the radio to allow the finite element simulations to be confidently validated. For validation purposes measuring transducers must be mounted onto the radio during testing. The additional cabling protruding out of the radio will further influence the rotation of the radio during free fall, making it harder to control the impact orientation using existing test procedures.

2.7. Development of Test Rig

For the purpose of validating the finite element analysis, a test rig capable of closely controlling the impact orientation of the test product was required. A test rig and test procedure was developed for

this project. A summary of the final design is presented below. For more detail on the test rig including design specifications, the design process and engineering drawings, see Appendix A.

The main design features of the rig that must be considered are the release mechanism, impact surface design, guide rail design, data measurement and acquisition, general usability and safety considerations.

2.7.1. Release mechanism

The purpose of the release mechanism is to hold the radio at a set orientation and to cleanly release the radio just before impact with the base of the test rig.

An electromagnetic design was selected to hold and release the radio (Figure 2.33). An electromagnet attached to an adjustable plate that facilitates adjustment of the impact orientation was used with electromagnetically conductive strips attached onto the radio. The release of the radio was done by removing the current from the electromagnet via an electrical switch. To ensure the radio is released at the appropriate time, a delay between dropping the table and switching off the electromagnet was tuned with the aid of high speed photography.

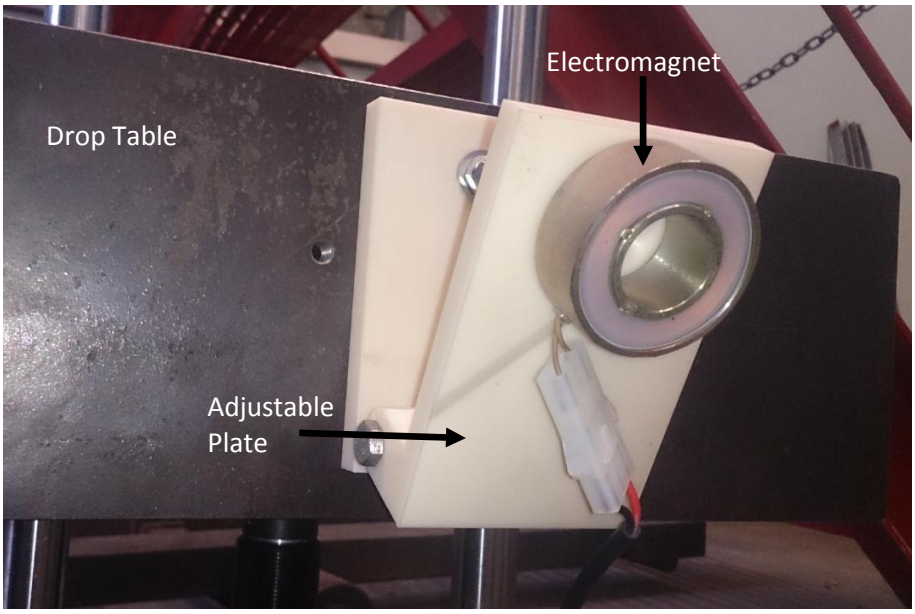

Figure 2.33 - Release mechanism and drop table design

2.7.2. Impact surface

The impact surface is important for recording the impact force and duration. Two load cells that were attached to a rigid impact plate, as shown in Figure 2.34. The impact surface was a 400 mm square plate, ensuring that all impact orientations could be tested. S-type load cells were used with

each load cell having a rated loading of 1 tonne; a sampling rate of 50 kHz was used. The impact surface and load cell are mounted such that they were isolated from the rest of the test rig so that only the impact of the radio was measured.

Figure 2.34 - Impact surface design

2.7.3. Guide rails

The guide rails allow for the controlled drop of the release mechanism. Two 50 mm rods were used as the guide rails for the drop table. The rails were attached to the base of the test rig via a sleeve heat shrunk to the rails. Polymer bushings were used as the contact surface between the guide rails and the drop table. The bushings have a relatively loose fit against the guide rails, reducing the sliding resistance during free fall.

2.7.4. Data acquisition

A significant amount of data was required to fully verify the finite element model. Acceleration and strain acting on critical components were monitored. A lightweight shock accelerometer was attached to the outside of the radio to provide a basic representation of the acceleration experienced by the radio. Strain gauges were attached to the PCB's so that their deformation could be monitored. All the data from the measurement equipment was handled by a National Instruments DAQ which was controlled by their system design software LabVIEW. LabVIEW outputs a data file, with the data processed using MATLAB.

2.7.5. Usability and safety considerations

Safety considerations as well as ease of use were incorporated into the test rig. The drop table was raised via an electric hoist mounted above the test rig. The drop table was dropped by using a quick

release rigging component that attached to the electric hoist cable. After releasing the radio the drop table was controlled by a shock absorber mounted to the base plate.

Figure 2.35 – Drop table release mechanism open and shut (top) and shock absorber (bottom)

2.7.6. Overall dimensions

The final design is shown in Figure 2.36. The test rig stands at 2.45 m tall and has an 830 x 700 mm base.

Figure 2.36 - Constructed test rig

2.8. Summary

There are numerous test methods that can be used to identify the impact resilience of handheld electronic devices. Each method can find use at various stages of the concept, development and validation stages of a product design. Board level testing and constrained system level tests provide good repeatable experimental data however these tests do not accurately recreate the behaviour (globally and locally) of unconstrained system level drops. Constrained tests are commonly used for comparative testing, for example, different solder compositions.

This project focuses on the behaviour of a fully assembled handheld radio; therefore, an unconstrained system level test state was most applicable. A test rig and procedure were developed so that reliable and repeatable impact data could be gathered and used to validate finite element results.

3. Impact Modelling using Finite Element Analysis

This chapter introduces finite element analysis and its application to impact modelling. The fundamentals of time dependent models, common solver methods and the key input parameters necessary for generating an accurate and robust drop-impact finite element model are explained. Finite element work relating to system level impact modelling of handheld electronic devices is reviewed.

3.1. Finite Element Introduction

Drop-impact testing can be very complex as discussed in Chapter 2. Numerous parameters influence the behaviour of a portable electronic system and this makes it difficult to get a complete understanding of product behaviour using solely test data. As designs become smaller and more complex, and the time to market shortens, finite element becomes an attractive option to avoid intensive testing programs. The advantages of using finite element analysis for evaluating impact events are as follows:

- Deformation, stress, strain, etc. can be evaluated at any point
- Geometries can be hidden (or sectioned to show parts that are normally hidden from view)
- The impact event can be slowed down giving a better understanding of how stress waves propagate through the system
- The simulation can be rescaled so that small deformations are more visible
- Different designs can be investigated without the need for physical prototyping
- Issues found during testing or use can be recreated in a finite element model to better identify the root cause of the problem. This understanding leads to the development of a solution which targets the root cause of failure(as opposed to an educated guess)
- Parametric studies can be performed to optimise designs

The issue with finite element analysis is that it can be very difficult to achieve accurate results, especially when events occur over a very short time period and complex assemblies are involved. To get usable results from finite element analysis a good understanding of the finite element analysis solvers becomes necessary. Finite element analysis does not render physical testing completely redundant; data from tests is required to validate the finite element model, to generate input parameters (such as material properties) and to complete final product validation before releasing the product to market.

3.2. Finite Element Fundamentals

The finite element method solves problems by discretising the geometry into a series of interconnected elements which form a representative mesh of the geometry. Governing equations are applied to the individual elements and the behaviour is integrated between the elements until a solution is achieved.

There are two different solver approaches, implicit and explicit, commonly employed when investigating time dependent problems. Each have their individual strengths and weaknesses so an understanding of both is important in order that that the correct method for a given application is selected.

3.2.1. Implicit solver

The implicit solver method uses the following governing equation:

$$\boldsymbol{M}\ddot{u}(t) + \boldsymbol{C}\dot{u}(t) + \boldsymbol{K}u(t) = F(t) \quad \textbf{(3.1)}$$

where, **M** is the mass matrix, **C** is the damping matrix, **K** is the stiffness matrix, $\ddot{u}$ is the nodal acceleration vector, $\dot{u}$ is the nodal velocity vector, u is the nodal displacement vector and F(t) is the applied force vector.

The Newmark method [20] is the most common approach to solving the governing equation. The equation that must be solved at the next time step (t_{n+1}) is as follows:

$$\boldsymbol{M}\ddot{u}(t_{n+1}) + \boldsymbol{C}\dot{u}(t_{n+1}) + \boldsymbol{K}u(t_{n+1}) = F(t_{n+1}) \quad \textbf{(3.2)}$$

where the mass, damping, and stiffness matrices are predefined. Once the acceleration at t_{n+1} is known ($\ddot{u}(t_{n+1})$), the velocity and displacement can be determined using the following equations:

$$\dot{u}(t_{n+1}) = \dot{u}(t_n) + [(1-\delta)\ddot{u}(t_n) + \delta\ddot{u}(t_{n+1})]\Delta t \quad \textbf{(3.3)}$$

$$u(t_{n+1}) = u(t_n) + \dot{u}(t_n)\Delta t + \left[\left(\frac{1}{2} - \alpha\right)\ddot{u}(t_n) + \alpha\ddot{u}(t_{n+1})\right]\Delta t^2 \quad \textbf{(3.4)}$$

where, Δt is the timestep, α and δ are integration parameters which determine the relative influence of the acceleration from time at t_n and t_{n+1}. Typical values for δ and α are 0.5 and 0.25 respectively.

The stiffness matrix is on the left hand side of the governing equation (3.2) so it must be inverted at each time step which is computationally expensive. The inversion of the stiffness matrix becomes especially expensive for nonlinear problems.

The implicit method is a very stable solver and conditionally stable for linear simulations. The method is widely used for transient events that consist of relatively long events (0.5 seconds and larger) and when low velocities are involved.

3.2.2. Explicit solver

The equations used in the explicit solver are the conservation of mass, momentum and energy within a Lagrangian coordinate system [21]. The mesh in an explicit dynamics model moves and distorts with the material which, in part, ensures that the conservation of mass is satisfied. The density of each element cell is calculated using the initial density, initial cell volume and the current cell volume (3.5).

$$\frac{\rho_0 V_0}{V_c} = \rho_c \tag{3.5}$$

where ρ_0 is the initial density, V_0 the initial cell volume, V_c the current cell volume and ρ_c the current cell density.

The conservation of momentum is satisfied by using partial differential equations that relate the acceleration to stress tensors σ_{ij}:

$$\rho\ddot{x} = b_x + \frac{\partial\sigma_{xx}}{\partial x} + \frac{\partial\sigma_{xy}}{\partial y} + \frac{\partial\sigma_{xz}}{\partial z} \tag{3.6}$$

$$\rho\ddot{y} = b_y + \frac{\partial\sigma_{yx}}{\partial x} + \frac{\partial\sigma_{yy}}{\partial y} + \frac{\partial\sigma_{yz}}{\partial z} \tag{3.7}$$

$$\rho\ddot{z} = b_z + \frac{\partial\sigma_{zx}}{\partial x} + \frac{\partial\sigma_{zy}}{\partial y} + \frac{\partial\sigma_{zz}}{\partial z} \tag{3.8}$$

The conservation of energy (3.9) is not enforced like the mass/momentum equations. It is accumulated overtime; this value is monitored throughout the simulation to ensure that the energy disparity does not become too large. A well-posed problem should have little to no energy conservation losses.

$$\dot{e} = \frac{1}{\rho}(\sigma_{xx}\dot{\varepsilon}_{xx} + \sigma_{yy}\dot{\varepsilon}_{yy} + \sigma_{zz}\dot{\varepsilon}_{zz} + 2\sigma_{xy}\dot{\varepsilon}_{xy} + 2\sigma_{yz}\dot{\varepsilon}_{yz} + 2\sigma_{zx}\dot{\varepsilon}_{zx}) \tag{3.9}$$

Explicit dynamics solves the solution at the next time step by using information based solely on values at the current time step. Small time increments ensure that a stable and accurate solution is achieved. The timestep of the explicit solver is controlled such that a stress wave cannot travel further than the length of the smallest element in a single timestep (3.10).

$$\Delta t \leq f \times \left[\frac{h}{c}\right]_{min} \tag{3.10}$$

where, f is a safety factor (commonly 0.9), h is the characteristic element dimension and c is the speed of sound within the material.

The explicit dynamics solver can be used to simulate nonlinear structural events which may include:

- Impact at low (1 ms^{-1}) or high (5000 ms^{-1}) velocities
- Stress wave propagations (through solids and liquids)
- High frequency dynamic responses
- Large deformations and geometric nonlinearities
- Complex contact conditions
- Material damage
- Buckling and snap failure
- Failures of bonds, welds and fasteners
- Flexible and rigid bodies

Explicit dynamics is most suited to short solver periods, a few milliseconds or less. Events longer than one second are possible however long computational times will occur due to the small timestep required by the solver.

After reviewing how each of the implicit and explicit solvers are implemented, it becomes clear that the explicit solver will be superior for the evaluation of short impact events like that of a handheld electronic device drop. The implicit solver is better for longer impact events (1 seconds and larger) but struggles with nonlinear events.

3.3. Important Finite Element Parameters

There are numerous parameters present during an initialisation of a finite element model. An understanding of how these parameters affect the behaviour of the impact system is vital for generating a model which appropriately reflects the physical system.

3.3.1. Material model

Material properties are needed to construct the mass and stiffness matrices. The quality of these properties will greatly affect the generated results. Several material models are used depending on the behaviour of the material as well as its loading conditions. There are several material models that can be used to describe the stress-strain (stiffness) behaviour of the material.

3.3.1.1. Linear elastic

The linear elastic model is the simplest stiffness model that can be used. It requires two input values to be fully defined, the Young's modulus and Poission's ratio of the material. This material model is appropriate for materials that behave in a linear manner and experience a stress level below the yield stress.

3.3.1.2. Bilinear hardening

If the material is likely to plastically deform, then bilinear hardening may be considered. Bilinear hardening has a linear elastic region and a linear plastic region. It requires the same inputs as per the linear elastic model with the addition of yield stress and tangent modulus. Kinematic and isotropic bilinear hardening models can be used, each model deals with strain hardening effects differently. The best demonstration of the difference between the two models is shown in Figure 3.1. Isotropic hardening does not account for the Bauschinger effect but is a more efficient model to solve. The Bauschinger effect refers to the change is stress/strain characteristics as a results of the microscopic stress distribution. For example in Figure 3.1 the specimen has yielded in the tensile direction which has in turn lowered the compressive yield strength. The Bauschinger effect only affects the result when cyclic loading occurs; this means the isotropic model should be used unless the loading is cyclic in nature (generally not the case for impact events).

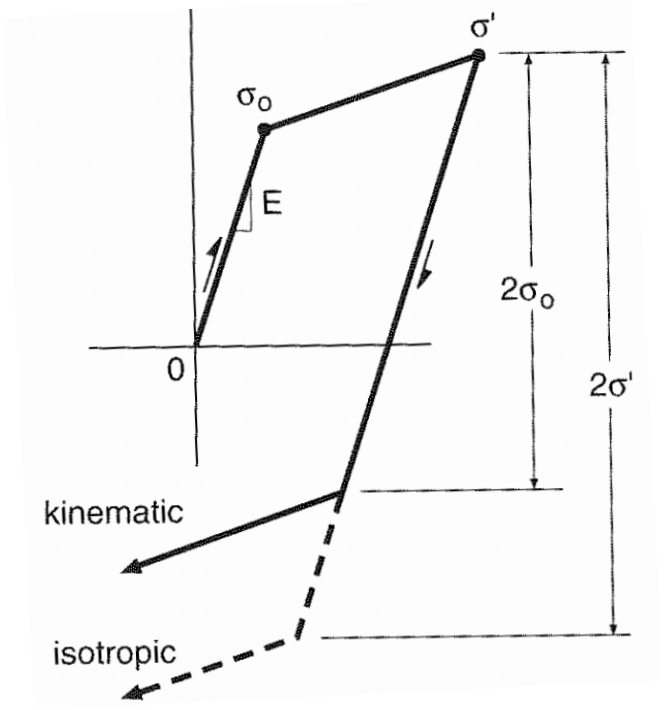

Figure 3.1 - Different unloading behaviour for kinematic and isotropic hardening [22]

3.3.2. Element types

There are a multitude of elements that can be used in finite element analysis, the three different element types used in this research are the default solid element, a solid shell element and shell element. The default solid element that is applied to the geometry does not consider bending within its elemental equations, this can generate excessive bending stiffness if an inadequate number of elements are used to define a thickness. The consideration for bending accuracy is particularly important for handheld electronics due to the thin nature of their components.

To demonstrate the accuracy of different elements for bending, the bending of a thin beam was simulated. The thin beam had dimensions of 1000 x 300 x 10 mm, was fixed at one end, a 1000 N force was applied on the top surface (Figure 3.2) and was meshed (Figure 3.3) using the three element types. The displacement at the end of the beam was generated for the three different element types; a comparison between the displacements is shown in Figure 3.5. The results show that the shell and solid shell produced comparable results, the solid element did not correlate well when only one layer was used. Adding more layers to the solid element (Figure 3.4) greatly improved the accuracy of its solution. The analytical solution of the same setup (E= 200 GPa, $d = wL^4/8EI$) gave a deflection of 25 mm, a 4% difference to the finite element result.

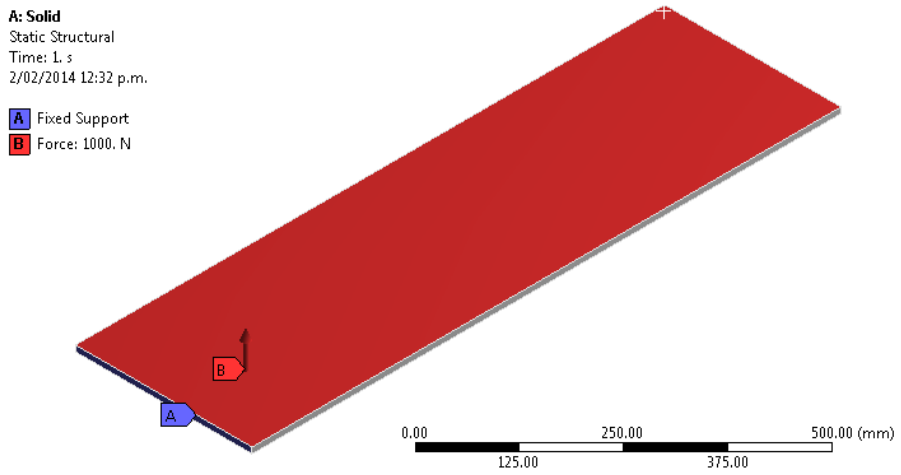

Figure 3.2 - Boundary conditions applied to beam, A (blue) is the fixed support and B (red) is where the 1000 N force was applied over

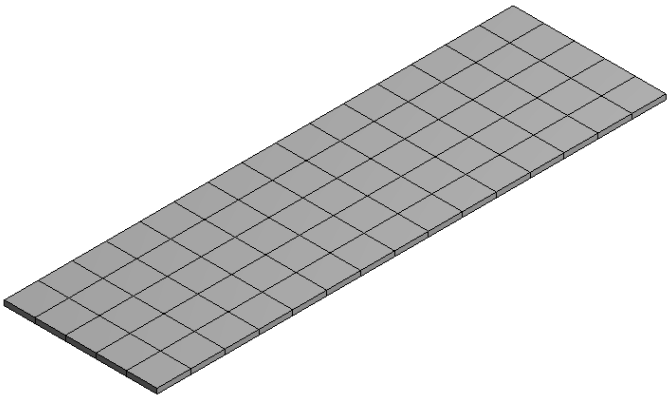

Figure 3.3 - Mesh of beam (solid shell elements used)

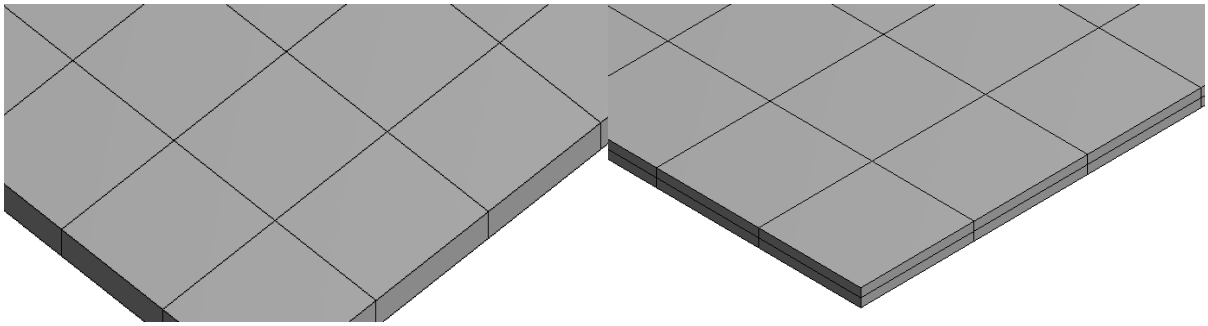

Figure 3.4 - Mesh of beam showing different number of solid element layers, one (left) and two (right)

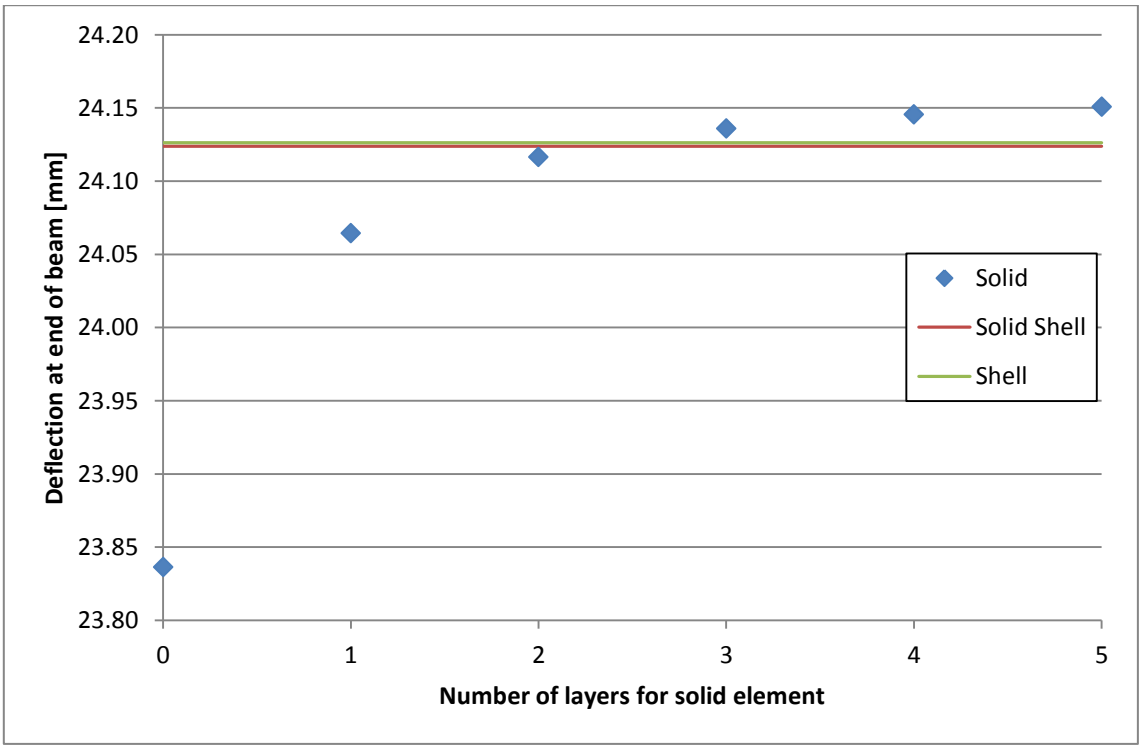

Figure 3.5 - Deflection of beam at far end for different solid element layers, compared against results of solid shell and shell elements under the same loading conditions

The solid elements shown in Figure 3.4 are solid hexahedron elements. Hexahedron elements have one of the lowest element and node counts per unit area compared to other solid element shapes. This makes the hexahedron the desirable element shape to use, however for more complex geometries the hexahedron shape is difficult to implement. Tetrahedron shaped (Figure 3.6) elements is used when the use of hexahedron elements are not possible.

The beam was remeshed with solid tetrahedron elements at different element resolutions (Figure 3.6). At low mesh resolutions the accuracy of displacement was poor, at higher resolutions the displacement compared well with that generated by the solid shell and shell element types (Figure 3.7).

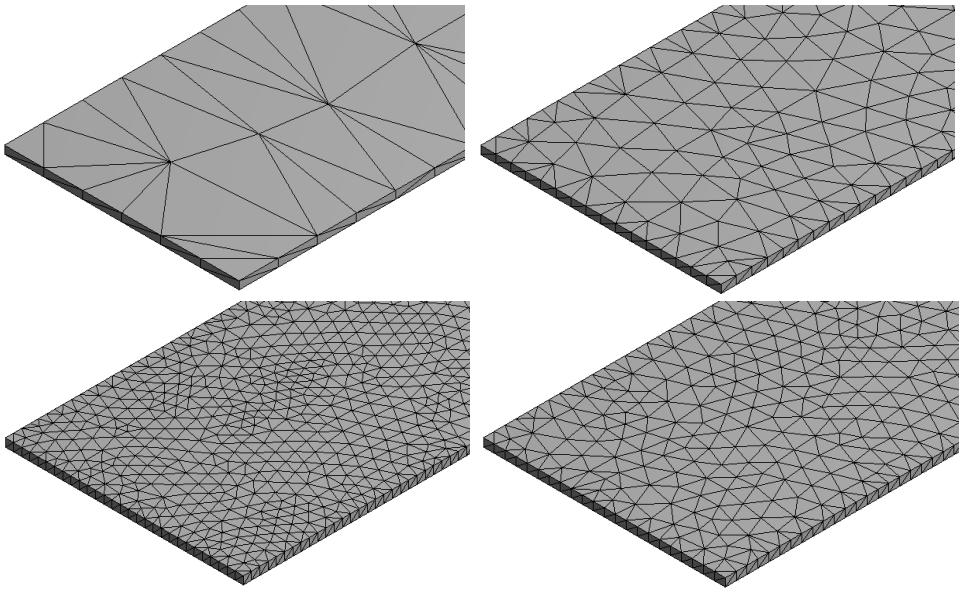

Figure 3.6 - Different mesh relevance centres for tetrahedron mesh of beam, top left clockwise, -100, -25, 25, and 100

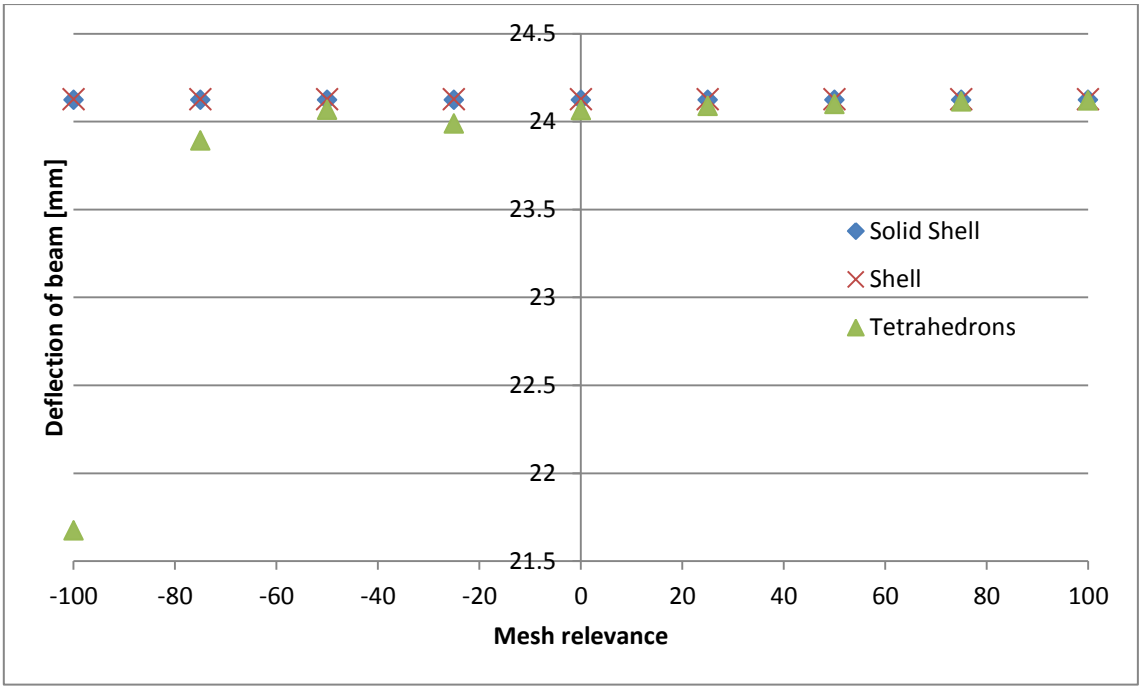

Figure 3.7 - Deflection at beam at far end for different tetrahedron element mesh relevance's (Figure 3.6), compared to results of solid shell (24.124 mm) under the same loading conditions

The results of the simple beam deflection simulation show that selecting the correct element type and resolution is an important consideration. The shell and solid shell element types are the best options for thin objects that are sweepable as they provide both accurate results with a small number of nodes/elements (Table 3.1). Solid hexahedron elements work well for elements that are thicker but still able to be swept. If geometries can be split to make sweepable bodies then this is will be helpful. If the geometry is too complex for hexahedron elements then tetrahedron elements will work well but will require a higher number of nodes/elements, leading to increased computational costs.

Table 3.1 - Comparison of different element and mesh types vs. node and element count for a simple beam (Figure 3.3)

Element/Mesh Type	*Nodes*	*Elements*
Solid shell	192	75
Solid – Hex 0 layers	628	75
Solid – Hex 3 layers	1352	225
Solid – Tetra -100 relevance	584	218
Solid – Tetra 0 relevance	6346	2929
Solid – Tetra 100 relevance	16711	8022

3.3.3. Mesh controls

The method with which the geometry is discretized can have a significant effect on the accuracy of the model as well as the solving time. For the explicit dynamic solver, the ideal mesh is uniform and as large as possible without the loss of important geometric features [23].

3.3.3.1. Element size

The size of the elements has a significant effect on both the solution accuracy and solver time as the timestep used for explicit dynamic events is dependent on the smallest element size. The element must be sufficiently small to accurately depict the geometry and produce reasonable results (Figure 3.6 and Figure 3.7). These conflicting requirements can result in a fast run-time that may not be accurate or a slower run-time that gives better results. The suggested procedure when developing a finite element model is to begin with a large mesh to check the behaviour and part interaction before moving on to a finer mesh. The element size can be controlled both globally, and locally (parts, face and edges) so less critical components can use a larger mesh to reduce computation time.

3.3.3.2. Pinch control

The pinch control is used to remove small features from the finite element model. The pinch feature works at the mesh level rather than at the geometry level of the model (i.e. Virtual Topology). The pinch control 'pinches out' small mesh features present in the model when they meet the user defined pinch size tolerance. An example of pinch control is shown in Figure 3.8.

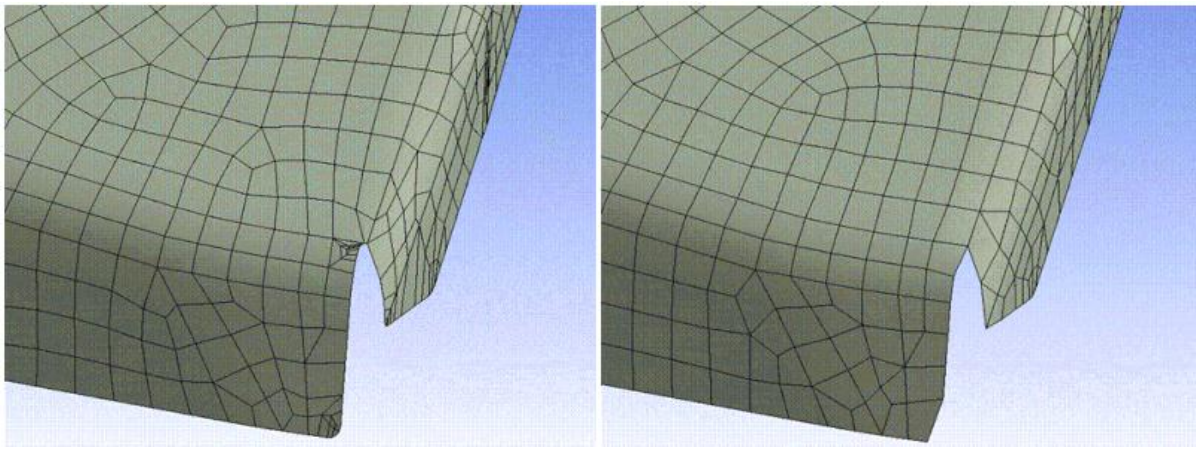

Figure 3.8 - Generated mesh before (left) and after (right) the pinch control has been applied [24]

3.3.3.3. Defeaturing control

The defeaturing tool automatically defeatures small features and dirty geometry based on the user specified defeaturing tolerance.

3.3.4. Contact conditions

The interaction between different parts is another important consideration when setting up the finite element model. There are three main contact conditions which are commonly used, bonded, frictionless and frictional. The bonded contact condition ensures that the two regions selected are 'glued together' unless the interface exceeds a specified stress limit at which point the contact between the two will break. The frictionless contact condition will allow the contact pair to slide against each other without any frictional effects but ensures that the two regions do not penetrate one another.

As well as the different contact behaviours there are different types of contact regions that can be defined, namely face to face, edge to edge, and a mesh to mesh contact condition. The mesh of the two contact regions should have matching nodes, failure to do so may lead to the applied contact constraint not behaving as desired, i.e. a face to face bonded contact may not hold or partial penetrations of parts may occur. When setting up contact conditions it is best to attempt to recreate the real life contact conditions.

3.4. Existing Impact Finite Element Analysis of Portable Electronics

One of the first published works on modelling an entire assembly was performed by Wu et al. [25]. Two examples of system level impact finite element analysis were presented; the first example analysed a cover pop off, the second focused on the robustness of the antenna housing.

The cover pop off event model used a combination of shell, solid and discrete (beam, spring etc.) element types and had a refined mesh around the area of interest (snapping hooks and locks). Results from the simulation showed that the cover pop off was a result of bending deformation of the cover. Two solutions were proposed to alleviate this problem. One solution involved the addition of foam to add pressure to the hooks, however this was found to add extra stress to the housing. The second proposed solution added tabs to the cover to restrict cover bending and prevented the hooks from sliding out. The second design was evaluated using finite element analysis and it was observed that the new design successfully eliminated cover pop off (Figure 3.9). This work demonstrated the use of finite element analysis to identify the mechanics behind a particular observed failure so that the solution can better target the problem.

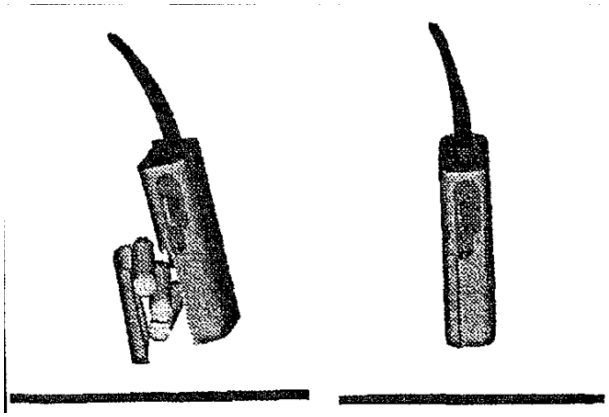

Figure 3.9 - Comparison between initial design (left) and improved design (right) with restricting tabs which successfully eliminated cover pop off [25]

The second case analysed a drop of the phone directly onto its antenna. Physical testing showed that the antenna boss was prone to breakages and cracks when directly impacted upon. A simulation was performed that evaluated the stresses around the antenna (Figure 3.10). Three design changes were proposed. The thickened antenna boss, an enlarged and thickened boss and a changed antenna support were found to reduce the local stress levels by 44%, 17% and 37% respectively. This type of investigation shows the advantage of using finite element analysis to generate quantitative data so that better informed design decisions can be made.

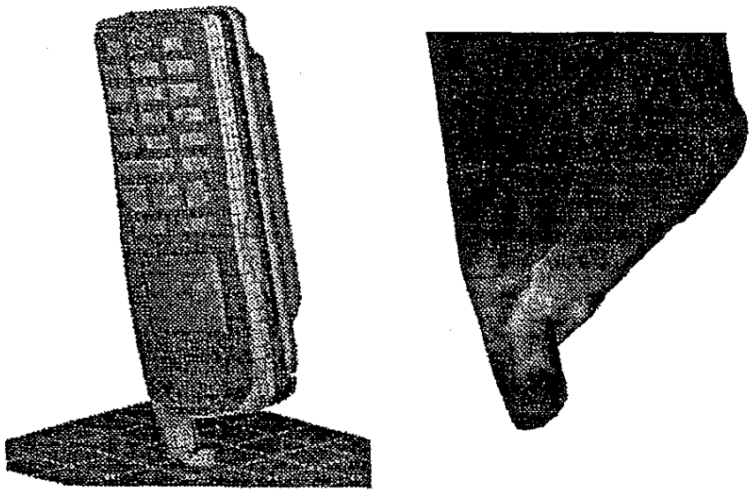

Figure 3.10 - Simulated phone drop onto antenna (left) showing stress around antenna boss (right) [25]

Liping Zhu [26] presented a modelling technique to assess the reliability of a portable electronic product under drop-impact loading. A mobile phone was modelled (Figure 3.11) and meshed using solid, brick and shell elements. At least two layers of solid elements were present to ensure bending

deformation was appropriately considered in the model. The minimum element size was controlled to ensure computational time was reasonable. Nonlinear material models were used for parts where failure (plastic deformation or otherwise) was likely to occur, for example the outer housing and the solder balls. A bilinear elastic model was used when only yield and ultimate tensile stress values were known and a piecewise linear model was used when more detailed stress strain data was available. The strain rate effect was taken into account for the PC ABS (polycarbonate – acrylonitrile butadiene styrene thermoplastic blend) material (Figure 3.12).

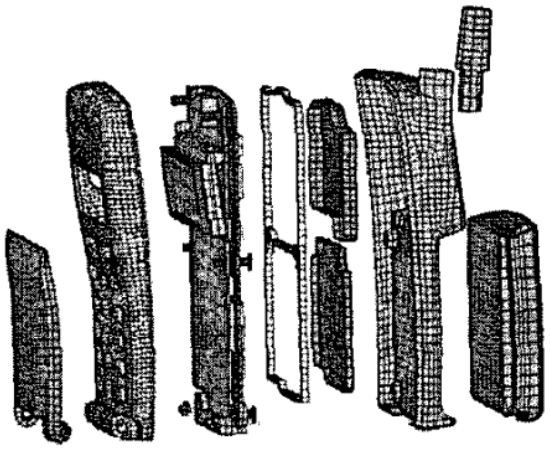

Figure 3.11 - Mobile phone modelled by Zhu [26]

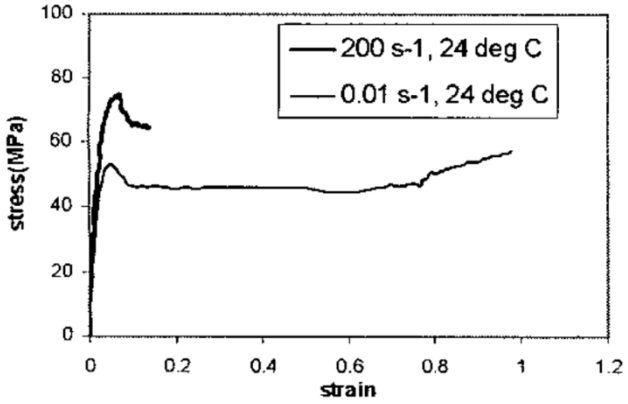

Figure 3.12 - Strain rate behaviour of PC ABS [26]

Liping Zhu used the developed model to demonstrate the disengagement of a snap fit (Figure 3.13), the disengagement of a leaf spring connector (Figure 3.14) and BGA (ball grid array) cracking in a CSP (chip scale package) (Figure 3.15).

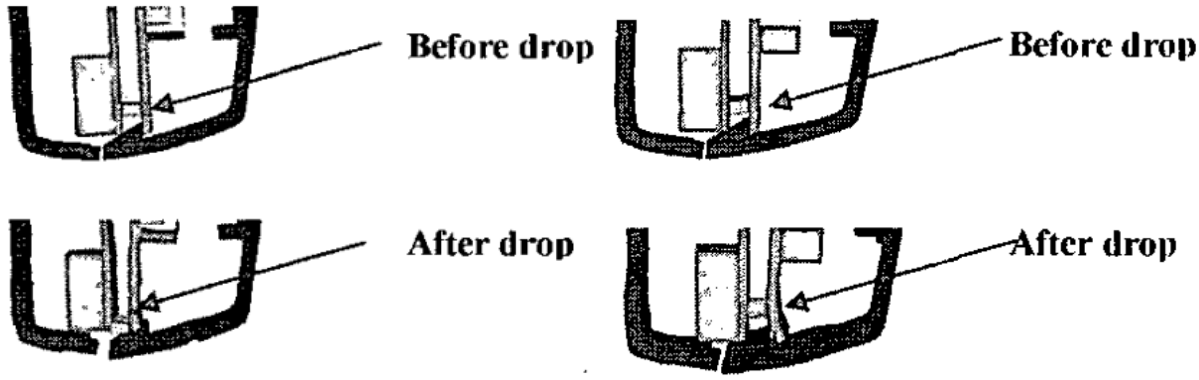

Figure 3.13 - Simulation of disengagement of snap fit before (left) and after (right) design modification [26]

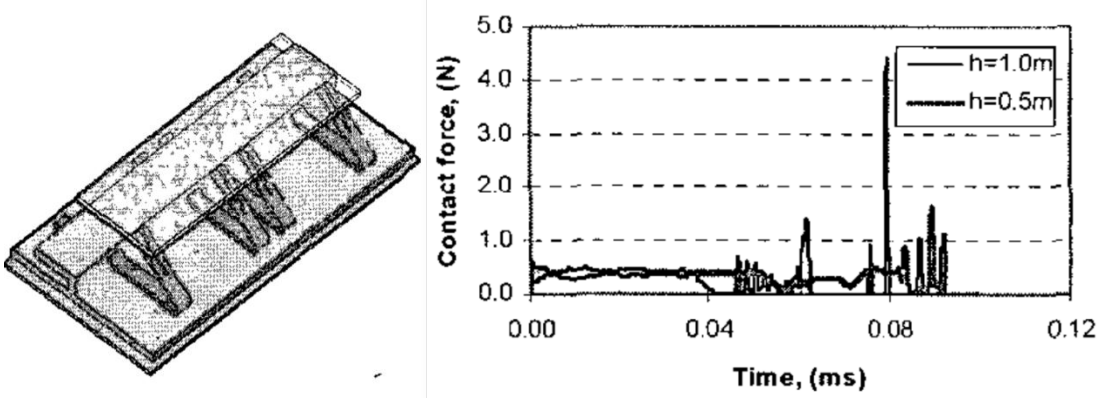

Figure 3.14 - Typical leaf spring design (left) and the contact force of leaf spring at different drop heights (right) [26]

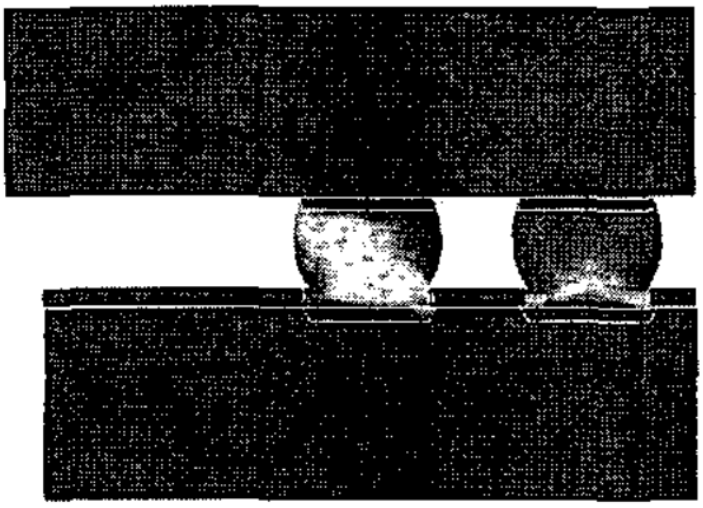

Figure 3.15 - Cross section of CSP showing plastic strain in the BGA [26]

3.5. Summary

The implicit and explicit solver methods both find applications in the evaluation of transient events. The explicit solver works better for highly transient, nonlinear, and complex contact events such as that experienced by the drop-impact of handheld electronic devices.

The element type, shape and size influence both the solver time and the accuracy mesh of the simulations. For the explicit dynamics solver, it is important to generate a uniform mesh to ensure accurate computation of the stress wave propagation. A slow transition between small and large elements should be applied. Shell or solid shell elements should be used for thin items wherever possible. Thicker geometries can employ hexahedron shaped elements rather than tetrahedrons, splitting geometries into sweepable parts if necessary. Tetrahedron shaped elements may be used as a last resort but will produce accurate results if uniform and sized appropriately, the only downside being a higher computational cost.

The accuracy of the simulation relies on the accuracy of the material properties and models used. For simple parts that are not likely to plastically deform under the loading conditions, a linear elastic material can be used. If plastic deformation is required, bilinear hardening or a multi-linear model should be used, depending on how much is known about the material's stress-strain behaviour. If a high loading rate is experienced by a critical part, i.e. the outer case of the handheld device, then a strain rate dependent model should be used.

Finite element analysis has been shown to be very useful during the development and validation of handheld electronic devices. It can be used to identify failure regions and failure modes so that targeted solutions can be developed that will effectively remedy troublesome areas. Proposed new designs and design changes can be easily evaluated using quantitative data from finite element analysis so that the best design solution is readily identified.

4. Simplified Radio Testing and Simulation

The drop tests and finite element analysis performed on a simplified handheld radio assembly are described. Impact hammer tests were performed on the radio, allowing insight into the natural dynamics of the radio, free of complex ground interactions. With minimal information, an initial finite element model replicating the impact hammer tests was constructed. The results from the initial simulation varied greatly from measurements gathered during experimental tests. Material properties, mesh refinement, contact conditions, part constraints, result filtering, system damping, element types and experimental inaccuracies were investigated to identify if and how they contributed to the disparity between the two results. Based on these findings the model was tuned to generate comparable results to those measured in the drop tests.

Drop-impact testing and equivalent simulations were performed on the simplified radio assembly. The findings from the impact hammer finite element model were applied to the drop-impact model.

4.1. Introduction

Achieving acceptable correspondence between experimental results and those generated by a finite element model the first time a simulation is run can be very difficult. Often, multiple input parameters need to be adjusted before correlation is met. The complex nature of the Tait handheld radio assembly (Figure 4.1) means there are a high number of parameters that have influence on the results, many of which are unknown quantities. The large number and complexity of parts within the Tait handheld radio assembly can cause long computation times so tuning of the finite element model would be a very time consuming process. A simplified radio was therefore initially investigated to reduce development time of the drop-impact finite element model.

Figure 4.1 - Tait's handheld radio

4.2. Simplified Radio Geometry

A mock radio assembly (Figure 4.2) was developed to loosely replicate Tait's handheld radio without the same level of complexity. The simplified geometry allowed for a cleaner and larger mesh to be used, reducing the solving time of the model. The simplified radio had a low number of parts (5) and materials (2) to minimise the number of input parameters present. The five parts that make up the simplified radio were the front panel, chassis, battery which are all made of ABS and the RF and MMI printed circuit boards (PCBs). The simplified radio had a similar overall size and wall thickness to the Tait handheld radio; its final dimensions were 131 x 56 x 38.5 mm (Tait radio is 140 x 60 x 43 mm). The PCB's used were the same as those in the Tait radio, however no electrical componentry was mounted to the boards. The boards are named RF and MMI because the RF board contains the radio frequency (RF) components while the MMI board contains all the multi-media interfaces (screen, keypad, speaker, and microphone). As the same PCB's were used, their attachment points were identical to the Tait radio, meaning similar board behaviours between the simplified and Tait radio should be expected. The simplified radio parts were designed to assemble in the same manner as

the Tait handheld radio: the mock battery attaches to the chassis, the chassis to the front panel, the RF board to the chassis and the MMI board to the front panel.

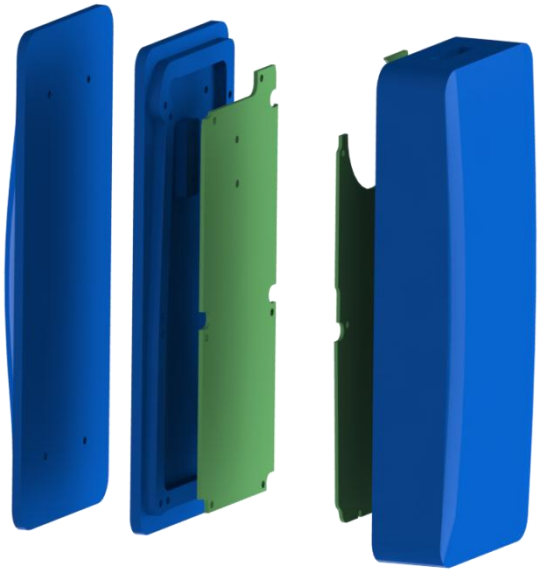

Figure 4.2 - Geometry of simplified radio (left to right), battery, chassis, RF board, MMI board and front panel

The front panel, chassis and battery were 3D printed (Figure 4.3) from ABS using fused deposition modelling (FDM). The printed product allowed experimental testing to be completed and the experimental data was used to tune and validate the finite element model.

Figure 4.3 - 3D printed mock radio, top and bottom views

4.3. Impact Hammer Testing

Initial testing consisted of an impact hammer striking the minimally constrained simplified radio (hung from a piece of string). The hammer test was used before drop-impact tests as it eliminated the complex ground contact interaction and gave insight into the natural dynamics of the radio assembly. The radio was struck in the centre of the front panel with an impact hammer (PCB Piezotronics, Model No. 086C01) that recorded the applied force and its duration. Two strain gauges were mounted on the radio, one placed on the RF board (Figure 4.4) and the other on the MMI board (Figure 4.5). The strain gauges were placed at locations where large deflections were likely to occur and were some distance away from the point of excitation. This meant that part interactions and shock wave transmission paths had to be correct to achieve conforming experimental and finite element results. The strain gauges used quarter bridge circuit boards to process the strain measurements, the circuit boards were mounted to the boards using a soft epoxy so they did not significantly influence the main boards' behaviour. A tri-axial accelerometer was mounted on the inside of the front panel (Figure 4.5).

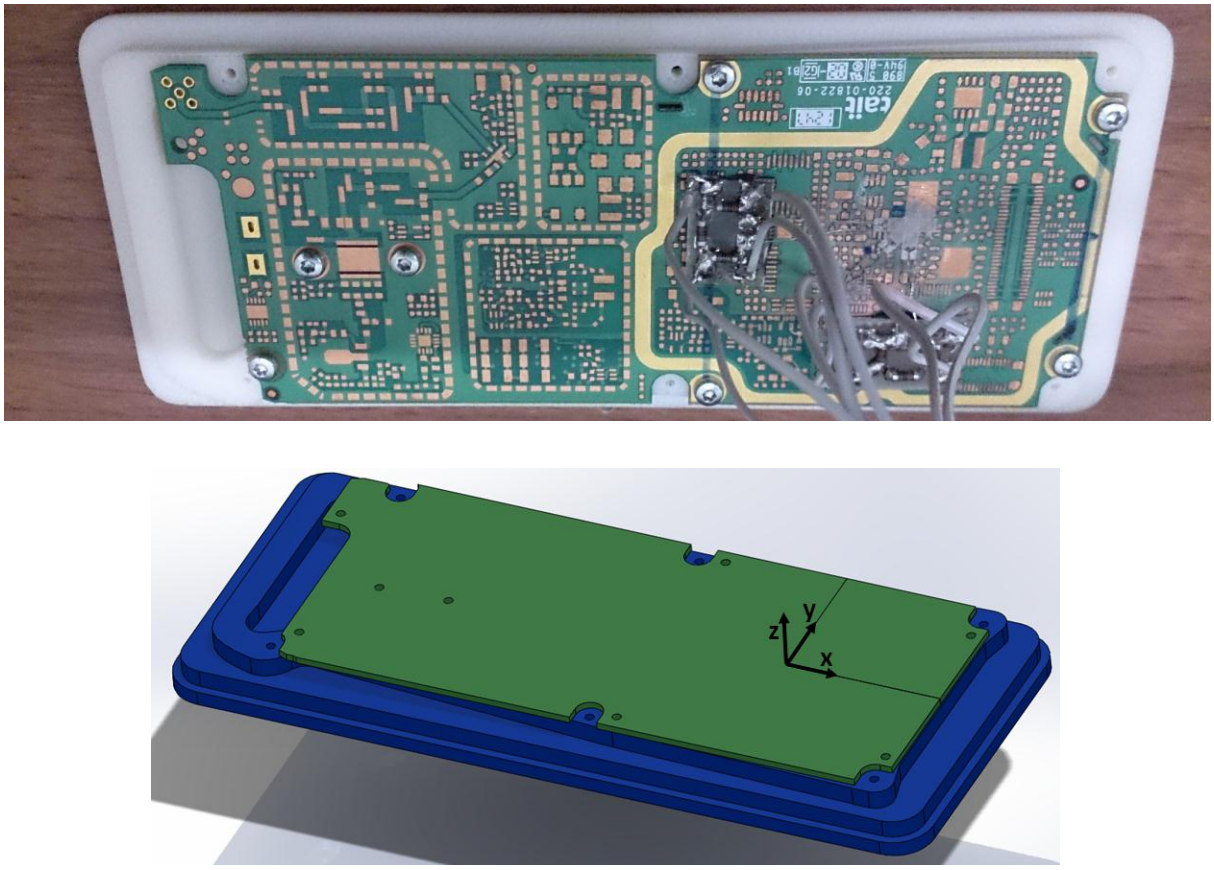

Figure 4.4 - Strain gauge mounted on RF board (top) and measurement location with coordinate system used for RF board (below)

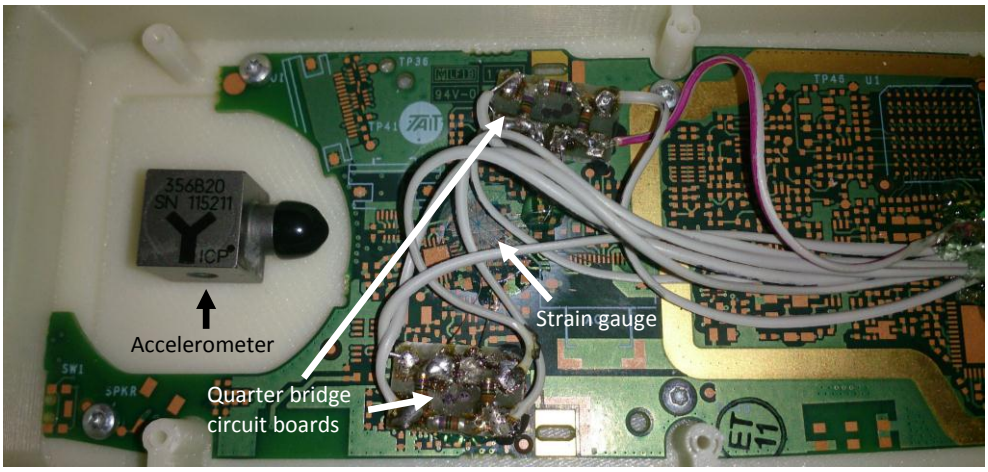

Figure 4.5 - Strain gauge and accelerometer positioning on the MMI board and front panel respectively. The strain gauge can be seen in between the two quarter bridge circuit boards. Accelerometer has measurement cable removed for clarity.

The impact force measured during the experimental tests was used as the excitation force for the finite element model. The impact hammer strikes were completed by hand which meant it was difficult to get repeatable excitation force durations and peaks between successive tests. Figure 4.6 shows the excitation pulse and subsequent strain measurements showed similar behaviours. This

consistency of the strain behaviour made it possible to use only one set of experimental measurements during the tuning and validation stages of the finite element model. Figure 4.7 shows the impact force used for the finite element analysis in addition to the strain measurements used for validation of said model. The test used during the finite element investigation has a peak excitation force of 329 N (Newton's), an impact duration of approximately 1.1 ms (milliseconds), a positive peak strain of 387 με (microstrain) and negative peak of -515 με in the x-direction and a peak of 349 με in the y-direction (coordinate system used is shown in Figure 4.4).

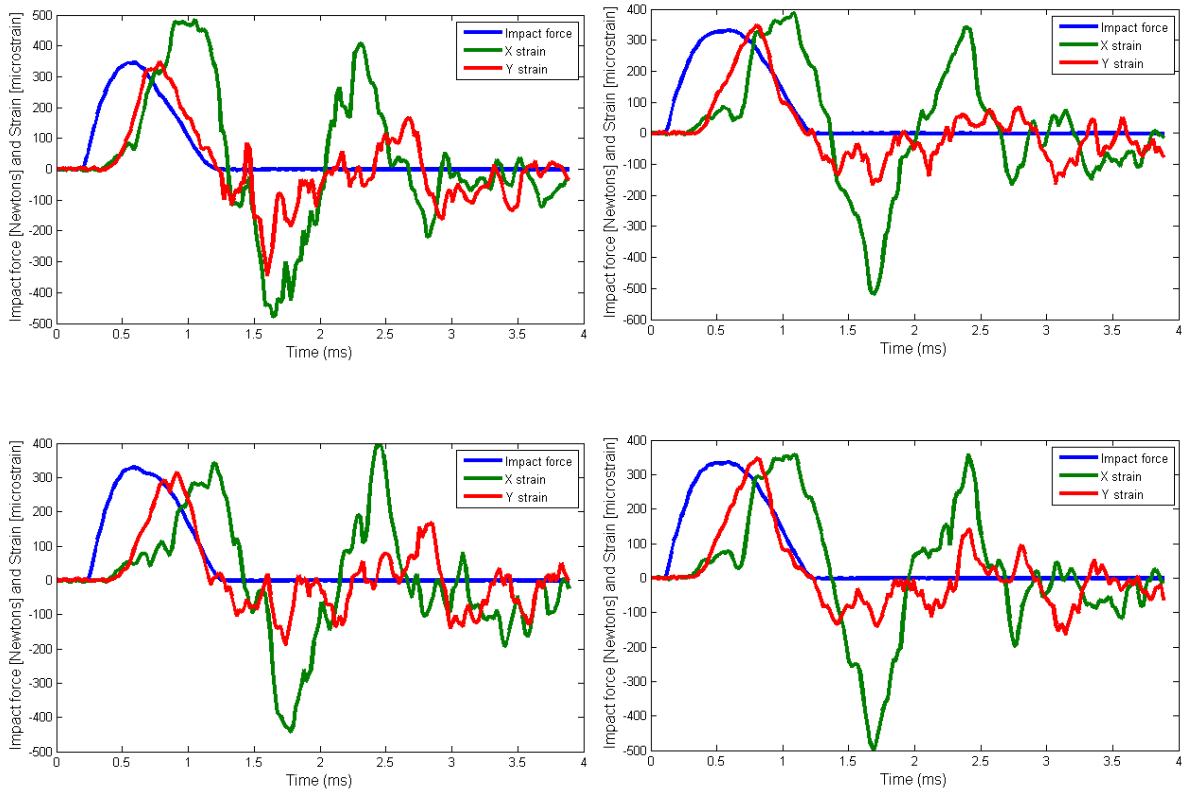

Figure 4.6 - Comparison of four impact hammer test results, showing strain measurement on RF PCB

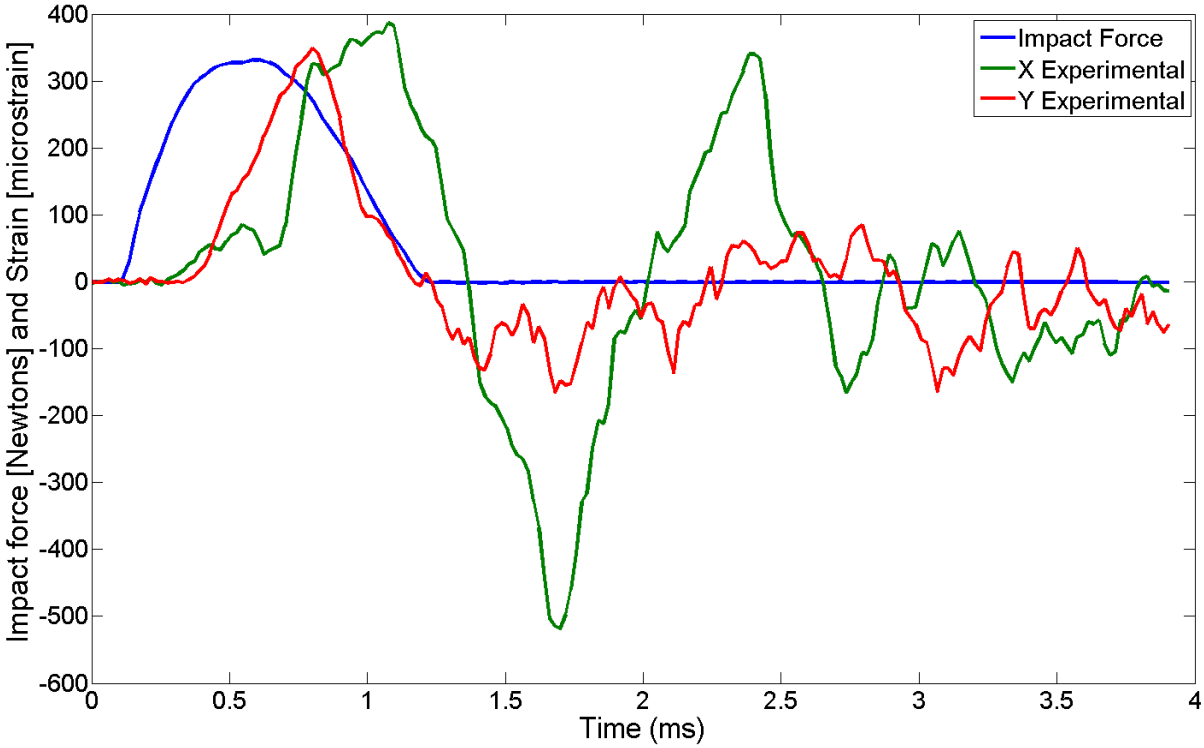

Figure 4.7 - Results from free-free impact hammer experimental tests (bottom right in Figure 4.6)

4.4. Initial Finite Element Model of the Simplified Radio

The impact hammer simulation was completed using the finite element software package ANSYS 14.5, employing the explicit dynamics solver package. A summary of the model setup is detailed below.

4.4.1. Boundary conditions

An impact force, identical in both location and magnitude to the experimental tests was applied to the front face of the radio (Figure 4.8). The rest of the radio model was unconstrained.

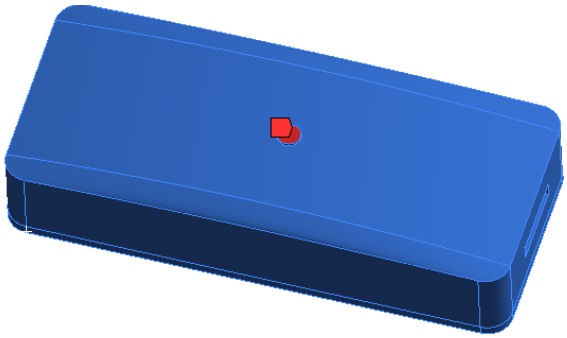

Figure 4.8 - Red circle indicating where impact force was applied, the force-time data used is shown in Figure 4.7

4.4.2. Material properties

No plastic deformation of the radio was observed during the experimental testing; therefore plasticity was not included in the material model. An isotropic, linear elastic material model was applied to all materials of the simplified radio assembly. The list of the material values used is presented in Table 4.1. The material values were assumed, taken from Ziemian et al. [27] and Amy et.al [28].

Table 4.1 - Summary of material properties used for the initial finite element analysis

Part	*Material*	*Young's modulus [GPa]*	*Poisson ratio*	*Density [kgm^{-3}]*
Front Panel	ABS	8	0.35	1100
Front Panel PCB	PCB	30	0.30	2400
Chassis PCB	PCB	30	0.30	2400
Chassis	ABS	8	0.35	1100
Mock Battery	ABS	8	0.35	1100

4.4.3. Contact conditions

Screws that were present in the physical model were not incorporated into the finite element model. The screws were replaced in the finite element model by an equivalent contact condition to increase the computational efficiency. A face to face bonded condition was used at all screw locations (Figure 4.9). The bonded condition meant that at screw locations the parts would not move or rotate relative to each other and therefore the two bodies were held together. For all other body to body interactions a frictionless contact condition was defined (Figure 4.10).

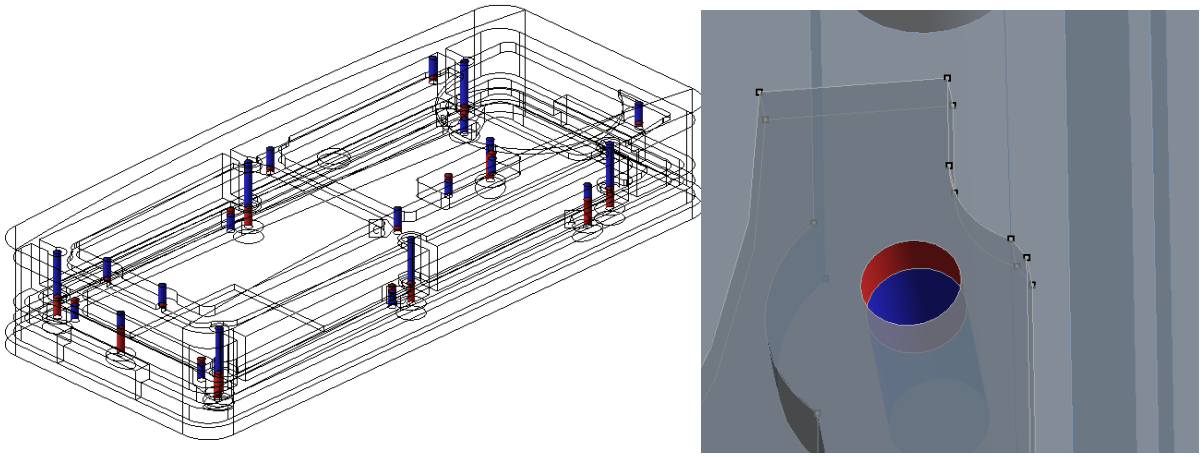

Figure 4.9 - Left – All screw locations present in simplified radio assembly where bonded contact conditions were applied, Right – an example of a face to face bonded connection for recreation of a screw constraint

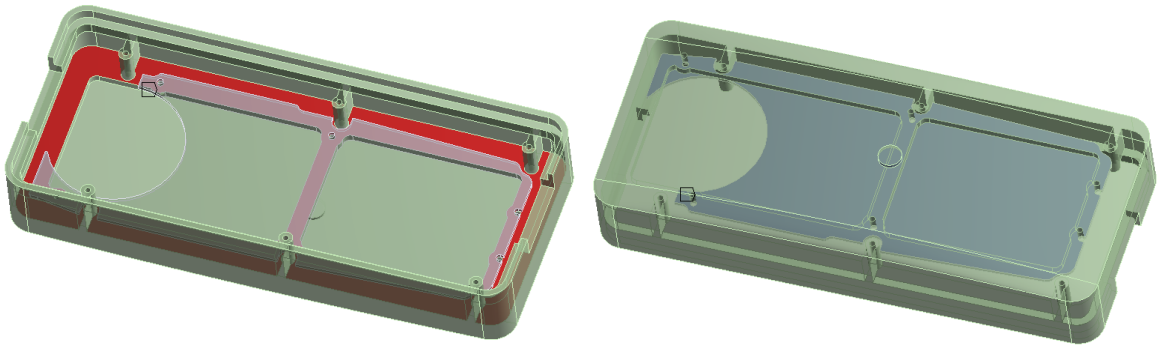

Figure 4.10 - Example of a frictionless face to face contact condition, in this case between the faces of the front panel (red) and the underside of the MMI board (blue)

4.4.4. Mesh

It was important to have a model with a relatively refined mesh (for accurate computation), but not so fine that the solving time became impractically long. The average mesh size was set to 1.5 mm, with a pinch tolerance of 0.3 mm and a defeaturing tolerance of 0.3 mm. Tetrahedral shaped elements were used to mesh the front panel, chassis and mock battery as their geometries were not easily sweepable. In areas where bending was likely to be significant (such as the front face of the front panel), the tetrahedral mesh was at least three elements thick (Figure 4.12). The two printed circuit boards were meshed with solid-shell hexahedron elements. The solid-shell element only has one element through the thickness of the board, however the solid-shell element should appropriately account for bending (as shown in Section 3.3.2).

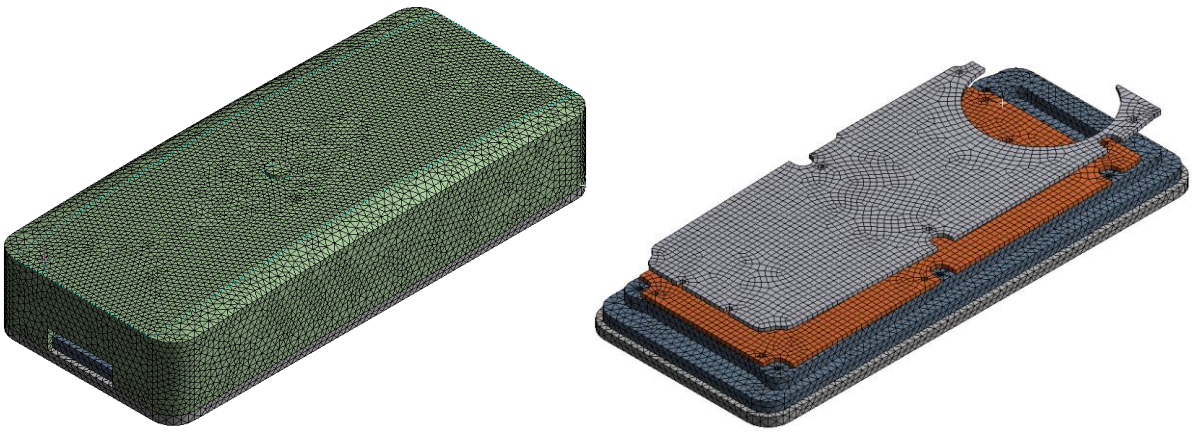

Figure 4.11 - Mesh of simplified radio for impact hammer simulation

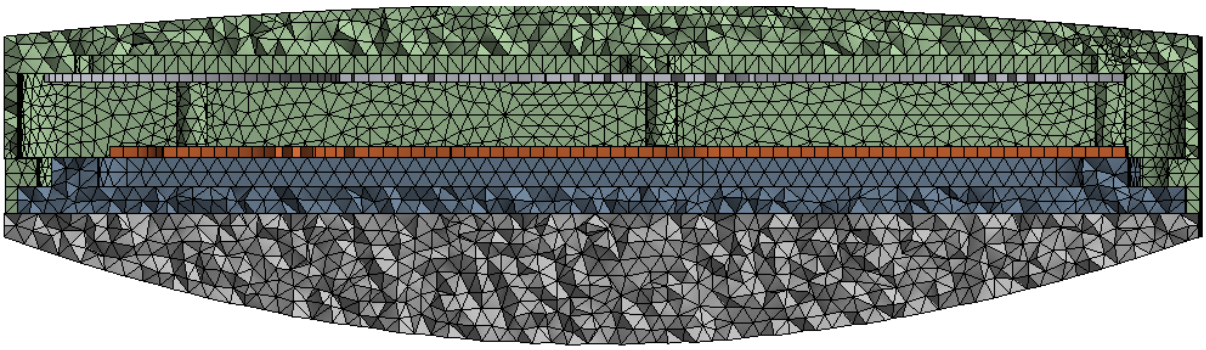

Figure 4.12 - Section view showing the generated mesh for the simplified radio

All generated elements were relatively uniform in size (1.5 mm in this case). Where smaller elements were present, such as around the screw bosses, the transition to larger sized elements was set to be slow. The smooth and slow transition of the mesh, as well as the general uniformity of the mesh aids in generating better accuracy during the computation of the stress wave propagation.

The ANSYS software is capable of evaluating the quality of elements created during the meshing process. An element quality factor is computed based on the ratio of the element volume to its edge length. Values range from 0-1, 1 indicates a perfect cube while 0 indicates a zero or negative element volume [24]. The average element quality of the generated mesh was found to be 0.808 with a standard deviation of 0.116 (Figure 4.13). The worst elements, in terms of element quality, were found to be predominantly around screw bosses (Figure 4.14).

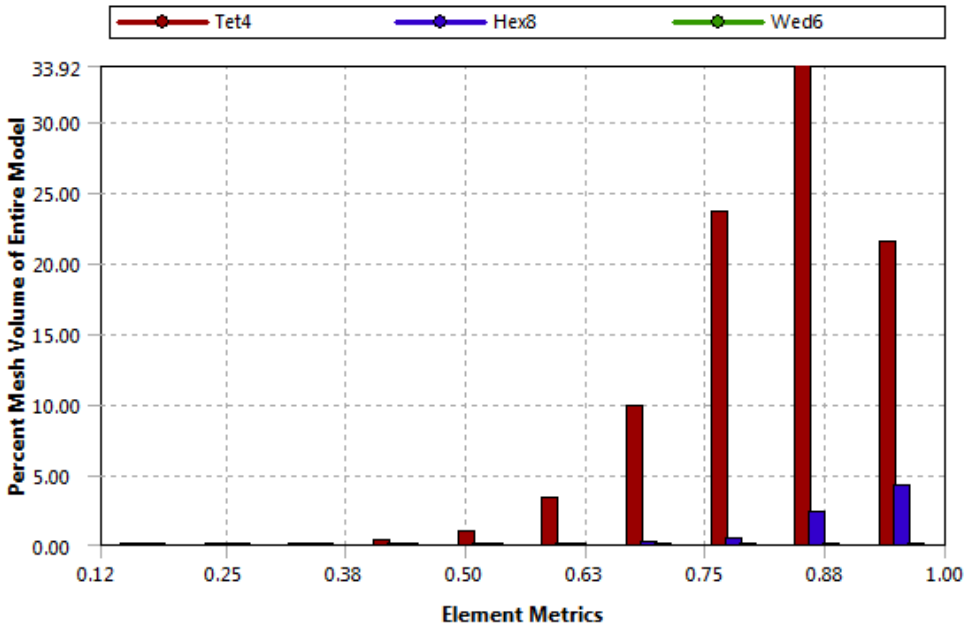

Figure 4.13 - Element quality for meshing used for simplified radio impact hammer tests

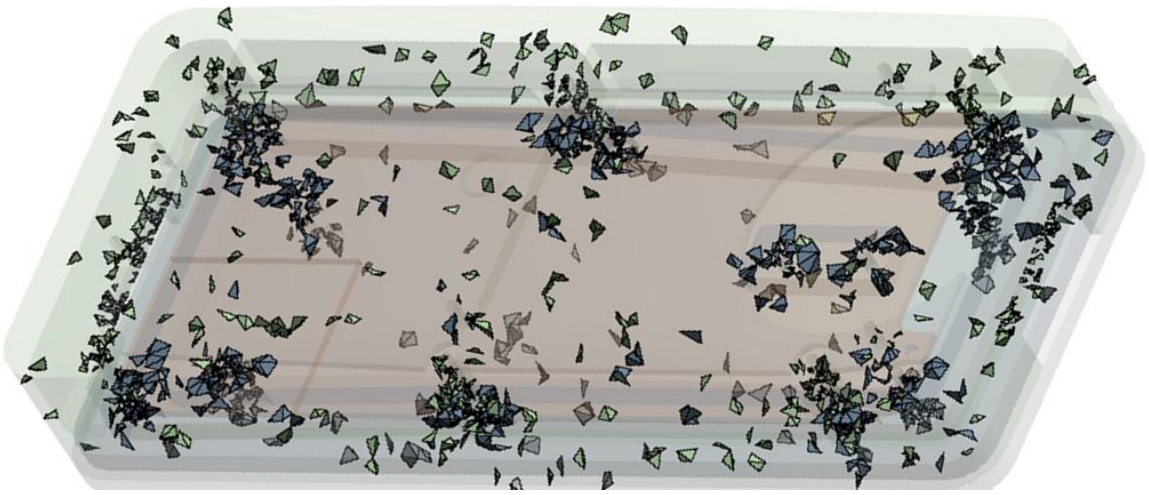

Figure 4.14 - Elements highlighted as having a low element quality value (between 0.38 and 0.5) which are predominantly localised around screw boss locations

4.4.5. Analysis settings

The solution end time was set to 3.5 ms, this end time sufficiently captures the first and second strain peaks which are enough to tune and validate the model. The time step for the analysis was program controlled, calculated with Equation (3.10) and using a time step safety factor of 0.9. A sampling rate of 100 kHz for the results was applied (350 data points were recorded throughout the simulation period). Generating a high measurement frequency gives the necessary resolution for the evaluation of critical information, such as peak values. The double precision solver option was selected under the solver controls tab. The use of the double precision option is encouraged when high accuracy is required, for example when simulating low velocity impacts. With double precision, real values are stored with a 64-bit floating point precision (compared with 32-bit for the single precision option). Using the double precision option will increase memory usage as well as the size of any restart files [29]. The rest of the analysis settings were left as default.

4.4.6. Initial impact hammer simulation results

Before any quantitative data was considered, the behaviour of the model throughout the simulation period was investigated to ensure intuitively reasonable results were produced. The stress wave route was considered; the wave started at the input force location on the front panel and propagated into the connected chassis. From there it excited the printed circuit boards, initiating at the board screw connection locations (Figure 4.15). The shock wave transmission path appears reasonable. The bonded connection at screw locations hold the parts together while other body interactions, set to be frictionless, were able to freely move while not penetrating through contacting parts. Deformations of the internally mounted boards and front panel also appeared reasonable.

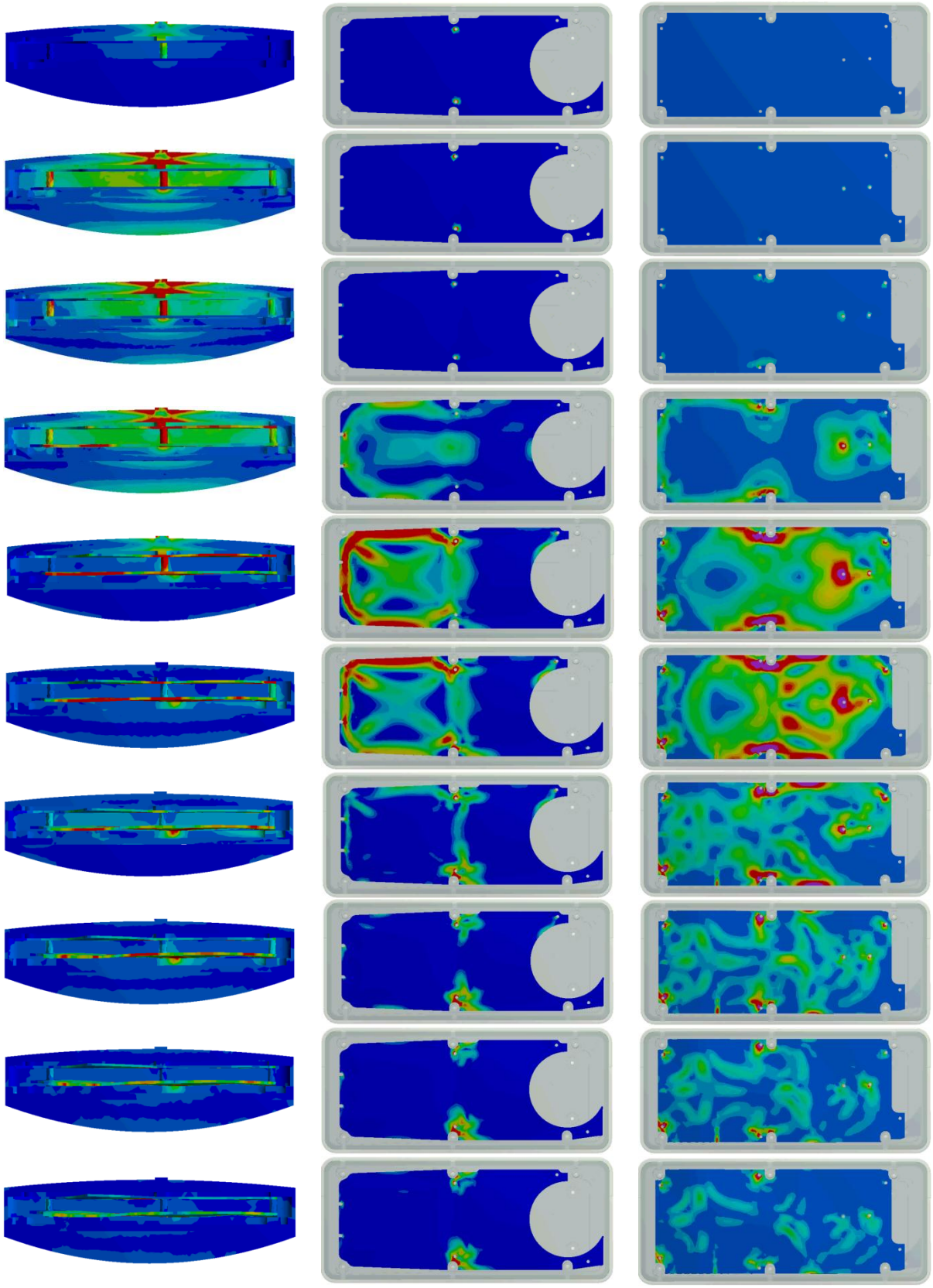

Figure 4.15 - Stress over time as a result of an impact hammer strike on top centre of the simplified radio for the sectioned assembly (left), MMI board (centre) and RF board (right). Time interval between frames is 0.2 ms, times shown from 0.2 ms to 2 ms. NB: The scale varies between views and therefore the images cannot be directly compared.

The finite element data from the initial simulation showed poor agreement with experimental results (Figure 4.16). The strain levels generated from the finite element model were significantly smaller than those present during the physical tests. The loading directions also varied between the physical and virtual models. The period of the strain response was also notably different.

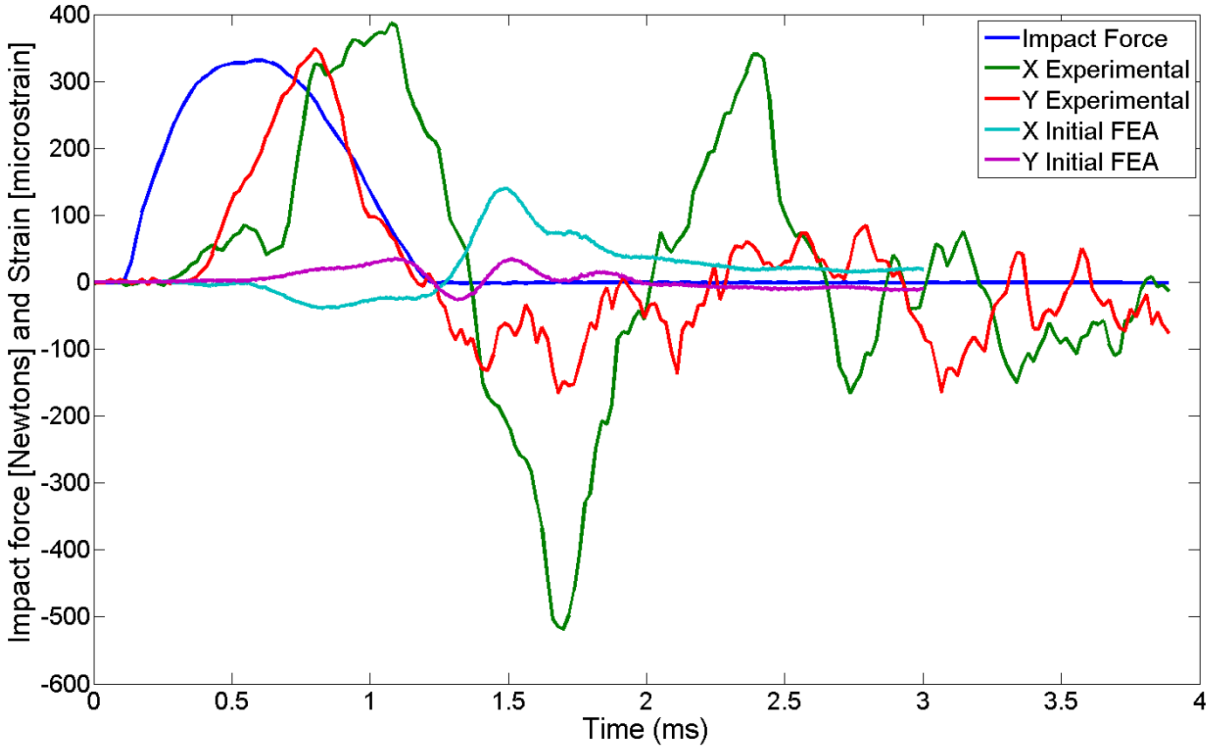

Figure 4.16 - Comparison of experimental and initial impact hammer tests

There are several possible settings used in the initial finite element model that may be contributing to the observed disparity between the two impact evaluation methods including:

- Material densities (Section 4.5)
- Material stiffness values (Section 4.6)
- Results filtering (Section 4.7)
- Contact conditions (Section 4.8)
- Mesh refinement (Section 4.9)
- Connections (Section 4.10)
- Damping (Section 4.11)
- Element types (Section 4.12)

Each of the outlined model inputs were investigated to identify if, how and why they influence the finite element model results.

4.5. Mass Effects on Finite Element Impact Hammer Results

The first parameter investigated was the density of the materials used. Test samples of both the ABS and PCB material were measured (volume and weight). The calculated densities of the materials are shown in Table 4.2. The initial simulation used assumed densities, these were found to be different to the measured material densities. Any change in density alters the inertial effects present in the model. The velocity experienced by parts during an impact hammer and drop-impact event makes inertial effects an important consideration.

Table 4.2 - Actual densities of ABS and PCB materials

	ABS1	*ABS2*	*MMI*	*RF*
Volume [mm^3]	7392	4466	4071.9	5561.7
Mass [grams]	6.84	4.24	12.95	16.63
Density [kgm^{-3}]	920	950	3180	3000
Average		**935**		**3090**

NB: The MMI and RF boards were full printed circuit boards, whereas the ABS were cut out samples

4.5.1. Impact hammer results after density changes

The simulation was re-run using the updated densities shown in Table 4.2. The change in mass of the parts within the assembly are summarised in Table 4.3, the total mass of the assembly changed from 167.96 to 152.90 grams. The ABS parts became lighter whilst the PCB parts heavier.

Table 4.3 - Summary of the change in mass of parts as a result of the change in density

Part	***Old mass [g]***	***New mass [g]***
Front panel	53.88	45.79
Chassis	28.00	23.80
Battery	62.91	53.47
MMI board	9.79	12.61
RF board	13.38	17.23
Total	**167.96**	**152.90**

The finite element strain results (Figure 4.17) show a slight increase in magnitude but overall follow a similar shape to the results from the initial simulation. The density of the material was thus corrected and the inertial effects appropriately considered. The small change in the simulation results was due to the fact that there was only a minimal change to the density and corresponding mass and not that the inertial forces are not influential in impact simulations. The results show that

the density, although changing the results was not the main contributor to the disparity between the modelled and physical test results.

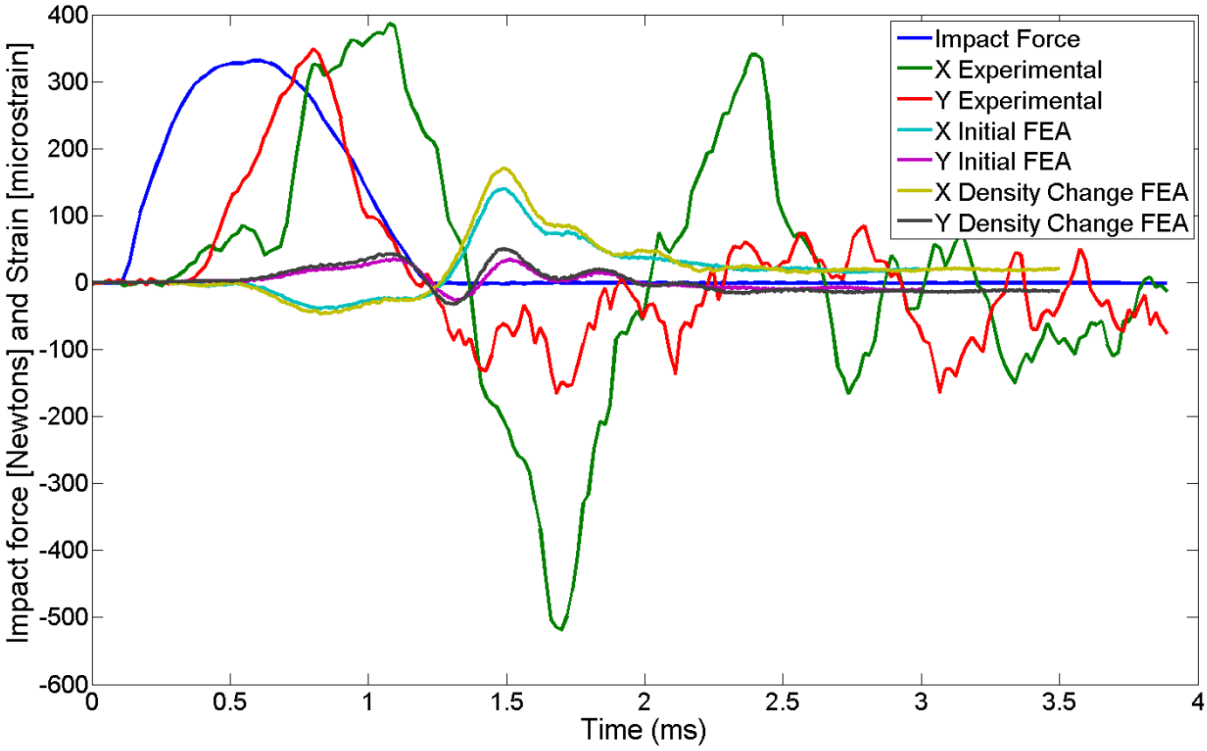

Figure 4.17 - Impact hammer simulation measurements as a result of changing the density of the ABS and PCB materials, compared to the initial simulation and experimental results

4.6. Material Stiffness Effects on Finite Element Impact Hammer Results

The low strain measurements observed during the initial simulation suggested that the Young's moduli may have been set too high. As the strain frequency varied between the experimental and the finite element results, the Young's moduli are adjusted by using the results of a modal analysis. The correct ABS and PCB values were identified by varying the Young's modulus values until the fundamental frequency of the modal simulation matched that observed during the experimental testing.

4.6.1. Tuning of finite element model using frequency response

The strain data from the experimental tests was used to find the fundamental frequency of the radio simply by measuring the time between two successive peaks.

$$\omega = 1/T \tag{4.1}$$

where ω is the natural frequency and T is the time between two successive peaks.

The strain peaks used for calculation were taken some time after the initial excitation occurred where the natural frequency could be clearly observed. Three peak-peak measurements were used, with the average period calculated, the peaks used for measurement are shown in Figure 4.18.

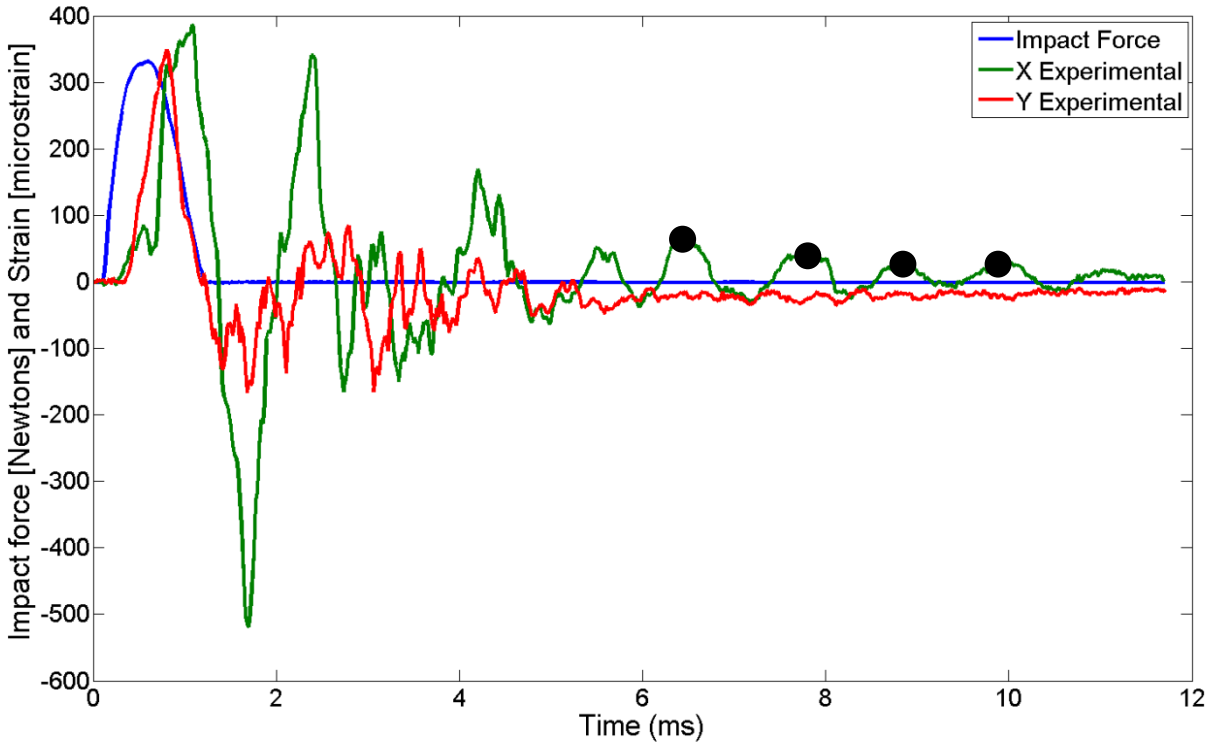

Figure 4.18 - Black points indicating the peaks used for calculation of the natural frequency of the radio system

Table 4.4 - Values from peaks found using Figure 4.18

Sample	*Peak 1 [ms]*	*Peak 2 [ms]*	*Frequency [ω]*
1	6.465	7.793	753.01
2	7.793	8.828	966.18
3	8.828	9.985	864.30
Average			861.16

The natural frequency of the radio system from the impact hammer experimental data was taken as 860 Hz (Table 4.4).

4.6.2. Modal analysis using finite element modelling

A modal analysis model was setup using the same Young's modulus for PCB and ABS as the initial impact hammer model. The simplified radio assembly used the same contact and boundary conditions as the initial impact hammer simulation (Section 4.4.3). The established densities replaced those used in the initial simulation. The model was completely unconstrained, and no forces were applied to the assembly.

The results from the simulation show the first mode occurred at a frequency of 1281 Hz (Figure 4.19), the mode shape excited at that frequency was highly localised at the top of the MMI board and therefore this excitation was disregarded. The second observed mode (Figure 4.20) was a bending mode occurring at a frequency of 2555 Hz, followed by a twisting mode at 2668 Hz (Figure 4.21) and a forth mode at 2842 Hz (Figure 4.22).

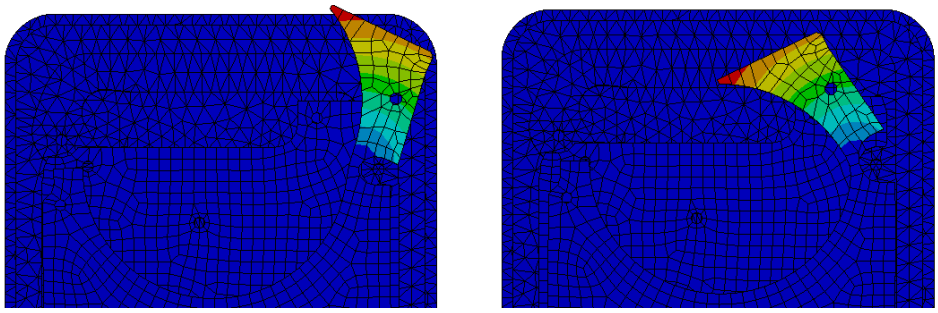

Figure 4.19 - First observed mode, twisting of the MMI board at a frequency of 1281 Hz

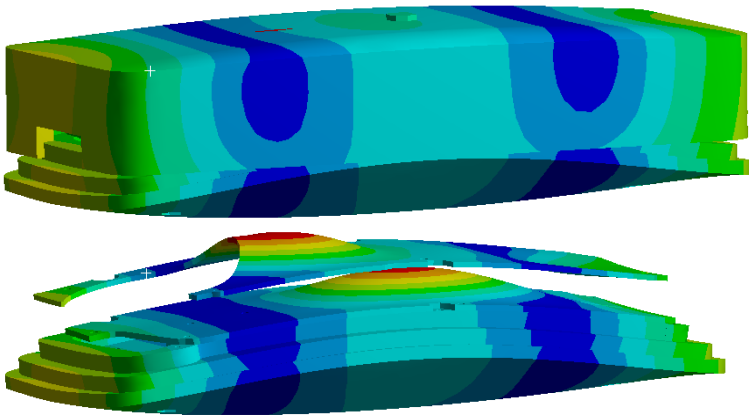

Figure 4.20 - Second observed mode, bending of the simplified radio assembly at a frequency of 2555 Hz

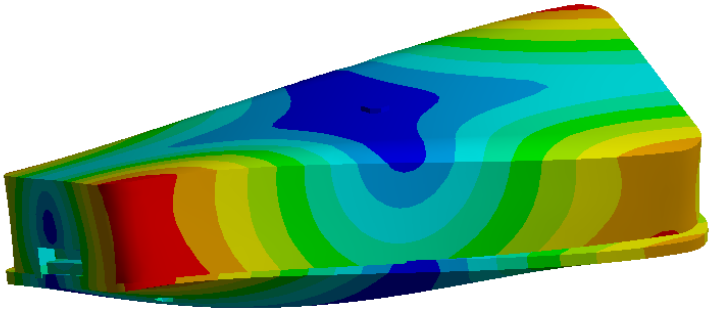

Figure 4.21 - Third modal frequency, twisting at a frequency of 2668 Hz

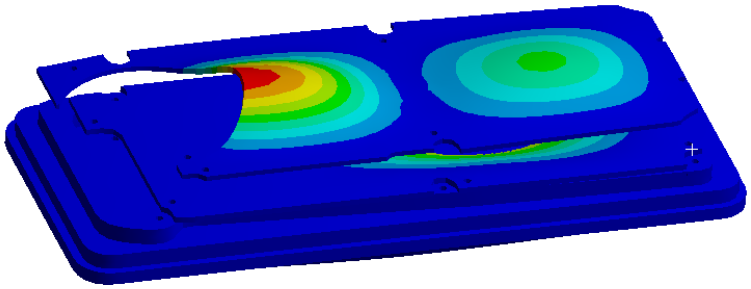

Figure 4.22 - Fourth mode at a frequency of 2842 Hz

The mode to be set as the objective during the optimisation study was the second observed mode (Figure 4.20), found to be at 2555 Hz using the initial material properties.

4.6.3. Material parameter optimisation using modal analysis

Having identified the target mode number (Figure 4.20), the Young's modulus of both the ABS and the PCB were adjusted until the frequency of that mode was 860 Hz. A design optimization study was performed in ANSYS to find the material property values necessary to achieve this goal. The Young's moduli were found to be 1.07 GPa and 12.61 GPa for the ABS and PCB materials respectively, these values gave a modal frequency result of 860.01 Hz at the mode of interest. The iteration process used by ANSYS (adaptive single objective algorithm) to find the optimal material properties is shown in Figure 4.23.

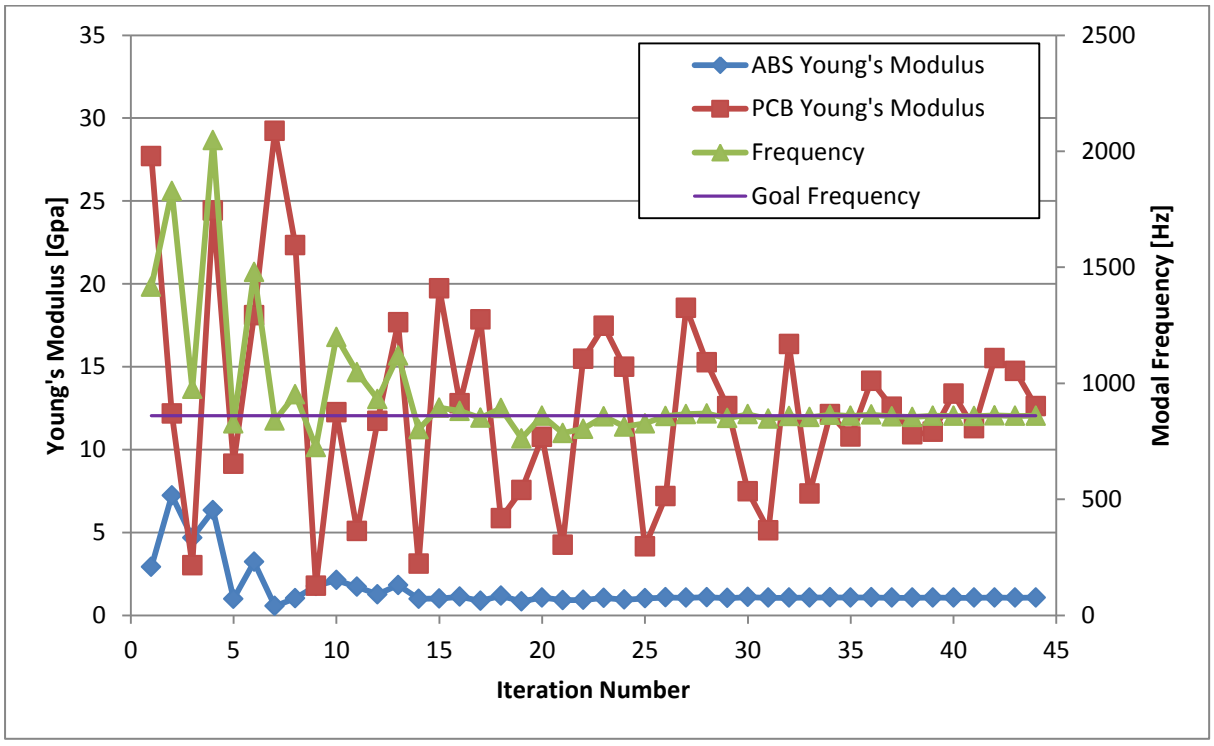

Figure 4.23 - Optimisation iteration results of changing the Young's modulus of both the PCB and ABS materials to obtain a fundamental frequency of 860 Hz

The iteration process showed that the modal frequency was highly dependent on the Young's modulus of the ABS material; conversely the PCB material had minimal influence. This reduced the confidence that the material values obtained using the modal analysis technique (particularly the PCB value) were accurate.

4.6.4. Modal analysis results using optimised material properties

The first mode shape observed using the optimised material properties was the same as found when using the initial values (Figure 4.19), however the frequency was shifted from 1281 Hz down to 715 Hz. The second mode (which was set as the target mode number) changed from a bending mode (Figure 4.20) shape occurring at 2555 Hz to a twisting shaped mode of 860.1 Hz (Figure 4.24). The third mode shape found was a bending mode, present at a frequency of 901.8 Hz (Figure 4.25). The forth observed mode occurred at a frequency of 1257 Hz (Figure 4.26).

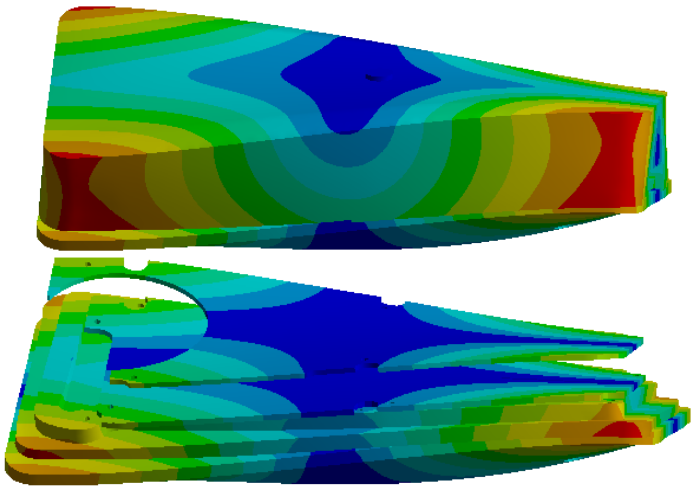

Figure 4.24 - Second mode at a frequency of 860.1 Hz

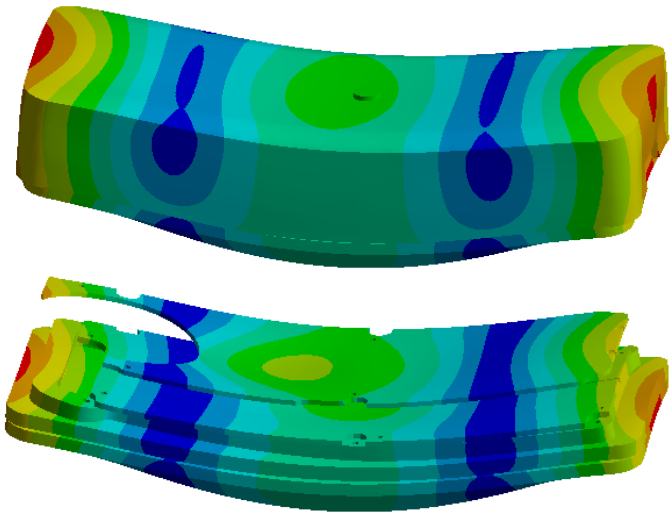

Figure 4.25 - Third modal shape at a frequency of 901.8 Hz

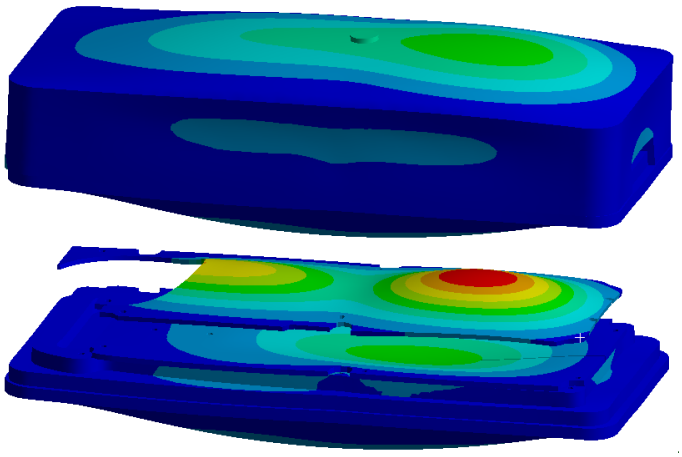

Figure 4.26 - Forth observed mode at a frequency of 1257 Hz

The results from the modal optimisation study show that by changing the material properties both the frequency and mode shape/order are changed. The modal optimisation used a mode shape number and not a specific shape, means there was a risk that the target mode number was of a shape that had minimal influence on the part of interest, i.e. where the strain/frequency measurement was taken and a generated mode shape like that shown in Figure 4.19. Another issue identified during the modal analysis was the lack of influence the change of the PCB Young's modulus had on the results, meaning there is a high level of uncertainty associated with this value. An impact hammer simulation was conducted to identify what effects changing the Young modulus has had on the finite element results.

4.6.5. Impact hammer results using modally tuned Young's modulus

The Young's moduli found using modal analysis was applied to the impact hammer simulation. The finite element model setup was identical to that of the initial baseline simulation, the only difference being the change in material properties (both density and now Young's modulus) of the ABS and PCB. The results show an improvement between the simulation and experimental results when compared to the baseline simulation (Figure 4.27). The moduli of both parts were lowered which meant higher deformations/strain could occur.

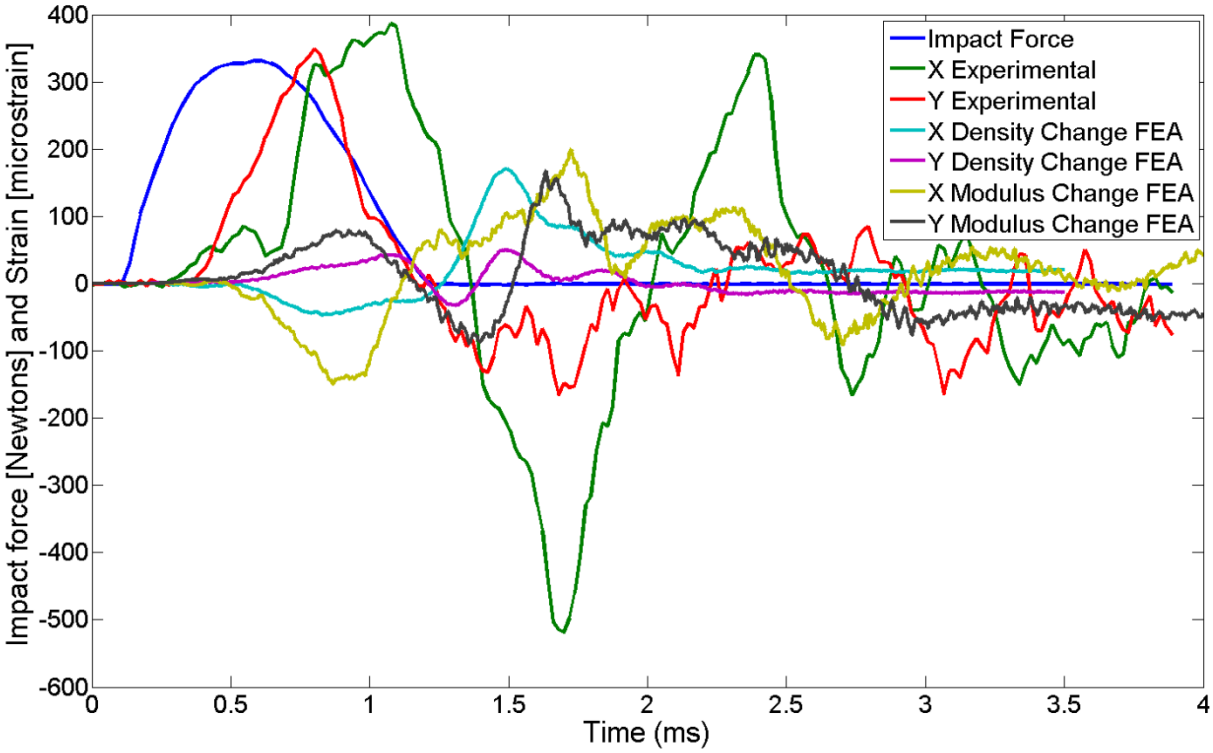

Figure 4.27 - Comparison of impact hammer experimental results with initial and modally optimized simulation results

Although the simulation produced better results, there was still a large disparity between the results. The change in moduli affected the impact hammer results a lot more dramatically than the density modifications, however it should be said that the change in Young's moduli value was more significant than the changes in density value.

The flaws identified when generating materials moduli using the modal technique (as discussed above) meant that the Young's moduli could not relied upon. However before the material modulus was further investigated other parameters were considered to see how they influenced the results.

4.7. Filtering Effects on Finite Element Impact Hammer Results

The results from the finite element analysis show some level of signal noise. Diehl et al. [30] discussed the applications of digital signal processing on explicit dynamic finite element impact problems. Their work focused around a ball bearing impacting the screen of a cell-phone assembly and presented the application of a 5 kHz lowpass Butterworth filter which greatly improved correlation between the experimental and finite element results (Figure 4.28).

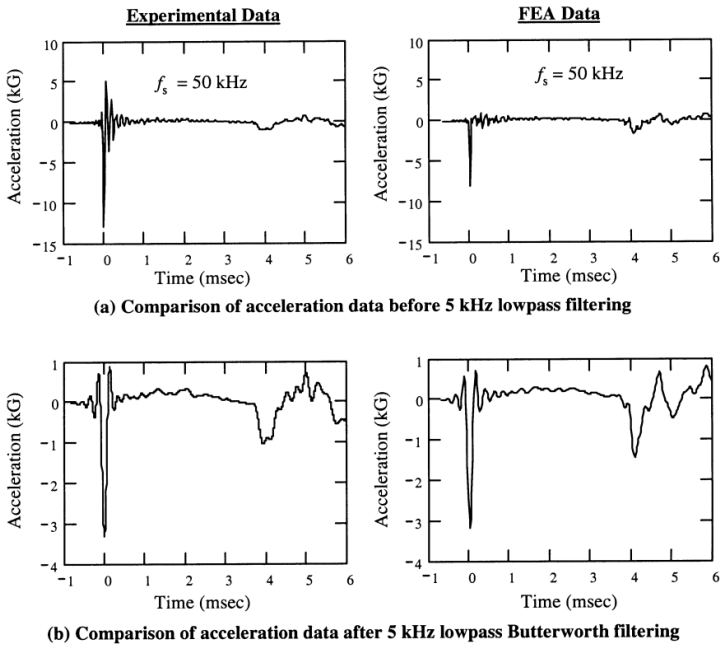

Figure 4.28 - Results from applying a 5kHz low pass filter on experimental and finite element results [30]

Based on this information, the results from the impact hammer simulation had a 5 kHz low pass Butterworth filter applied. The results with filtering are shown in Figure 4.29. The filtering removed the high frequency noise, making the measurements a lot cleaner. The filtering did not affect the overall strain shape or the peak values, suggests the signal noise was not a key contributor to the discrepancy between the measured and modelled results.

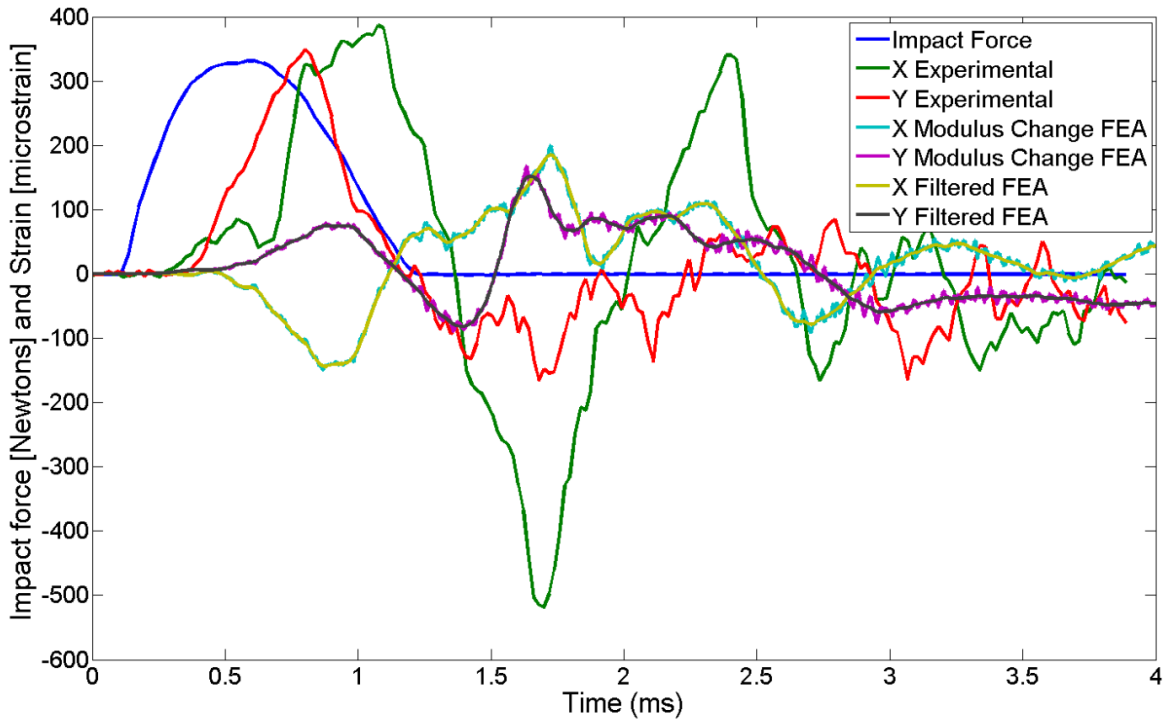

Figure 4.29 - Comparison of modal results with and without 5 kHz Butterworth low band filter

4.8. Contact Condition Effects on Finite Element Impact Hammer Results

There was concern that the frictionless assumption removed damping from the system as well as allowing parts to move too freely. A simulation was run that replaced all frictionless contact conditions between parts within the assembly with frictional contacts, a static and dynamic frictional coefficient of 0.3 was applied.

4.8.1. Impact hammer results using frictional contact conditions

The results (Figure 4.30) show little difference between frictional and frictionless contact conditions. The frictional contact condition was however maintained for the rest of the simulations. The reason frictional contact was not initially considered was that it was expected there would be a substantial increase in the computation time; as a result of this simulation this was found not to be the case.

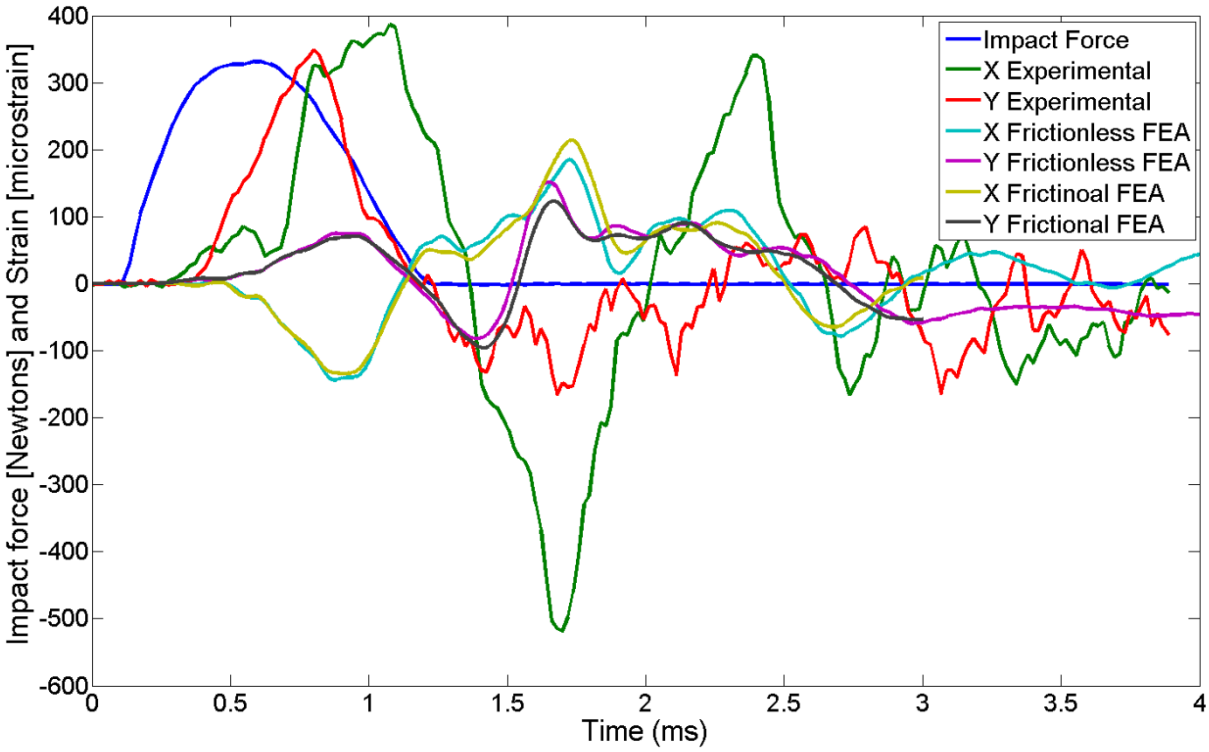

Figure 4.30 - Comparison of modal results with friction and frictionless contact conditions

4.9. Mesh Refinement Effects on Finite Element Impact Hammer Results

The size of the mesh is known to affect the accuracy of the simulation results (smaller generally being better). However it is important to have a model in which the results are independent of the mesh size. If the mesh becomes too refined it becomes computational expensive. Different global mesh sizes were investigated to find when mesh independence occurs. A solver time of 1.2 ms was used so that the initial peak could be captured but was still a relatively short time to allow for a large

number of simulations to be completed. A summary of the different mesh sizes used and their associated parameters are shown in Table 4.5. As mesh size reduced the number of nodes and elements increased. Generally, the solver time increased with decreasing mesh size. There were however some inconsistency to this trend, most likely down to 'rogue' elements which reduced the critical element size, reducing the time step of the model. The x and y strain measurements (including images zooming in on peaks) for the different mesh sizes are presented below (Figure 4.31 to Figure 4.34).

Table 4.5 - Mesh properties and solver times for different mesh sizes applied to simplified radio assembly

Mesh Size [mm]	***Nodes***	***Elements***	***Solver time [hours]***	***Time step [seconds]***	***Element quality [average]***	***Element quality [standard deviation]***
0.7	303699	1273275	11.5	5.186E-08	0.82968	0.09468
0.8	219935	900483	9.4	4.728E-08	0.82951	0.09570
0.9	173238	697949	6.3	5.230E-08	0.82831	0.09703
1.0	140900	560512	6.1	3.706E-08	0.82615	0.09930
1.1	127618	515109	4.3	4.669E-08	0.82397	0.10086
1.2	106307	425094	4.5	3.728E-08	0.82173	0.10283
1.3	92657	369546	3.1	4.679E-08	0.82043	0.10288
1.5	73081	290738	4.8	2.344E-08	0.81567	0.10644
1.7	60518	241791	1.9	5.092E-08	0.80931	0.11067
2.0	50068	199303	2.2	3.534E-08	0.79953	0.11840
2.5	38763	158653	2.2	2.782E-08	0.77642	0.13360
3.0	33183	139048	2.0	2.744E-08	0.76071	0.14134

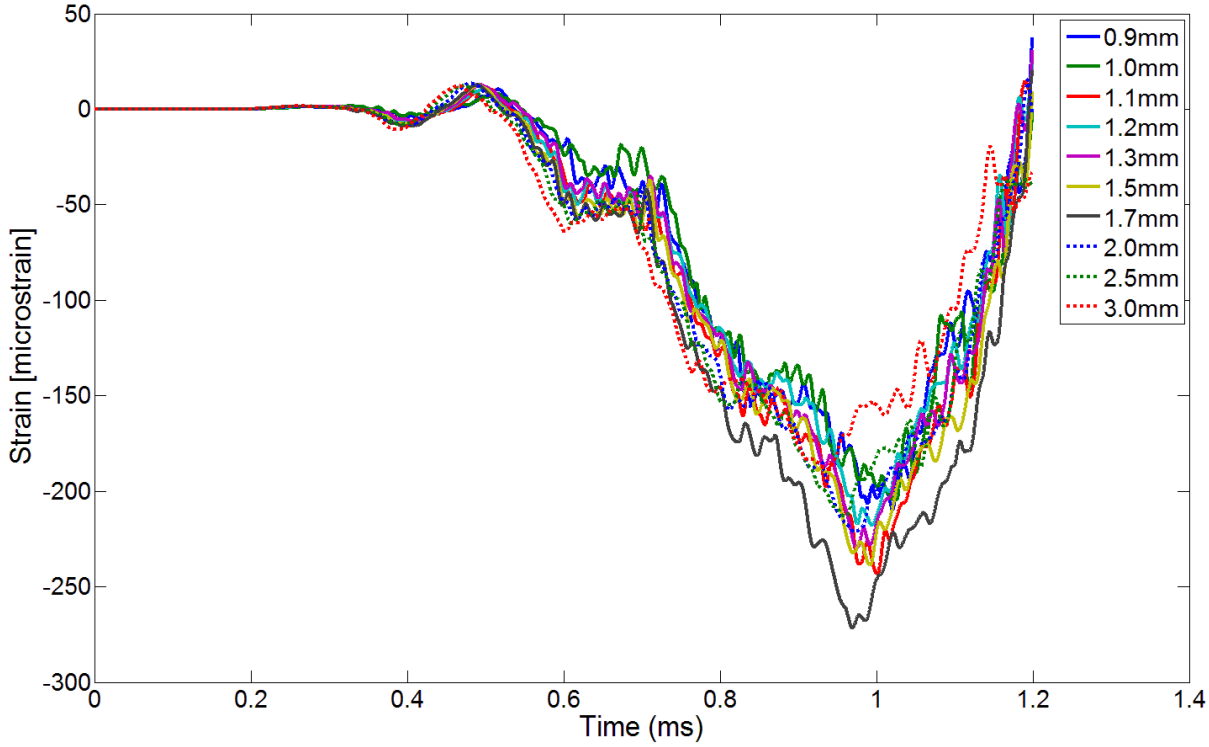

Figure 4.31 - RF board x-strain measurements for impact hammer simulation using different global mesh sizes

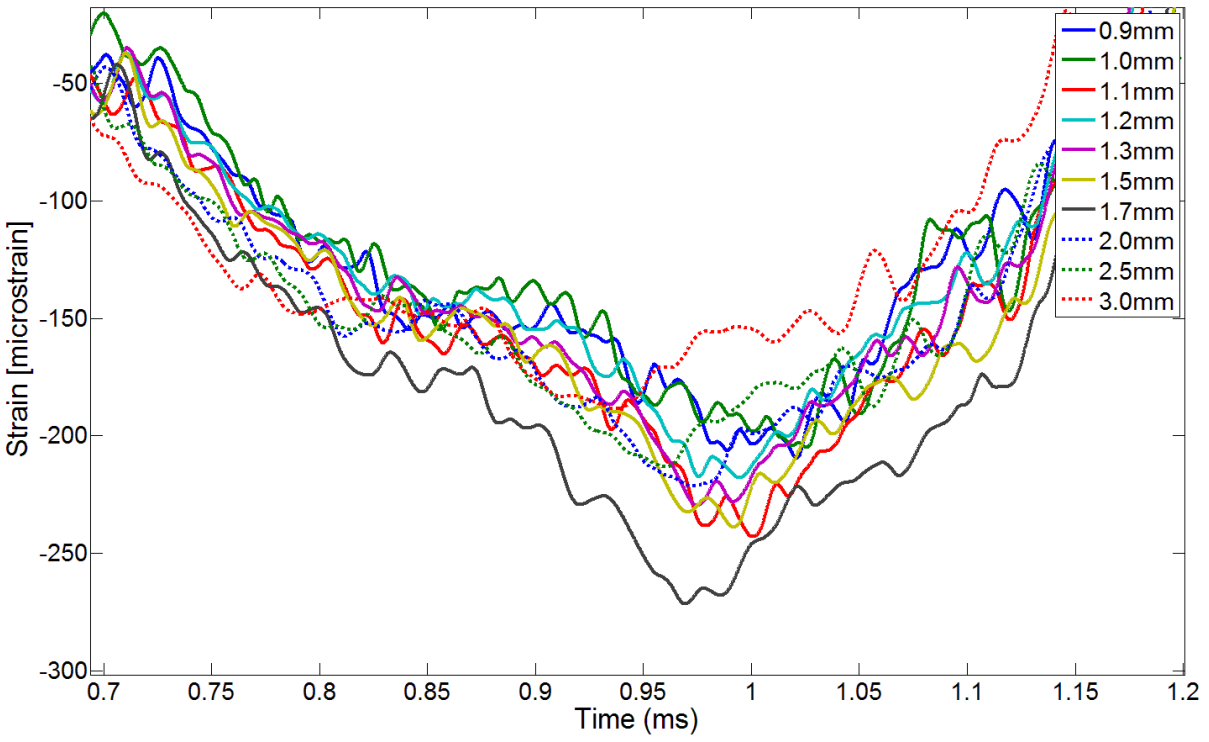

Figure 4.32 - RF board x-strain measurements zoomed in near the 1 ms peak for impact hammer simulation using different global mesh sizes

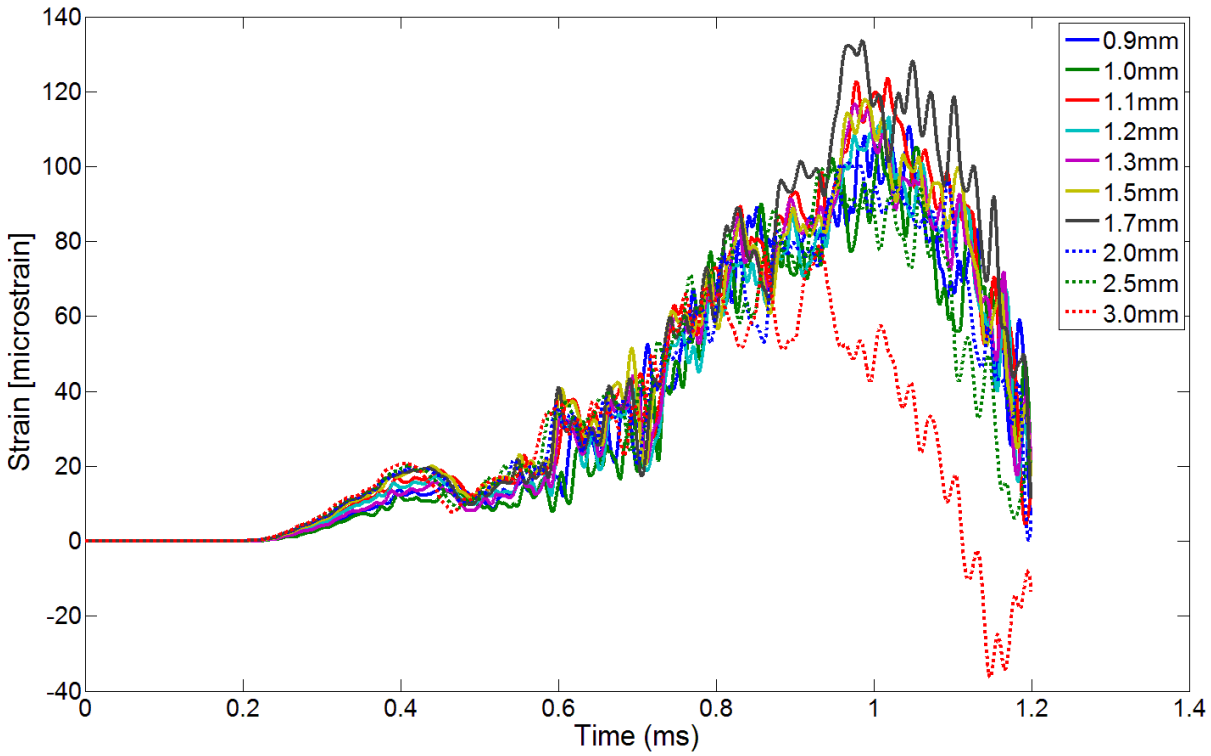

Figure 4.33 - RF board y-strain measurements for impact hammer simulation using different global mesh sizes

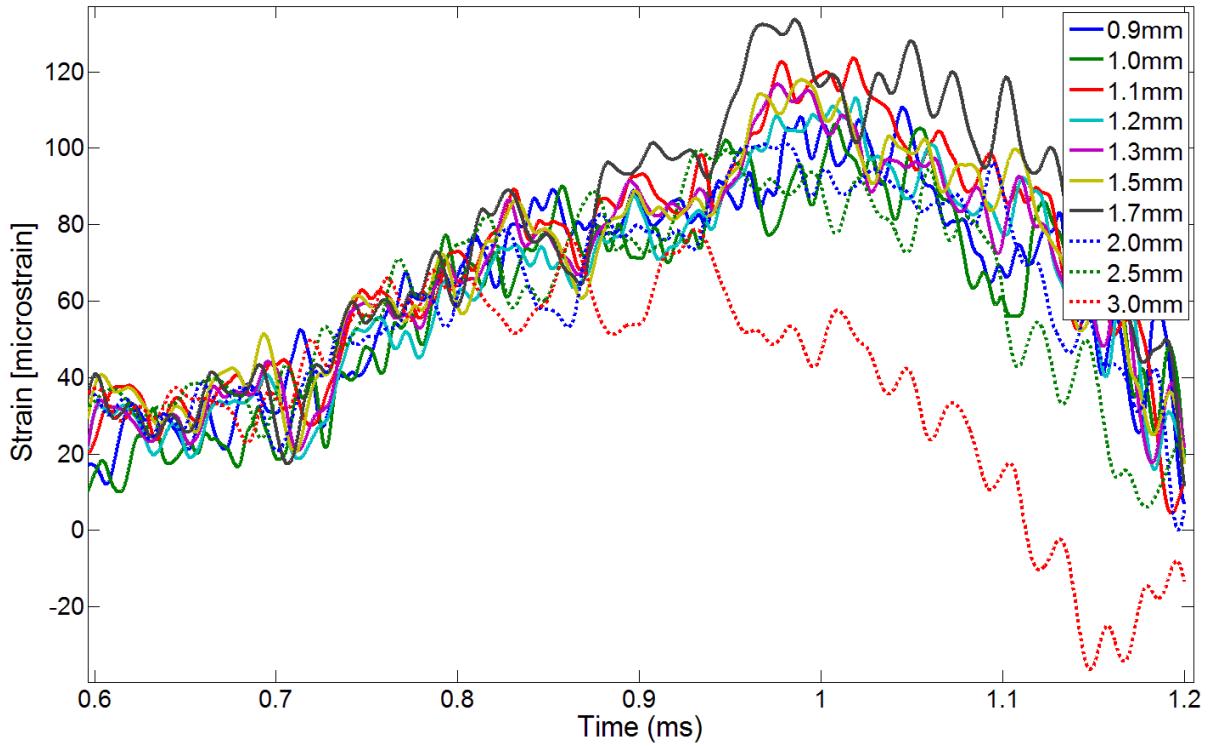

Figure 4.34 - RF board y-strain measurements zoomed in near the 1 ms peak for impact hammer simulation using different global mesh sizes

The impact hammer simulations show that as the global mesh size is decreased the variance between strain measurements is reduced. It can be said that a mesh smaller than 1.3 mm will provide results that are mostly independent of the mesh size. For future simulations the global mesh size was set to 1.2 mm. As the mesh size becomes smaller the solver times grows to a level where it becomes impractical for use during the development stages of a finite element model. It is important to note the solver times displayed in Table 4.5 are for a simulation lasting 1.2 ms, the solver times would need to be tripled to have a long enough solution time (∽3.5 ms) to appropriately capture the impact event in its entirety.

4.9.1. Impact hammer results using refined mesh size

The impact hammer simulation was run using a global mesh size of 1.2 mm (previously 1.5 mm), the material values used for this simulation are shown in Table 4.6 (the same as used in Section 4.6 through 4.8).

Table 4.6 - Material properties used for simulation involving a mesh size of 1.2 mm

Material Property	*ABS*	*PCB*
Density [kgm^{-3}]	935	3090
Young's modulus [GPa]	1.07	12.61

The simulation results using a mesh size of 1.2 mm is shown in Figure 4.35. The results show consistent behaviour between the 1.2 and 1.5 mm mesh sizes up to a time of 1.2 ms, after this time the results began to lose coherency. The behaviour of the radio up to 1.2 ms is a result of the direct excitation (while the impact hammer is still in contact with the radio). The results following the impact strike are dependent on how the shock excitation travelling throughout the assembly is calculated. The disparity between the different mesh sizes is related to how each mesh evaluates the shock wave propagations and its associated reflections. It is expected that the smaller mesh size would compute the shock behaviour with better accuracy.

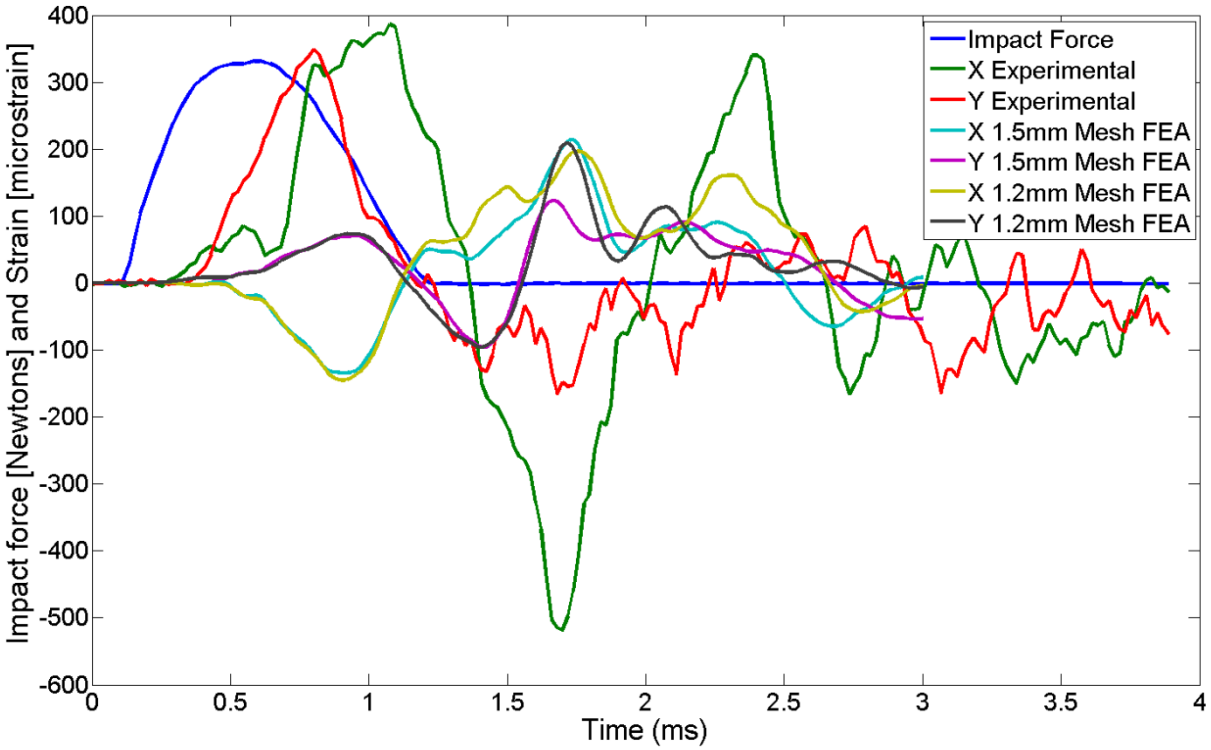

Figure 4.35 - Comparison between different mesh sizes and experimental results. NB: 1.5 mesh results are the same as the frictional results in Figure 4.30.

4.10. Connection Effects on Finite Element Impact Hammer Results

In addition to the body to body interactions of moving parts already investigated (frictionless vs. frictional, Section 4.8), it is possible that the constraint applied at screw locations may not be accurately representing the real life screw connection. Screws are introduced into the finite element model to understand how their constraints differ from the current face to face bonded connection. The contact condition between the screw and the parts it connects needs to be defined. Parts that the screw is screwed into are bonded (fixed) to the screw (Figure 4.36), while parts located on the upper section of the screw (on and near head of the screw) have a frictional contact condition applied (Figure 4.37).

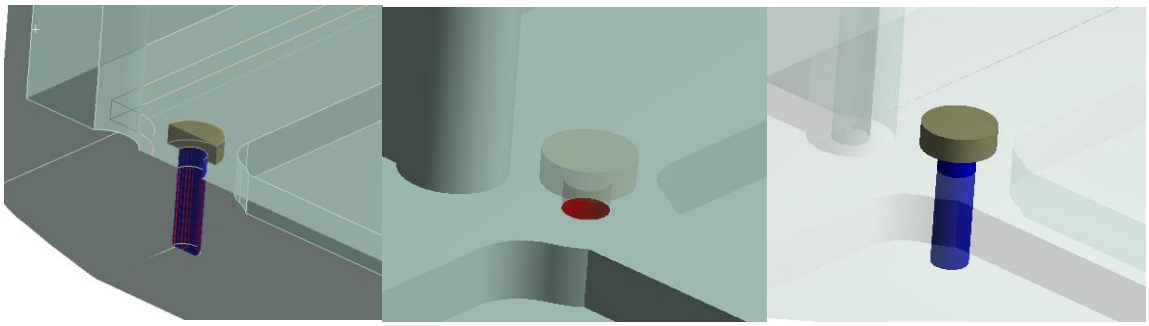

Figure 4.36 - Bonded contact between screw and front panel. The screw shown is used to hold the MMI board in place (can be seen in the far left image)

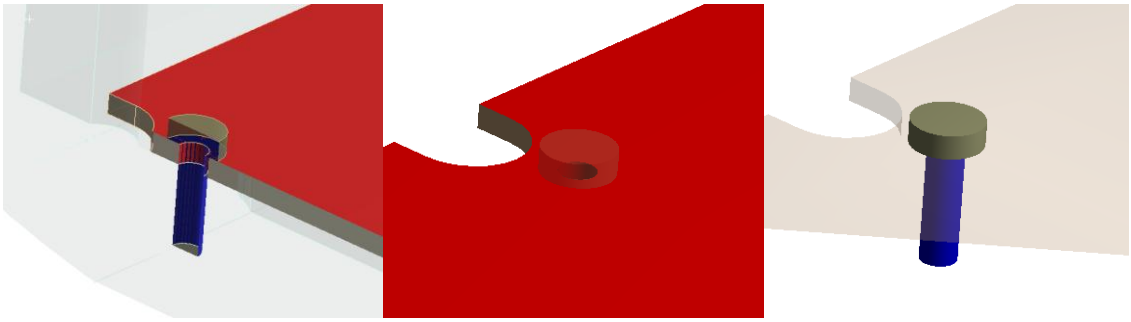

Figure 4.37 - Frictional contact between screw and MMI board. The screw shown is fastened into the front panel

By allowing a less restrictive contact condition at the top section of the screw it allows for more movement of the top part (mostly rotational movement).

4.10.1. Impact hammer results from using real screw constraints

A mesh size of 1.2 mm was used; the material properties for the ABS and PCB are displayed in Table 4.6. A linear elastic model was used for the screws, using a density of 7850 kgm^{-3}, Young's modulus of 20 GPa and a Poisson's ratio of 0.3. The RF board strain results are shown in Figure 4.38, in which they are compared against the model developed in Section 4.9 which used face to face bonded connections and a 1.2 mm global mesh size and the same material properties.

The results show a slight change in behaviour between the two screw constraint models. The strain peaks are slightly higher when using the screw connection; this is likely due to the less restrictive connection between parts.

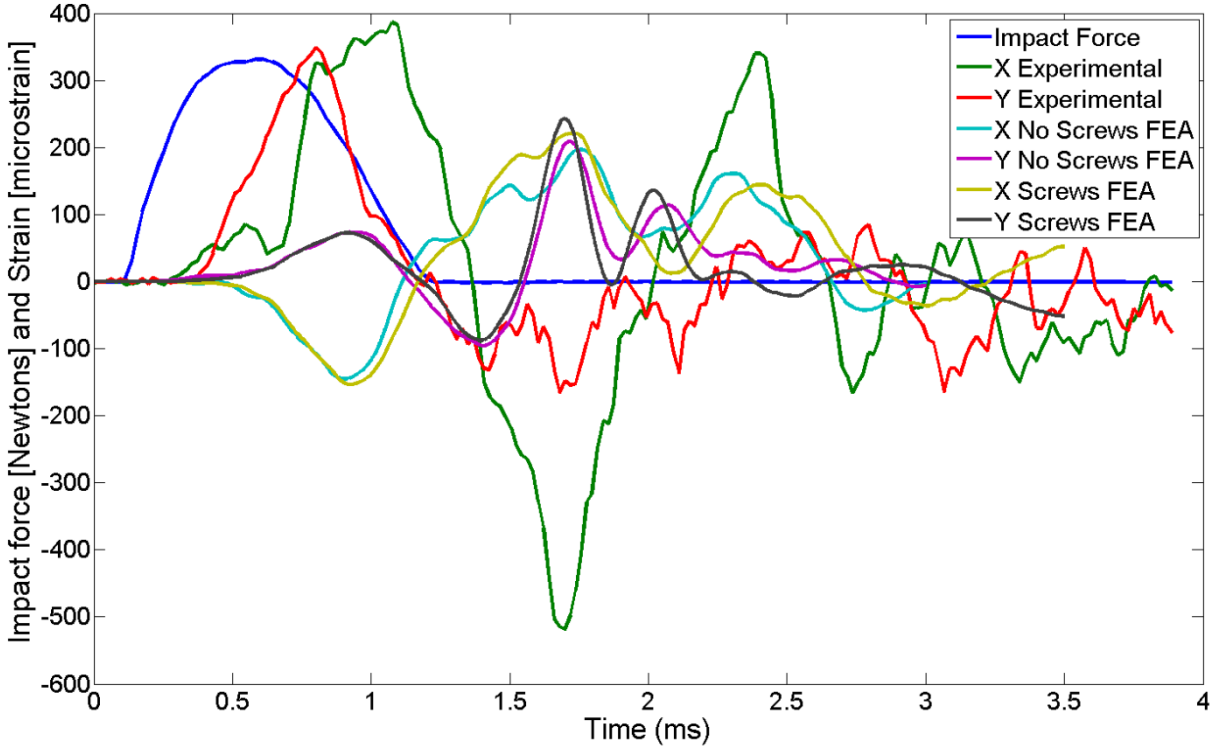

Figure 4.38 - RF board strain results of an impact hammer test, with and without the incorporation of screws within the model

These results are improved, in terms of increasing peak strain values. However the use of the explicit solver made it difficult to apply pre-stressing at the screw locations, so the behaviours would still not completely emulate real life behaviour.

4.11. Damping Effects on Finite Element Impact Hammer Results

The results from the latest model show that the finite element system may have issues damping out the applied excitation, as shown by the large peak in the y-direction at a time of around 1.8 ms (Figure 4.38). The explicit dynamics solver does not provide specific damping values for each material used within the model, instead a range of different global damping behaviours can be defined.

There are several different forms of damping that can be set and tuned, each targeting different characteristics within the finite element solver. Some are specific to damping issues associated with the finite element method while others are used for physical damping.

4.11.1. Artificial viscosity damping

Viscous terms are introduced into the explicit dynamics solver to reduce the likelihood of shock discontinuities occurring. The artificial viscous damping spreads out shock discontinuities over

several elements allowing the simulation to generate a smooth solution result. An example of the artificial viscosity damping influence is shown in Figure 4.39.

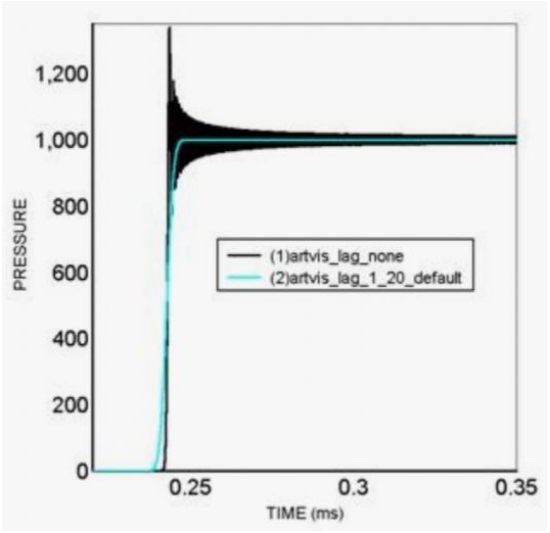

Figure 4.39 - Comparison of a pressure solution at a shock wave discontinuity, using no artificial viscosity (black) and using artificial viscosity (cyan) [31]

The explicit solver uses artificial viscous damping terms based on the following equation:

$$q = \rho\left[\left(C_Q d\left(\frac{\dot{V}}{V}\right)\right)^2 - C_L c d\left(\frac{\dot{V}}{V}\right)\right] for\ \frac{\dot{V}}{V} < 0$$
$$q = 0\ for\ \frac{\dot{V}}{V} < 0 \qquad \textbf{(4.2)}$$

where C_Q is the quadratic artificial viscosity coefficient, C_L is the linear artificial viscosity coefficient, d is a typical element length scale and $\dot{V}/V$ is the rate in change of volume [31]. Different values were investigated for both the quadratic and linear artificial viscosity coefficients.

The linear viscosity coefficient term reduces shock noise, as seen in Figure 4.40. The linear viscosity term was increased from the default value of 0.2 to a value of 0.4 to see what influence this term has of the impact hammer simulation. The quadratic artificial viscosity term smooth's out any shock discontinuities, stabilizing the system (Figure 4.40). The quadratic term was changed from a value of 1 to a value of 2 so that any influence on the impact hammer simulation could be identified.

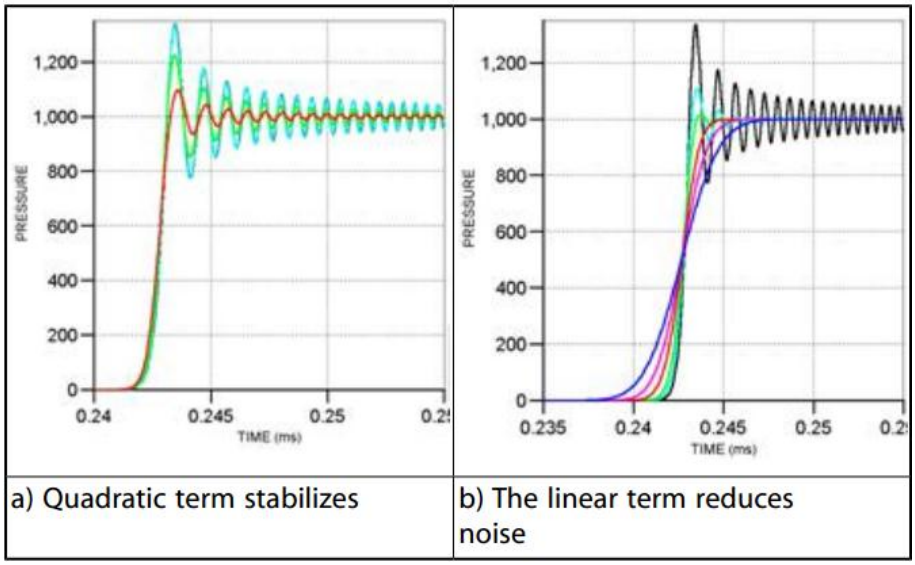

Figure 4.40 - Effect of changing, a) quadratic artificial viscosity coefficient and b) linear artificial viscous coefficient [31]

The increased linear and quadratic viscosity terms were included within the same impact hammer simulation. Results show (Figure 4.41) that the increased artificial viscosity damping coefficients had little effect. The viscosity coefficients are returned back to default values (0.2 and 1) for future simulations.

0

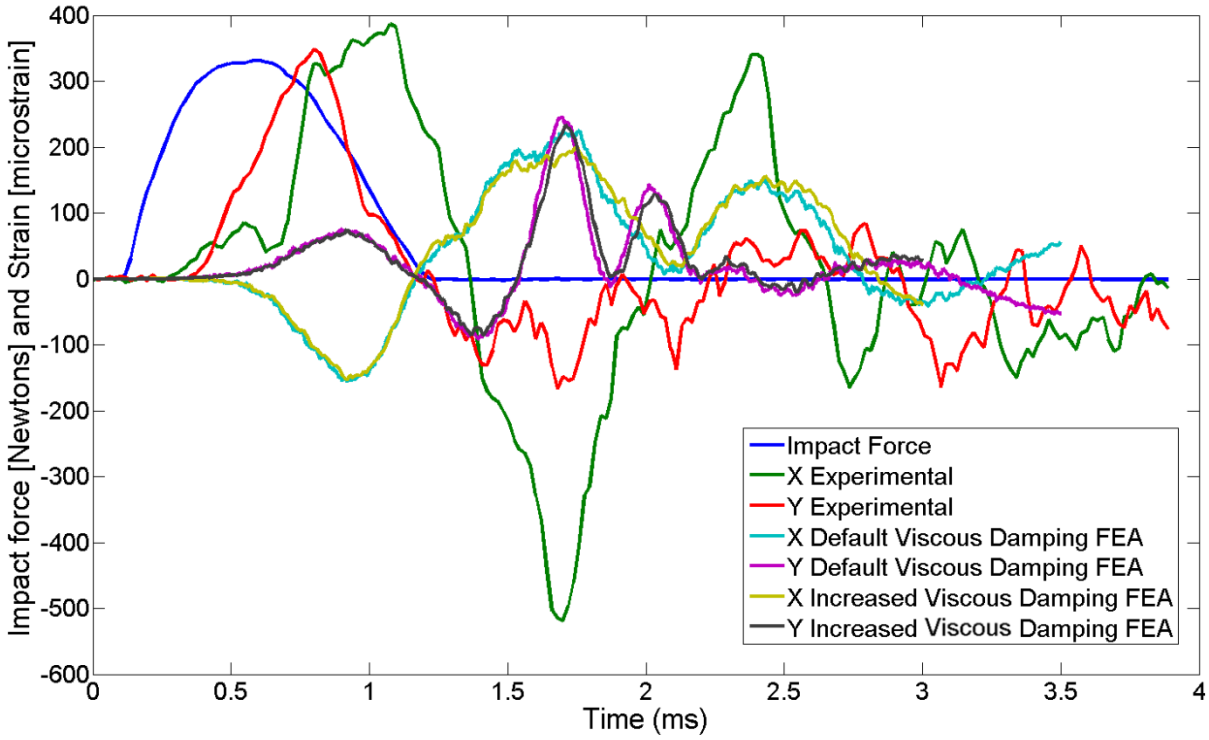

Figure 4.41 - Effect of increasing linear (0.2 – 0.4) and quadratic (1 - 2) artificial viscosity terms on impact hammer simulation results. No low pass filtering was applied, so it could be investigated whether the higher frequency noise was damped out as a result of increased damping

4.11.2. Static damping

Static damping is another damping control present in the explicit dynamics solver. Static damping is used when a static equilibrium solution is wanted. The static damping applies a damping force which is designed to critically damp to the lowest mode of oscillation. To apply the correct static damping value, an understanding of when the equilibrium state is expected to be occur and the period of the lowest mode is required. The damping force is proportional to the nodal velocity ($\dot{x}$), the nodal velocity is modified using the following equation:

$$\dot{x}^{n=1/2} = (1 - 2\pi R_d)\dot{x}^{n-1/2} + (1 - \pi R_d)\ddot{x}^n \Delta t^n \quad \textbf{(4.3)}$$

where R_d is the static damping coefficient, and is given by:

$$R_d = \frac{2\Delta t/T}{1 + 2\pi\Delta t/T} \quad \textbf{(4.4)}$$

where T is the period of the lowest mode of vibration of the system.

The ANSYS Mechanical User Guide [31] states that the static damping coefficient can be used to establish initial stress distribution prior to solving a transient event (i.e. gravity loading) or to establish the final static equilibrium after the transient dynamic event (i.e. position of a structure after it has undergone large plastic deformation). This means that the static damping method is designed for use before and after a transient event. For the case of the impact hammer test and drop-impact events there are no loading of parts prior to impact and no static behaviour after the impact of particular interest, therefore static damping has been ignored.

4.11.3. Hourglass damping

Hourglass damping is incorporated into the finite element solver to apply corrective forces to resist hourglass deformation modes occurring within the mesh. The hourglass effect is a zero energy mode; it is oscillatory in nature and tends to have periods much shorter than the overall structural response. The hourglass mode is found in hexahedral mesh and has a zig-zagging appearance (Figure 4.42).

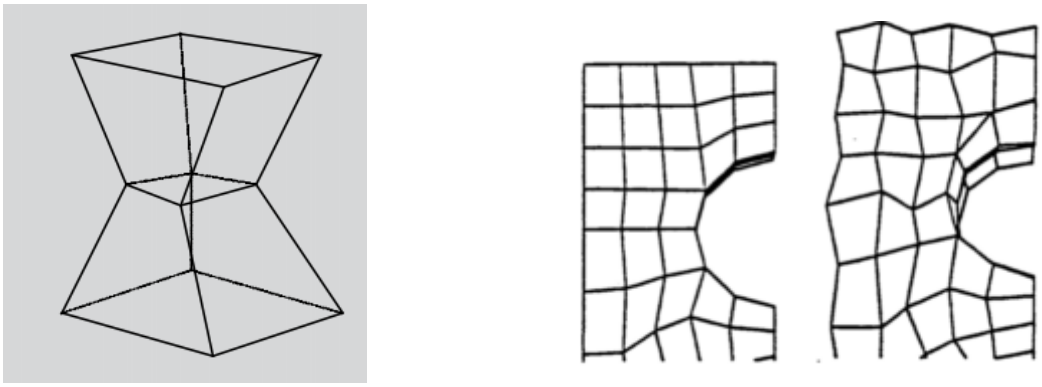

Figure 4.42 - Hourglass effect in a hexahedral mesh [31]; undeformed mesh (middle) vs a deformed mesh (left) demonstrating hourglassing effects

The formula used in the explicit dynamics solver that applies a force to resist hourglass modes forming is:

$$F_H = C_H \rho c V^{2/3} \times f_{KF}(\dot{X}) \tag{4.5}$$

where F_H is an hourglass force vector, C_H is the viscous coefficient and f_{KF} is a vector function of element nodal velocities aligned with the hourglass shape vector [31]. The default value for the hourglass viscous coefficient for the solver was 0.1.

Before the introduction of a larger hourglass damping value, the hourglass energy present in the current finite element model was investigated. The observed hourglass energy (Figure 4.43) was especially high in relation to the other energies calculated (kinetic, contact and internal energy).

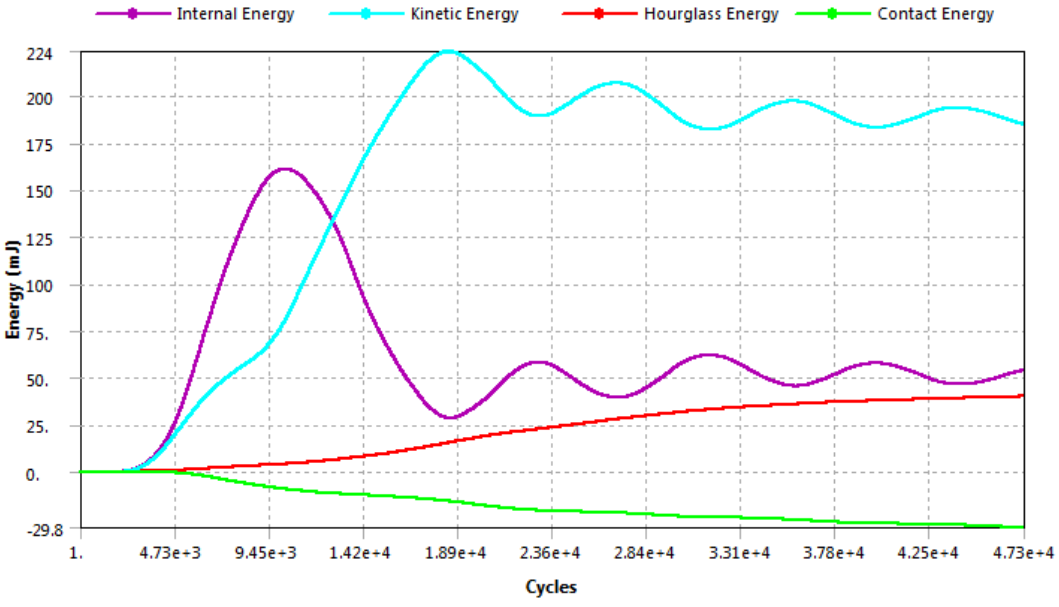

Figure 4.43 - Energy summary of impact hammer simulation showing high hourglass energy contribution

4.12. Element Types and Hourglass Energy

After identifying the presence of a large hourglass energy value in the impact hammer simulation, ways of reducing this component were investigated before changing the hourglass damping component.

4.12.1. Refinement of hexahedral elements

Hourglass error is usually prominent in hexahedral elements, a more refined hexahedral mesh is expected to lower hourglass energy values. Instead of one layer of the solid-shell elements to mesh the PCBs, three layers were used (Figure 4.44).

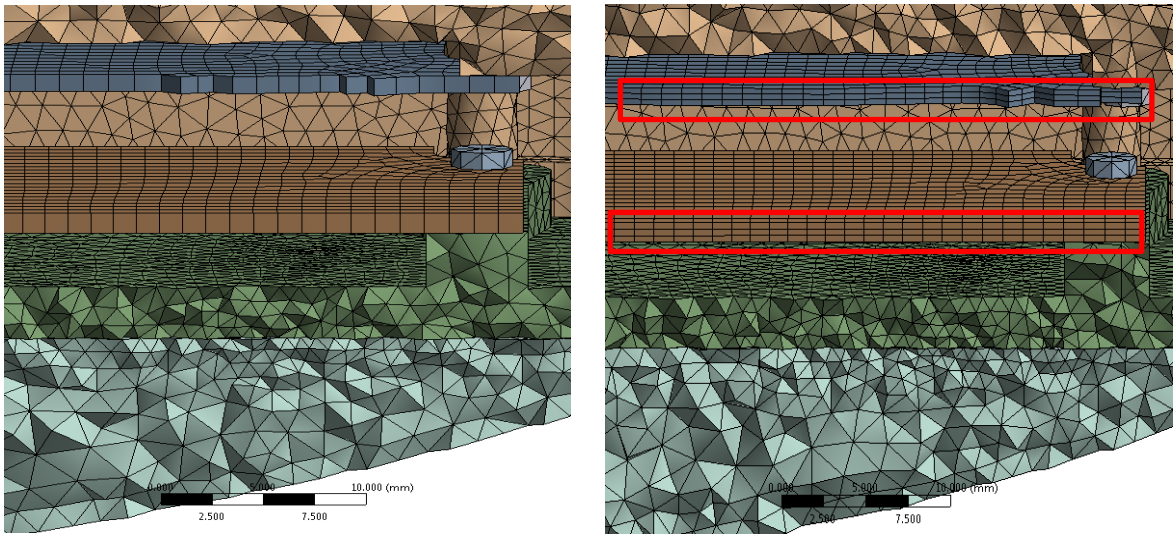

Figure 4.44 - Single layered solid-shell elements vs. three layered solid-shell elements applied to the PCBs

4.12.2. Results of refining the hexahedral elements

Three element layers applied to the PCBs reduced the hourglass energy from approximately 38 mJ (millijoules) to 27 mJ (Figure 4.43 and Figure 4.45). The strain measurements from the RF board (Figure 4.46) show a significant shift between the one and three layered models. The change in strain results was a lot more substantial than expected, and therefore required further exploration.

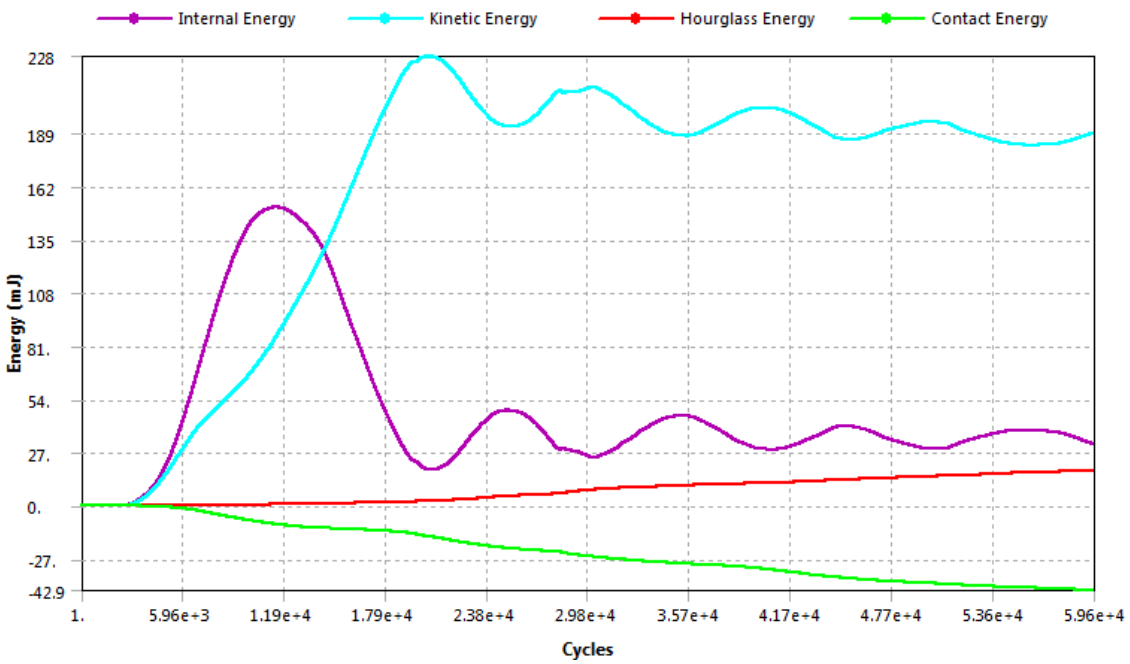

Figure 4.45 - Energy summary showing reduced hourglass energy as a result of introducing more element layers on the printed circuit board

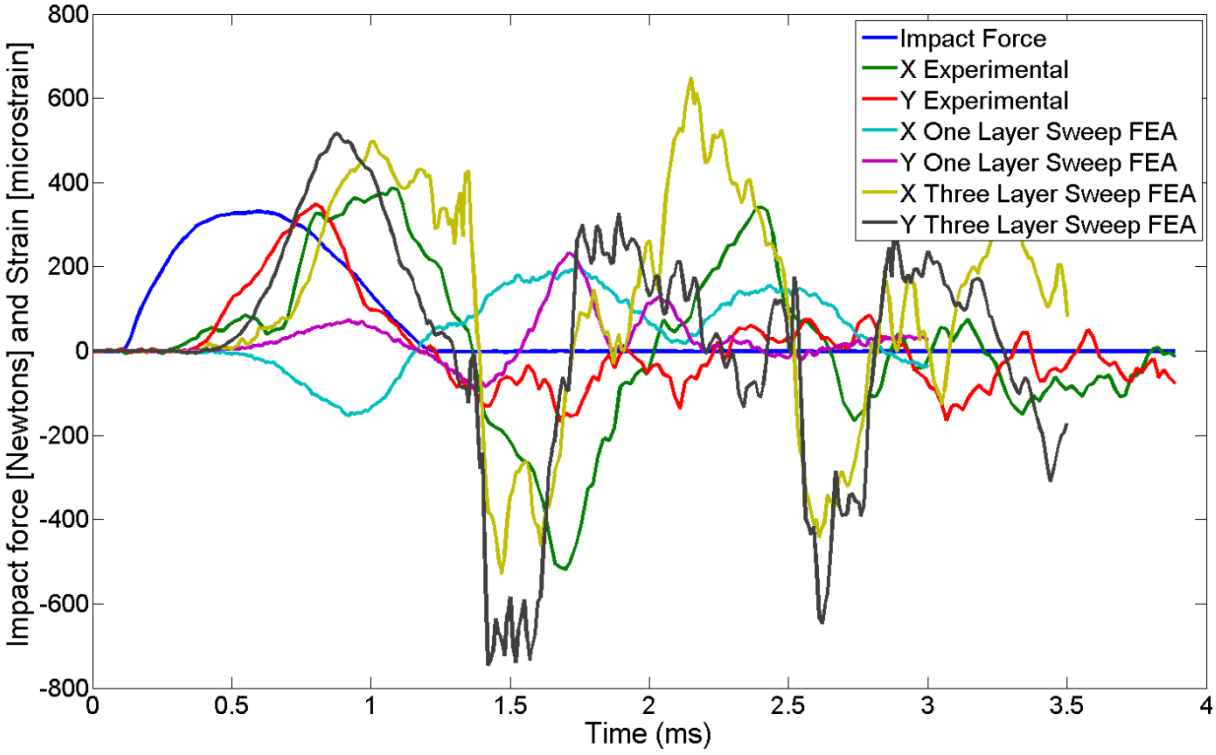

Figure 4.46 - Comparison of a one element thick printed circuit board sweep vs. a three layer element sweep

4.12.3. Investigation of the observed variance between one and three layered solid-shell mesh

To better understand the big change in results between the one layer and three layer models, a simplified impact involving a thin plate was introduced, using different elements types and layers. The model consisted of a plate (150 x 65 x 1.2 mm), with initial velocity of 4 ms^{-1}, striking a hemisphere (Figure 4.47). A fixed support was applied to the underside of the sphere and a symmetry plane was used to reduce solution times. Five different element types were investigated:

- Solid-shell elements (1 and 3 layers)
- Solid elements (1 and 3 layers)
- Shell elements (quad and triangle mesh)

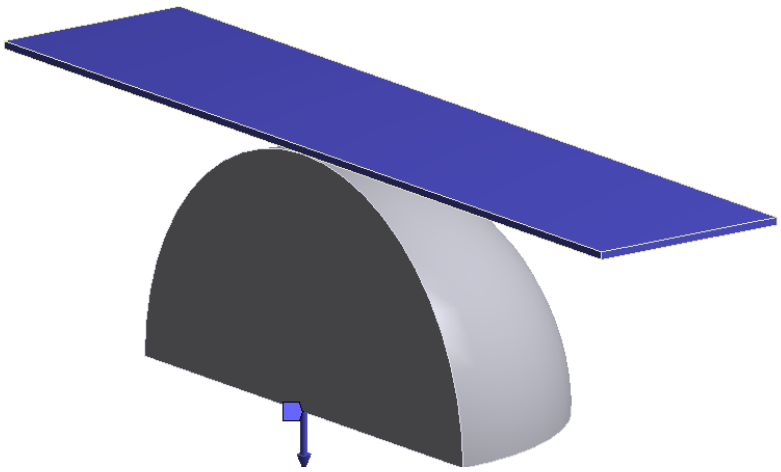

Figure 4.47 - Finite element model of plate (150 x 65 x 1.2 mm) impacting a hemispherical surface, symmetry region applied and a fixed support applied to the underside of the hemisphere

The results from the simplified impact model again show a large change in deformation behaviour between a 1 layered and a 3 layered solid-shell (Figure 4.48 and Figure 4.49). The solid-shell elements produced identical behaviours to the solid element model (Figure 4.49). This infers that the solid-shell elements are not incorporating bending into the model and are instead just solid elements. The difference between the solid and solid-shell elements was previously investigated in Section 3.3.2, using the static-structural solver; it showed that the solid-shell elements appropriately addressed bending modes whereas the solid elements did not. It was concluded that although the solid-shell element option is available in the explicit dynamics solver, the solid-shell elements are not actually applied and solid elements are present instead.

The attempted use of solid-shell elements in the explicit dynamics solver was an unfortunate mistake and could have been avoided if the element types were more stringently evaluated for their

use within the explicit dynamics solver. The element types were investigated in a static solver and were assumed to behave similarly in the explicit solver, however, because of the numerous differences between the two solver methods this was an incorrect assumption. Future simulations will use solid elements with at least three element layers through their thickness to account for bending loads.

Shell elements were also investigated in this simplified impact model. The shell elements showed similar behaviour to three layered solid elements. This confirmed that the shell elements are accurately computing bending and therefore may also be used in explicit dynamics models.

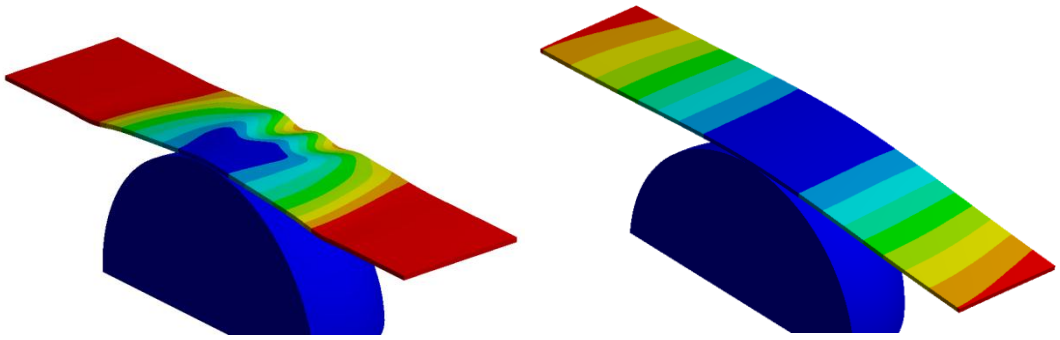

Figure 4.48 - Deformation plot in the z-direction of board impact at t=1 ms, left using 1 layer solid-shell elements and right using 3 layers of solid shell elements

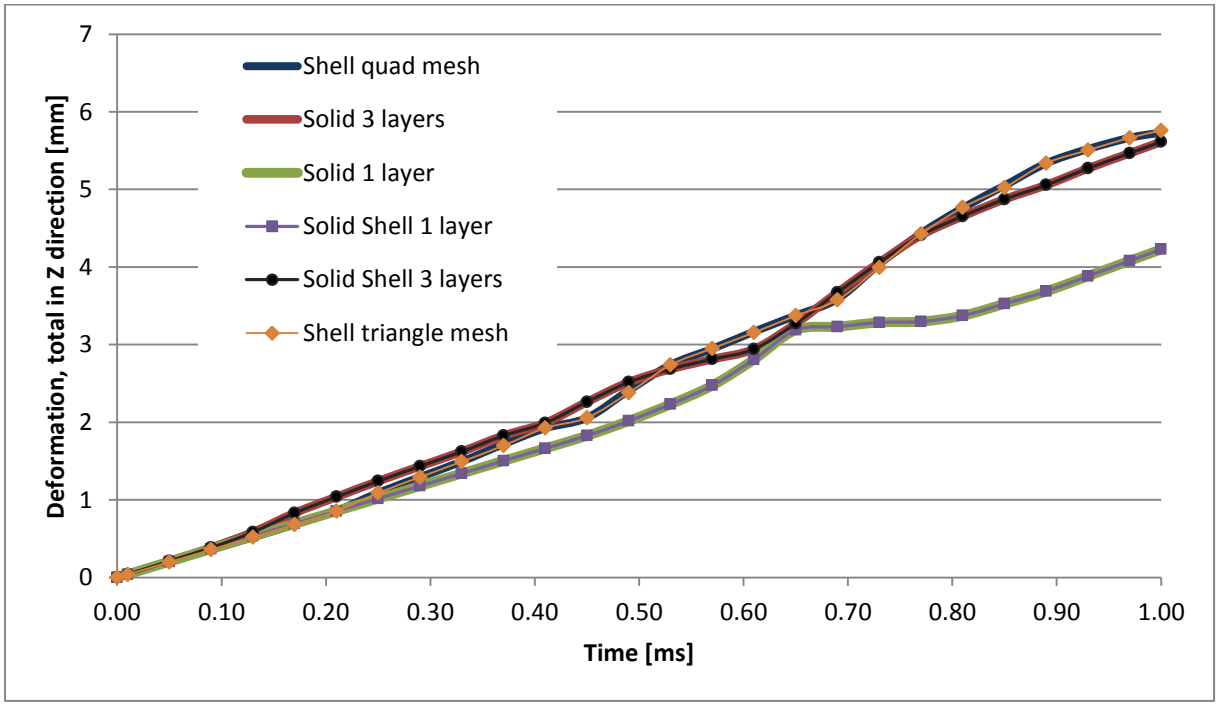

Figure 4.49 - Comparison of deformation of the board during impact of different element types

4.12.4. Refinement of tetrahedral elements

The discovery of the solid-shell elements not performing as thought raised questions about the tetrahedral elements present in the explicit dynamics solver. The tetrahedral elements present in the model used average nodal pressure integration. There are three available integration methods that can be applied to tetrahedral elements [32]: standard constant pressure integration [33], average nodal pressure integration [34] and nodal based strain integration [35, 36]. The standard constant pressure integration is the most basic of the three methods and is intended for use as a filler element only, its use can result in locking during bending and constant volumetric straining loads. The average nodal pressure integration method, which is currently used, was developed to address the problems of volumetric locking exhibited by the standard constant pressure method. The third method, the nodal based strain method, is an extension of the average nodal pressure method, developed to further overcome volumetric and shear locking issues.

The nodal based strain integration method is best suited to problems involving bending loads, as is the case with the impact hammer simulation. The nodal based integration method is applied to the tetrahedral elements and compared against the average nodal pressure integration method to see what effect it has on the finite element results.

4.12.5. Results of modification to the tetrahedral elements

Results show increased levels of deformation when the nodal based strain method is used (Figure 4.50). This is expected as this integration scheme reduces that risk of element locking, particularly for bending loads, allowing the elements to deform in a more realistic manner. For future simulations, the nodal based strain method is used for the tetrahedral element integration method.

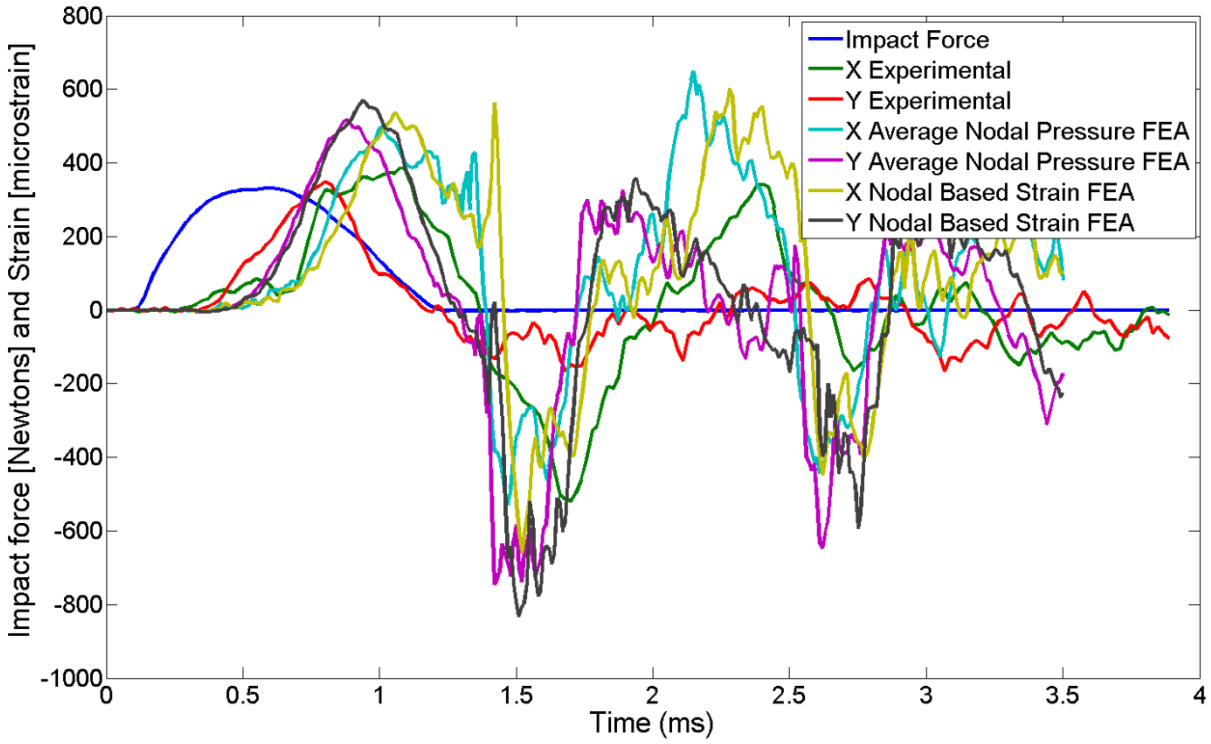

Figure 4.50 - Comparison between two different tetrahedral elements, average nodal pressure and nodal based strain

4.13. Hourglass Damping Effects on Impact Hammer Results

With both the tetrahedral and hexahedral elements appropriately considered, hourglass damping was evaluated. The hourglass viscous coefficient (C_H), used within the hourglass forcing vector equation (4.5), has a default value of 0.1. The viscous coefficient was increased to 0.3 to investigate what effect increased hourglass damping has on the finite element results.

4.13.1. Results of increasing hourglass damping

The finite element results with increased hourglass damping coefficient, when compared against default values, were near identical (Figure 4.51). The hourglass energy at the end of the simulation was also found to have a similar energy value as the default hourglass damping values. As little is known about identifying what viscous coefficient is best and because raising the damping value had little effect, the default value of 0.1 was maintained for remaining simulations. It should be noted that a damping coefficient of 0.4 was attempted but the solver did not complete stating that the energy was too high.

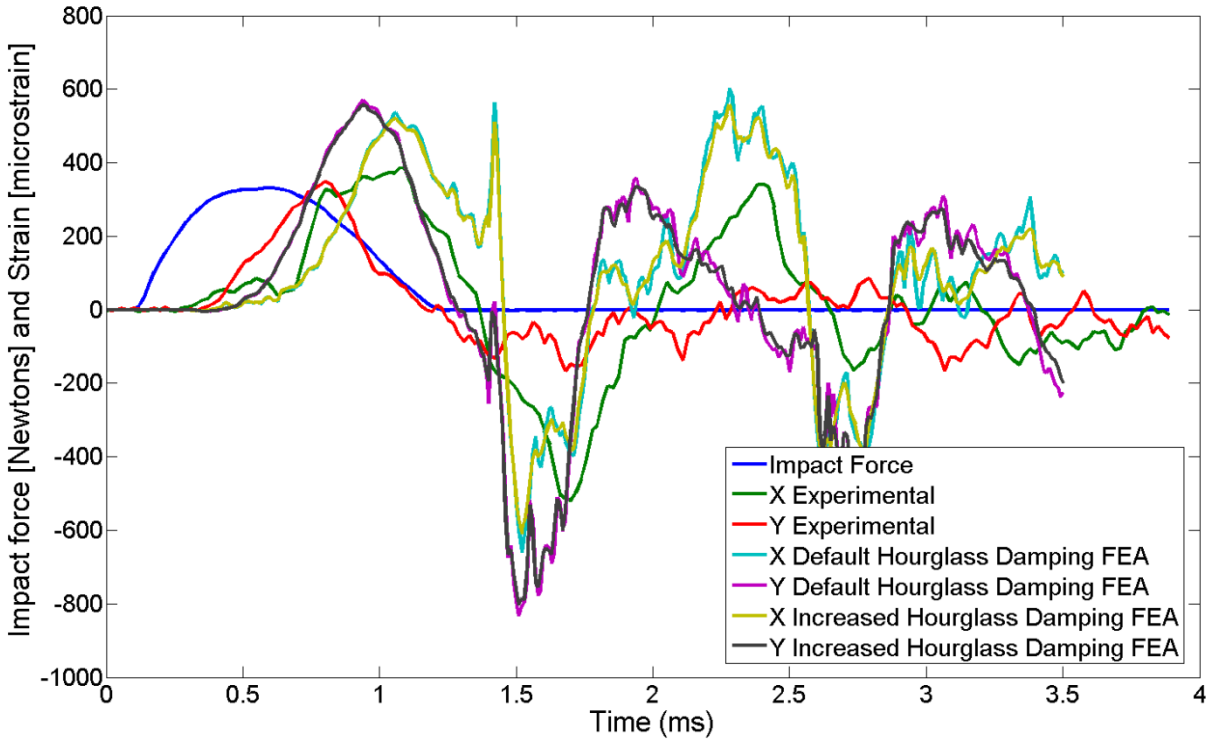

Figure 4.51 - Comparison between finite element results of impact hammer simulation measuring the strain on the RF using two different hourglass viscous coefficients, default (0.1) and increased (0.3)

4.14. Optimisation of Young's Modulus

After evaluating many of the finite element parameters including contact conditions, filtering, mesh size, element types and damping, the unknown parameter which had greatest effect on the finite element results was found to be the Young's modulus. Although the material properties were reviewed using a modal analysis (Section 4.6) there were a number of flaws identified with this technique which suggested the results could not be relied upon.

A second optimisation study was completed within ANSYS, using the impact hammer experimental results and the impact hammer simulation to find what material values produced matching results. The optimisation goals were taken from the experimental results, summarised in Table 4.7. The solution time was set to 1.8 ms so that both the positive and negative peaks of the strain in the x-direction could be used as optimisation targets.

Table 4.7 - Optimisation goals for simplified radio impact hammer simulation

Goal	*Measurement value*	*Maximum/minimum*	*Target Value [με]*
1	x-strain	Maximum	370
2	x-strain	Minimum	-515
3	y-strain	Maximum	349

4.14.1. Results of Young's modulus optimisation

The optimisation process gave Young's moduli of 13.69 GPa and 4.87 GPa for the PCB and ABS materials respectively. The optimisation process used was the multi objective genetic algorithm (MOGA) within ANSYS; the iteration process is shown in Figure 4.52 and Figure 4.53. The newly found material values were introduced into the impact hammer simulation (Figure 4.54 - Figure 4.56).

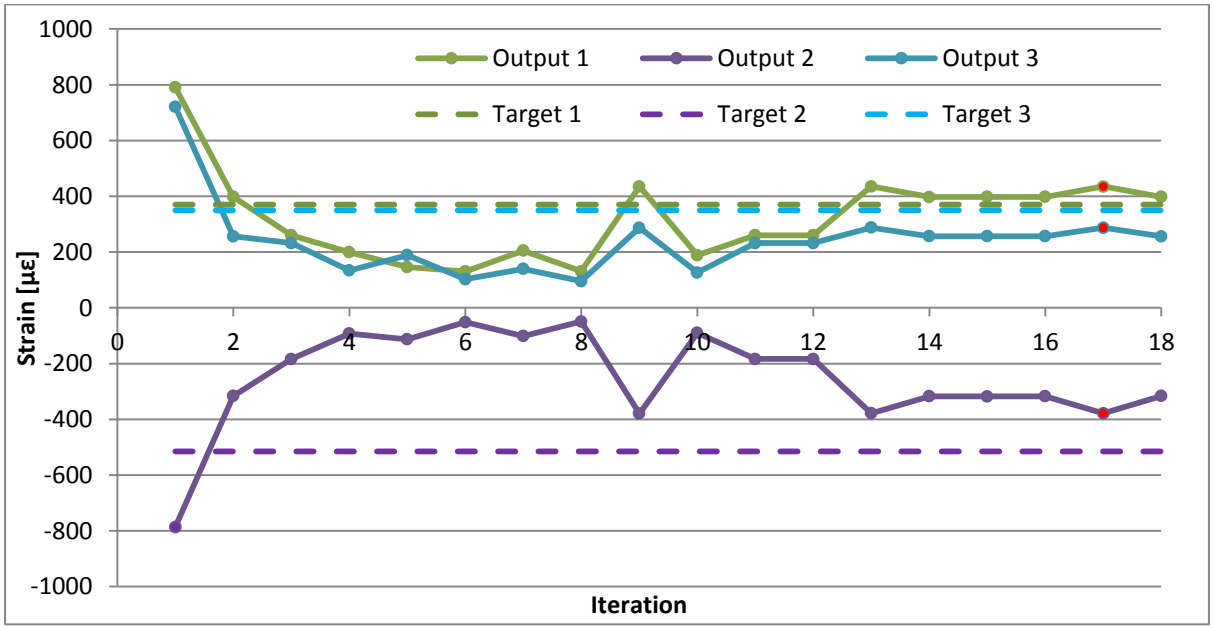

Figure 4.52 - Optimisation process of impact hammer simulation showing the three target peaks (Table 4.7) and outputted simulation results (black indicating optimal design point)

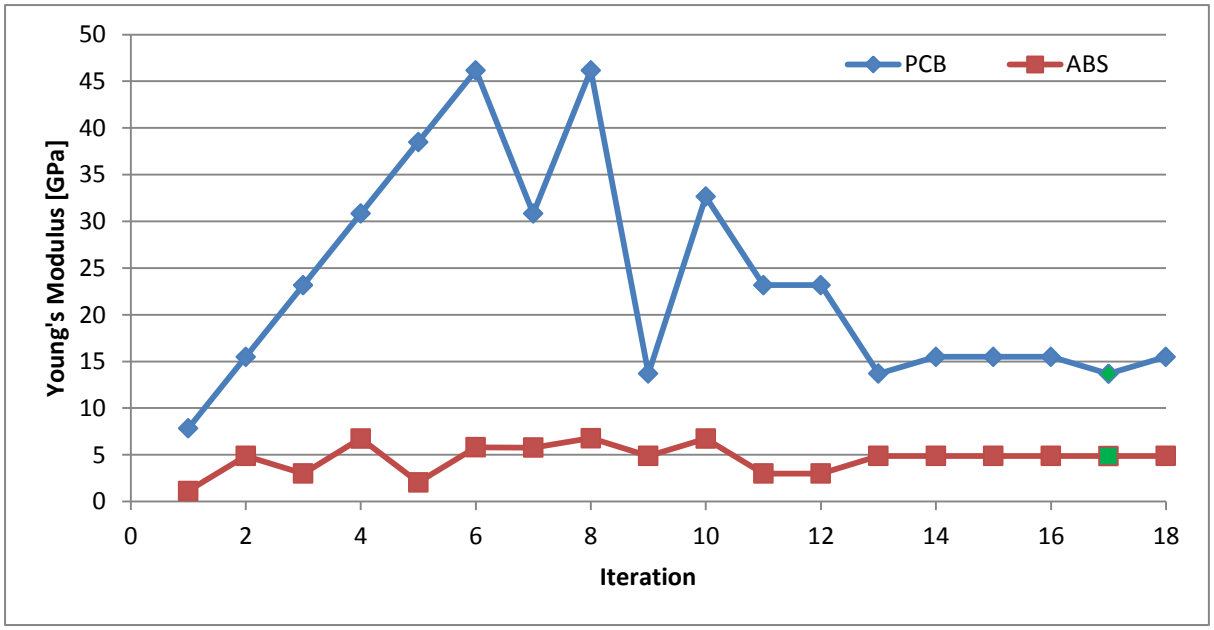

Figure 4.53 - Optimisation process of impact hammer simulation showing the change in material properties over the iteration process (green indicating optimal material properties)

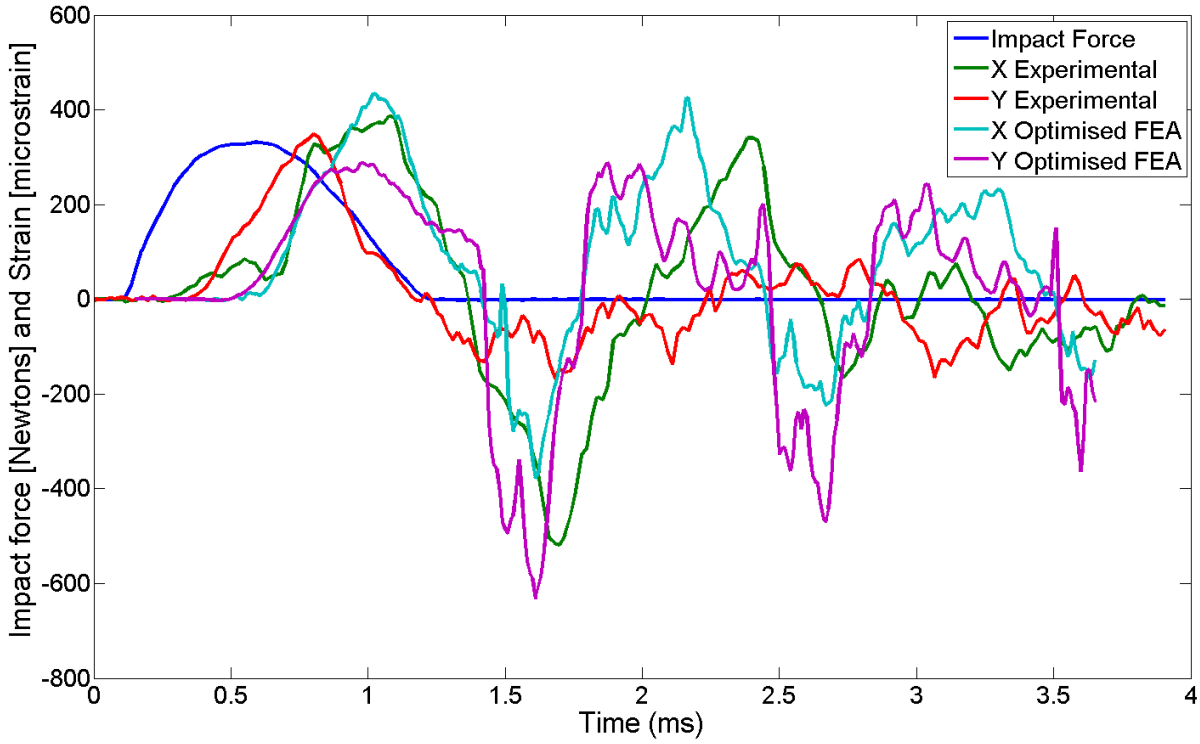

Figure 4.54 - Impact hammer finite element results using optimised material properties

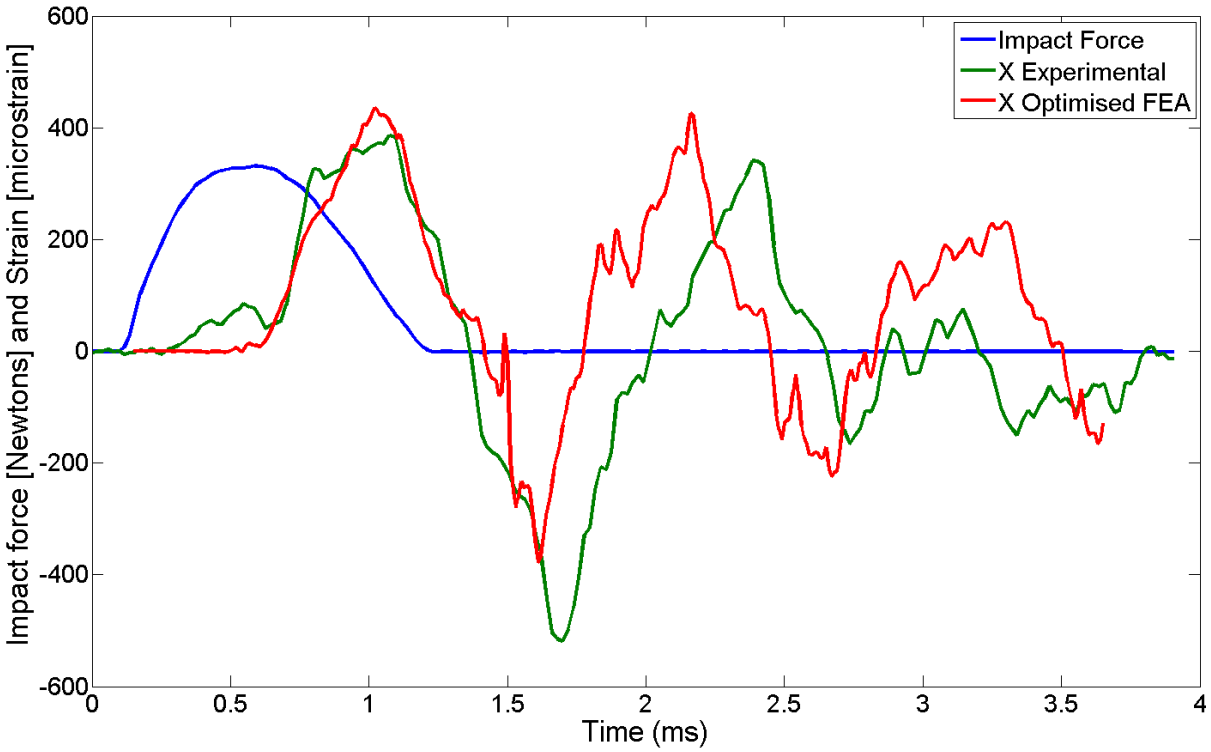

Figure 4.55 - Impact hammer results in the x strain direction using optimised material values

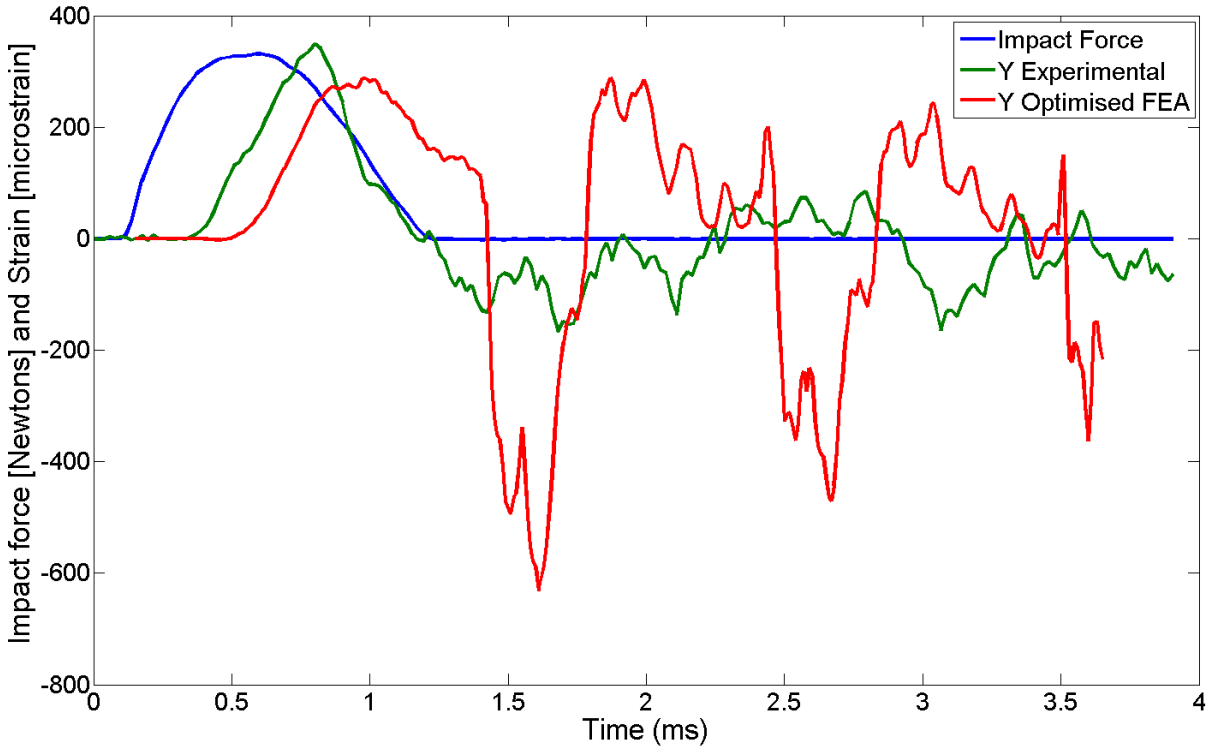

Figure 4.56 - Impact hammer results in the y strain direction using optimised material values

The results from the impact hammer simulation that used the optimised Young's moduli produced improved agreement with experimental data. The x directional strain matched much better than the strain in the y direction. It is believed that the model produced is now setup to give the best results. There is still some disagreement between the two methods, in particular the secondary y strain peak. Possible reasons for the variances between the two values are discussed below.

4.15. Discussion of the Developed Impact Hammer Model

A comprehensive review of the explicit dynamic solver including the associated settings and parameters has now been completed. The development process concluded in a more realistic model being presented, contrasting greatly with the initial model which predominately used default settings and over simplified assumptions.

The development of the impact hammer model of the simplified radio assembly has demonstrated the influence of a number of finite element parameters. In addition to the parameters already investigated there are additional inaccuracies related to intrinsic disparities between the physical and virtual models.

4.15.1. Material model

An isotropic, linear elastic material model was used for both the ABS and PCB materials in the finite element simulation. This material model assumes that the material behaviour is identical, regardless of loading direction (isotropic) and that the stress-strain behaviour is of a linear nature (linear elastic).

The assumption of isotropy is questionable for both the ABS and PCB materials. The fused deposition modelling method used to make the ABS parts does not result in a completely solid part (Figure 4.57), instead there are air gaps and artificial 'grains' present. The PCB is constructed of a glass fibre composite, the fibre layup is a cross ply alternating between 0° and 90°. The construction of these materials indicate that there is potential for variation in behaviour for different loading directions, i.e. when the PCB material is loaded parallel/perpendicular to the fibre vs. when loading occurs at some angle to the fibres.

For parts that use shell elements, only isotropic materials can be used. Tetrahedral elements also have some material model restrictions depending on which integration method is used. Standard constant pressure integration has no material restrictions, average nodal pressure integration only allows isotropic materials and nodal based strain requires that ductile materials are used [32].

It would be difficult to apply an anisotropic material to the ABS as the deposited material follows the contours of the part and not a direction which can be applied globally. The anisotropy of the PCB is believed to be minimal and additionally the boards are often modelled with shell elements so therefore anisotropic behaviours cannot be applied.

Figure 4.57 - 3D printed chassis showing 'grains' and material gaps as a result of the FDM printing process

4.15.2. Mesh

Meshing simplifies solid geometries to a series of lines and points, when the mesh size is large this leads to bigger approximations and overall, a lower quality result. The variance of behaviour as a result of changing the mesh size (Section 4.9) shows the importance of this feature. The 1.2 mm mesh size used provides a fair representation of the physical model geometry. The mesh was set to be patch conforming which means that it matched the outside geometry to the best of its ability, this allowed for an accurate representation of part dimensions as well as their interactions with other parts. The size of the mesh was small enough that most parts have at least three elements through their thickness, so the calculation of bending was significantly more accurate than if only one element were used. Ideally the mesh size should be further reduced for a final simulation model to get higher accuracy as well as better understanding of stress at localised areas (i.e. at screw locations).

A finer mesh was deemed unnecessary during the impact hammer development model as it was established that the results did not change significantly if the global mesh size was lower than 1.3 mm (Section 4.9). Additionally employing a finer mesh would lead to a longer development time as there were a large number of simulations performed during this investigative period. A finer mesh size (0.9 mm) was used for the drop-impact simulation where the results were of greater interest.

4.15.3. Material damping

The explicit dynamics solver does not generate damping values for individual materials within the model, instead global damping values are applied. This means that the damping is approximated and cannot be altered between materials, even if vastly different damping characteristics are present. Both hourglass damping and artificial viscosity damping values were found to have little influence on the finite element results and were therefore left as default. The static damping method was designed for damping of events that occur before or after the primary transient event. For the case of the impact hammer test and drop-impact events, there were no loading of parts prior to impact and no static behaviour after the impact that were of particular interest and therefore static damping was ignored.

4.15.4. Experimental testing

The impact hammer experimental results used to evaluate the accuracy of the finite element model were from one test only and not an average over a series of different tests because of the difficulty in repeating the impact hammer force. Additionally the comparison of the experimental to finite

element results was primarily looking at one measurement location (strain of RF board); this put a lot of reliance of the accuracy on the measurement location.

4.15.5. Measurement locations

The strain measurements from the finite element model were taken from a single point (Figure 4.58). The strain measurements completed in the physicals tests used a strain gauge with a diameter of approximately 10 mm. To ensure the measurement of a single point was equivalent to the strain as measured by the strain gauge, additional finite element strain measurements were made. Five locations were chosen within a 5 mm radius of the original measurement location (Figure 4.58). The additional finite element strain results (Figure 4.59) showed similar measurement values, confirming that the use of a single measurement point to replicate a strain gauge measurement was an acceptable practice.

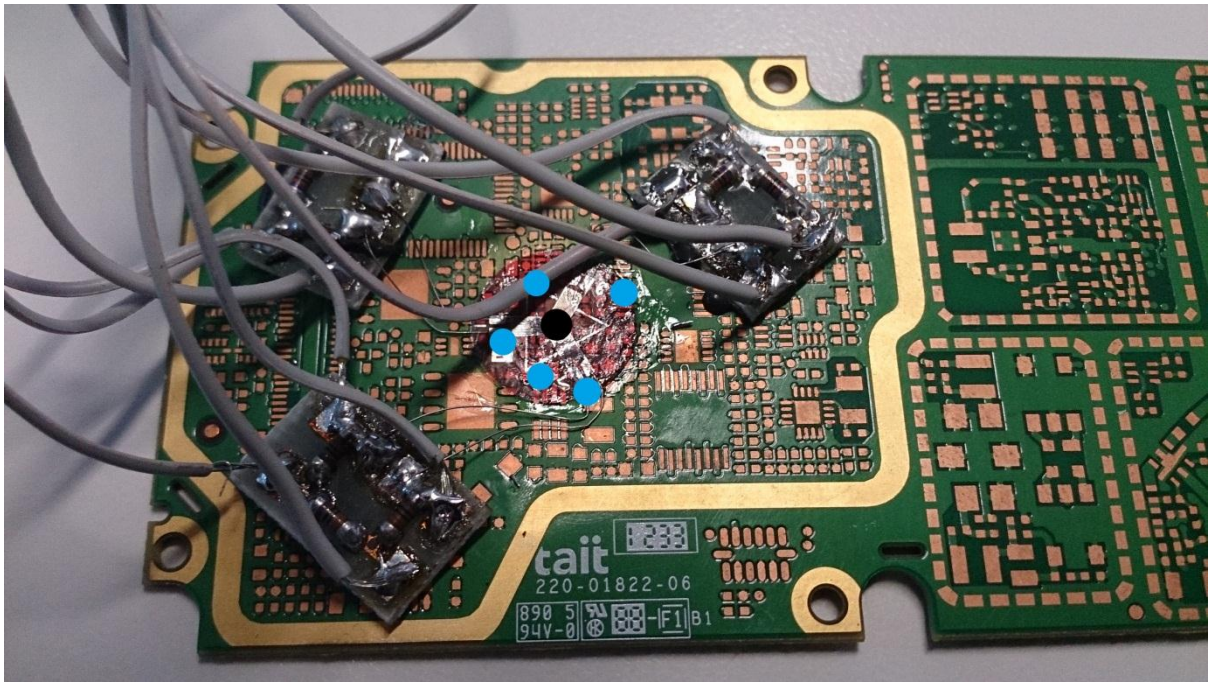

Figure 4.58 - Strain gauge of RF board, black point indicates where finite element measurements were taken from, blue points indicate approximate locations of additional strain measurements used in Figure 4.59

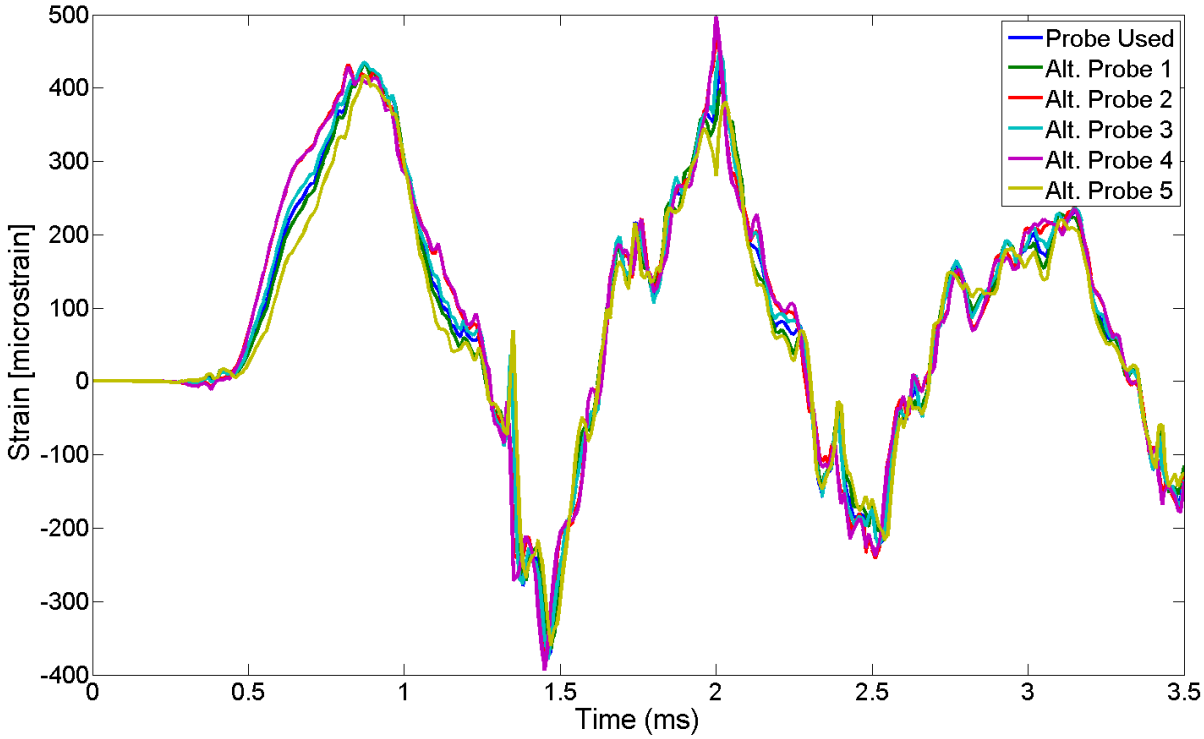

Figure 4.59 - Strain results in the x-direction at different locations directly around initial measurement location

4.15.6. Extrapolation of measurement data to entire radio behaviour

The validation of the finite element model used minimal measurement locations to validate the correctness of the entire radio assembly behaviour. There were few locations where transducers could be mounted due to the compactness of the radio assembly and in any case transducers do influence the behaviour of the radio assembly due to the added weight and stiffness. The transducer locations were chosen to be at points where maximum deformation was likely to occur, and also far away from the initial excitation point to ensure that the complete shock wave transmission path (point of excitation to furthest point) was considered.

The transducers were placed on the PCBs and not the ABS parts because they were considered the most important part. Reducing loading and deformations of the PCB would have the greatest influence on increasing survivability of the overall product as this is the failure location for most the portable electronic devices. If a specific area were identified as having a high number of failures, it would be appropriate to place transducers there so data could be directly matched to the finite element model.

4.16. Conclusion of Impact Hammer Model

Overall, the developed impact hammer finite element model provided reasonable results; however there was still some disagreement between the physical and virtual models. The development of the impact hammer model was considered to be exhausted in terms of the modification of influential settings found within the explicit dynamics solver. The discussion above outlines the inherent disparities between physical and virtual models, indicating that there is always potential for disagreement between experimental and finite element results, even when all physical attributes are well established. Focus was now shifted to the more severe drop-impact event in which the findings from the impact hammer model are applied.

4.17. Drop-Impact Modelling of the Simplified Radio

Drop-impact simulation and testing was investigated as the drop-impact behaviour of the simplified radio is expected to differ from the impact hammer analysis for the following reasons:

- All bodies in the assembly have an initial velocity (and therefore momentum)
- The test product would interact with a solid, fixed body (ground)
- Higher velocities are involved
- Loading on parts will be higher than with an impact hammer

The main change from the impact hammer model was the introduction of the impact plate. The behaviour of this was considered before the simplified radio drop-impact model was run.

4.18. Impact Surface Response

The drop-impact model incorporates an impact plate that replaces the impact plate-load cell-ground arrangement present in the physical environment (Figure 4.60). The impact plate used in the finite element model has the dimensions of 200 x 100 x 20 mm. Instead of including the entire impact plate and load cell system, the material properties of the impact plate are set to match the physical system. To generate the necessary behaviour a simple, steel ball impact was tested and modelled.

Figure 4.60 - Experimental impact plate setup

4.18.1. Steel ball impact testing

A solid, hardened steel ball with a diameter of 50 mm was dropped onto the impact surface from a height of 1 m, the test was performed 20 times. The results show an average peak force of 7158 N (Table 4.8).

Table 4.8 - Peak impact forces from experimental tests of a 1 m steel ball drop onto impact plate

Test	*Peak Impact Force*	*Test*	*Peak Impact Force*
1	7305	11	7360
2	6323	12	7441
3	6576	13	6550
4	6712	14	8697
5	7276	15	8032
6	7675	16	7275
7	7126	17	6420
8	6605	18	7478
9	6564	19	7589
10	6827	20	7342
Average			**7158.6**

4.18.2. Steel ball simulation

A ball impact simulation was developed so that different impact plate material properties could be investigated. An initial velocity of 4.43 ms^{-1} was applied to the ball and a fixed support was applied to the underside of the plate, the fixed support was used to measure the impact force transferred from the ball to the plate.

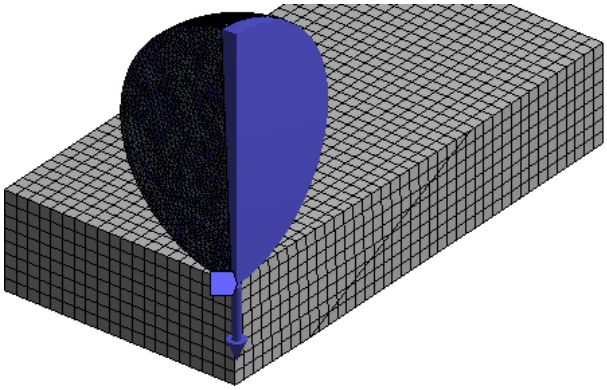

Figure 4.61 - Ball impact simulation, quartered to make use of symmetry of model

A parametric study was completed using a range of Young's moduli for the impact plate; the peak impact force for each value is presented in Figure 4.62.

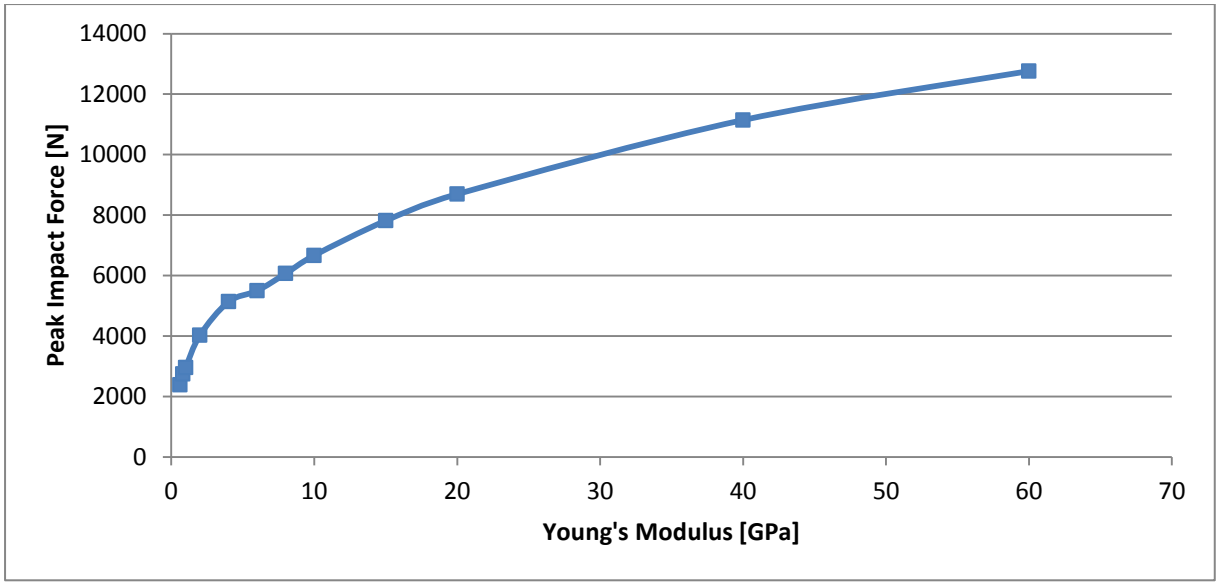

Figure 4.62 - Peak impact force of ball impact from a height of 1 m for a range of different impact plate material values

To achieve the same impact force as the experimental tests, a Young's modulus of 12.15 GPa was required (calculated by interpolating between points in Figure 4.62). A comparison between the experimental results and the ball impact simulation using a modulus of 12.15 GPa is shown in Figure 4.63, the peak impact force of the finite element model was 7210 N.

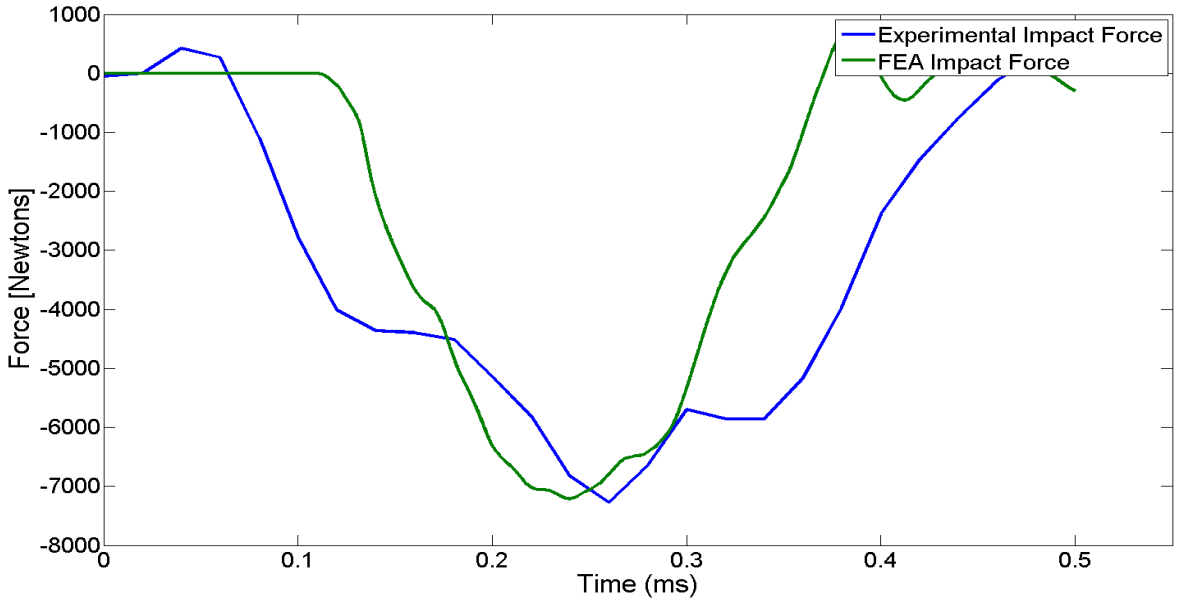

Figure 4.63 - Comparison of impact force of 1 m steel ball drop between experimental (Test #5 - Table 4.8) and finite element results

4.19. Drop-Impact Finite Element Model of the Simplified Radio

An initial model was completed using analysis settings, materials values and geometric settings established during the impact hammer model.

4.19.1. Drop-impact model setup

The same simplified radio assembly and its associated contact conditions were used for the drop-impact model. A plate with dimensions 200 x 100 x 20 mm was used as the impact surface (Figure 4.64). A fixed support was applied to the underside of the impact plate. The fixed support was used to constrain the impact plate and to calculate the force of the radio drop-impact event.

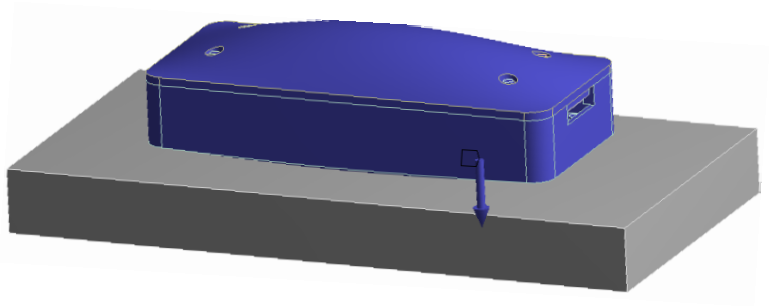

Figure 4.64 - Drop-impact model showing initial velocity direction and impacting surface

The key input parameters are summarised in Table 4.9. Most of the settings were the same as used in the final impact hammer model; the only significant change to the model was the decrease of the global mesh size from 1.2 mm to 0.9 mm (Figure 4.65).

Table 4.9 - Summary of initial drop-impact model settings and parameters

Setting	*Parameter*	*Value*	*Unit*	*Reference Section*
Material values	Density (ABS)	935	kgm^{-3}	4.5
	Young's modulus (ABS)	4.87	GPa	4.14
	Density (PCB)	3090	kgm^{-3}	4.5
	Young's modulus (PCB)	13.69	GPa	4.14
	Density (Screw)	7850	kgm^{-3}	4.10
	Young's modulus (Screw)	20	GPa	4.10
	Density (Impact plate)	7850	kgm^{-3}	4.19
	Young's modulus (Impact plate)	12.15	GPa	4.18
Mesh	Global mesh size	0.9	mm	4.15.2
	Pinch and defeaturing tolerance	0.3	mm	4.4.4
	PCB layers	3		4.12.1
	Number of elements	750,233		

Setting	*Parameter*	*Value*	*Unit*	*Reference Section*
	Number of nodes	228,854		
	Average element quality	0.8244		4.4.4
	Standard deviation of element quality	0.1045		4.4.4
Contact conditions	Screws (lower)	Bonded		4.10
	Screws (upper)	Frictional (0.3)		4.8
	Part – part (general)	Frictional (0.3)		4.8
	Radio – impact plate	Frictional (0.3)		
Boundary conditions	Bottom plate	Fixed		
	Radio velocity	4.43	ms^{-1}	
Solver settings	Analysis end time	2.5	ms	
	Precision	Double		4.4.5
	Tetrahedral integration method	Nodal based		4.12.4
	Result output	100	Hz	4.4.5
	Solution time	23.3	Hours	

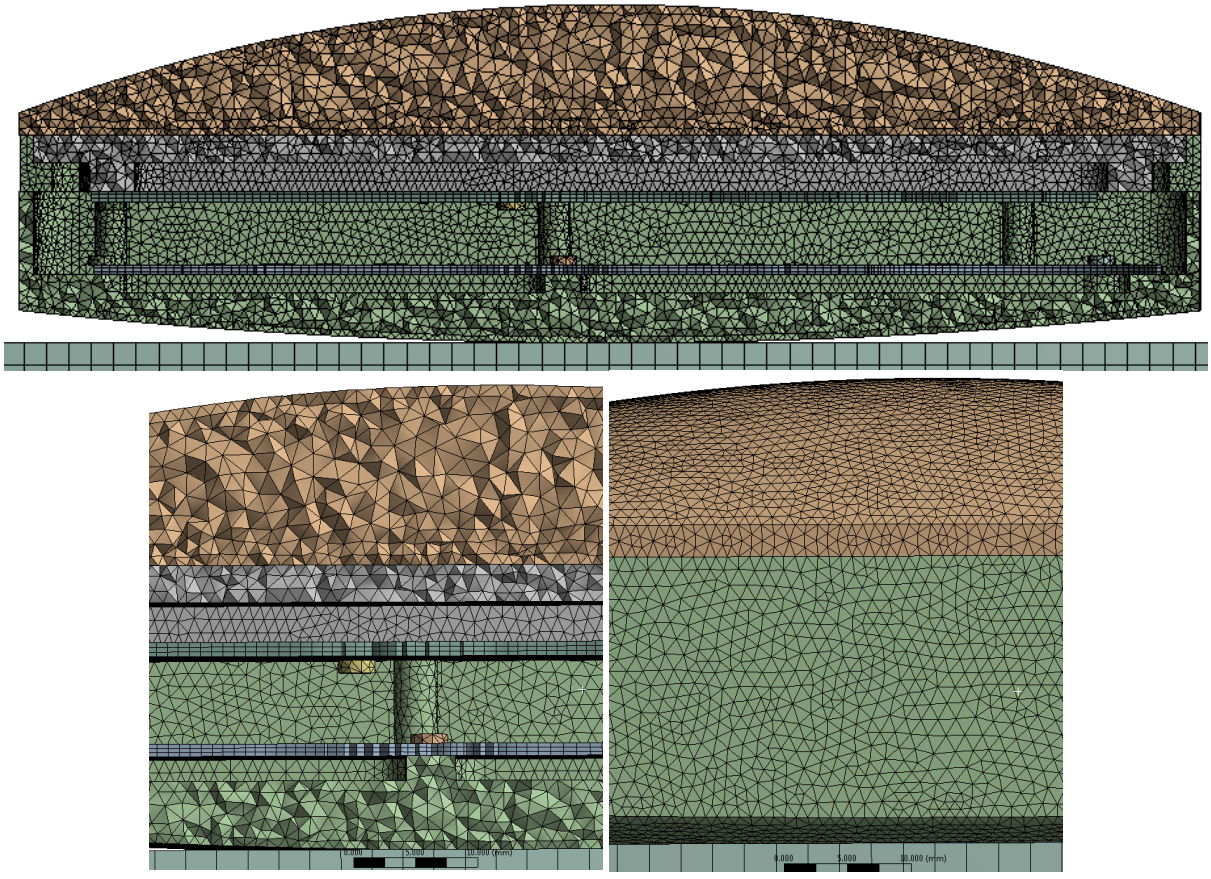

Figure 4.65 - Mesh of simplified radio drop-impact model, showing impact surface positioned under radio

4.19.2. Drop-impact model results

The stress wave propagation through the model was evaluated to ensure the global behaviour of the radio was acceptable and that all contacts and part interactions behaved as desired. Strain measurements from the finite element model at the experimental measurement locations (on the RF and MMI board, Figure 4.4 and Figure 4.5) are shown in Figure 4.67. The impact force results are shown in Figure 4.68. Both the magnitude and time response of the force and strain measurements from the finite element model appear reasonable. The peak force and strain measurements are higher than those experienced during the impact hammer testing (~400 N and με vs. ~4000 N and με) which is expected due to the increased severity of the event.

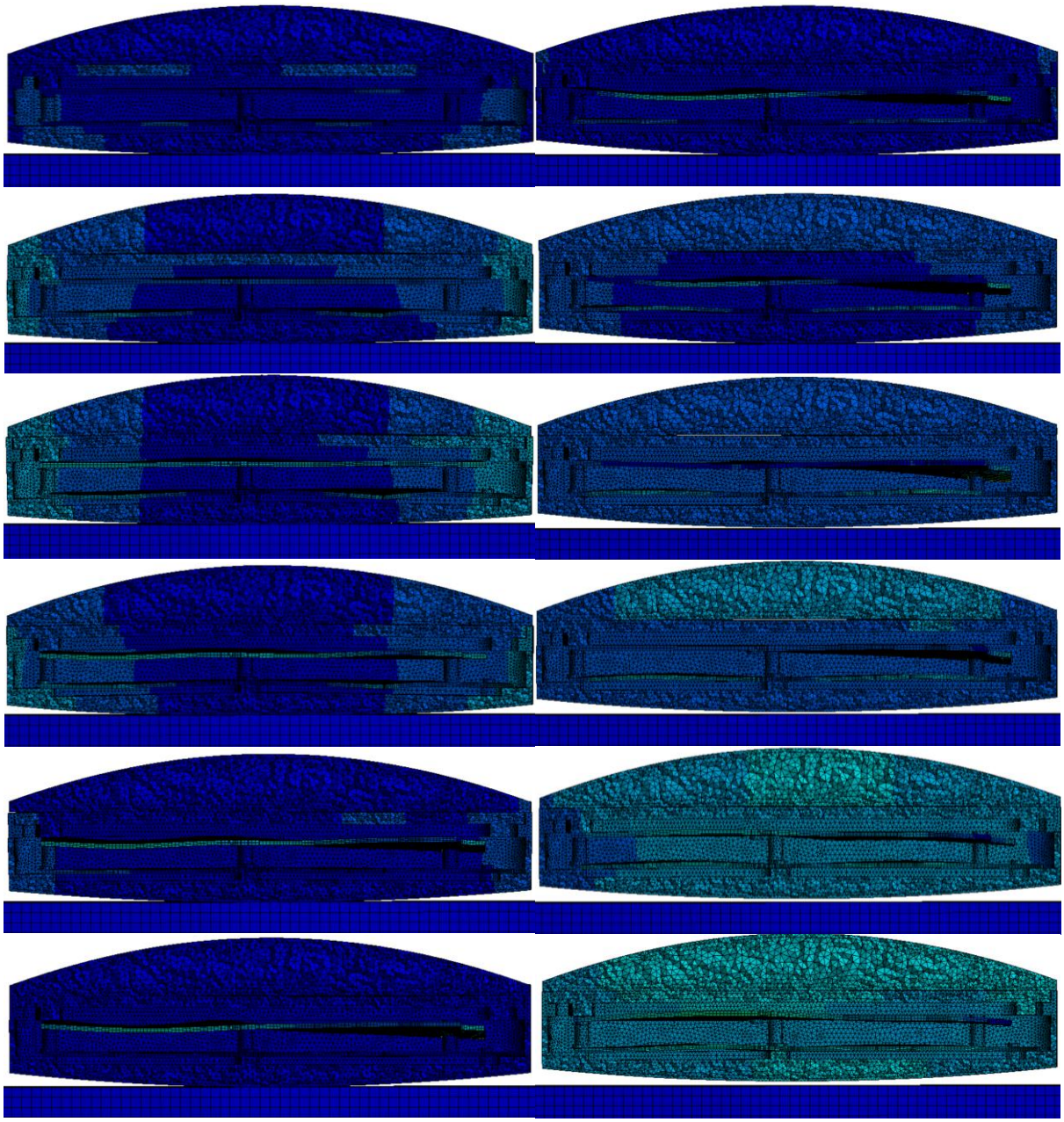

Figure 4.66 - Deformation of simplified radio during horizontal impact event from a height of 1 m (end time 1 ms). NB: The order of images follows down the first column then moves down the second column

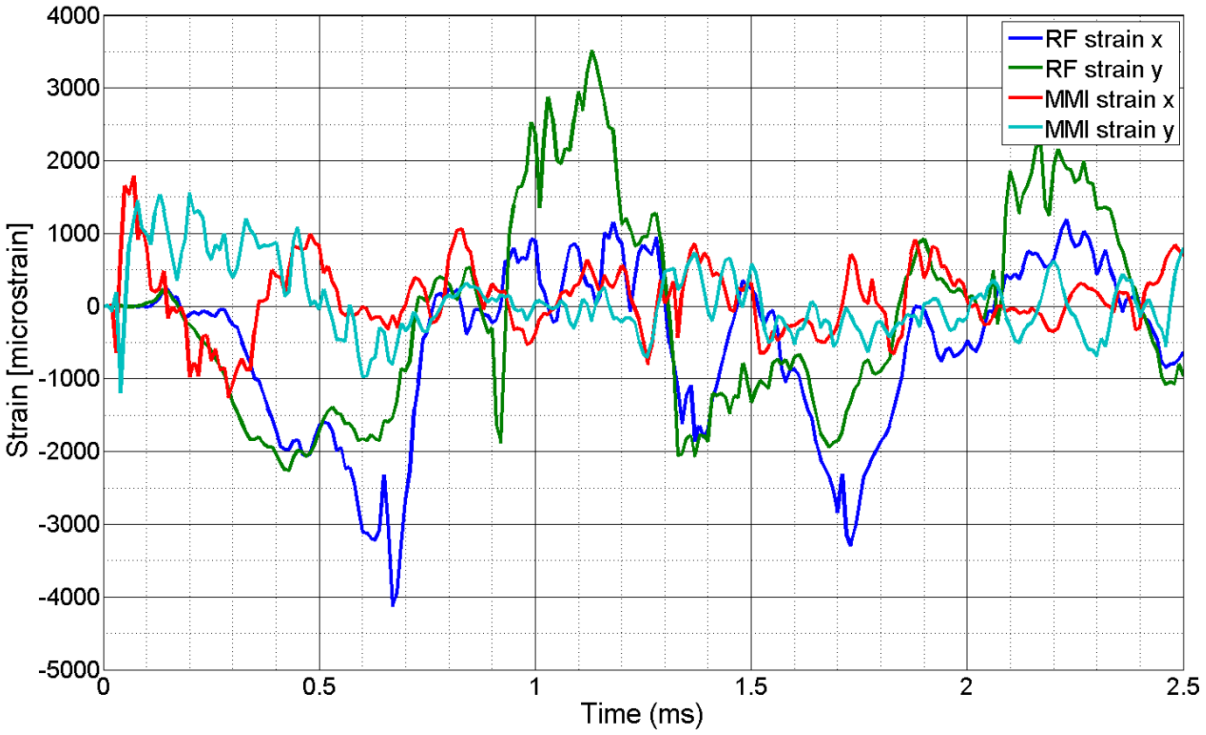

Figure 4.67 – Simulation results of strain in the x and y direction at measurements points on the RF and MMI PCBs (Figure 4.4 and Figure 4.5)

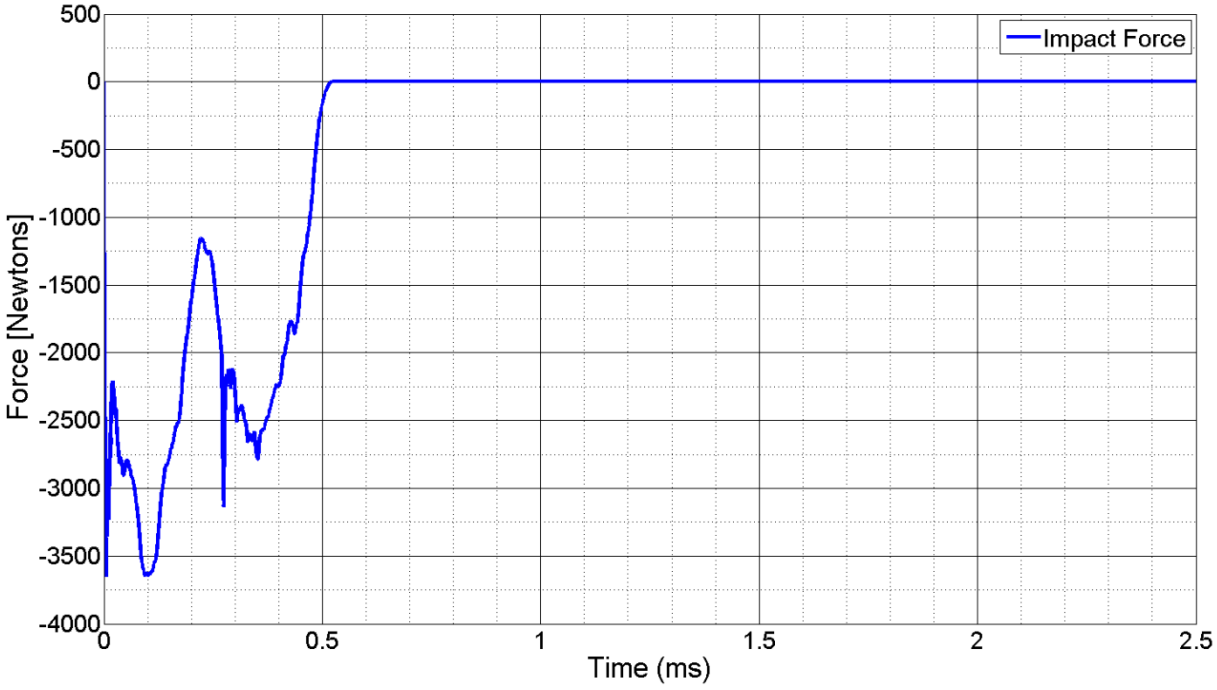

Figure 4.68 - Impact force of simplified radio dropped from 1 m as measured at the impact plate within the finite element simulation

4.20. Drop-Impact Testing of Simplified Radio

The drop-impact testing used the test rig developed for this project (Appendix A). The tests involved dropping the simplified radio from a height of one metre to match the drop-impact event simulated.

4.20.1. Drop testing results

During drop testing of the simplified radio assembly it was found that the 3D printed radio was too fragile for the 1 m drop-impact event, as shown in Figure 4.69. Several front panels were printed and failed in similar ways. It was decided that the method of printing the radio (layer by layer) made the radio too susceptible to failure between the printed layers. The simplified radio produced was deemed unsuitable for testing when severe loadings occur, like those experienced during the drop-impact tests.

Figure 4.69 - Damage to simplified radio assembly, in particular the damage to the screw bosses which connect the front panel to the chassis

4.21. Discussion of the Drop-Impact Model

Having already developed a working impact-hammer model, the development of the drop-impact finite element model was a lot more straightforward. The presented results were however not able to be compared to experimental results as the severity of the drop-impact event was too high for the printed radios to withstand. Comparing the impact hammer force strains to the drop-impact simulation strains showed that the drop-impact event gave higher peak forces and strains which were as expected. Increasing the severity of the impact did not to create issues when running the finite element simulation.

4.22. Summary

A simplified radio assembly was developed to create a better understanding of the finite element model without the presence of a complex, long solving models. An impact hammer model was initially investigated before a drop-impact model was developed.

The impact hammer model was tuned via a series of simulations, with one parameter modified each instance. All changes to the solver were found to have an influence on the results generated, however with varying degrees. As understanding of the finite element model and physical properties of the simplified radio assembly became known, agreement between the experimental and finite element results also improved. The material and mesh (refinement and element types) settings were found to have the most influence. Material properties were generated using optimisation studies to give the best agreement between the experimental and finite element results.

Having developed the impact hammer model to give acceptable agreement with experimental results, focus shifted to drop-impact events. Before the drop-impact simulation was conducted, a study of the impact surface was performed. A steel ball was dropped onto the impact plate and a similar finite element model developed. The material properties for the impact plate used in the finite element model were modified until there was close agreement with experimental results. The initial drop-impact simulation used the findings from the impact hammer model and the newly found impact plate properties.

Drop-impact tests were performed to generate the necessary experimental data to validate the model. Test data was not able to be acquired due to the fragility of the 3D printed radio.

Overall, the analysis of the simplified radio showed that without detailed knowledge of the simulated model, including well established material properties, understanding of how part

interactions, and part constraints it becomes extremely difficult to develop a model which produces accurate results. In addition the physical knowledge of the impact model, understanding of the finite element solver and its associated settings are vital to get agreeable results.

5. Detailed Radio Testing and Simulation

Results from testing and simulation of a detailed radio assembly are presented. The detailed radio assembly was based on Tait's current handheld radio, with only minor modifications made to ensure usability within the finite element environment.

Drop-impact testing was performed on the detailed radio assembly. Drops were completed from a height of 1.8 m onto the front face of the radio.

Setup and simulation of the detailed radio assembly was completed, with the aid of findings from the simplified radio previously developed. The finite element results were compared to the experimental drop test results. The generated finite element model was analysed to show its use within a product development environment.

5.1. Introduction

With reasonable agreement between experimental and simulation results achieved for the simplified radio assembly, a more complex system was investigated. The results from the simplified radio, although successful, were for an over simplified model, consequently the behaviour of Tait's current handheld radio could not be determined. To understand the behaviour of Tait's handheld radio, a finite element model using a more representative assembly was developed.

This chapter takes the findings from the simplified radio model and applies them to a more detailed model of the assembly. The implementation of a more complex assembly was expected to create its own set of issues which would need to be addressed before reasonable finite element results could be achieved. The aim was to present the realities of using finite element models for analysing commercially realistic products and to discuss the associated issues and benefits.

5.2. Detailed Radio Model

Ideally, it would be possible to import the geometry of the Tait radio into the finite element solver and produce a solution in an efficient manner, without any interferences, overly detailed mesh or connection issues present. The level of detail contained in the Tait radio makes this difficult. Parts were simplified and insignificant parts removed to make the Tait radio assembly more functional within the finite element environment. A description of the parts present in the Tait radio assembly and the changes made to create a workable model are detailed, in Appendix B.

A comparison between the initial Tait handheld radio and the geometry used in the finite element drop-impact model is shown in Figure 5.1. The majority of modifications to the CAD geometry consisted of removing small geometric features including:

- Filet radii
- Small part recess (provided for labels etc.)
- Locating tabs and notches

Parts removed from the assembly due to their small size or location included:

- Small electrical items, including the majority of the board mounted components
- Antenna, channel and volume selectors
- Side button assemblies

Figure 5.1 - Tait handheld radio before and after modifications to CAD geometry

5.3.Finite Element Model Setup of the Detailed Radio

A full description of the geometry, material properties and part interactions are presented in Appendix B. A summary of the finite element model is presented below.

5.3.1. Material properties

The material properties for the finite element model used information provided by material suppliers. The supplier information included values such as material densities, shrink rates/percentages, and tensile/flexural information including yields, strains, strengths and moduli. The material model used in the finite element model was a linear elastic model which required a

Young's modulus, Poisson's ratio and density to be fully defined. The Poisson's ratio was assumed to be 0.3 for all materials apart from the softer materials (keypad, seal etc.) which used a value of 0.49. Some of the material data supplied included both tensile and flexural modulus values. Due to the likelihood of bending loads acting on parts, the flexural modulus was used.

Softer materials including the keypad, seal and front panel/battery over-moulding did not have tensile or flexural moduli values available, so Shore A hardness values were used. Kunz et al. [37] developed a way of converting Shore A hardness information to Young's modulus using the following equation:

$$E = \frac{1-\mu^2}{2 \cdot R \cdot C_3} \cdot \frac{C_1 + C_2 \cdot Sh_A}{100 - Sh_A} \cdot (2.6 - 0.02 \cdot Sh_A) \quad \textbf{(5.1)}$$

where, E is the Young's modulus, μ is Poisson's ratio, Sh_A is the measured Shore A Hardness, R = 0.395 mm, C_1 = 0.549 N , C_2 = 0.07516 N, and C_3 = 0.025 mm. This method can only be applied to materials that have a Shore A hardness in the range between 30 and 95 (all the materials used were within this range).

The PCB material properties were not provided; however the material properties were established during the development of the simplified radio model in Chapter 4.

The impact plate used material properties established in Section 4.18.

A summary of the material values used for each part are shown below in Table 5.1. For more information about the materials used, refer to Table B.1 (Appendix B).

Table 5.1 - Material properties used for finite element analysis of detailer radio model

Part	*Material*	*Property*	*Value*	*Units*
Front Panel	Makroblend® UT250	Density	1210	kgm^{-3}
		Flexural modulus	2.3	GPa
Battery Case	Makrolon 3103 MAS157	Density	1190	kgm^{-3}
		Flexural modulus	2.3	GPa
Over-moulding (Front Panel, Battery Case)	Desmopan 5377A	Density	1140	kgm^{-3}
		Young's modulus*	11.1	MPa
Battery Lid	PC Impact Modified RTP 399 X 62313B	Density	1190	kgm^{-3}
		Flexural modulus	2.206	GPa
Chassis	LM20/AlSi12Cu/A413	Density	2650	kgm^{-3}
		Young's modulus	71	GPa
Keypad	Silicone KE-961T-U [38]	Density	1170	kgm^{-3}
		Young's modulus*	7.08	MPa
Lens	PMMA [39]	Density	1190	kgm^{-3}
		Flexural modulus	3.1	GPa
Rear Panel	Glass Reinforced Nylon TDS Grilon® BG-50 [40]	Density	1580	kgm^{-3}
		Tensile modulus	11.5	GPa
Seal	Liquid Silicone Rubber XIAMETER®RBL-2004-40 [41]	Density	1143	kgm^{-3}
		Young's modulus*	4.2	MPa
RF/MMI Board	Glass Fibre Reinforced	Density	3090	kgm^{-3}
		Young's modulus**	13.69	GPa
FIBS Shield	Conductive Silicone Nolato Silicone 8630 [42]	Density	1900	kgm^{-3}
		Young's modulus*	10.3	MPa
EMI Shield	Tin plated steel	Density	6000	kgm^{-3}
		Young's modulus	50	GPa
AA Battery	Lithium Ion	Density	4200	kgm^{-3}
		Young's modulus	20	GPa
Super-X adhesive	Super X No.8008 – black [43]	Density	1270	kgm^{-3}
		Young's modulus*	4.38	MPa
Impact Plate	Steel	Density	7850	kgm^{-3}
		Young's modulus***	12.15	GPa

* Calculated using "Calculation of Young's Modulus using Shore A Hardness" [37], Section 5.3

** Calculated using bend tests coupled with FEA, Section 4.14

*** Calculated using steel ball impact coupled with FEA, Section 4.18

5.3.2. Contact conditions

The detailed radio was held together via screws, adhesives and clips. Contact conditions were applied to best match conditions present in the physical assembly. Table 5.2 summarises all part to part interactions within the model and the contact condition applied, examples of the different contact conditions are depicted (Figure 5.2 - Figure 5.5). Frictional contact conditions used static and dynamic friction coefficients of 0.3. The assembly used face to face bonded connections in place of modelled screws at most screws locations. The only exception was at the RF board where screws were used because of the difficulty of establishing bonds between the solid elements of the chassis and shell elements of the RF board.

Table 5.2 - Summary of part contacts and interactions

Part 1	***Part 2***	***Contact Condition***	***Example***
Front Panel (body)	MMI Board (body)	Frictional	Figure 5.2
Front Panel (screw face)	MMI Board (screw face)	Bonded	Figure 5.3
Front Panel	Glass LCD	Frictional	Figure 5.2
Front Panel	Seal	Frictional	Figure 5.2
Front Panel	Front Panel Over-moulding	Bonded	Figure 5.4
Front Panel (body)	Chassis (body)	Frictional	Figure 5.2
Front Pane (screw face)	Chassis (screw face)	Bonded	Figure 5.3
Front Panel	Lens	Frictional	Figure 5.2
Front Panel	Lens	Bonded	Figure 5.4
Lens	Glass LCD	Frictional	Figure 5.2
MMI Board	Ceramic Antenna	Bonded	Figure 5.4
MMI Board	Keypad	Frictional	Figure 5.2
MMI Board	FIBS Shield	Frictional	Figure 5.2
Glass LCD	PC LCD	Bonded	Figure 5.4
Seal	Chassis	Frictional	Figure 5.2
AA Battery (x6)	Battery Foam	Bonded	Figure 5.4
AA Battery (x6)	Battery Case	Bonded	Figure 5.4
Chassis (body)	Rear Panel (body)	Frictional	Figure 5.2
Chassis (screw faces)	Rear Panel (screw faces)	Bonded	Figure 5.3
Front Panel	Rear Panel	Frictional	Figure 5.2
MMI Board (body)	PC LCD (body)	Frictional	Figure 5.2
MMI Board (tab faces)	PC LCD (tab faces)	Bonded	Figure 5.3
Antenna	Chassis	Frictional	Figure 5.2
Chassis (body)	RF Board (body)	Frictional	Figure 5.2

Part 1	*Part 2*	*Contact Condition*	*Example*
Chassis Screws	RF Board	Frictional	Figure 5.3
Chassis Screws	Chassis	Bonded	Figure 5.3
Battery Case	Rear Panel	Frictional	Figure 5.2
Battery Lid	Chassis	Frictional	Figure 5.2
Battery Lid	Battery Case	Bonded	Figure 5.4
Antenna	RF Board	Bonded	Figure 5.4
RF Board	EMI Shields	Bonded (Mesh – Mesh)	Figure 5.5

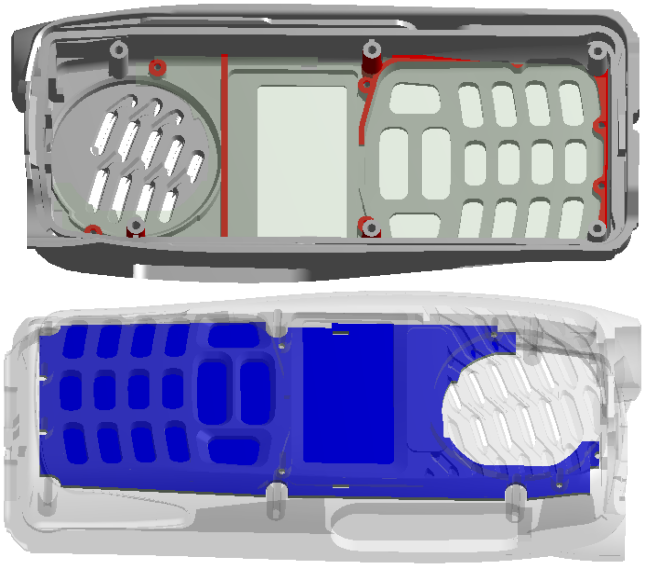

Figure 5.2 - Frictional contact interaction between front panel (red) and MMI board (blue)

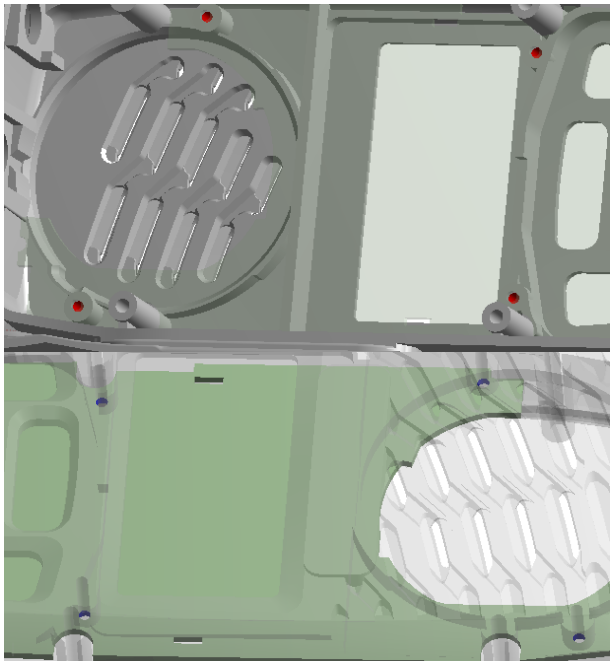

Figure 5.3 - Face to face screw imitation connection between front panel (red) and MMI board (blue)

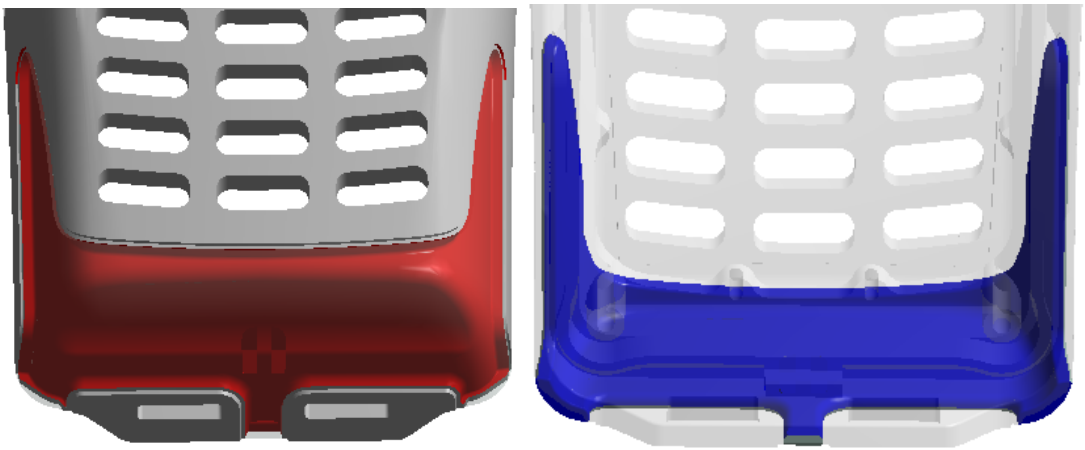

Figure 5.4 - Face to face bonded condition between front panel (red) and front panel over-moulding (blue)

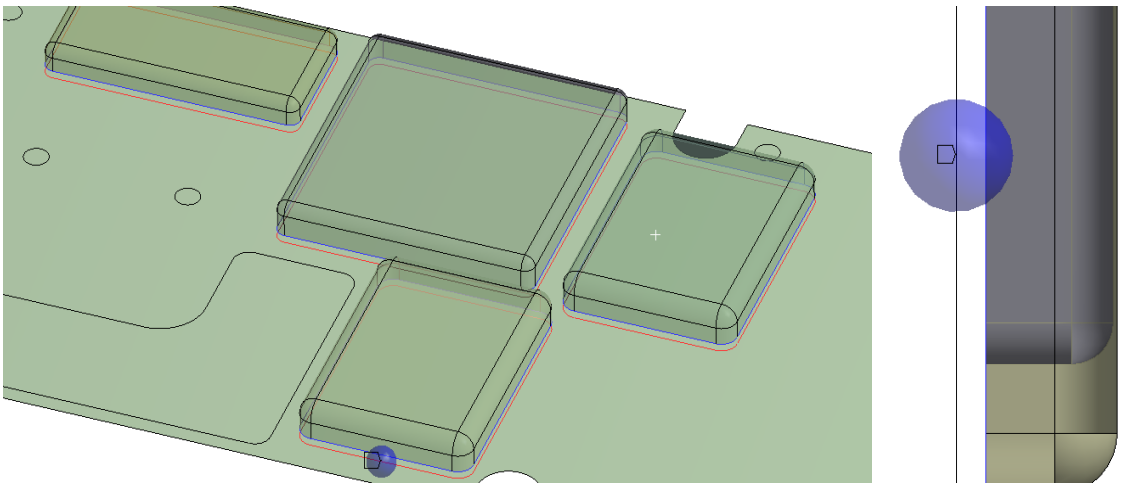

Figure 5.5 - Mesh to mesh contact condition between RF board (red) and EMI shields (red), blue sphere indicating contact tolerance (necessary for surface to surface body contacts)

Contact between the shell (RF board and EMI shields) and solid elements (remainder of the radio assembly) required special consideration. As default, body interactions had a shell thickness factor (STF) of zero. This meant that the generated thickness applied to surface bodies was not considered and contact was instead calculated to be at the mid plane of the body. A shell thickness factor of one meant that the thickness of the body was appropriately considered and the contact calculated at the outer most surface, this is demonstrated in Figure 5.6. A comparison between a STF of zero and one during an impact event is shown in Figure 5.7. The simulation was of a simplified chassis and RF board assembly, the RF board was constructed using shell elements. The results show that if the thickness of the surface is not considered then such parts will partially penetrate other bodies. It was found that only symmetric extrusions off mid planes were available for explicit dynamic analysis, i.e. it was not possible to extrude off a surface in only one direction or to extrude the part asymmetrically.

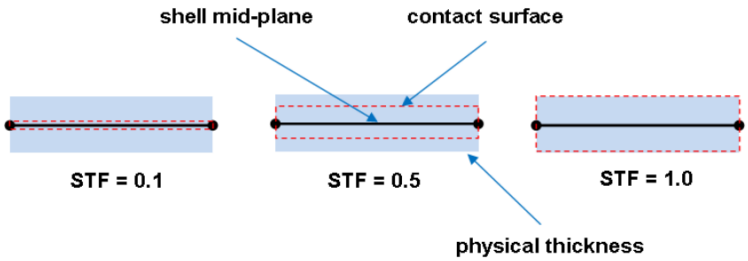

Figure 5.6 - Description of shell thickness factor

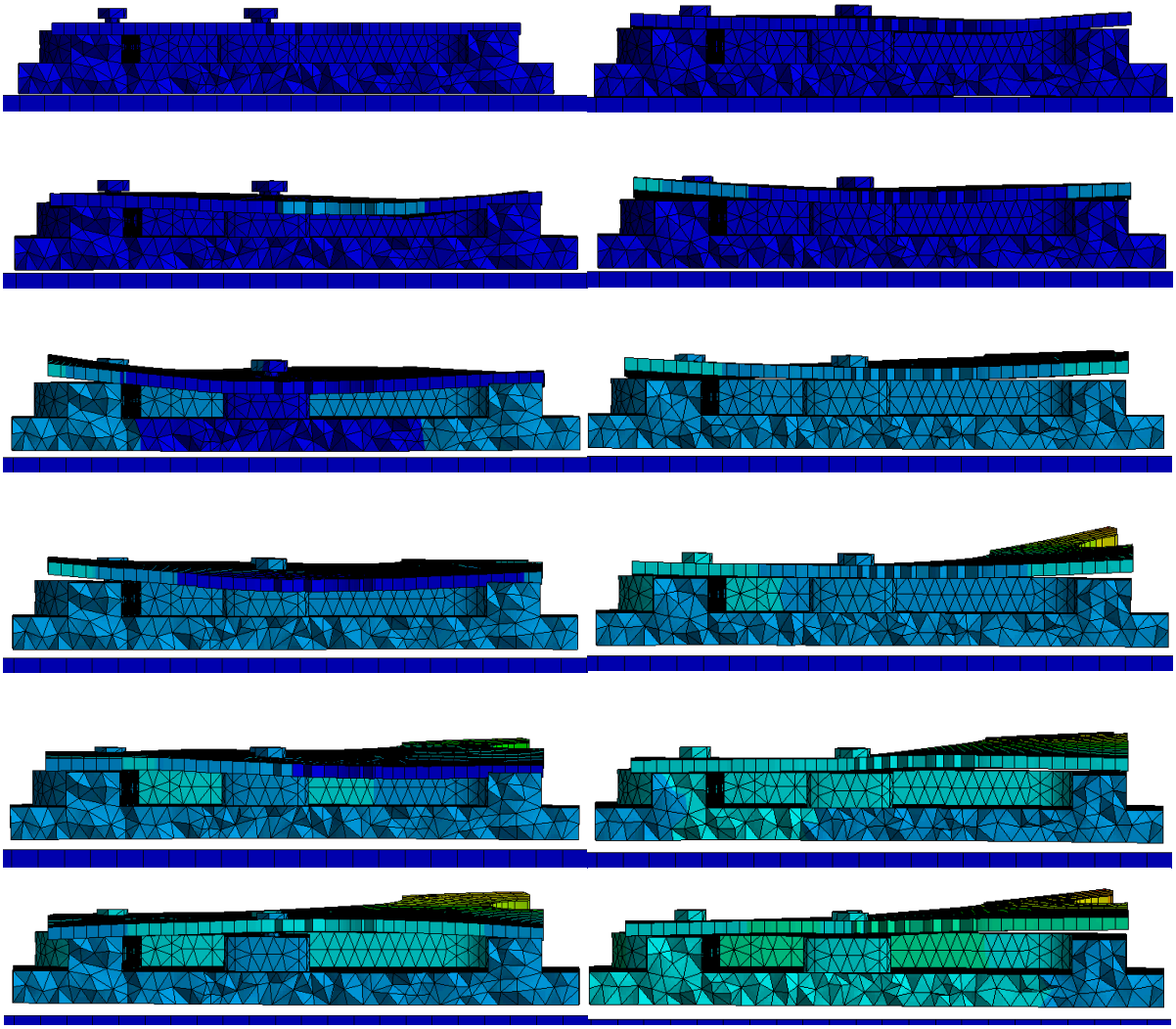

Figure 5.7 - Demonstration of the effect of different shell thickness factors. Images on the left show an impact using a STF of 0 and an impact using STF of 1 is shown on the right. The screws and chassis are made of solid elements and the PCB is made of shell elements

In addition to body interactions, bonded contacts between shell and solid elements were investigated. It was important to ensure that solid elements were able to bond to shell elements as both shell and solid elements were used in the detailed radio model. To understand the different contact conditions available a simple impact model was developed. The model consisted of a large rectangular sheet, 2 mm thick, modelled with shell elements using a reference mid plane (Figure

5.8). Blocks were offset from the mid plane by 1 mm such that they were positioned at the outer surface of the sheet once meshing was complete (Figure 5.9). The assembly was given an initial velocity and set to impact a solid surface. The investigated contact conditions between the rectangular sheet (shell elements) and the blocks (solid elements) are summarised in Table 5.3.

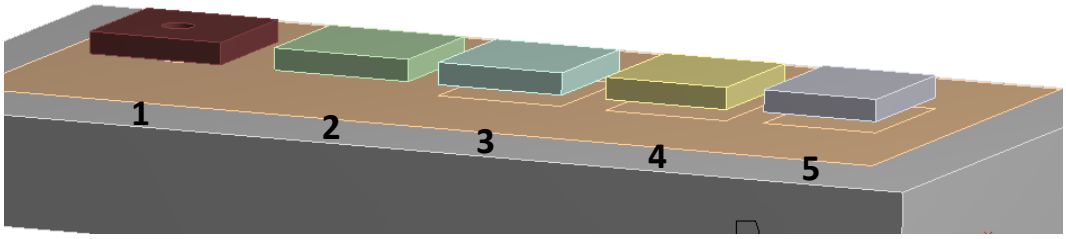

Figure 5.8 - Model setup to investigate different contact conditions between solid and shell elements, the blocks are numbered 1-5, left to right

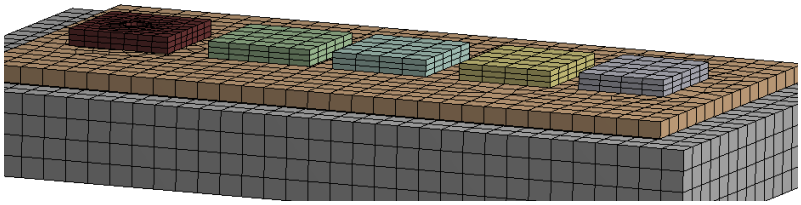

Figure 5.9 - Meshed model used to investigate solid and shell element contact conditions

Table 5.3 - Summary of different contact condition investigated and their results

Block	*Contact Description*	*Held*
1	Edge to edge contact between holes, maximum offset of 1 mm	No
2	Face to face contact, non-matching mesh (Figure 5.10), maximum offset of 1 mm	Yes
3	Spot weld at each corner of the block, maximum offset of 1 mm	Yes
4	Face to face contact, matching mesh, default maximum offset of $1x10^{-4}$ mm	No
5	Face to face contact, matching mesh, maximum offset of 1 mm	Yes

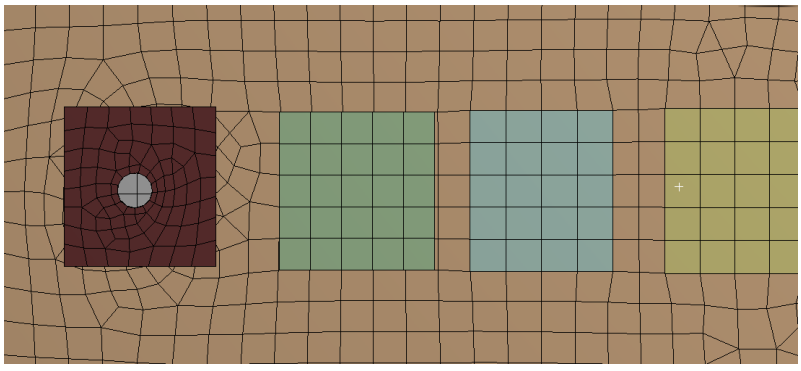

Figure 5.10 - Mesh of contact simulation indicating what elements have matching mesh between bodies (blue and yellow on the right) and are not matched (green and brown on the left). NB the mesh on the block with the hole has matching elements at the hole location

The simulation results (Figure 5.11) show which contact conditions and parameters create effective bonded contacts. Block 1 shows that edge to edge contact conditions cannot be used in explicit models between solid and shell element types and should therefore be avoided. If an edge to edge bond is required then spot welds may be an alternative solution. Spot welds were used on Block 3 and successfully held. Spot weld may only be applied at vertices, so a matching pair of vertices must be present in order for a spot weld contact to be created. Block 2 used a face to face contact condition with the maximum contact offset set to 1 mm, which successfully held. The maximum contact offset must be greater than or equal to the distance between the faces (1 mm) for the contact pair to be detected and applied. If the maximum contact offset was left at the default value of $1x10^{-4}$ mm, as was the case for Block 4, then the contact pair would not be generated. The final parameter investigated was to see whether a matching mesh was required for the contact faces. Block 2 did not have matching mesh and the contact condition still held; this meant that this was not a critical feature however using a matching face mesh (Blocks 3-5) is still encouraged due to its superior contact detection.

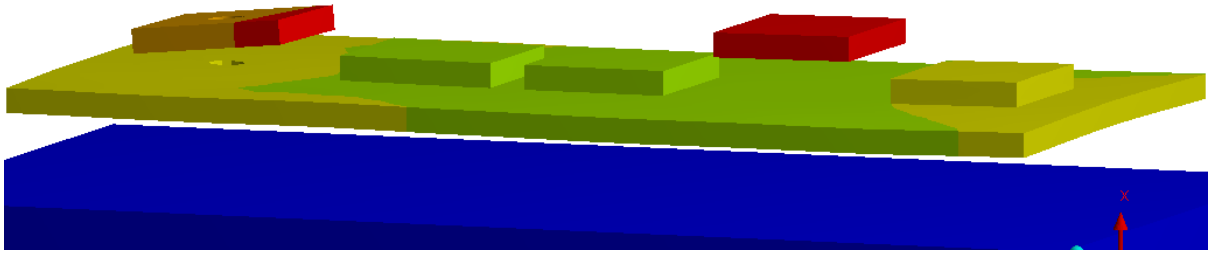

Figure 5.11 - Results from impact simulation demonstrating what connection types hold (Table 5.3)

5.3.3. Mesh control

The global mesh size for the detailed radio model was set to 1.3 mm. The PCB's, LCD, ceramic antenna and battery lid were swept with three elements through their thickness. The seal and FIBs shield used a mesh size of 1.1 mm, the batteries 2 mm, the impact plate 2.5 mm and the front panel and chassis were 1.2 mm. The pinch and defeaturing tolerances were 0.5 mm and 0.4 mm respectively. A summary of the final mesh properties are shown in Table 5.4. The resulting mesh is shown in Figure 5.12 and Figure 5.13.

Table 5.4 - Summary of mesh properties of detailed radio assembly

Mesh Quantity		Element Quality	
Nodes	191,688	Average	0.79
Elements	475,177	Standard Deviation	0.14

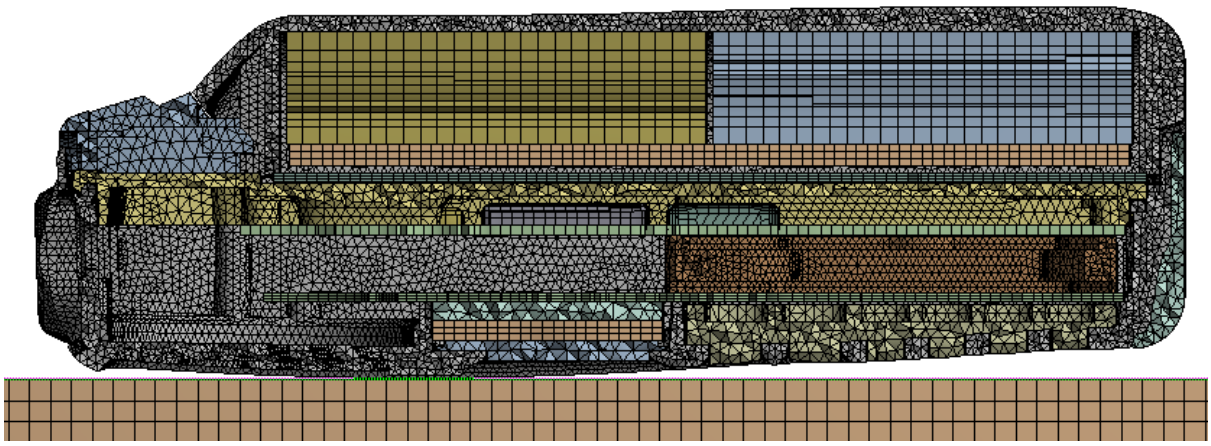

Figure 5.12 - Sectioned view of meshed detailed radio

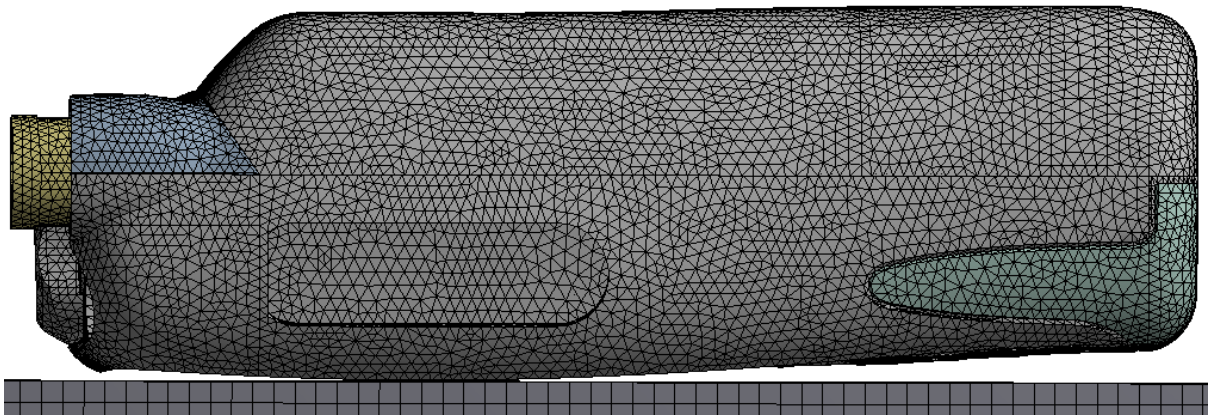

Figure 5.13 - Side view of meshed detailed radio

5.3.4. Initial conditions

An initial velocity of 5.94 ms^{-1} was applied to all radio parts; equivalent to a drop height of 1.8 m. A fixed support was applied to the underside of the impact plate.

5.3.5. Analysis settings

A solver time was set to 2 ms. The double precision solver was used (Section 4.4.5). Two hundred data points were recorded throughout the simulation and a sampling rate of 100 kHz was used. The tetrahedral integration method was set to the nodal strain integration option (Section 4.12.4). All other settings were left as default (damping values etc.) or were program controlled (time step etc.).

5.4. Finite Element Simulation of the Detailed Radio

5.4.1. Issues found during initial simulations

The first simulation performed did not run to completion. The simulation aborted after 1.03 ms due to the energy error being too high (Figure 5.14 and Figure 5.15). A relationship between stress and

the energy error was observed (Figure 5.16). The maximum stress present was investigated as a likely cause of the large energy error. The maximum stress was located on one of the EMI shields. The mesh deformation and stress at the final time step before the simulation was aborted is shown in Figure 5.17. The results show that collapsing/high deformation of the mesh was the likely cause of the energy error.

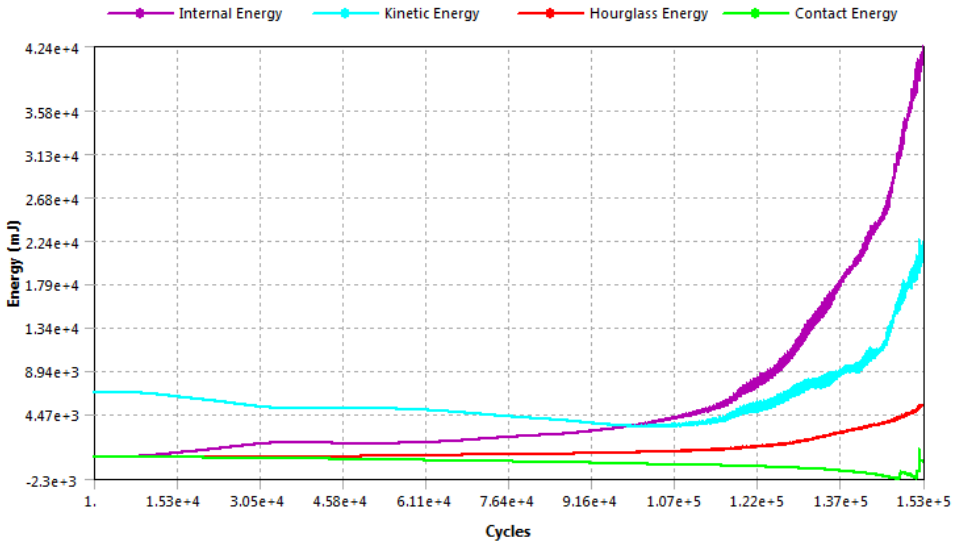

Figure 5.14 - Summary of energy during the initial simulation of the detailed radio assembly

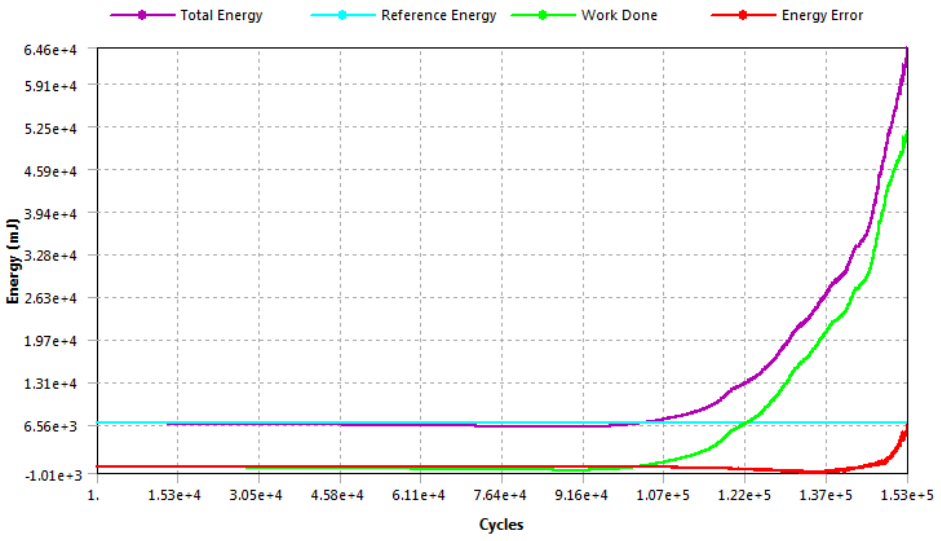

Figure 5.15 - Summary of energy conservation during the initial detailed radio simulation

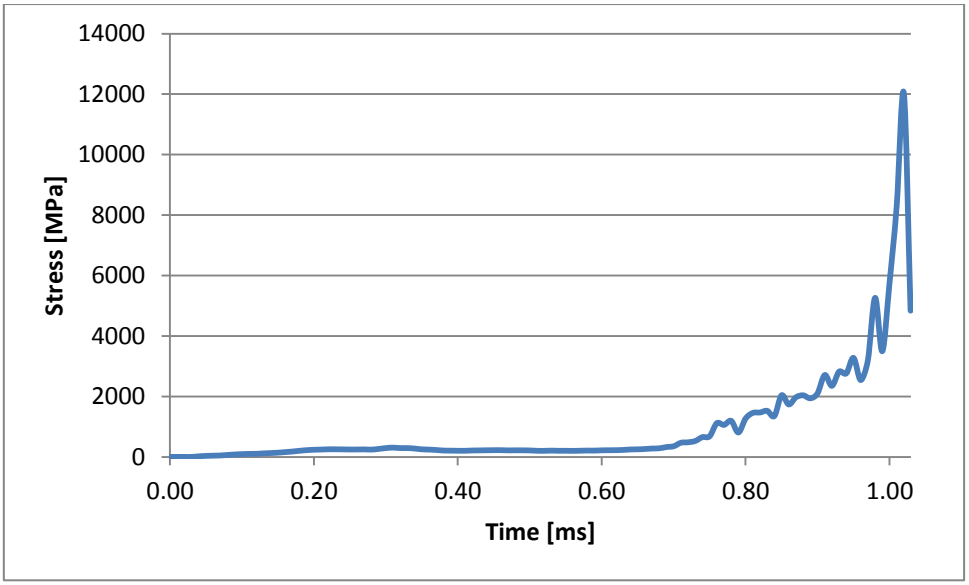

Figure 5.16 - Maximum stress present in the detailed radio assembly throughout the simulation time

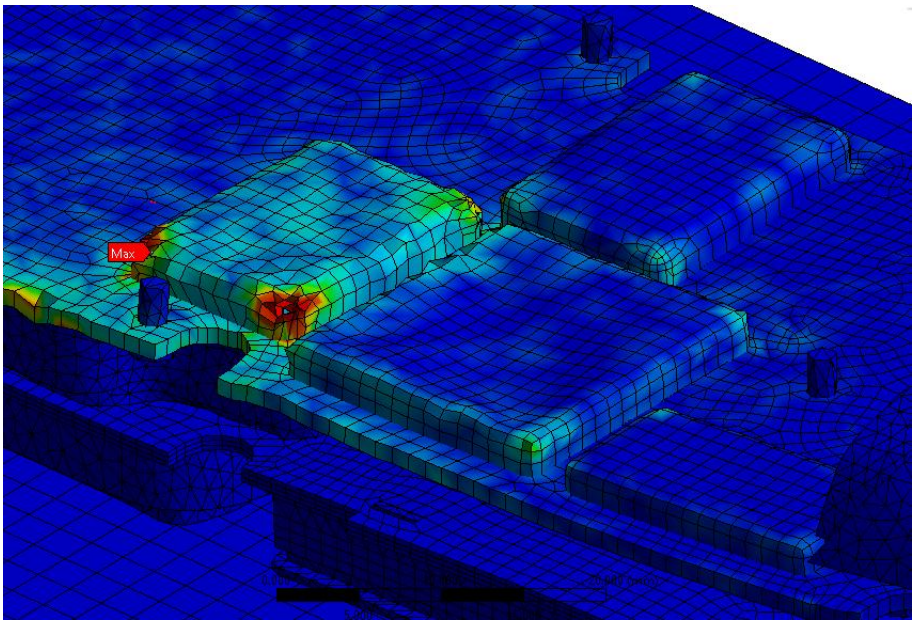

Figure 5.17 - Stress and deformation of shield at time when the problem was aborted

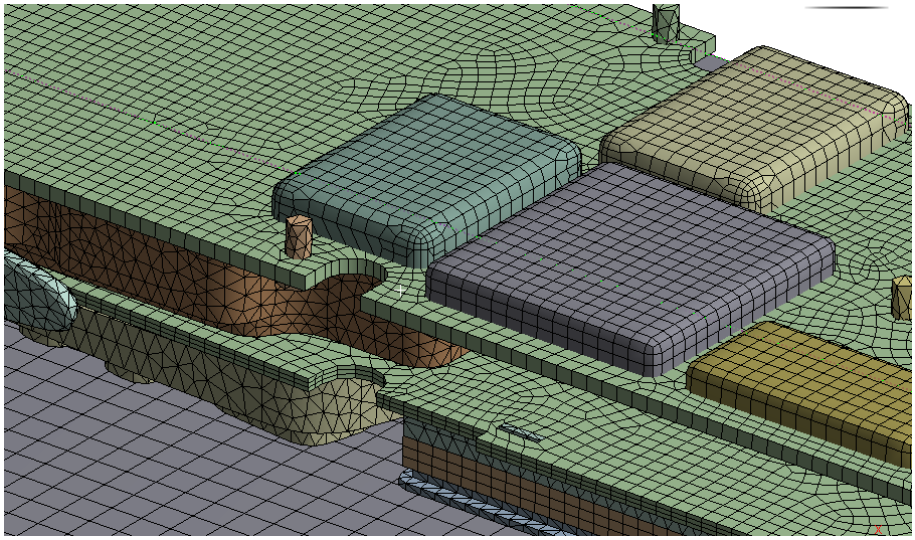

Figure 5.18 - Mesh used during the initial simulation

The zig-zagging nature of the mesh surrounding the high stress region (Figure 5.17) indicates that the error was potentially related to the hourglassing effect (presented in Section 4.11.3). The hourglassing effect is common in brick and quadrilateral shell elements and is often caused by high loads applied at concentrated points. Ways to minimising the occurrence of hourglassing include using a uniform, well refined mesh, using triangular elements and avoiding concentrated loads on single points. To ensure that the effect was hourglassing, a less refined geometry and mesh for the shields was used (Figure 5.19).

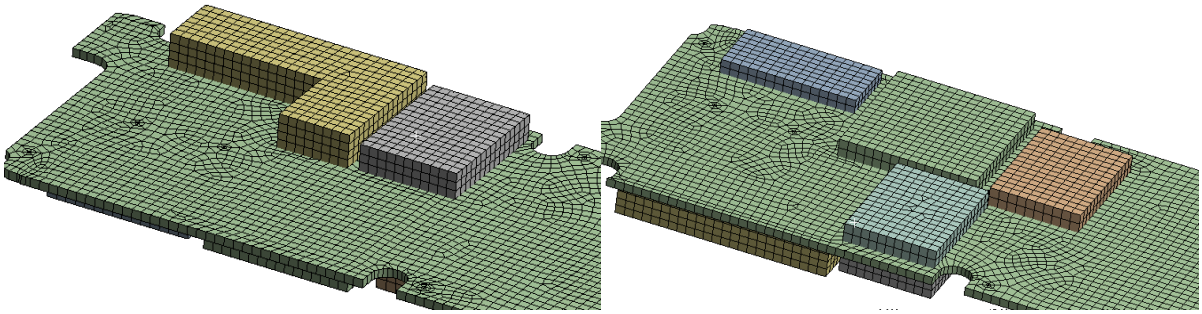

Figure 5.19 - Simplified shields (meshed)

The solver aborted a lot sooner than the initial model; a time of 0.05 ms was completed compared with 1.03 ms for the initial solution. Stress was again used to identify the problematic area, the issue again occurred at the location of one of the shields (Figure 5.20). The hourglass zig-zagging behaviour is clearly shown in Figure 5.21. Results indicate that the hourglassing effect was the likely cause for the impact model failure.

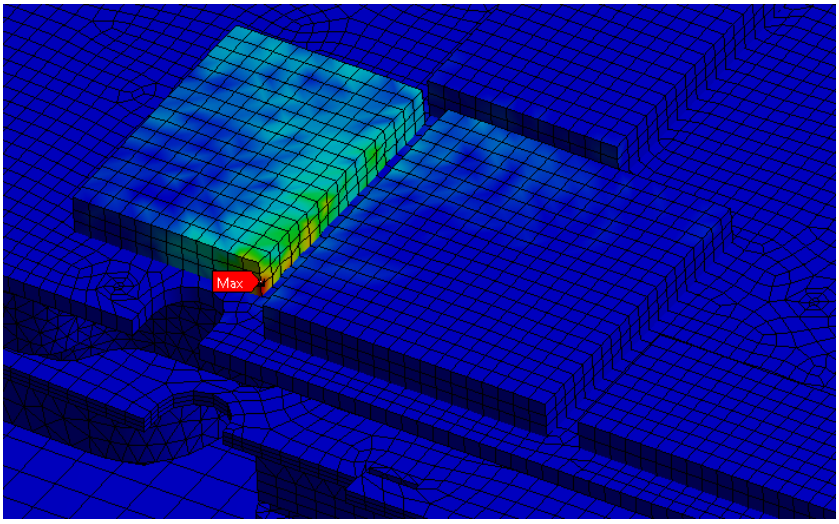

Figure 5.20 - Region of high stress, likely where the energy error was located

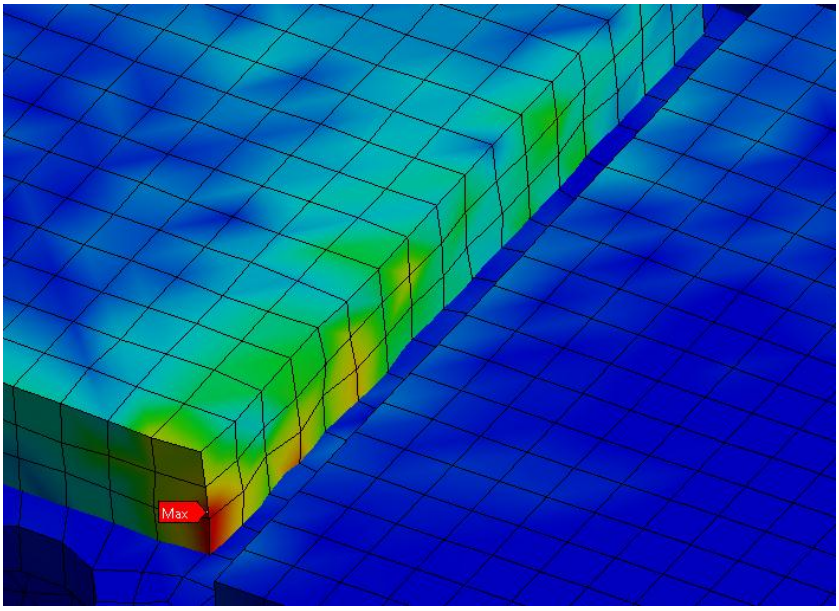

Figure 5.21 - Close up view of high stress area, hourglass behaviour being demonstrated

To reduce the risk of energy errors occurring, it was proposed to change the contact condition between the shields and RF board. It was thought that creating a contact that can break when the loading gets too high would minimise the risk of initiating hourglass deformation. Spot welds were considered as there is an option for their contact to break if a certain force or stress (defined by the user) is experienced; the mesh to mesh connection used does not provide this option. It was found that in the current assembly (shell elements for both shields and RF board) it was not possible to apply spot welds. As demonstrated in Figure 5.22, the issue was that the selected vertices moved once meshing was completed. Moving the vertex on the RF board to locate the outer vertex of the meshed shield did not solve the problem. Changing the RF board from shell to solid elements also

did not create an effective spot weld connection. Changing the shields from shell to solid elements was found to increase the solver time dramatically as the 0.2 mm thickness of the shield resulted in very small elements. This meant that the mesh to mesh contact condition was the only practical option to bond the EMI shields to the RF board.

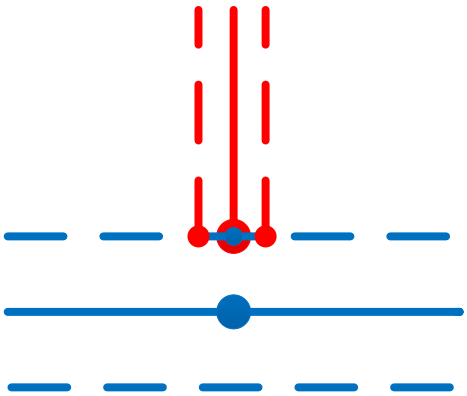

Figure 5.22 - 2D schematic of proposed spot welded connections, red indicates an EMI shield, blue indicates the RF board. Solid lines are the mid-surface locations and dashed lines are the outer surfaces of the parts once meshed. The larger circles indicate the location of the vertices selected for the connection, the smaller circles indicate the location of the vertices once meshed.

The second solution investigated was to alter the mesh of the shields and RF board. Further refinement of the mesh was not practical as the solver time became too large. It is known that quadrilateral elements are more susceptible to hourglassing than triangular elements. The shields were therefore remeshed using triangular shell elements (Figure 5.23), the solver time was found to be comparable to the model which used quadrilateral elements even though more elements were required to mesh the shields. The mesh shape of the shell elements has previously been shown to not affect the results (Section 4.12.3).

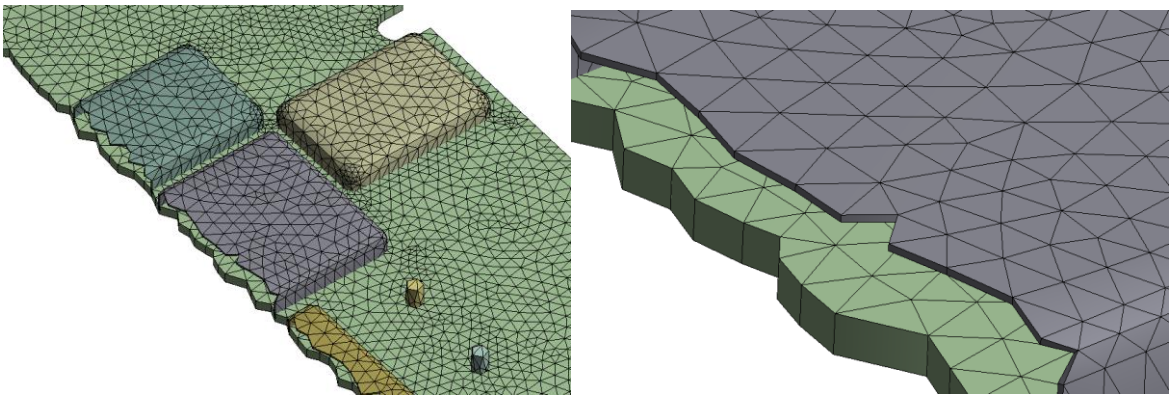

Figure 5.23 - Partially sectioned view showing shields meshed with triangular shell elements

Changing the element shape of the RF board and shields was found to not resolve the energy error problem, the mesh deformation occurred again at the corner of the EMI shields (Figure 5.24).

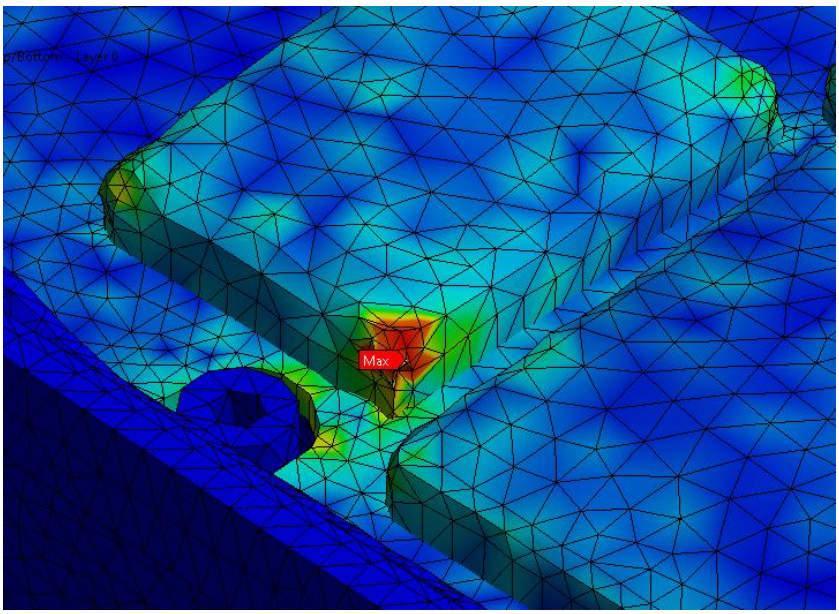

Figure 5.24 - Stress and deformation of triangular elements of RF board and EMI shields causing energy error

Further possible solutions were not investigated, it being decided to model the detailed radio without the EMI shields. A simulation was run using quadrilateral shell elements (Figure 5.25). The simulation was automatically aborted before the desired solver time, however at a much later time of 1.88 ms (2 ms was the chosen end time). The area causing issues was at the connection between the RF board and antenna connector (Figure 5.25). The antenna connection acts as a constraint for the RF board. This result showed that any localised and severe loading on elements increases the risk of generating hourglassing errors. Previously run simulations using shell elements which did not experience such severe localised loads have been shown to run to completion without hourglassing issues.

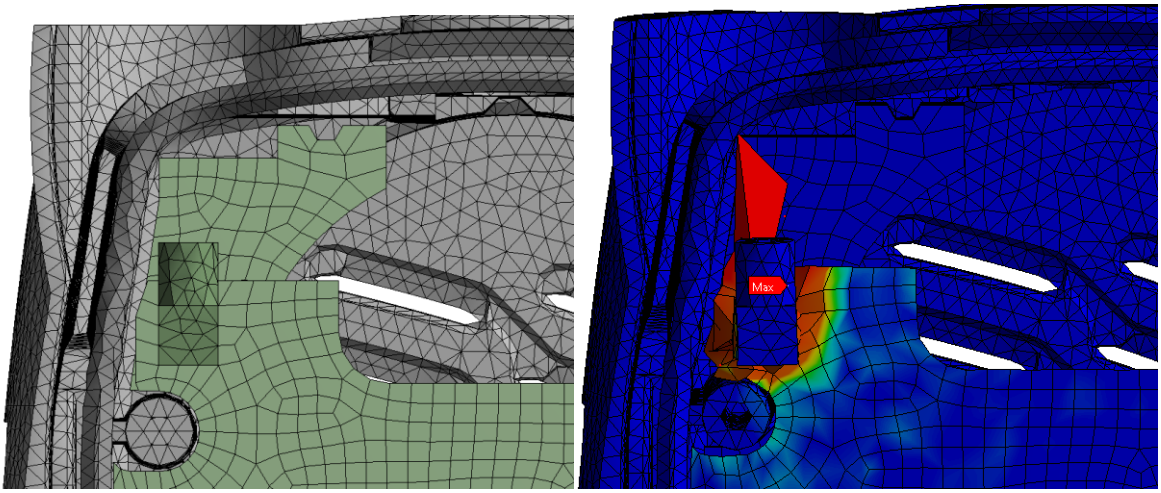

Figure 5.25 - Mesh before simulation - left, stress at end of simulation showing mesh deformation - right

To avoid any issues relating to hourglassing on the RF board two further simulations were completed. One simulation used triangular shell elements, the other simulation used three layers of solid elements (the same as used in the simplified radio and on the MMI board of the detailed radio simulation).

Both simulations solved to completion, the results are discussed below.

5.4.2. Solver results from successful detailed radio simulation

The detailed radio simulation using triangle shell elements for the RF board took 90 hours to solve. The time step of the model was 6.74 nano seconds. The final momentum of the handheld radio in the z-direction was 1.2 N.s (Figure 5.26); this gave an exit velocity of 3.2 ms^{-1} and a resulting rebound height of 0.52 m.

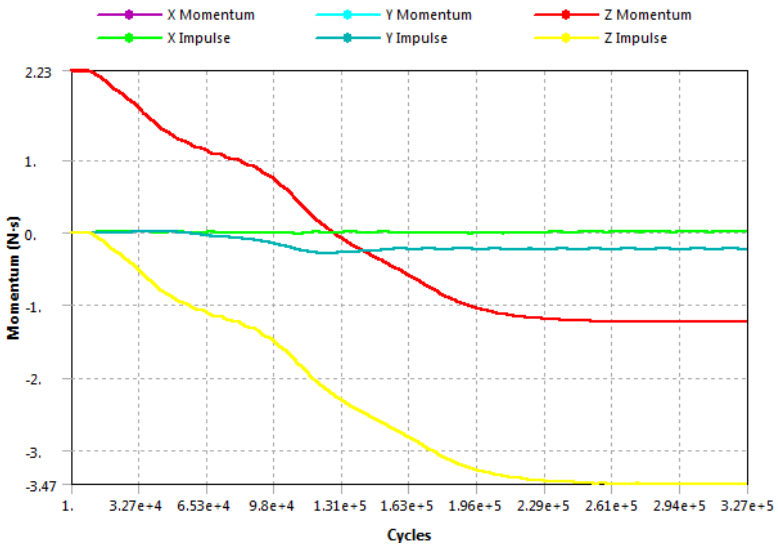

Figure 5.26 - Momentum summary from detailed radio drop-impact simulation

The detailed radio impact simulation using layered solid elements for the PCB's took 124 hours to solve. The time step of the model was 4.56 nano seconds. The change in mesh of the RF board from shell to solid elements was shown to negatively affect the solver time. The final momentum of the handheld radio in the z-direction was 1.2 N.s, the same as the simulation which used shell elements for the RF board.

The hourglass energy in the simulation using only solid elements was significantly higher than that found in the model which used shell elements for the RF board, as shown in Figure 5.27 and Figure 5.28. The higher energy error was generated at the connection between the RF board and chassis (Figure 5.29). This result demonstrates the issues involving severe loading at individual elements. The model using shell elements incorporated screws which distributed the load over more elements making it less susceptible to such errors.

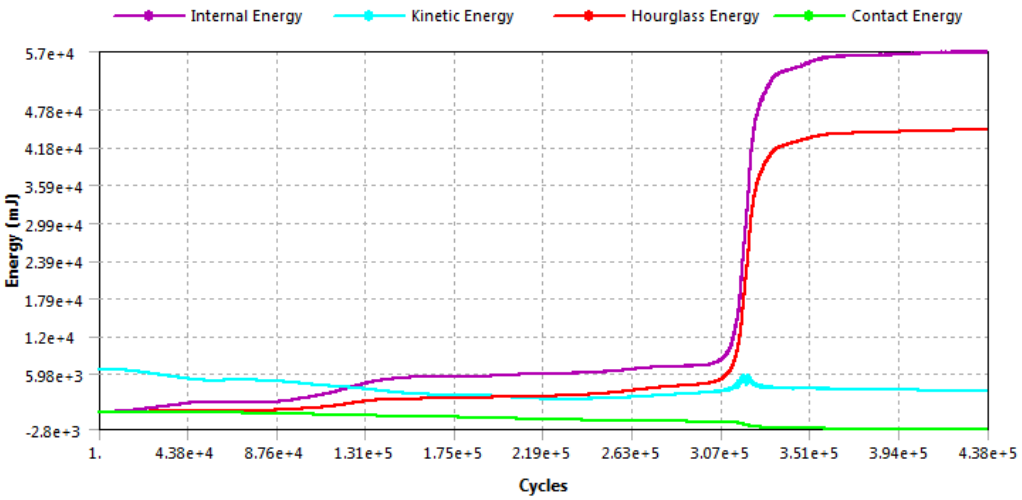

Figure 5.27 - Energy summary for detailed impact simulation using all solid elements

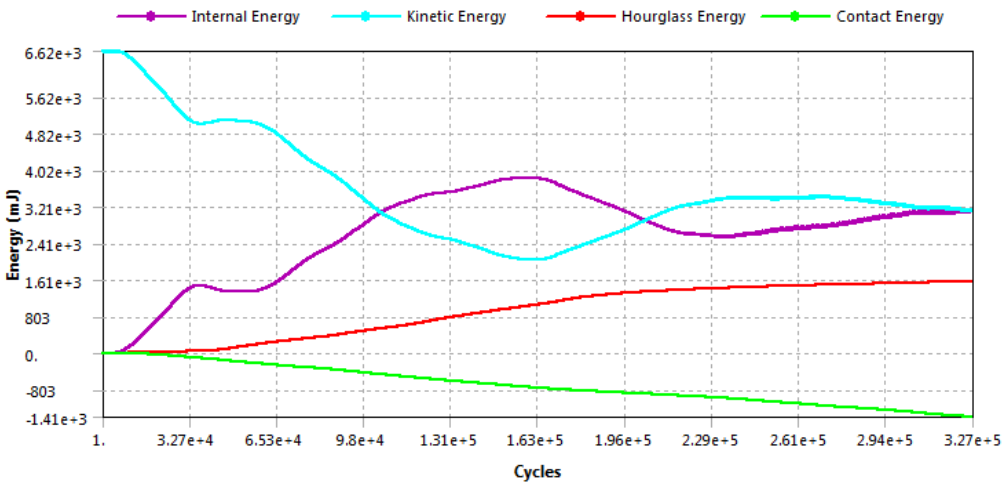

Figure 5.28 - Energy summary for detailed impact simulation using solid elements and shell elements for RF board

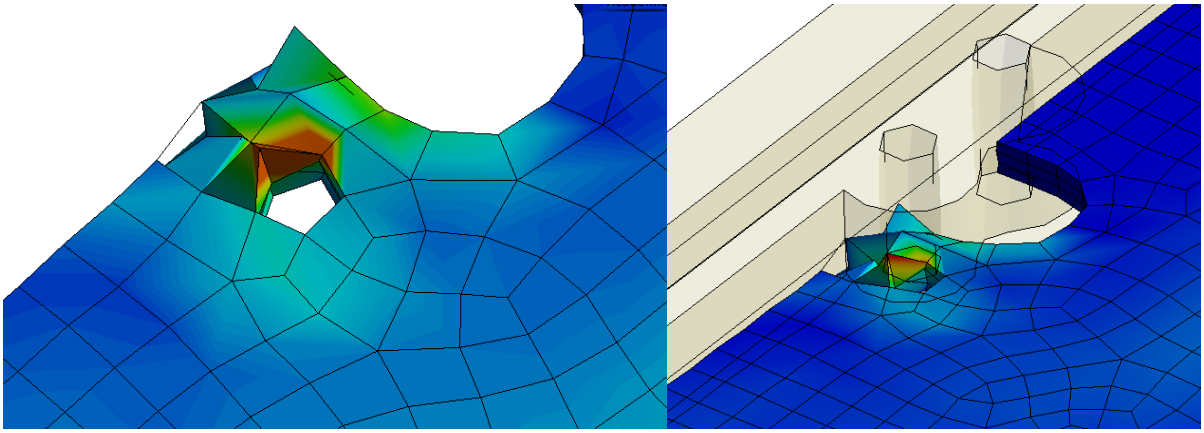

Figure 5.29 - Mesh deformation on the RF board at a face to face screw connection with the chassis

Although there are issues associated with the implementation of shell elements, ultimately their incorporation gave superior results and a more efficient finite element model than simulations which use layered solid elements. The use of shell elements is therefore preferred wherever applicable.

5.5. Drop Testing of the Detailed Radio

5.5.1. Radio model used for experimental testing

The detailed radio used for testing was assembled such that it replicated the geometry used in the finite element model as closely as possible. Parts removed from the finite element assembly were also excluded from the physical radio assembly. The test assembly is shown in Figure 5.30.

During the simplification process of the finite element model geometry small features were removed from the model, however, the parts used in the physical model maintained such features. The variance in the small details between the physical and virtual models was negligible. For example, the volume of the physical front panel body was 54.6 cm^3 and 53.6 cm^3 in the finite element model, a difference of around 3%. When the geometry was being modified for modelling purposes it was ensured that any changes did not alter part contacts and interactions.

Figure 5.30 - Assembly for detailed handheld radio drop-impact testing (front and back)

5.5.2. Drop testing procedure

Drop testing of the detailed handheld radio used the same drop conditions that are implemented at Tait. The radio was dropped from a height equivalent to a 1.8 m free-fall impact velocity (5.94 ms^{-1}), a front face, horizontal impact was performed.

Figure 5.31 - Impact orientation tested during experimentation

Measurement equipment included two strain gauges, tri-axial accelerometer (PCB Piezotronics 5200B), two load cells (PT AST-1t) and a high speed camera. The placement of the strain gauges on the PCB's were at the same location as the simplified radio tests (Figure 5.32). The tri-axial accelerometer was mounted to the outside of the radio, screwed into the front panel using the screw boss present (Figure 5.33). The front panel was cut slightly to allow the strain gauge cabling to exit the radio (Figure 5.34).

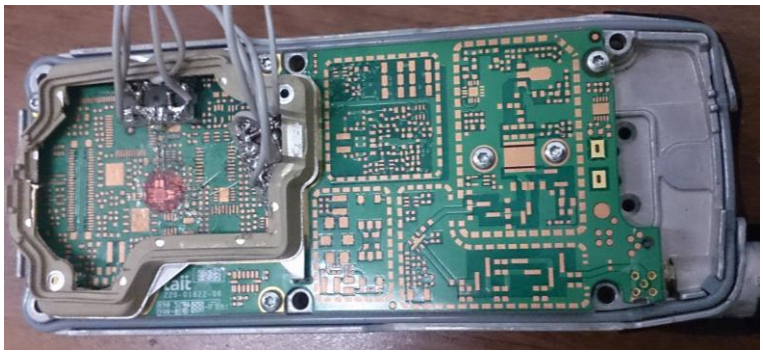

Figure 5.32 - Strain gauge placement on the RF board

Figure 5.33 - Mounting point on the front panel for tri-axial accelerometer

Figure 5.34 - Cable routing for strain gauges out of the front panel of the detaield radio

5.5.3. Drop testing results

5.5.3.1. Impact force and duration

The impact force and duration of the radio assembly dropped from a height of 1.8 m onto its front face are summarised in Table 5.5. The experimental results show a range of impact forces and duration values were recorded.

Table 5.5 - Summary of impact force and duration from experimental testing, compared against results from the finite element model

Drop Number	*Impact Force [N]*	*Impact Duration [ms]*
1	1739	2.33
2	1750	2.74
3	2229	2.58
4	1430	2.64
5	1627	2.12
Average	**1755**	**2.48**
Finite Element Result	**3993**	**1.83**

The sampling rate of 50 kHz was found to provide enough data points near or at peak values to ensure that the measured peak force was appropriately captured. The two load cells used were rated to a force of ± 10000 N (1 tonne), the measured force was much lower than this (≈ 1800 N) so the force limits of the load cell were not reached. The total impact force was calculated by summing the force measured by the two load cells (Figure 5.35). Figure 5.35 shows that the force peaks from the load cells were synchronised, resulting in minimal force cancellation occurring during the summing process.

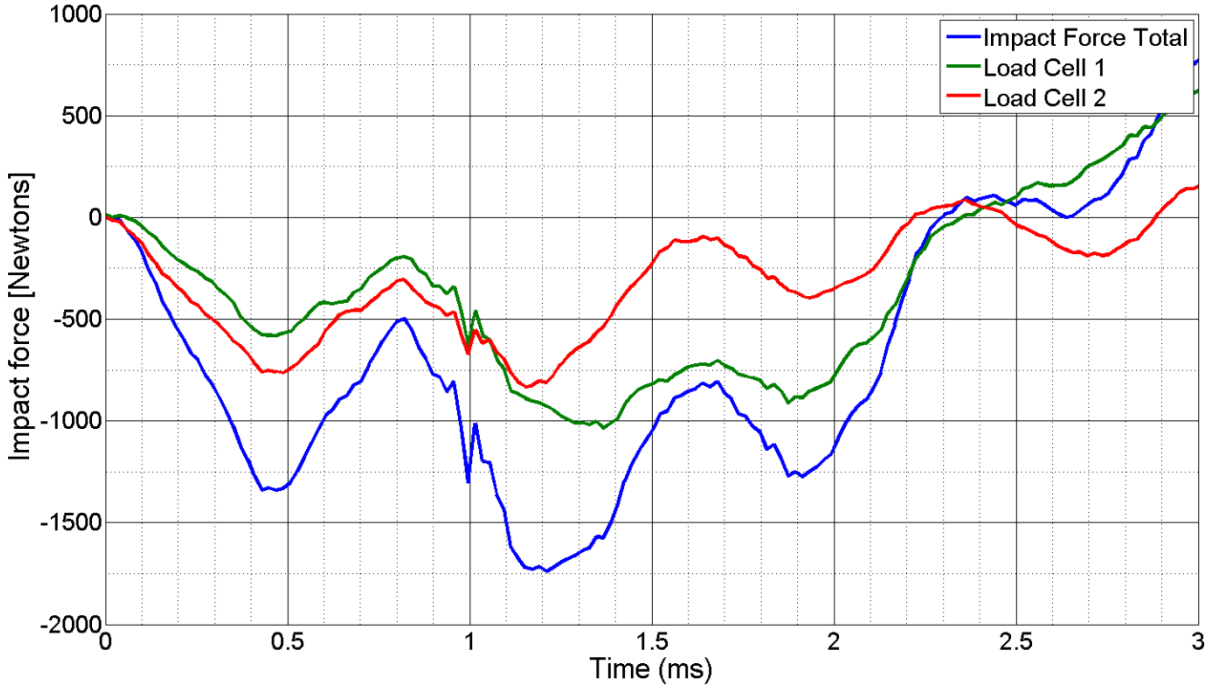

Figure 5.35 - Summation of force measurements from the two load cells mounted under the impact plate, giving the total impact force (Drop 1)

The five experimental force-time plots are shown in Figure 5.36. The results show the overall force-time forms varied but general trends can be observed. The load cell records positive force values after the impact event because the impact plate travels upwards after the impact, causing tensile loading of the load cells. Reasons for the variation in the force measurements include slight change in impact orientation and different impact locations on the impact plate. The change in impact orientation was minimised but not completely eliminated with the use of the impact test rig. The load cell was designed for predominantly weighing applications so the dynamic behaviour of the load cell, particularly for impact events, may have been inadequate.

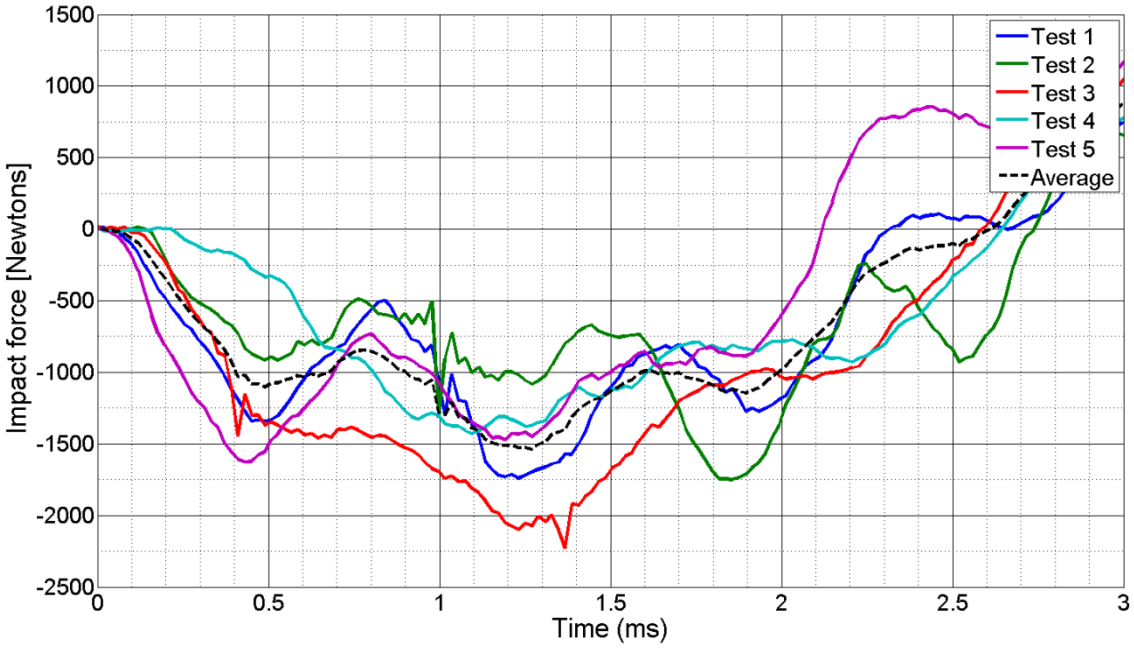

Figure 5.36 - Experimental impact force for five experimental impacts

The averaged experimental impact force is compared against the finite element result in Figure 5.37. The experimental results show a longer impact duration and smaller peak force than the finite element model. For identical impact events (same impact velocity/momentum) an impact event with a longer impact duration will, in most cases, result in higher peak forces. It is expected that if the impact duration of the experimental and finite elements were equivalent then the impact force would also have better agreement. Reasons for the variation in impact duration are discussed below.

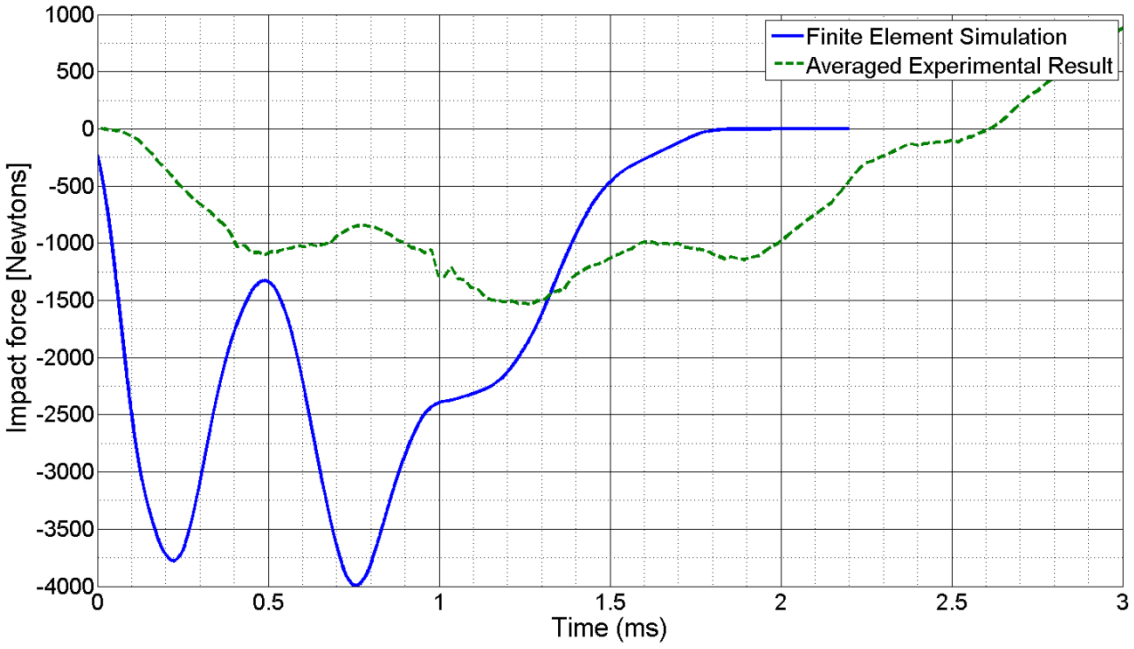

Figure 5.37 - Finite element impact force of the detailed radio compared to the average experimental impact force

The impact plate behaviour used in the finite element model was tuned using a steel ball dropped from a height of 1 m (Section 4.18). The tuned finite element result gave the same peak force as the experimental data (7210 N) but the duration of the event was much shorter than that observed during the experimental tests (0.26 vs. 0.4 ms respectively). This implies that the impact surface used in the finite element model may have been more rigid than the impact plate used during experimentation. The difference in impact plate behaviour may therefore be contributing to the observed disparity of both the impact force and duration results.

Another possible contribution to the difference in impact force and duration was the material properties used for the detailed radio assembly. The material properties were not explicitly determined, therefore the values used in the solver may have been incorrect. The material properties for the front panel are likely to have the greatest influence on the impact force and duration of the parts used within the detailed radio assembly. The results imply that the front panel material used for the finite element model was too rigid; using a lower Young's modulus would generate better correlation.

To improve the impact force and duration agreement between the finite element model and experimental results, several unknowns should be addressed:

- Front panel material properties
- Response time of the load cell to dynamic events needs further consideration, possibly upgrade to a higher quality load cells
- Inclusion of the entire impact structure (impact plate, load cells and mounting plate) into the finite element model so impact dynamics are identical. This would require more understanding of the impact plate load cell dynamic behaviour as well as the respective material properties.
- Further mesh refinement

5.5.3.2. Acceleration

The acceleration experienced by the detailed radio assembly was captured experimentally. There was insufficient space within the assembly for the accelerometer to be placed internally therefore was mounted to the outside of the radio (Figure 5.33). The results from the experimental impact events are summarised in Table 5.6.

Table 5.6 - Acceleration measurements from 1.8m front face impact of the detailed radio assembly

Drop Number	*Peak x-acceleration*	*Peak y-acceleration*	*Peak z-acceleration*
1	-500,488	-1823,2003	4867*
2	-1195,913	-1276,2166	4867*
3	-559,629	-1550,1398	4587
4	-537,466	-1116, 900	4867*
5	-587,883	-1206,1447	4867*

*Measurement limit of accelerometer

The experimental acceleration results show large fluctuations in both the x and y directional components. In the z-direction, the measuring limit of the accelerometer was consistently met. The finite element results (Figure 5.38) at the accelerometer location show a high level of noise and also instability towards the end of simulation period. For these reasons, the acceleration results were not used for validation or comparison.

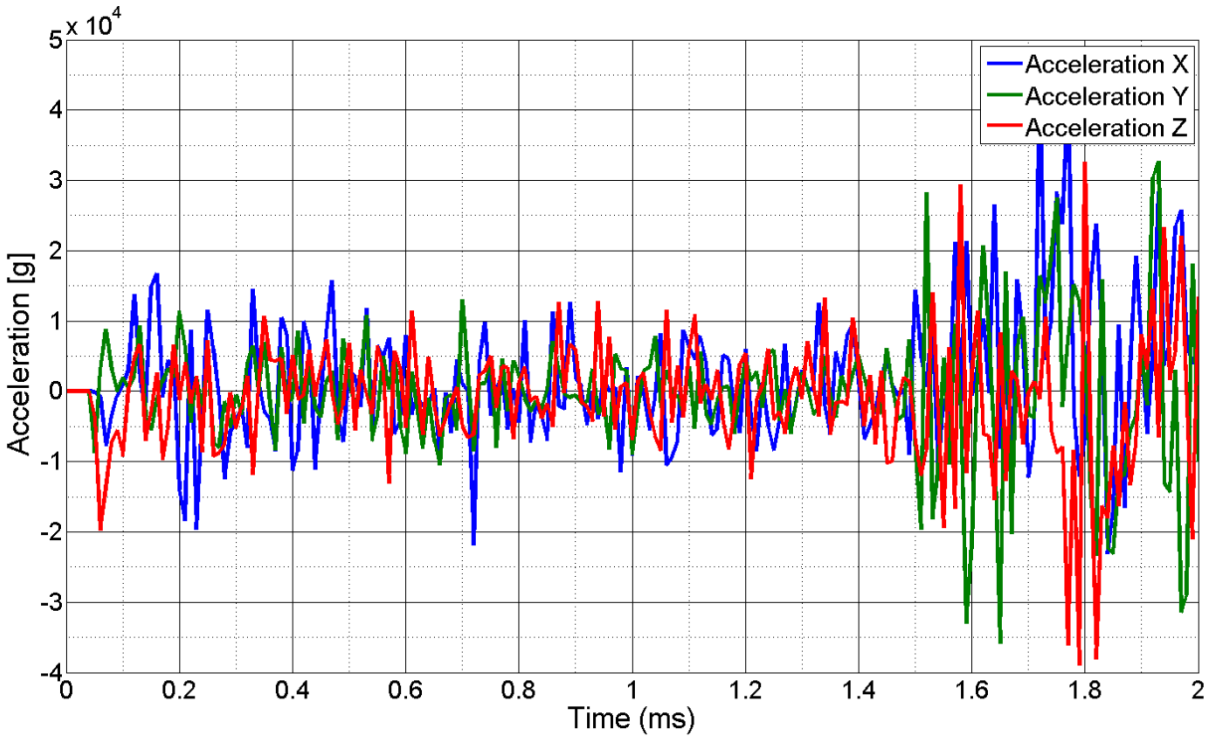

Figure 5.38 - Finite element acceleration results at the location of the screw boss on the front (where the accelerometer was placed during experimentation)

5.5.3.3. Strain

Two locations were used for strain measurements, on the RF board and MMI board. Due to the limited data channels and room within the assembly for cabling, the strains from each board were

measured in separate impact tests. The measured strain in the x and y direction for the RF board are summarised in Table 5.7.

The peak strain values by the RF board during experimentation were comparable to that recorded by the finite element model. The x and y strain-time behaviour for the RF board during impact are shown in Figure 5.39 and Figure 5.40 respectively. The strain from the finite element simulation varies with time more rapidly than the experimental results. This is likely caused by the difference impact durations.

Table 5.7 - Summary of RF strain impact results

Drop Number	*Peak Strain - x [με]*	*Peak Strain - y [με]*
1	1247	721
2	1311	637
3	787	752
4	1216	782
5	1522	869
Average	**1216**	**752**
Finite Element Result	**913**	**752**

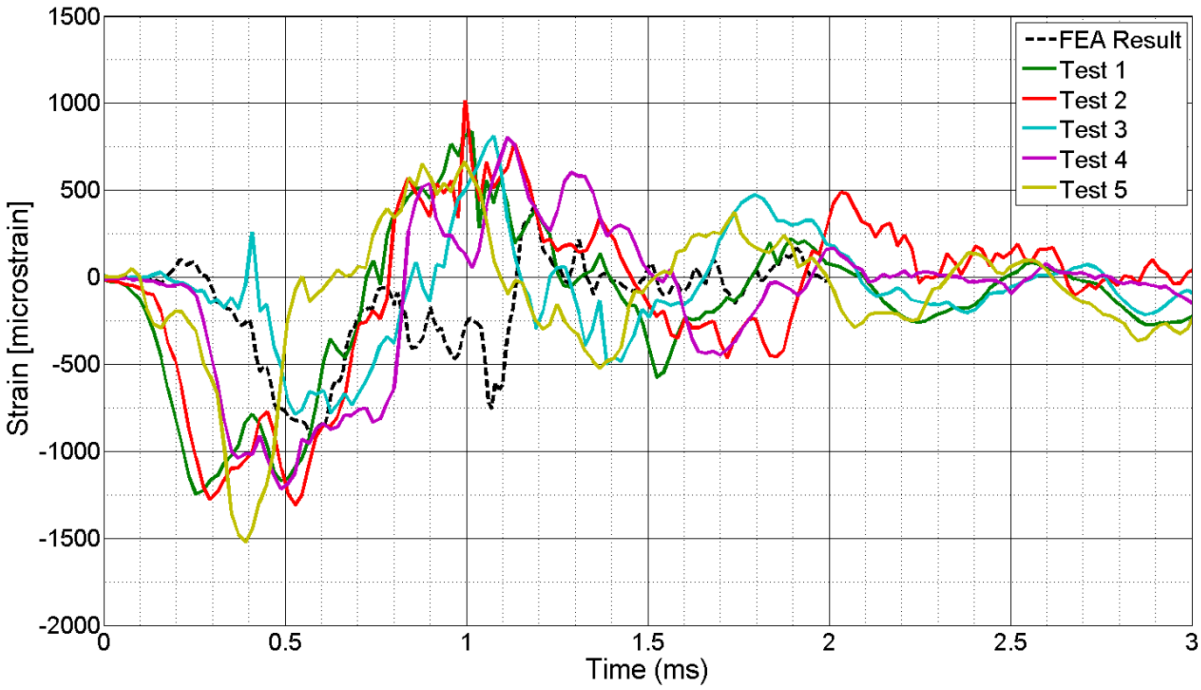

Figure 5.39 - Strain of the RF board in the x direction, experimental and finite element results

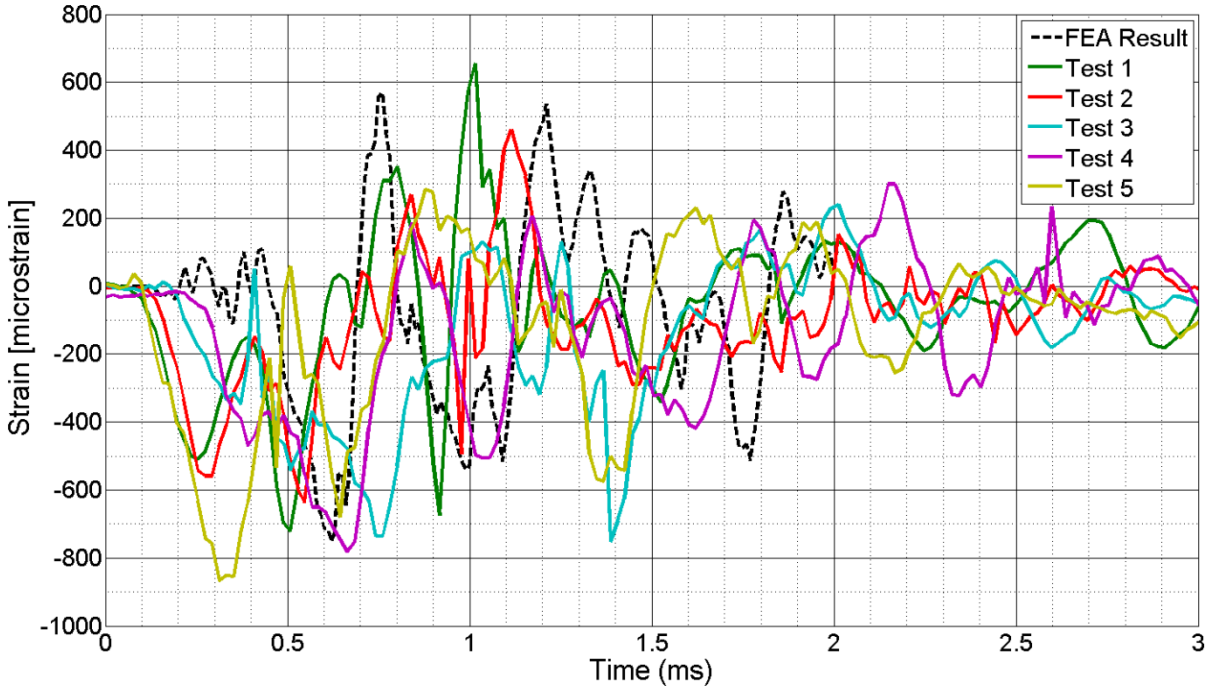

Figure 5.40 - Strain of the RF board in the y direction, experimental and finite element results

5.6. Comparison of Simulation and Experimental Results

The finite element model and experimental at the measurement locations did not result in very close agreement. This was expected due to the number of unknowns that were used in the model, particularly the material properties. The results however were reasonably close and show that with further studies to understand the unknowns present there is potential to generate a completely agreeable finite element solution. Ways for improving the accuracy of the model and also the inherent differences between the experimental and finite element models are discussed at the end of this chapter (Section 5.8).

5.7. Analysis of the Detailed Radio Behaviour

Although the simulation results did not provide perfect correlation to experimental data, the simulation results can still be analysed to obtain useful information. The ability to generate stress, strain and acceleration at any point of interest has already been presented; some of the other uses are outlined below.

5.7.1. Global assembly behaviour

One of the benefits of the finite element model was that the impact could be slowed down and the geometry sectioned to provide insight into the behaviour of the radio assembly. The entire event simulated is shown in Table 5.8.

The simulation shows the radio ‘rolling’ along the curved face of the front panel, the front panel and other parts within the assembly deforming, before finally rebounding. The last area to leave the impact surface was at the bottom of the front panel where the softer over-moulding was located. The results show that the batteries deflect the surrounding parts significantly; this was expected due to the large amount of mass that they contribute to the assembly.

The stress propagation during the impact is shown in Table 5.9. The high regions of stress were observed on the front panel at the initial point of impact and also at the end of the front panel where the radio rebounds last. The chassis was found to experience high levels of stress throughout the impact event, the highest level occurred when the force from the batteries was at its highest. The high stress loading of the chassis was expected as it is designed to provide the main structural integrity of the radio as well as having mounting points for all major parts (battery, front panel and RF board).

The visualisation of the entire radio assembly during the impact event allow the user to identify regions of high deformation, stress, observe the interaction of parts and to understand the full sequence of the impact event. Potentially troublesome areas/behaviours identified during observation at a global level can then be studied in further detail; examples of these are discussed below.

Table 5.8 - Behaviour of radio throughout the impact event (deformation in reference to initial location)

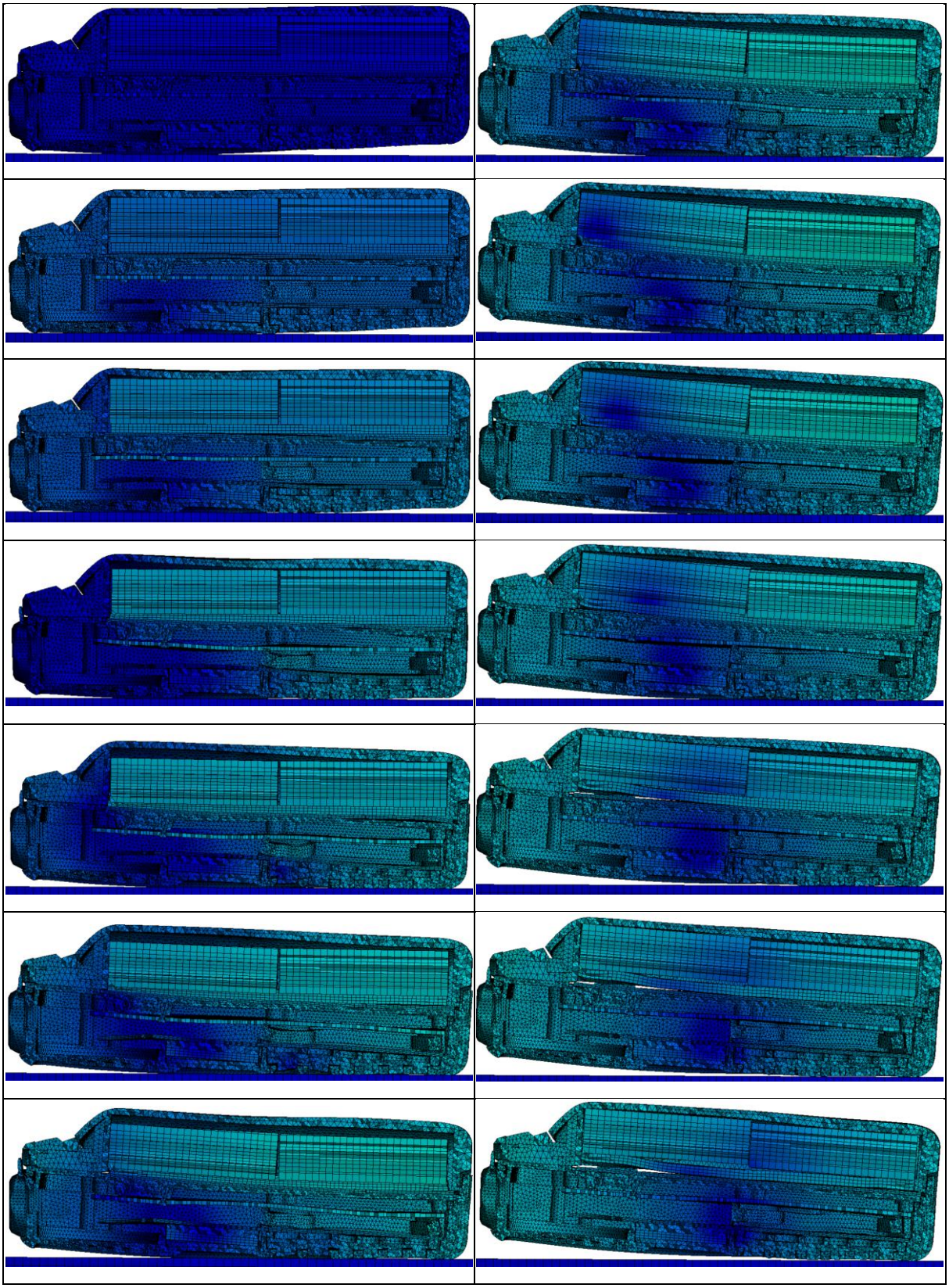

Table 5.9 - Stress propagation throughout the detailed radio assembly during drop-impact event

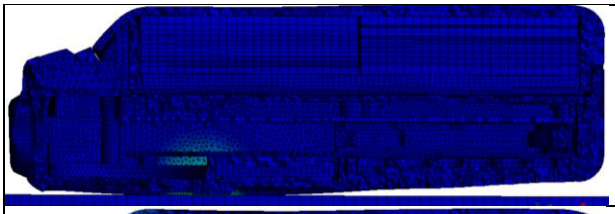	Stress wave propagating out from initial point of impact
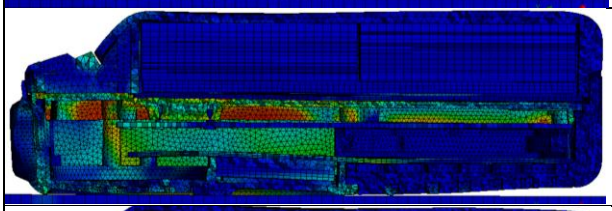	High stress levels occurring along the side of the front panel and also on the chassis
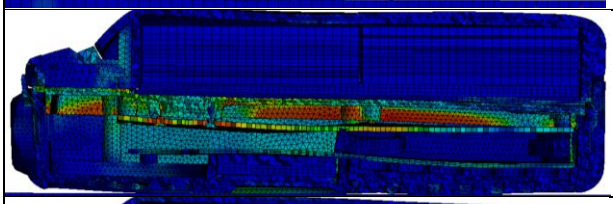	Furthest points away from the initial impact point still unaffected
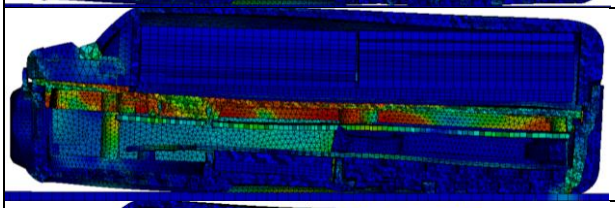	
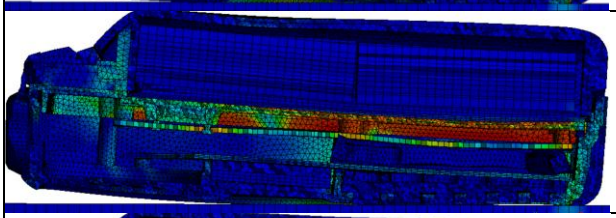	
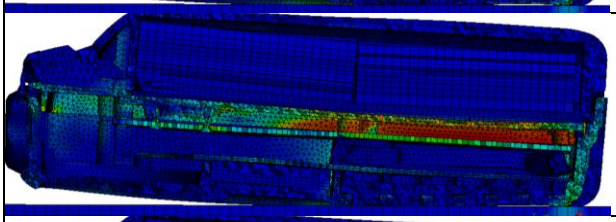	
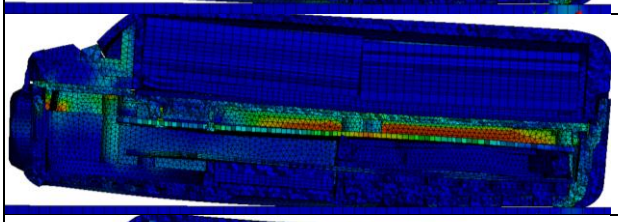	
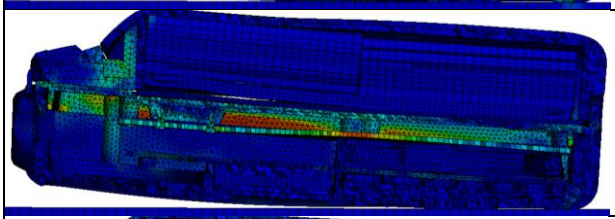	
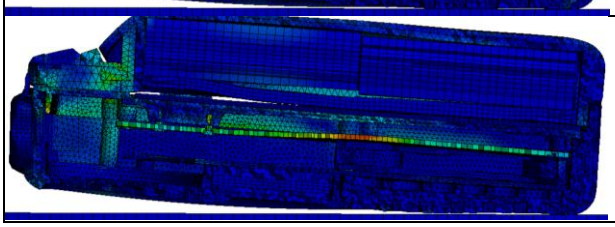	End of simulation, radio no longer in contact with the impact surface

5.7.2. Battery disconnect

One common issue that occurs during the impact of handheld radios is the disconnection of the battery [25]. If the connection between the radio and battery is interrupted then this may result in the radio resetting, and in some instances the disconnection may be so severe that the battery comes completely free from the radio assembly.

During the observation of the global radio behaviour it was noticed that the front panel moves away from the battery pack (Figure 5.41), this has the potential for the battery to detach from its contacts, cutting power to the radio. The impact was analysed near the deformation of the front panel (Table 5.10) so that the mechanism(s) causing this behaviour could be understood. The results show the initial shock wave from the front panel contact with the impact surface generated a transverse wave, as the wave reached the bottom of the front panel it causes the side of the front panel to move outwards.

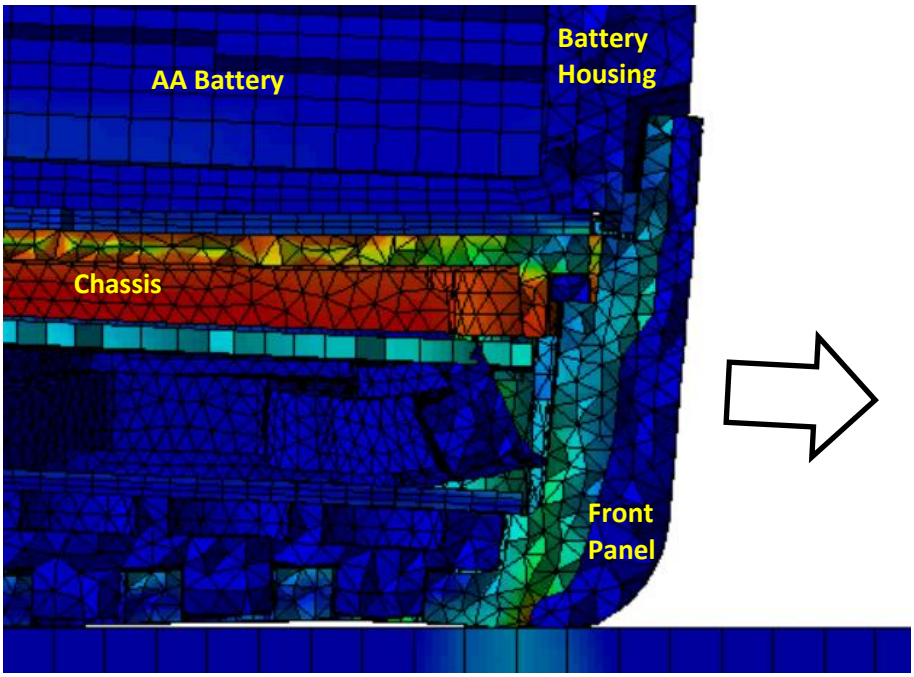

Figure 5.41 - Deformation of front panel causing separation between the front panel and battery pack

Table 5.10 - Stress wave propagation path showing potential battery disconnect issues

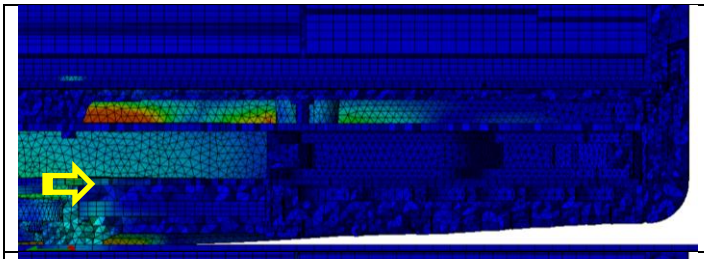	Just after impact, showing stress wave travelling from point of impact outwards
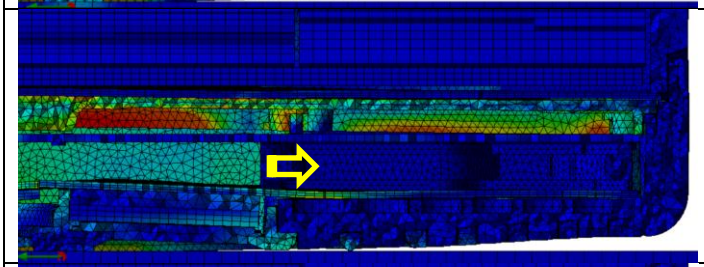	Stress wave travelling down the front panel
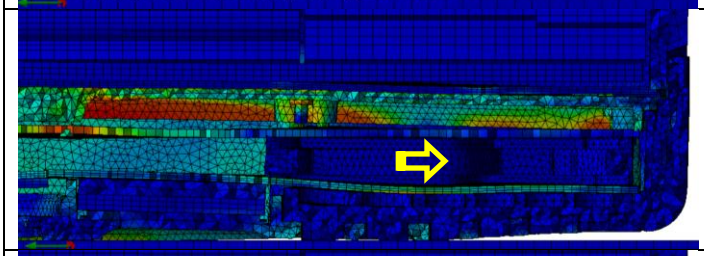	Stress wave halfway between initial contact point and end of the radio
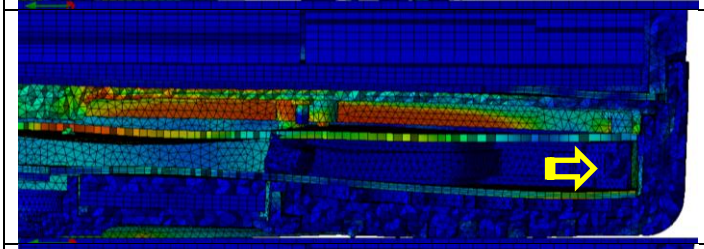	Stress wave towards the end of the radio
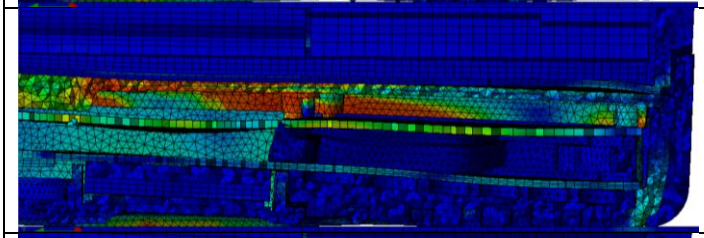	Stress intensifying around the corner of the front panel and the end begins to move outwards
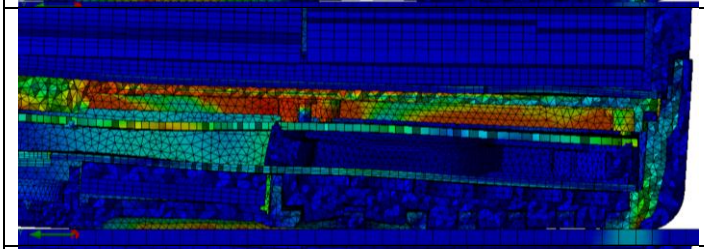	Further increase in stress at the corner of the front panel and along the end of the front panel also
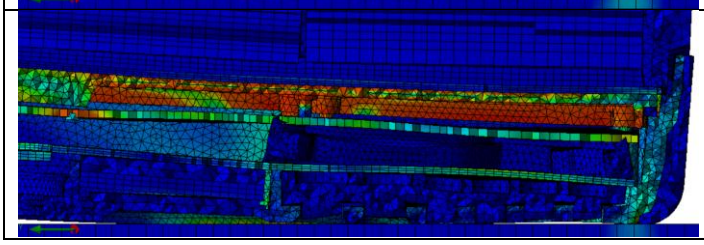	Maximum gap that is formed between the front panel and battery pack

5.7.3. Board to board contact

Contact between circuit boards is an important consideration during the design of the board and associated housing. Boards contacting each other during an impact event can lead to electrical shorting or general damage to board mounted components. An understanding of where large board displacements are present and the mechanisms behind such behaviours would lead to the development of a more robust product.

To clearly visualise the board deflection behaviour and to gauge the distance between the boards all other parts were hidden to provide an unobstructed view (Table 5.11). The results show that contact between the MMI and RF boards did not occur. The closest the boards came to each other was at a time of 0.55 ms, shown in Figure 5.42. The introduction of EMI shields and board mounted components into the model will close this gap even further, risking board to board contact and therefore the current board deflection and constraints should be understood.

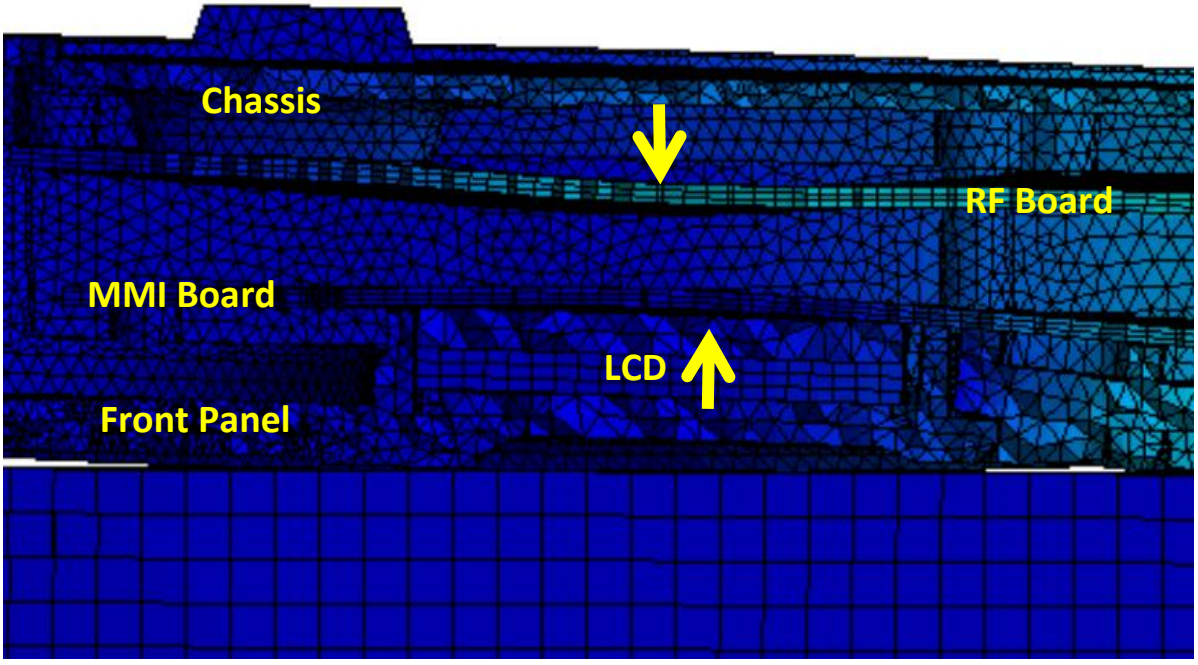

Figure 5.42 - Sectioned view showing smallest gap between the two PCB's during drop-impact event at a time of 0.55 ms

Table 5.11 - Behaviour of the PCB's during impact. The left column shows deformation of the boards on their own and with the nearby parts visible. The right column shows strain acting on MMI board (bottom board)

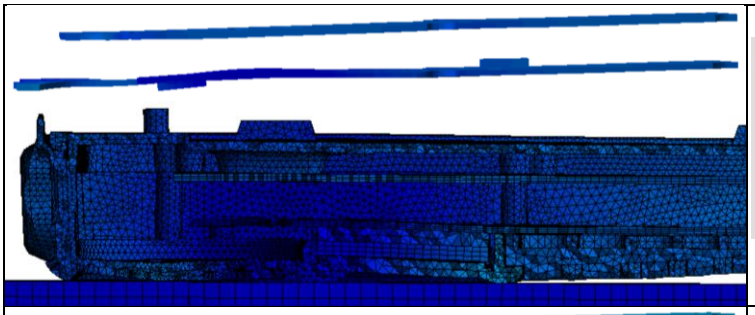	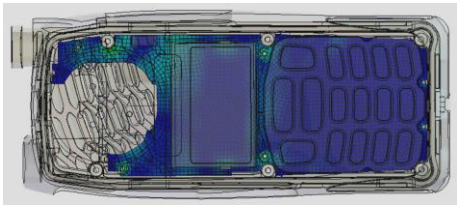 0.206 ms
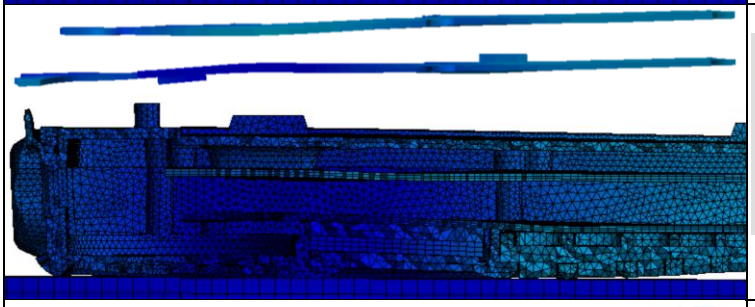	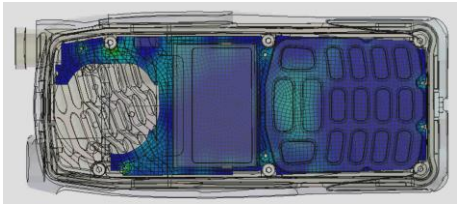 0.275 ms
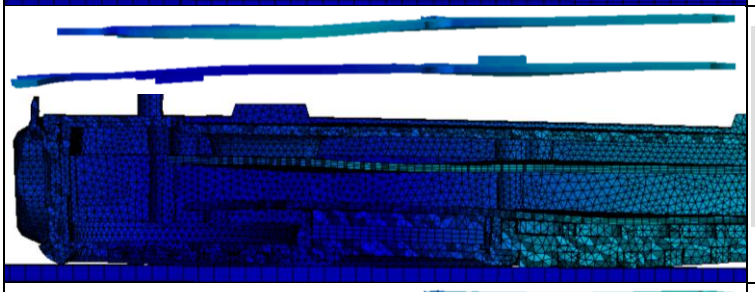	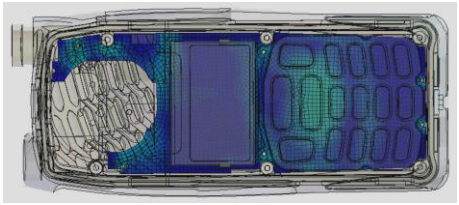 0.345 ms
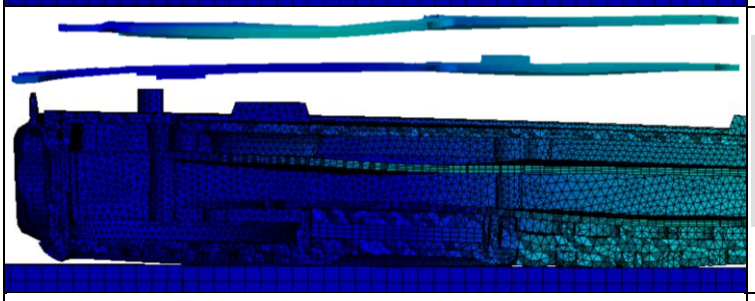	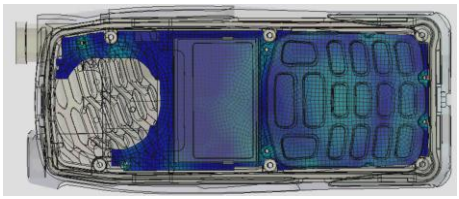 0.414 ms
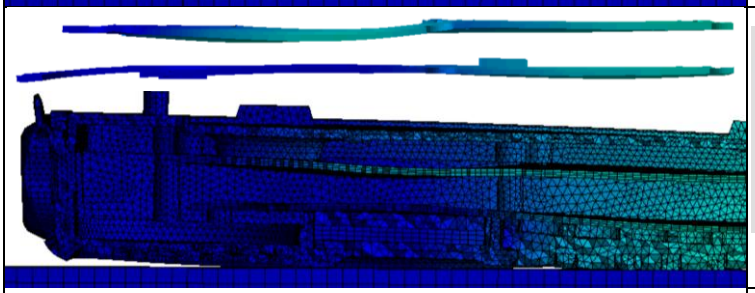	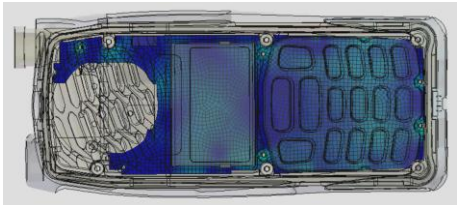 0.483 ms
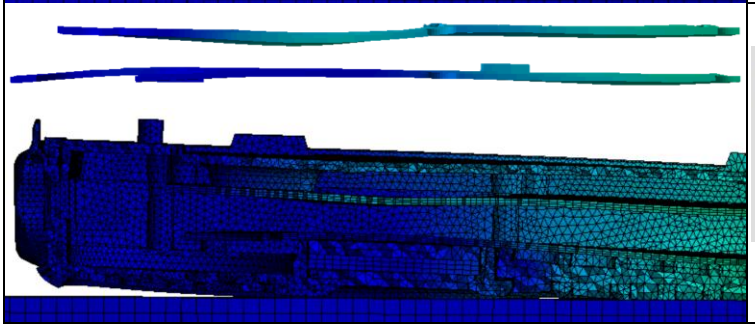	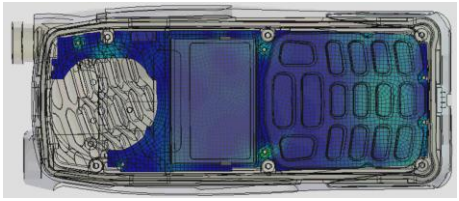 0.55 ms

The captured images (Table 5.11) show the events that lead to the small board gap at a time of 0.55 ms. A region of increased rigidity on the front panel assembly where the LCD screen was located resulted in the MMI board rebounding quickly. The other contributing factor for the small gap between boards was the deformation of the RF board. The RF board was still travelling downwards as the MMI board was travelling upwards. The RF board bowed between two constraint points, the centre point between these constraints sat directly over the centre of the LCD assembly.

Critical review of the clearance between the two circuit boards made it significantly easier to propose solutions that would effectively target any potential board contact problems. For this case the best way to minimise the risk of board contact is to constrain the RF board at points in line with the LCD assembly or to increase the rigidity of the RF board. The proposed solutions can easily be investigated by modifying the CAD geometry or changing the material properties, the simulation then rerun with the effects of the changes observed and evaluated further.

5.7.4. Board mounted components

For future models it would be beneficial to include board mounted electrical components in the assembly. To understand what effects these components have, several board mounted components were included in the current simulation. Two ceramic antennas were mounted on the MMI board; they were used because of their reasonable size and simple geometry. One of the ceramic antennas was positioned near the cut out for the speaker (Figure 5.43), this antenna was investigated.

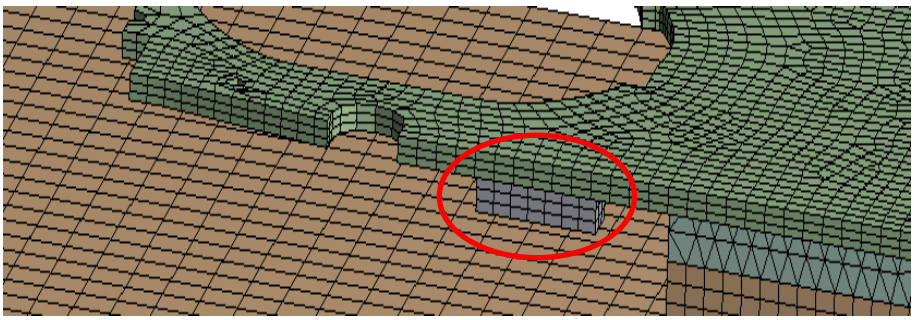

Figure 5.43 - Ceramic antenna location used for analysis (circled)

A stress contour map was used to understand the effect of the ceramic antenna. Table 5.12 shows the stress over time of the MMI board, LCD screen and ceramic antenna. The results illustrate that the antenna has some influence on the behaviour of the board. The antenna restricts the amount of bending occurring at its location because of the rigidity it provides.

The resolution of the results was reasonably high, however if the stress acting at a soldered connection was to be investigated a significantly finer mesh would be required. Providing detail down to a level that includes solder joints within a system level simulation would significantly increase the solver time of the model. Larger components that mount on the boards, such as the ceramic antennas should be included in simplified form (face to face bonds or welds instead of solder ball connections) as the larger components (processors etc.) are likely to have measurable influence on the board behaviour.

Table 5.12 - Simulation results showing the effect the attached ceramic antenna has on the behaviour of the MMI board. NB initial velocity of MMI board is out of the page

Image	Comment
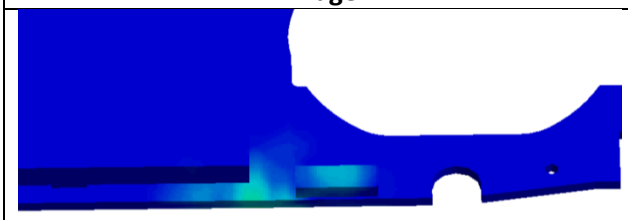	Initial impact with ground. It should be noted that velocity of the MMI board prior to impact is such that in this image orientation the MMI board is travelling out of the page at a direction normal to the MMI board surface
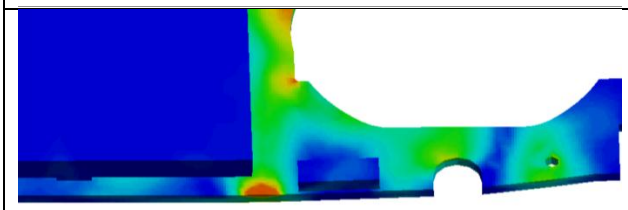	The ceramic antenna appears to restrict bending of the MMI at its location.
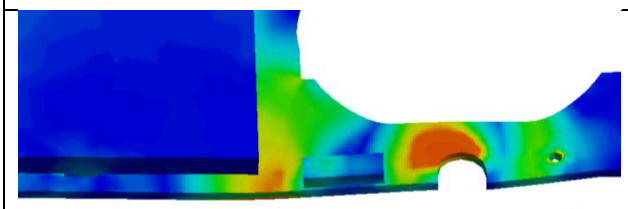	Stress appears to be concentrated at the connection between the MMI board and front panel screw boss. Another area of high stress is near where the LCD screen contacts the MMI board
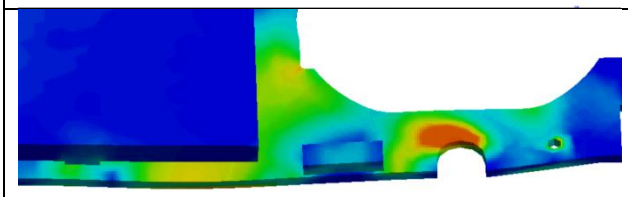	
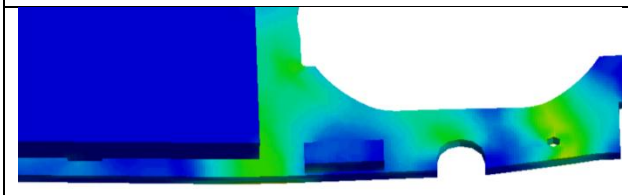	
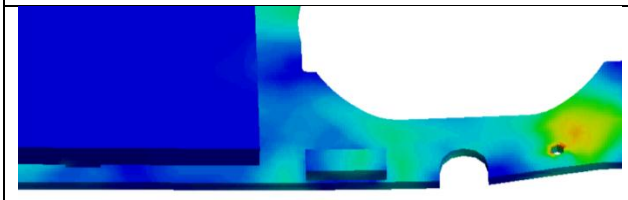	

Image	Comment
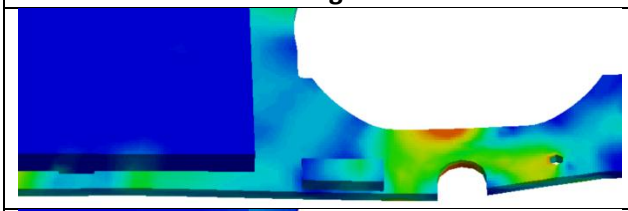	
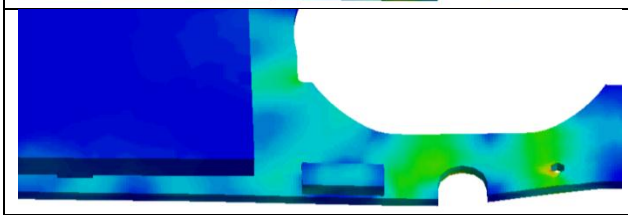	

5.8. Discussion

The detailed radio simulation demonstrated that the finite element method developed can effectively generate results for a commercially realistic product. The results from the finite element simulation show that producing accurate results is challenging.

The main issue experienced when moving from the simplified radio assembly to the Tait handheld radio was the increased geometric detail. The simplification of parts for the detailed radio simulation helped to eliminate unnecessary complexity from the model. The simplification process relied on identifying geometric features, finding the unwanted feature within the CAD environment and suppressing it. Complex parts such as the front panel and chassis which each had over a thousand features were difficult to simplify as unwanted details were often linked to other features, making it challenging to supress these items without causing errors. If more time was available, it would be better to model the parts from scratch so that any unwanted complexity was not present in the first place. Global meshing controls could be used to simplify the geometry but the risk with this approach would be that some of the important smaller details that effect results may be removed.

The shields generated a lot of problems within the finite element model due to their size (0.2 mm thick). The thinness of the shields meant that modelling the shields with shell elements was the only viable option. The shell elements were found to be problematic when creating contact conditions, their inclusion also lead to hourglassing errors. Hourglassing was a result of the use of shell coupled with concentrated loading of individual elements. Further size reduction of the quadrilateral elements would likely have eliminated this, however by doing this the already high solver time would have increased further. Changing the shape to triangular elements did reduce the risk of hourglassing occurring but did not eliminate it.

The severity of the impact event (i.e. high impact velocity) contributed to the presence of the hourglassing error. If the impact velocity was decreased (i.e. lower drop height) the simulation would likely to run to completion. Mesh refinement at points where forces are likely to be high will also aid in reducing loads on individual elements.

The shields provided a lot of rigidity to the RF board so were an important inclusion within the model. EMI shields are included in most handheld communication devices and are likely to be used in years to come so their behaviours should be understood. The correct incorporation of items similar to the EMI shields (thin, structural items etc.) within the finite element environment will come increasingly important as handheld assemblies continue to be miniaturised. Although the issues surrounding the shields were not resolved due to time constraints several solutions show promise including mesh refinement, changing elements types, reducing localised loads, changing connection types and applying a more complex material mode which includes plasticity.

It was difficult to apply the appropriate contact conditions to the shelled RF board. Simulations were run to understand what contact conditions were achievable. It was found that face to face contacts or spot welds between shell and solid elements were the only viable options to get the two parts to bond and hold. It was important to set the maximum offset such that the contact could be appropriately detected. Other contact arrangements such as edge-edge and face-edge did not hold, even when the nodal points were matched between each part. Shell to shell connections (between the RF board and EMI shields) where generated using the mesh-mesh connection; this functioned well, holding the shields in place.

The mesh applied to the detailed radio assembly could be refined even further. Reducing the mesh size would increase the resolution and accuracy of results providing a better understanding of the stress distribution. Higher resolution results would be beneficial when looking at stress acting at areas where stress concentrations occur (screw connections, small board mounted components, rib connections etc.). Further mesh refinement would increase the solver time significantly. Having more elements means that more calculations must be completed each time step, secondly the time step will be shortened so more time steps would need to be calculated for the same simulation time. The solver time was already reasonably high (~80 hours) so it was decided that further mesh refinement should not be investigated during this project.

The material properties were provided from material supplier data. A basic linear elastic model was also used for all materials. Although no significant material damage was observed during the experimental tests, because of the severity of the impact some non-linearity should be considered. A better understanding of the material behaviour and values would greatly improve the results. This was shown during the development of the simplified radio model.

Non-bonded part interactions were set to have a frictional coefficient (static and dynamic) of 0.3. The values were taken as approximations only and may not be indicative of the real behaviour. Applying the correct frictional interactions would increase the accuracy of the model. Frictional values between parts should therefore be investigated further.

Screws and the clamping forces they apply to the parts they constrain can influence part behaviour during the impact event. It was shown during the development of the simplified model that the introduction of screws to replace the face to face bonded screw hole connection allowed for more movement of the parts that they constrained. Screws were introduced into the model but no static clamping force applied was applied. A static clamping force applied to screws should be considered in future models.

The simulation of the detailed radio provided great insight into behaviour of the handheld radio design. Common issues from drop-impact events, including board to board contacts and battery disconnection were able to be identified. The underlining mechanisms causing these issues were able to be understood, making it easier to propose solutions to help mitigate these potential problems. This understanding would ultimately lead to more robust products being developed.

The inclusion of the board mounted ceramic antenna into the finite element model gave insight into what effects such items had on the board behaviour. As most electrical failures are likely to be a result of solder connection damage the behaviour around board components is an important consideration. The larger board mounted components such as the ceramic antennas and microprocessors are likely to be of the greatest interest during such analysis because of their increased risk of damage (due to the stiffness disparity between the component and board causing separation and therefore solder damage). In the current model the solder connection detail is difficult to implement because of its small size. However, the larger components could be modelled in a similar way that the ceramic antennas were (rectangular boxes with face to face bonded connections). Spot welds may also be used in place of solder ball connections, these are able to

break when certain forces/stresses are experienced. These force/stress levels can be set to match limits that match solder ball values, making it easier to identify problematic areas. Introducing such components into the finite element model will give a basic idea of expected behaviours and aid in identifying better locations where damage risks may be reduced.

5.9. Summary

This chapter investigated the drop-impact behaviour of the Tait handheld radio assembly. Before any testing or simulations were completed, the geometry of the radio was modified. Some parts had smaller, inconsequential details removed, whilst other parts were removed from the detailed radio assembly altogether. The simplification process was completed to make it easier for the detailed radio to be used with the finite element environment.

Drop-impact testing was completed using the drop-impact test rig, the result were used to be compared against the equivalent finite element simulation.

A simulation of the detailed radio was performed, the results were found to show some disparity with experimental results. Explanation into the differences in the experimental and finite element results was discussed; reasons include inaccurate material models, mesh refinement and incorrect contact conditions between parts. The simulation was used to show what information and analysis techniques may be used to better understand impact behaviour.

6. Conclusions and Review

A summary of the work completed in this project are presented. The project outcomes were the development of a drop-impact test rig, drop-impact testing, development of a finite element model using a simplified radio assembly and the finite element model of a more detailed handheld radio device. The effectiveness and limitations of the finite element analysis are discussed. Future work related to the development of a more comprehensive finite element model is suggested.

6.1. Project Outcomes

This project involved the development of a finite element model for evaluating the behaviour of handheld radios subjected to a drop-impact event. During the course of the project a drop-impact test rig was developed. The test rig controlled the impact velocity and orientation of a handheld electronic device. Data from drop testing was used to evaluate the finite element models created. A simplified handheld radio was initially used to investigate the settings and parameters of the finite element solver. Impact hammer and drop-impact models were investigated using the simplified radio model. Once the simplified finite element model was fully developed, simulation and testing was completed on Tait's detailed handheld radio assembly.

6.1.1. Test rig development

A drop test rig was designed and fabricated. The key performance requirements for the impact tests included the control of both impact orientation and velocity of the product being tested. Strain, acceleration and impact force were recorded for each of the impact events. The results provided consistent data between equivalent tests. Strain gauge measurements were principally used to evaluate the finite element models.

6.1.2. Simplified radio impact model development

Simulation of an impact hammer test generated poor results initially. Material properties, mesh size, body contacts, screw connections, damping and element types used in the model were investigated. As understanding of the finite element model developed and settings altered accordingly, correlation between experimental measurements and the finite element model improved. The investigative approach taken to understand the input settings and parameters eliminated much of the uncertainty associated with the finite element model. The final simplified radio impact hammer model agreed well with experimental data, suggesting that the finite element model was valid.

6.1.3. Drop-impact simulation results of simplified handheld radio

Simulation of a drop-impact event of the simplified radio from a drop of 1 metre was completed. A simple ball impact test and simulation gave realistic impact surface behaviour. Comparison to experimental data was not possible as the 3D printed radio was too fragile for the drop-impact event, however simulation results did appear reasonable.

6.1.4. Drop-impact simulation results of detailed handheld radio

A detailed radio model was developed using the design of Tait's current handheld radio. A simplification removing small and insignificant parts and simplifying parts was performed. The

simplification process resulted in a representation of the Tait radio that was usable within a finite element solver.

Using the developed drop-impact model, the behaviour of the radio throughout the impact event was able to be observed. The finite element model made it possible to identify any potential problems during the impact event. Common radio behaviour issues were analysed including battery disconnection, board to board contact and the influence of board mounted components. Once these issues were identified the mechanisms contributing to the behaviours were able to be better understood and design solutions identified.

6.2. Effectiveness and Uses of the Finite Element Drop-Impact Model

An accurate finite element model of the simplified radio was eventually achieved however it was a time consuming process. The large number of parameters that influence the results coupled with the 'black box' nature of the finite element package made it difficult to generate acceptable results. If any such finite element model is to be incorporated in the product development cycle and used for making critical design decisions then the results must be corroborated in some way. This is because generating results from a finite element model can be relatively straightforward, but this does not imply that the results generated are correct. Confidence in the solver method, assumptions made and the user set parameters need to be high or experimental results need to be present to validate the model. Having confidence in results can be a time consuming process especially if multiple simulations are required to understand how certain parameters affect results or if an extensive testing procedure is used. Initially, the time taken to develop the finite element model to an acceptable level may be longer than alternative investigative process, such as build and test. However, less development time of such models will be required as material libraries are generated, geometries are developed for finite element modelling purposes and the organisation's understanding of finite element analysis grows. Developing new finite element capabilities must be weighed up against the time required in attaining a workable model and the long-term benefits of having such an analytical tool. Some advantages of having a finite element model that can accurately model drop-impact events include:

- Deformation, stress, strain, etc. can be evaluated at any point of interest
- Parts that are normally obscured from view can be easily observed
- The impact event can be slowed down giving a better understanding of how stress waves propagate through the system

- The simulation can be scaled so that small deformations are more visible
- Different designs can be investigated without the need for physical prototyping
- Issues found during physical testing or customer use can be recreated in a finite element model to better identify the root cause of the problem. This understanding often leads to the development of a solution which effectively targets the design weakness
- Parametric studies can be performed to optimise designs, improving overall performance or reducing the amount of material used

Additionally, a lot of the finite element principles and approaches developed during the impact model investigation can be transferred to other finite element analyses such as static structural models, thermal models, and electromagnetic simulations. Techniques developed that are transferable to other analyses include:

- Creating a geometry that can be easily incorporated into a finite element environment
- Meshing principles
- Material models and properties
- Element types
- Solver options
- Iteration, timestep and convergence concepts
- An appreciation of the importance of knowing each parameter influences on the solution
- Knowing when to utilise experimental data for validating finite element models and improving existing models

Examples of when the development of a finite element model would be an ineffective use of time and resources include:

- Low cost and low volume products
- One off designs
- Existing designs that are going to be discontinued in the near future
- Off the shelf parts where there is no opportunity for modification (i.e. single external supplier that has little incentive to change design)

6.3. Future Work

Further work is required to accomplish better agreement between the experimental and simulation results of the detailed radio assembly in a drop-impact simulation. The results from the simplified

radio show that good agreement is attainable; indicating that modelling such a complex assembly is possible. The development procedure of the simplified radio could be used for the tuning of the detailed radio model.

The two items that were found to have the greatest influence on improving the experimental-simulation agreement were the material properties and mesh refinement. Little was known about the behaviour of the materials used in the detailed radio, parameters being mostly drawn from data provided by the materials suppliers. Some of the softer materials had increased uncertainty as their material values (Young's modulus) were converted from Shore hardness values. Completing material testing for each of the materials used within the assembly should be completed; doing so will give confidence that the material values used in the finite element model are correct.

The element size could be further refined to increase the result resolution and accuracy. A smaller mesh was not employed during this project as the solver time became impractically long; if more time were invested developing a detailed model of the radio then a smaller mesh could be applied to the model. To aid in a better refined mesh it would be beneficial to remodel some of the more complex parts, such as the front panel and chassis so the unnecessary detail present would not cause meshing issues.

Hourglassing and energy errors were present when the thin EMI shields were included within the finite element model. The errors were not fully resolved during this project. The mesh on the shields particularly at its corners and the connection with the RF board could be refined. The connection between the RF board and EMI shields was a rigid bonded connection which may have been the origin of the hourglassing error due to the high, concentrated loading of individual elements it caused. This connection did not sufficiently reflect the real life soldered connection between the RF board and Shields. Different connection interfaces between these parts should therefore be investigated.

When a working impact model has been developed additional impact orientations should be investigated. Throughout the project horizontal impacts were predominantly examined because of the high deformation such impacts caused on the internally mounted circuit boards. Models of different impact orientations would provide a more comprehensive understanding of the behaviour and survivability of the radio for all drop-impact events.

Eventually, the detailed impact model should be used as a tool for investigating any common failures from impact events on the existing Tait radio. The model would be able to investigate the cause of the failure and be used in evaluating possible solutions.

For future radio designs (the next design iteration), the drop-impact finite element model should be integrated earlier in the design process. Simulation results would provide insight into the impact performance of different designs, giving a more informed decision on which concepts should be developed further. As the radio design is developed and geometries become more fixed, optimisation studies could be performed to select what materials should be used and where material can be removed.

Appendices

There are 2 appendices included to support the main thesis report:

A – Development and Design of a Drop-impact Test Rig

B – Detailed Handheld Radio Finite Element Analysis Setup

A Test Rig Design

This appendix presents the development and final design of a test rig capable of performing drop-impact tests on portable handheld electronic devices.

A.1. Introduction

The primary function of a drop-impact test rig is to control the impact conditions of the product tested. A controllable impact orientation is vital for gathering reliable and consistent information about the performance of the test product at different impact orientations and drop heights.

This report identifies and selects the critical design features and components that are incorporated into the constructed test rig. The test rig is divided into separate functions so that the best overall design can be developed.

The overall design of the drop-impact rig is to be similar that shown in Figure A.1. It consists of a guide rail system that controls the fall of a drop table. The drop table contains a holding mechanism that secures the test product at the desired impact orientation. The test rig triggers the holding mechanism to release the test product as it approaches the impact surface, so that the test product is freely constrained at impact with the ground.

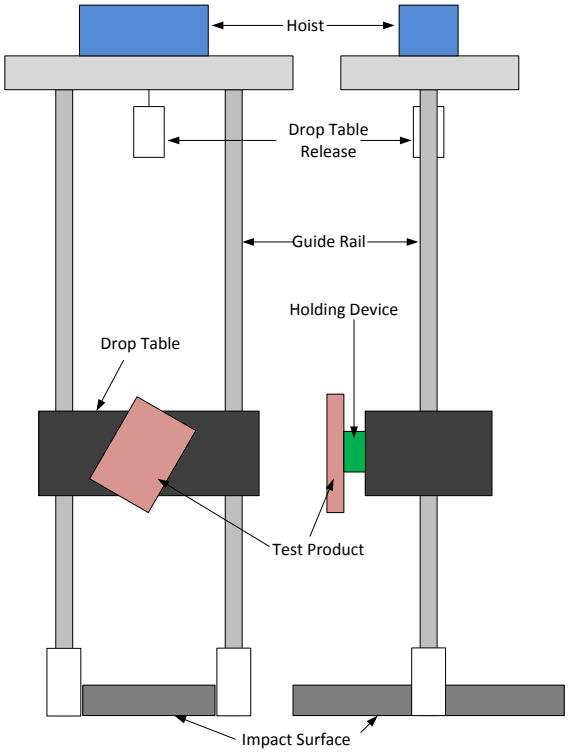

Figure A.1 - Basic schematic of a drop tower

A.2. Test Rig Design Selection

Different components are required to be designed or acquired during the development of the drop-test rig. Each of the individual functional requirements are discussed, several concepts presented and then the best option selected.

A.2.1. Holding mechanism

The holding mechanism must be able to hold the test product in place and maintain that orientation until the test product is released. The holding device is required to release the test product with a simple action that does not induce a rotation to the test product. The holding device must also be able to hold items as large as 200 mm and as small as 25 mm (largest overall dimensions of the Tait handheld radio), this ensures that any impact orientation of the handheld radio can be tested. The holding mechanism must be able to tilt/rotate to achieve different impact orientations.

A.2.1.1. Two point clamp

The two point clamp design consists of two arms clamping either side of the test product (Figure A.2). This design makes it easy to position the test product at the desired orientation and clamping/release actuation of the device would be relatively simple. Two point clamping means it may be difficult to hold the product securely in place, rotation between the two clamping points could be an issue. A high-speed and symmetric release of the clamping arms would be required to ensure no rotation is applied to the radio upon release.

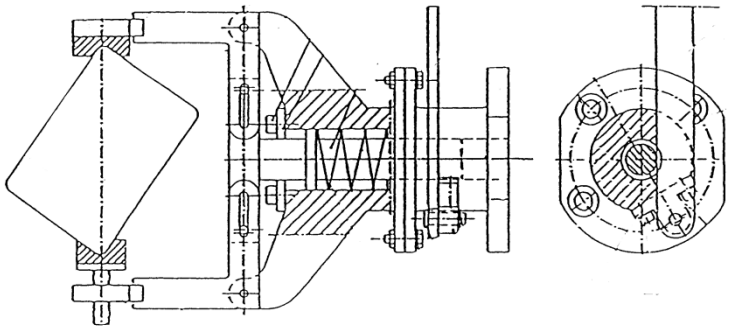

Figure A.2 - Example of a two point clamp [14]

A.2.1.2. Three or four point clamp

Three or four jaws (Figure A.3) may be used to hold the device in place. This design would hold the product more securely, however it may be difficult to release the component due to the complex clamping arrangement. The three or four point clamping device is generally designed for circular clamping and where the complex geometry of the test product makes it difficult for designing an adjustable clamping arrangement.

Figure A.3 - Example of a three point clamping device

A.2.1.3. String attachment

The test product could be held in place by a series of strings (Figure A.4). The strings would be cut or released to free the product prior to impact. The mounting process would be timely due to the string having to be cut to the right length and attached accurately onto the radio. The lack of rigidity in the strings means that the device would be able to swing during free-fall, reducing the accuracy of the impact orientation.

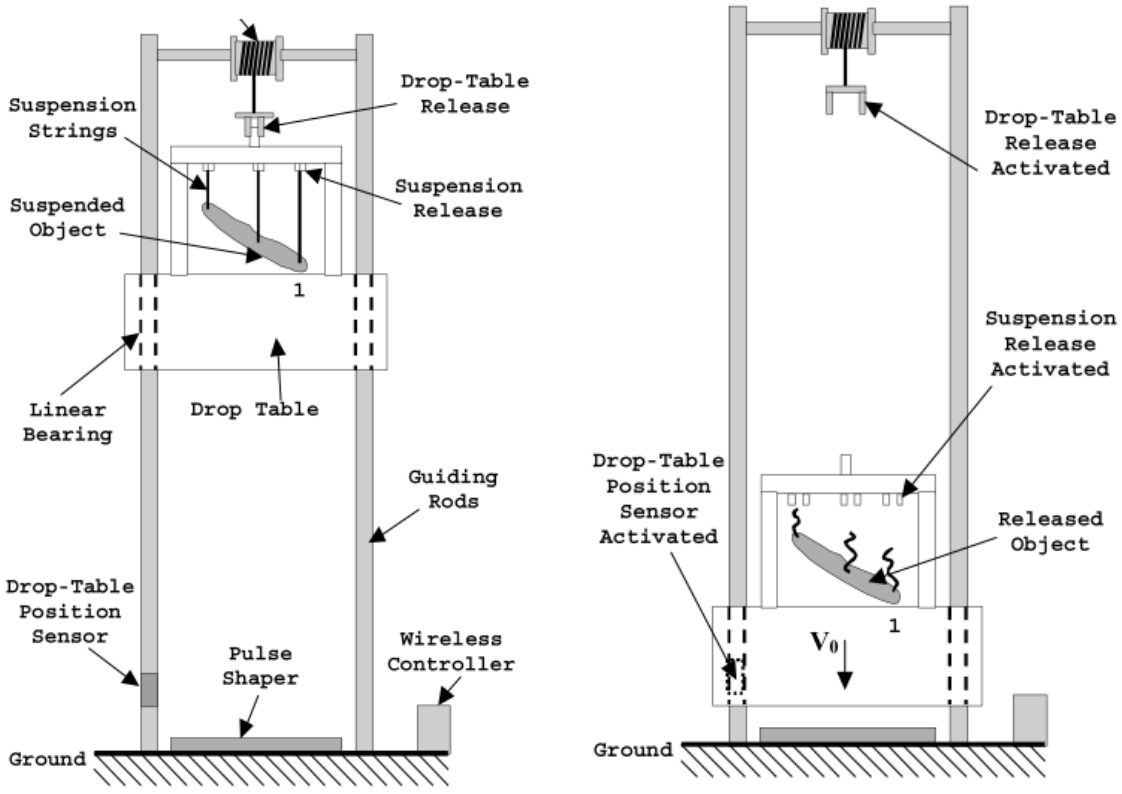

Figure A.4 - Schematic of a string attachment/release drop tower [17]

A.2.1.4. Electromagnet

An electromagnet could be used to hold the radio in place (Figure A.5). A strip of magnetically conductive material would need to be attached to the radio. Depending on the strength of the

electromagnet, only one electromagnet could be required. The orientation of the radio would be easily adjustable whilst still secure once the orientation is set. The release actuation would be by removing the current from the electromagnet which can be done via an electrical switch, making triggering easy. After the release there may be some influence of the magnet which may result in undesired rotation of the product.

Figure A.5 - Electromagnet holding an iPad in place

A.2.1.5. Vacuum suction

Vacuum suction could be used to hold and release the test product. Creating a secure hold requires that the vacuum suction is placed onto a relatively flat surface, i.e. grills or edges would not be able to be used. The test product would be easy to position at the correct release orientations, depending on the strength and size of the vacuum pad it is likely to hold the desired orientation with relative ease. Releasing the product may involve applying a burst of air out of the suction area, if the suction area is not positioned in line with the centre of gravity of the test product a rotation would be induced.

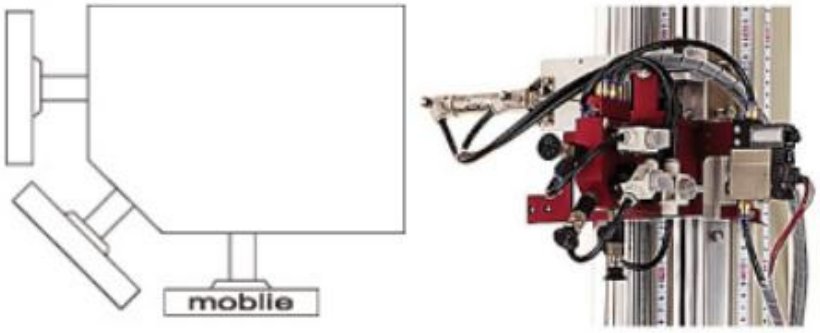

Figure A.6 - Examples of a drop test rig using suction cups

A.2.1.6. Selected option

From the methods outlined above, the options with the best potential for success are the two point clamp and electromagnetic release. Further investigation of both designs needs to be completed to understand the practicalities of implementing each configuration. No further development work is required on the electromagnet design before final review. Investigation into how the two point clamp will be actuated and triggered need to be completed before a final decision is made.

A.2.2. Actuation force of two point clamp

The two point clamp needs to be actuated in some way so that the jaws can open and release the test product. A fast action is required to ensure that the clamps clear the radio once the test product has been released.

A.2.2.1. Spring

A spring can give a quick and smooth release on the two point release mechanism. A straight or torsional spring can be used depending on the design of the release mechanism. Being purely mechanical, the device would require a separate actuation to trigger. It should be relatively easy to interchange between different spring strengths and sizes to suit the variance of release action required for the different impact orientations and test products.

A.2.2.2. Solenoid

A solenoid would provide actuation similar to that of a straight spring. It would be easier to trigger and release via an electrical switch as opposed to the spring which would require a secondary release mechanism. The solenoid would be harder to adjust for different clamping dimensions due to its fixed dimensions.

A.2.2.3. Electric motor

An electric motor can be used to apply either a linear motion or rotational motion to the two point clamp design. Triggering of the electric motor would be straight forward, requiring only an electric switch. The release speed would likely be slower than a spring or solenoid which may be an issue.

A.2.2.4. Selected option

A solenoid actuation is the best option to actuate the opening of the two point clamping mechanism. The solenoid would have a similar release action to the spring and be significantly easier to trigger. The solenoid is superior to the electric motor as it has a much faster action which is vital for a clean release of the test product.

A.2.3. Release triggering

A.2.3.1. Photoelectric sensor

Photoelectric sensors positioned on the side of the test rig would be able to identify when the drop tower passes a certain point and activate the trigger. The photoelectric sensor would be wired such that the solenoid or electromagnet is 'switched off' when the drop table movements are detected. The photoelectric sensors would be easy to mount and their height adjustable to get the timing of the release correct.

A.2.3.2. Timed release

A time delay between initial release of the drop table and the release of the test product can be programmed into the control system. This method does not require any additional triggering sensors but does require an electronic initial release and a known time delay for each drop height tested, most likely achieved through trial and error. A timed release relies on a consistent free-fall but would eliminate the risk of a sensor not detecting the drop table.

A.2.3.3. Selected option

The timed release is the more practical of the two triggering schemes. Both methods require an initial setup and tuning to get the triggering of the release correct, the photoelectric sensor adds another level of detail into the control system and provides very little extra accuracy in terms of release timing. The photoelectric sensor would find application if a wide range of drop test heights were used, this is not the case for this test rig.

With a better understanding of how the release mechanism is likely to be triggered and how the clamping mechanism would be actuated a decision on which of the electromagnet or two point clamp designs should be used cold be made.

The electromagnet was selected to be used for the release of the test product due to its simple holding method and the ease with which it could be electrically triggered. The two point clamping mechanism would require a complex actuation and triggering setup and provide little additional advantage over the electromagnet in terms of product placement/positioning as well as the cleanliness of the release.

A.2.4. Impact surface layout

The impact surface is used for gathering consistent and accurate impact force measurements. The surface is to be designed to incorporate load cells capable of measuring the forces that are applied to the test product during impact. Investigation into the type of load cells, the number of load cells, impact surface design and connections are considered in this section.

A.2.4.1. No load cell

One option is to not incorporate impact force into the measurement scheme. However impact force would be valuable for evaluating the energy absorbed and length of the impact event. The gathered data could be used for validating the finite element model and identifying critical impact orientations.

A.2.4.2. Exposed single load cell

An exposed load cell would be an easy design to implement, however it would be very difficult to ensure that the test product contacts squarely onto the load cell due to the small surface of the load cell in relation to the test product.

A.2.4.3. Impact plate

An impact plate could be mounted to the top of the load cell(s). This would provide a bigger surface for the product to strike and different surface treatments can be applied to simulate different impact surfaces. Plate resonances may be an issue when collecting the impact force data. The plate would ideally be designed to ensure that resonant frequencies are away from the impact pulse frequency.

A.2.4.4. Preloaded impact plate

The impact plate could be designed so that there are bolts running between a raised impact surface and a ground mounting plate. By tightening these bolts the load cell would be compressed slightly. Pre-loading the impact plate would aid in damping out any resonance created by the impact surface/impact event. Preloading will also increase the rigidness of the impact surface, and therefore make it more comparable to a real-life ground impact.

A.2.4.5. Selected option

The selected option was to use an impact plate that was sufficiently stiff such that the natural frequencies were away from the impact impulse frequency. The plate should also be relatively light compared to the tested product and only be large enough so that all impact surfaces can consistently strike onto the plate. The option to preload the impact plate may be implemented if the initial tests result in resonances that interfere with measured data.

A.2.5. Load cell layout

A.2.5.1. Single, centred load cell

A single load cell could be positioned in the centre of the impact surface. This option would be the most cost effective option however there are several drawbacks. Any off-centre impacts (to the load cell) would induce a bending moment onto the load cell that would not be accurately measured.

A.2.5.2. Two load cells

Having two load cells aims to address the bending moment induced by off-centre impacts present in the single load cell schematic, however there are still issues with impacts that are offset from the line running between the two load cells. The overall impact force would be found by summing the forces measured from the two load cells. If the point of impact is designed to be along the line between the two load cells (which is possible with a drop table/release mechanism arrangement), then two load cells would be sufficient.

A.2.5.3. Three of more load cells

Having three or more load cells in a ring arrangement would further minimize the risk of bending moments being transferred into the load cell matrix and ensuring the impact plate remains stable during the impact event. This type of load cell arrangement would be more expensive due to the cost of each load cell in addition to the number of channels required for the data acquisition system.

A.2.5.4. Selected option

Two load cells would provide a rigid impact surface with minimal bending moments induced onto the load cell, especially with the impact being along the same line. Using more than two load cells would result in a more expensive test rig but would not provide significantly better measurements. If the two load cell impact plate were found to be unstable there is room for more load cells to be incorporated into the design.

A.2.6. Rated loading

It is important that the selected load cell has a large enough load rating to handle and accurately record the force of the impact events. There is a risk of selecting a load cell which is too large for the application and thus the measurement results would have poor resolution. Previous testing which involved investigating the impact force of a dropped iPad used two 10 kN load cells; the highest recorded peak impact force was 5 kN, well within the load cells rating. The iPad dropped from a height of 1 m; however it had a similar rigidity and a larger mass to the test product (Tait's handheld radio) so the measured peak force is likely to be less than that observed during the iPad testing. Therefore two load cells with an individual rating of 10 kN were sufficient for this test rig.

A.2.7. Guide rail

The guide rail is designed to control the descent of the drop table which holds the release mechanism and test product.

A.2.7.1. Single guide rail

A single guide rail would be the simplest design to implement. Compared with having multiple rails, there is a lower risk of the drop tower jamming during the free-fall. The main disadvantage with using a single guide rail is that there would be reduced stiffness and stability of the test rig. If a circular guide rail is used then the table would be able to rotate, reducing the accuracy of the impact location.

A.2.7.2. Two parallel guide rails

Two guide rails would create a more stable structure. It is important that the guide rails are parallel with each other to ensure that the drop has little friction and to reduce the risk of jamming.

A.2.7.3. Selected option

Loading during an impact, particularly when a large mass and high impact speeds are involved it becomes very important to have a rigid structure. Two guide rails will ensure a more sturdy design,

with careful design and tight tolerances the guide rails would provide a low friction, jam-free decent of the drop table.

A.2.8. Sliding surface

The sliding surface between the drop table and guide rails is important for creating low friction sliding, repeatable and high impact velocities.

A.2.8.1. Roller linear bearings

Linear roller bearings would provide a smooth and repeatable free-fall of the drop table. To get the best performance from the bearings tight tolerances would be needed for the guide rails. Failure to meet set tolerances would mean the drop is likely to be variable; there is also a risk of the bearing jamming if the diameter and distance between the rails is inconsistent.

A.2.8.2. Polymer/composite bushing

A polymer or composite bushing can be a cost effective and low maintenance sliding surface solution. The tolerances on the bushing can be larger than the linear bearings due to the way they are designed to operate. The bushings are most likely not to be in contact with the guide rails for the majority of the drop event and just hitting from time to time as the drop table moves from side to side. The bushing needs to be appropriately sized so that jamming is minimised and low friction running is achieved. The larger the diameter of the bushing in relation to the guide rails would mean that the sideways movement and misalignment maybe large; this means that when contact between the rails and bushing occurs it can have a large effect on the free-fall velocity and stability. This contact may not occur with every drop and therefore the repeatability of the impact velocity may be affected.

A.2.8.3. Selected option

Using polymer bushings opposed to the linear roller bearings means that there is a lot more flexibility within the design in terms of dimensional tolerances. Correct sizing of the bushing in relation to the guide rails is also critical to gaining a smooth and consistent drop of the release mechanism and product.

A.2.9. Guide rail mounting and alignment

A.2.9.1. Threaded rod/screwed in

The guide rails would be screwed into the base mounting plate. This design would work well to initially hold the rails in place; however it would be difficult to get the good alignment between the rails, necessary for a smooth fall of the drop tower.

A.2.9.2. Sleeve – Grub screw

A mounting sleeve would ensure a greater surface area in contact with the guide rail, resulting in a secure fit. The sleeve could be positioned to create good alignment between the two guide rails. Grub screws would be used to hold the guide rails in place, notches could be machined into the guide rails to reduce the risk of the rails working loose over time. The guide rails could be removed easily for disassembly or readjustment simply by unscrewing the grub screws.

A.2.9.3. Sleeve – Heat shrunk

Instead of using grub screws to hold the guide rail in place a sleeve would be heated up, slid onto the guide rails and cooled to create a solid grip onto the guide rails. The alignment of the guide rails can be adjusted by machining the base of the sleeve where it is mounted to the base plate. It is important to ensure that the sleeve is as designed before attachment as it would be difficult to remove the sleeves once they are mounted.

A.2.9.4. Selected option

The threaded rod would not provide a rigid enough connection and alignment between the two guide rails is difficult. A heat shrunk sleeve over the guide rail is the preferred option as it would provide the most secure fit ensuring that the guide rail would not move over time. Care needs to be taken to ensure the heat shrunk sleeve is correct before attachment as once it is mounted as it will be difficult to remove.

A.2.10. Measurement equipment

Various sets of data are to be measured and recorded during the impact event so that the behaviour can be appropriately analysed. The collected data provides understanding of what is occurring to the test product during and after the impact event.

A.2.10.1. Strain measurement

Strain gauge rosettes are to be used to measure the strain of the test device at various locations. It is important that the wires running from the strain gauges do not interfere with any components during the free fall of the radio during the impact events.

A.2.10.2. Acceleration measurement

During the impact testing an accelerometer is to be mounted on the test product. Accelerations in the region of 2-3000g's are expected during impact; therefore an accelerometer capable of measuring this level of acceleration is required. Adding a large amount of mass to the system would greatly affect the dynamic response of the radio, therefore the lighter the accelerometer the better. Another consideration is the dimensions of the accelerometer as there is limited room in which the accelerometer can be internally placed, therefore the smaller the better.

Due to the various impact orientations that are to be tested, a tri-axial accelerometer would make it significantly easier to evaluate the principal acceleration experienced by the test product. A single axis accelerometer could be used if the acceleration in a certain direction is of interest, i.e. the flex on the PCB (acceleration normal to the board).

A.2.10.3. Impact visualisation

High speed photography may be used to aid in gathering understanding of the handheld radio products during drop-impact events. The high speed camera can also be used to estimate the impact velocity of the radios as well as evaluating the impact orientation, ensuring the release is clean and that the radio is released before impact with the plate. If the high speed camera is not available a CCD camera that is set up to trigger just before impact could be used to ensure the impact orientation is correct.

A.2.11. Data acquisition and post-processing

With a large amount of testing expected to be completed over the course of this project it is important to consider how this information is handled. Minimal manual processing of data is desirable.

A.2.11.1. LabVIEW

LabVIEW is a common data acquisition used to triggering, recording and processing information from the attached measurement equipment. LabVIEW capabilities include being able to apply filters directly to the data (high/low pass etc.) as well as zeroing data. LabVIEW can plot the responses of

each sensor in real time on screen as well as outputting to various file formats that can be used for further post processing.

A.2.11.2. Matlab

With the use of Simulink, Matlab can identify the National Instrument data acquisition systems and its related measurement equipment. As well as instantaneous data output, Matlab has a large set of analysis , processing and plotting capabilities that are not available in programs such as LabVIEW.

A.2.11.3. Excel

Excel is able to process raw data but struggles to efficiently process large volumes of data when compared with the likes of Matlab. Considering the sampling rate (large data sets) and the amount of tests that are required to be processed, Excel would be a lot less effective.

A.2.11.4. Selected option

For an all in one solution, Matlab would be the best data handling system. However LabVIEW is currently used for data acquisition systems at the University of Canterbury so would be easiest to implemented, a .txt file output can be easily handled in Matlab for post processing and analysis.

A.2.12. Raising of drop tower

A hoist can raise and lower loads via a remote control and would hold in place once the object is at its desired height. The hoist would compactly mount onto the top of the test rig and could easily attach to the drop table through a shackle, eyebolt or similar.

A.2.13. Protection from falling objects

The initialisation of the drop test should be set up so that it is triggered at a distance/remotely from the test rig. As a secondary safety precaution the test rig should have a protective shield surrounding it so that any falling objects are isolated and cannot cause injury to the user. A frame is to be built to hold the hoist in place so that the drop table can be raised and lowered. Perspex can be mounted to the side of the frame to prevent nearby users from getting injured from falling and rebounding objects.

A.2.14. Momentum trap for drop table

A.2.14.1. Shock absorber – Pneumatic/Hydraulic

Industrial absorbers are designed specifically for this type of application. The absorber would easily mount onto the base plate and have a long operational life. Shock absorbers are commonly

adjustable so that the best settings can be tuned to provide minimal rebound of the release mechanism.

A.2.14.2. Spring

Using a spring to absorb the drop table momentum would be a simple and cheap solution but requires the design of a mounting system. The spring system may result in a large rebound of the release mechanism thus putting greater stress on the guide rails and bushings.

A.2.14.3. Foam

Foam provides good absorption characteristics, however after a few drops the foam would start to lose its effectiveness due to the crushing of the foam cell walls. Its absorbent nature means it would become dirty and un-presentable over time. The correct foam for the application would be difficult to select initially.

A.2.14.4. Selected option

A shock absorber would be the best performing and most durable momentum trap. The foam would deteriorate over time and the spring requires more design work while still not being as effective as a shock absorber.

A.3. Test Rig Design Specifications

A list of design specifications has been developed to aid the development and evaluation stages of the test rig design.

Table A.1 - Overall assembly design specifications

Specification	*Comments*
Allow for a drop height of 2 m	In accordance with current testing procedures at Tait of a 1.8 m drop test, however the fall may be slowed due to friction between the guide rails and drop tail. To gain equivalent impact velocity the release height would need to be approximately 2 m.
Secure to the ground	Ensures there is no unwanted movement during tests
Protection from any flying components	Health and Safety issue, risk reduction
Mount for hoist mechanism	Drop table could be heavy therefore not feasible to manually lift the weight and thus a lifting mechanism must be employed
Momentum trap for drop tower	Reduce damage to drop table and tower
Guides to control fall of drop tower	
Guides parallel with each other/straight	To ensure little interference at allow for realistic free fall

Provide area for NI chassis that is protected from falling objects	Keep National Instrument Chassis protected from drop tests whilst ensuring close proximity for cables
Eliminates risk of entanglement of wires on/around guides	Cables from instrumentation are generally fragile and expensive so therefore the risk of the cables getting caught and pulled must be minimized as much as possible
Protection from users when object is falling – safeguards	Risk of entanglement
Guide rods appropriately spaced to easily house drop table	
Rubber mounts to isolate any ground vibrations during testing	Reduce transfer of vibrations etc. that could have an effect on gathered data
Unlikely to 'lockup' during free fall	Ensure a smooth free-fall, if mechanism lockup it will most likely result in damage to the guide rails and or the drop weight/release mechanism
Impact surface not obstructed, so that impact can easily be viewed and filmed	

Table A.2 - Drop table and release mechanism design specifications

Specification	*Comments*
Able to hold item as small as 25 mm	So that the smallest part of the handheld radio can be held
Able to hold item as large as 200 mm	So the largest length of the radio that will need to be held in the release mechanism so all orientations can be effectively tested
When released will not apply a rotation to the product it is holding	A very critical design feature as the release mechanism needs to provided consistent drop orientations
Release mechanism/drop table will not interfere with impact event	Needs to be well clear before impact with surface
Able to release product before impact	To ensure that the product is freely constrained during impact
Drop tower will stop or be slowed before bottom of the tower	Reduce damage to release mechanism and also ensure that the orientation of holders do not move and therefore numerous drops can be made with the exact orientation
Will not interfere with instrumentation cables	Cables from instrumentation are generally fragile and expensive so therefore the risk of the cables getting caught and pulled must be minimized as much as possible
Adjustable orientations	Release mechanism able to be rotated (better for consistent orientation setup) or the product can be held at different orientations by the release mechanism

Release will open far enough so that it doesn't interfere with falling object	
Rigid design, namely release mechanism, so that successive drops are consistent.	
Fall smoothly against guide rods i.e. not slowed down significantly by guide rods, maintain free-fall conditions as close as possible	Slowing the release mechanism will result in a large difference between the release height of test rig and the effective release height (the height at which the impact velocity will be the same as if the product was free falling

Table A.3 - Impact surface design specifications

Specification	*Comments*
Impact plate/load cell with sufficient area to log impact of handheld radio devices	
Eliminate any resonance of load cell during impact	
Reduces the risk of any cables getting caught around impact plate	
Isolated from any noise from guide rails and release mechanism impact	Ensure the readings from the impact are as clear as possible, shocks from the release mechanism have the potential to interfere with the data from the
Ensure that an impact of the same magnitude will give the same reading regardless of location of where that impact occurs	Load cells will need to be positioned as such that no large bending moments of the plate can occur, i.e. a single load cell placed in the centre of the impact surface will not behave the same with an impact on the edge of the plate when compared with an impact near or directly onto the load cell

A.4. Final Drop Test Rig Design Description

The design has been broken up into five major design components: the drop table/release mechanism, impact surface design, guide rail design, data measurement and acquisition, general usability and safety considerations.

A.4.1. Drop table/release mechanism

The purpose of the release mechanism is to hold the radio at a set orientation and to cleanly release the radio just before impact with the impact surface of test rig.

An electromagnetic design was selected for the holding and release of the radio (Figure A.7). The design consists of an electromagnet attached to an adjustable plate so that various impact

orientations can be tested. Conductive strips are required to be attached to the radio. The release of the radio will be done by removing the current from the electromagnet via an electrical switch. To ensure the radio is released at an appropriate distance from the impact, an time delay between the release of the drop table and the switching of the electromagnet was applied. The time delay was tuned using the high speed camera to ensure the test product was released at an appropriate instance.

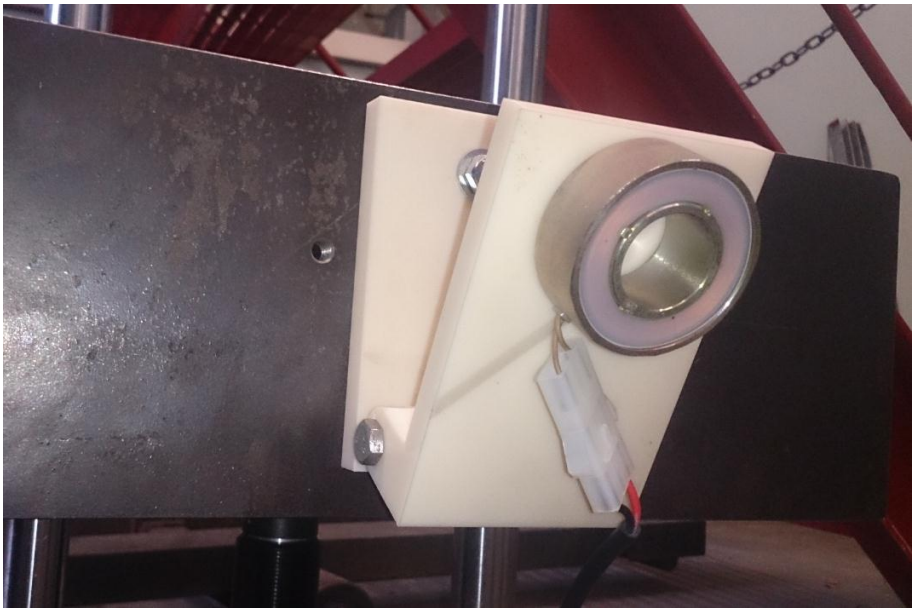

Figure A.7 - Drop table and release mechanism design

A.4.2. Impact surface

The impact surface is important for gathering accurate impact forces measurements. The design incorporates two load cells that are attached to a rigid impact plate, as shown in Figure A.8. The impact surface will be 400 mm square so that all impact orientations can be tested. S-type load cells will be used with each load cell having a rated loading of 1tonne and have a sampling rate of 50 kHz. The impact surface and load cell will be mounted such that they are isolated from the rest of the test rig so that only the impact of the radio will be measured.

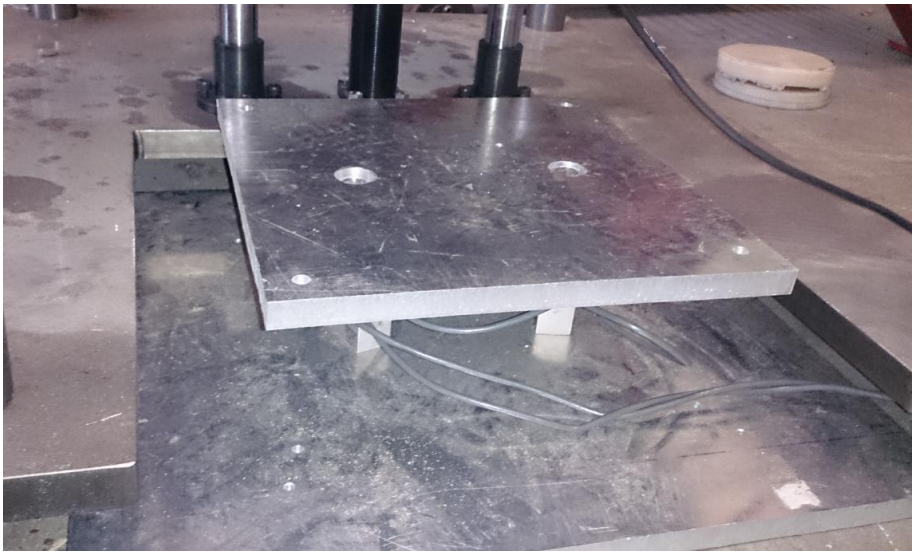

Figure A.8 - Impact surface design

A.4.3. Guide rails

The guide rails allow for the controlled drop of the release mechanism. The connection between the release mechanism and the guide rails is also detailed in this section. Two 50 mm solid cylindrical rods will be used as the guide rails for the release mechanism. The rails will be attached to the base of the test rig via a sleeve that has been heat shrunk around the guide rails. Polymer bushing will be used as the contact surface between the guide rails and the release mechanism. The bushing will have a relatively loose fit against the guide rails reducing the sliding resistance during free-fall.

A.4.4. Data acquisition

A significant amount of data is likely to be required to fully verify the finite element model. Accelerations and strains on critical components are required to be monitored. A lightweight shock accelerometer will be attached to the outside of the radio to get a basic representation of the accelerations experienced by the radio. Single axis miniature accelerometers may be attached to the PCB's to get a better understanding of their behaviour under impact. Strain gauges will be attached to the PCB's so that their deformation can be monitored. All the data from the measurement equipment will be handled by a National Instrument DAQ which will be controlled by their system design software LabVIEW. LabVIEW will output a data file, with the data being processed through Matlab.

A.4.5. Usability and safety considerations

Safety considerations as well as ease of use have also been incorporated into the test rig design. The release mechanism will be raised via an electric hoist mounted above the test rig. The release

mechanism will be dropped by using a quick release rigging component that will be attached to the electric hoist cable. After releasing the radio the release mechanism will be slowed down using a shock absorbers that were mounted to the base plate.

A.4.6. Overall dimensions

The final design is shown in. The test rig stands at 2.45 m tall and has an 830 x 70 mm base. It consists of a guide rail system that allows a release mechanism to drop in a controlled manner. The rig has a timer which when the release mechanism is near the impact surface it triggers the release of the radio. The rig is capable of measuring the impact force, acceleration and strain at certain points on the radio.

Figure A.9 - Constructed test assembly

A.5. Engineering Drawings

The engineering drawings produced for the construction of the test rig are shown in the following pages. The rig was constructed as drawn.

DRAWING: G:\Masters 2.0\2 Experimental Testing\Test Rig Developement\CAD Files\Finished Design w Drawings\Assembly Drawing

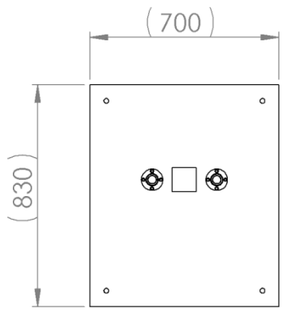

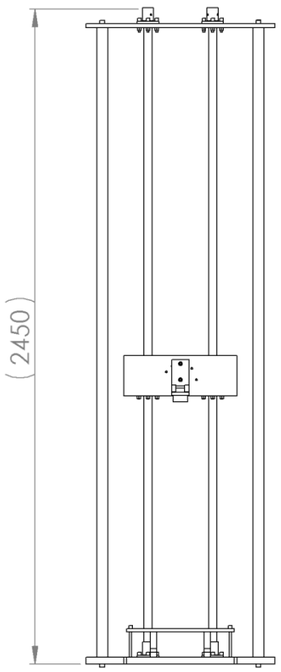

BILL OF MATERIALS

ITEM NO.	PART NAME	QUANTITY.	DRAWING
1	Base Mounting Plate	1	001
2	Support Column	4	002
3	Top Mounting Plate	1	002
4	Top Guide Rail Mount	2	003
5	Guide Rail Base Mount	2	003
6	Guide Rail	2	004
7	Drop Plate	1	004
8	Top Impact Plate	1	005
9	Base Impact Plate	1	005
10	Bushing Housing	2	006
11	SKF Bushing	2	006
12	Electromagnet Mount	1	
13	Electomagnet Pivot	1	
14	Electromagnet	1	
15	AST 1t Load Cell	2	
16	M8 Nut	16	
17	M8x30 Cap Screw	18	
18	M3 x 15 Grub Screw	5	
19	M8x140 Cap Screw	4	
20	M12x30 Grub Screw	4	
21	M8 x 55 Cap Screw	1	
22	M12x80 Cap Screw	8	
23	M8x40 Cap Screw	8	

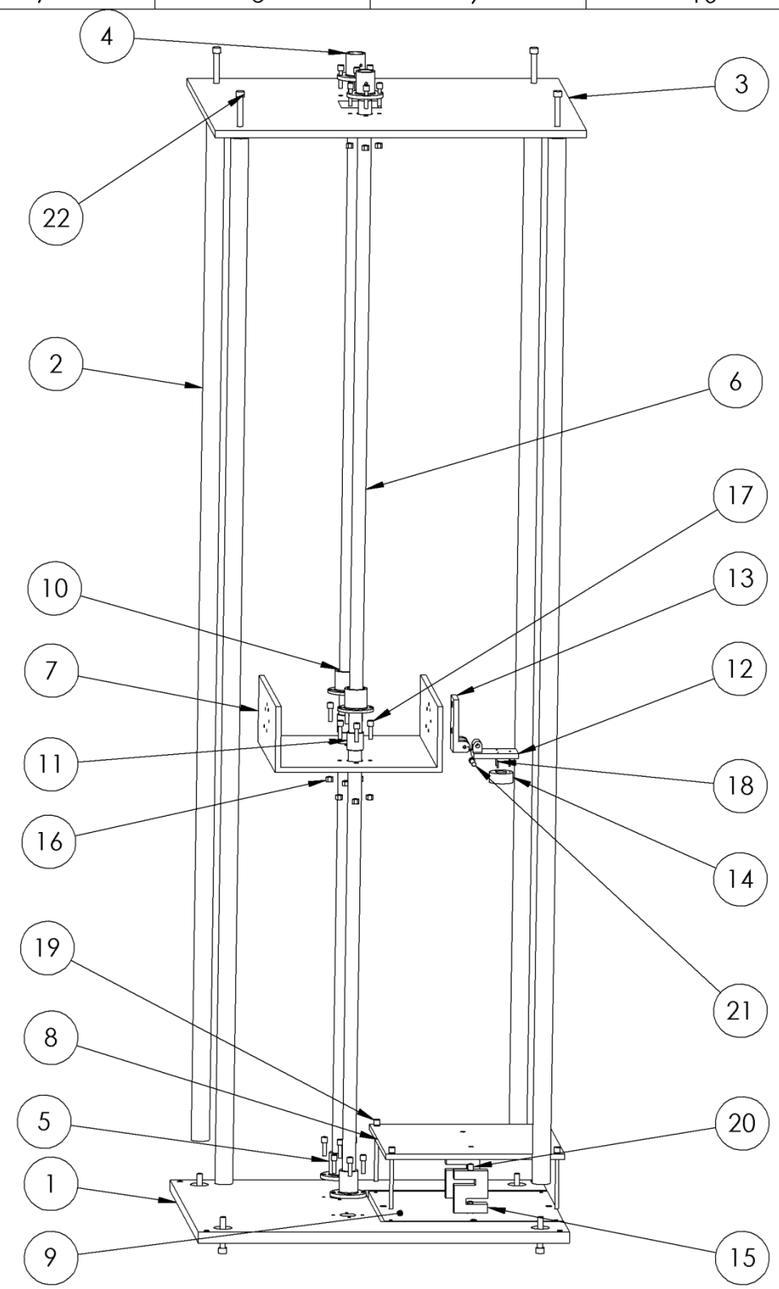

UNIVERSITY OF CANTERBURY
Te Whare Wānanga o Waitaha
CHRISTCHURCH NEW ZEALAND

ACOUSTICS RESEARCH GROUP
DEPT OF MECHANICAL ENGINEERING
COLLEGE OF ENGINEERING
PRIVATE BAG 4800
CHRISTCHURCH 8140
NEW ZEALAND
Ph: +64 3 3642987
Fax: +64 3 364 2078

JOB No.

CONTRACT No.

AUTHORIZED BY

DATE

THIRD ANGLE PROJECTION
DO NOT SCALE FROM THIS DRAWING
IF IN DOUBT - ASK
DIMENSIONS ARE IN MILLIMETRES
DIMENSIONS ARE OF FINISHED PART
DO NOT PASS THIS DRAWING TO ANY THIRD PARTY WITHOUT AUTHORIZATION
DEBUR AND BREAK SHARP CORNERS

COMPONENT OR ASSEMBLY IS NOT TO BE MANUFACTURED UNLESS PROPERLY AUTHORIZED

Drawn By E BARCLAY
Date Drawn feb2013
Checked By
Date Checked

Tolerances
0 ±0.25 Unless
0.0 ±0.13 otherwise
0.00 ±0.05 specified

Project:
Product:
Materials:
Finish:
Heat Treatment:
Material Stock

Part
Dwg No. 000
Part No.
SHEET 1 OF 1 A3
OEM No.

MODEL:G:\Masters 2.0\2 Experimental Testing\Test Rig Developement\CAD Files\Finished Design w Drawings\Assembly Drawing

DRAWING: G:\Masters 2.0\2 Experimental Testing\Test Rig Developement\CAD Files\Finished Design w Drawings\Base Mounting Plate

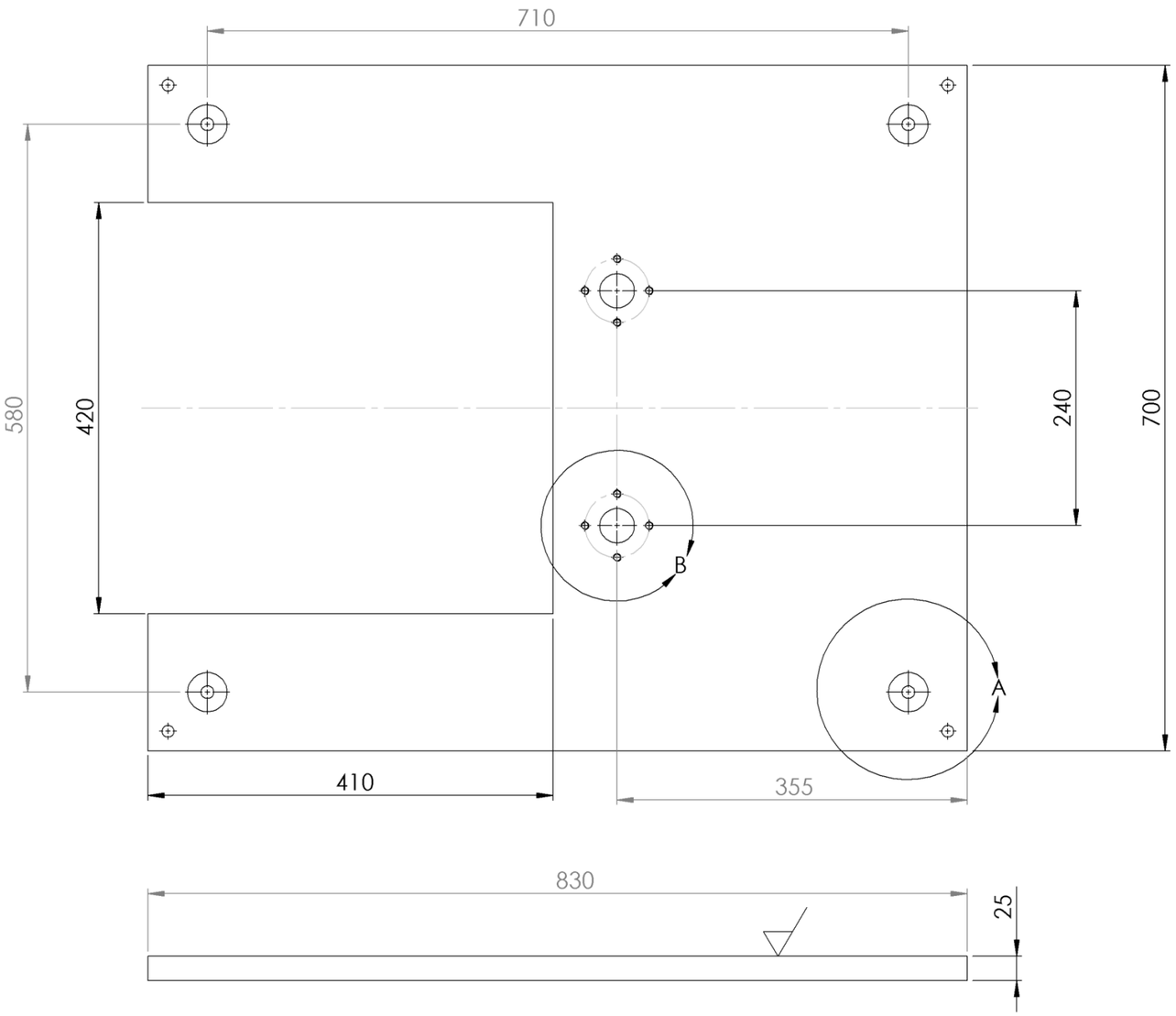

TYP FOR TWO LOCATIONS

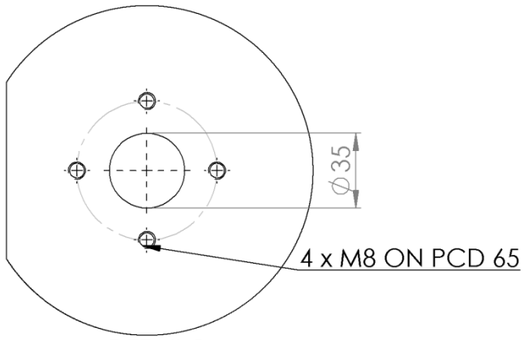

DETAIL B
SCALE 2 : 5

TYP FOR EACH CORNER

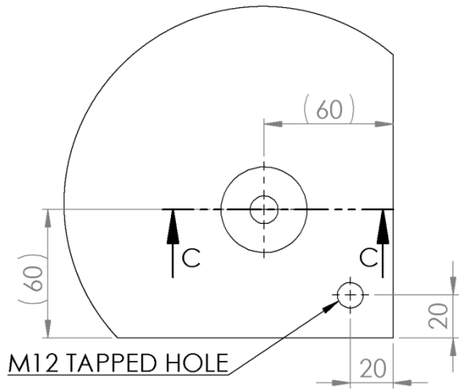

DETAIL A
SCALE 2 : 5

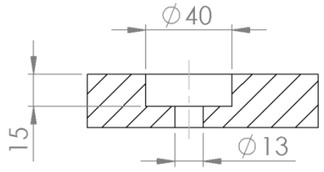

SECTION C-C

BASE MOUNTING PLATE

NOTE: IT IS SUGGESTED THAT THE HOLES FOR THIS PLATE ARE DRILLED AT THE SAME TIME AS THE TOP MOUNTING PLATE (002) FOR BETTER ALLIGNMENT

UNIVERSITY OF CANTERBURY
Te Whare Wānanga o Waitaha
CHRISTCHURCH NEW ZEALAND

ACOUSTICS RESEARCH GROUP
DEPT OF MECHANICAL ENGINEERING
COLLEGE OF ENGINEERING
PRIVATE BAG 4800
CHRISTCHURCH 8140
NEW ZEALAND
Ph: +64 3 3642987
Fax: +64 3 364 2078

JOB No.

CONTRACT No.

AUTHORIZED BY

DATE

THIRD ANGLE PROJECTION
DO NOT SCALE FROM THIS DRAWING
IF IN DOUBT - ASK
DIMENSIONS ARE IN MILLIMETRES
DIMENSIONS ARE OF FINISHED PART
DO NOT PASS THIS DRAWING TO ANY THIRD PARTY WITHOUT AUTHORIZATION
DEBUR AND BREAK SHARP CORNERS

COMPONENT OR ASSEMBLY IS NOT TO BE MANUFACTURED UNLESS PROPERLY AUTHORIZED

Drawn By E. BARCLAY
Date Drawn FEB 2013
Checked By
Date Checked

Tolerances
0 ±0.25 Unless
0.0 ±0.13 otherwise
0.00 ±0.05 specified

Project: DROP TOWER
Product:
Materials: STEEL
Finish:
Heat Treatment:
Material Stock

Part BASE MOUNTING PLATE
Dwg No. 001
Part No.
SHEET 1 OF 1 A3
OEM No.

MODEL:G:\Masters 2.0\2 Experimental Testing\Test Rig Developement\CAD Files\Finished Design w Drawings\Base Mounting Plate

DRAWING: G:\Masters 2.0\2 Experimental Testing\Test Rig Developement\CAD Files\Finished Design w Drawings\Top Mounting Plate

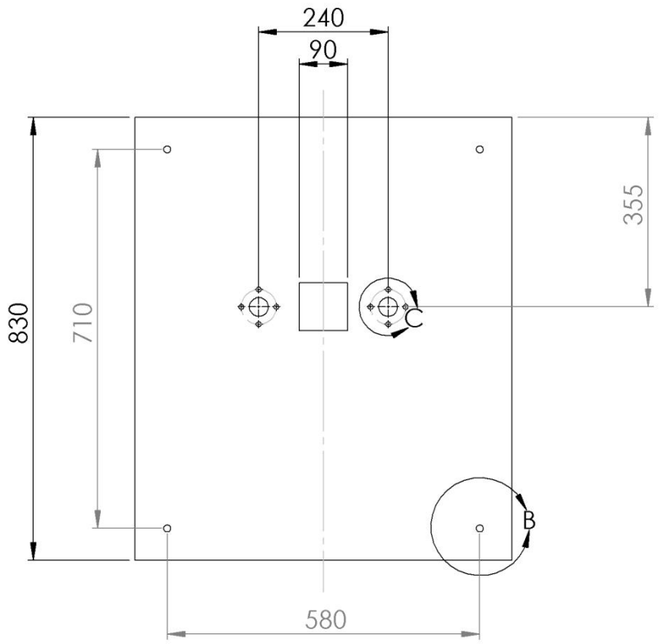

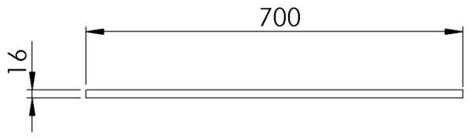

TYP FOR EACH CORNER

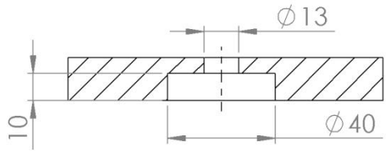

SECTION G-G

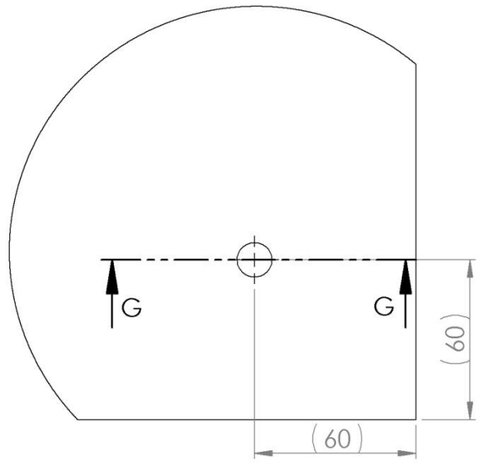

DETAIL B

TYP AT TWO LOCATIONS

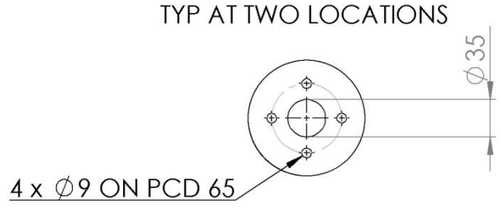

DETAIL C

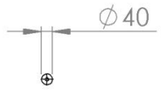

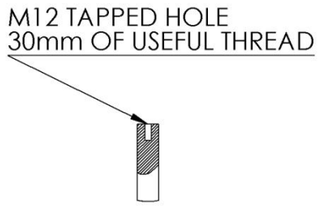

DETAIL H

TOP MOUNTING PLATE

NOTE: IT IS SUGGESTED THAT THE HOLES ARE DRILLED AT THE SAME TIME AS THE BASE MOUNTING PLATE (001) TO GET THE BEST ALLIGNMENT POSSIBLE

SUPPORT COLUMNS

QUANTITY: 4

UNIVERSITY OF CANTERBURY
Te Whare Wānanga o Waitaha
CHRISTCHURCH NEW ZEALAND

ACOUSTICS RESEARCH GROUP
DEPT OF MECHANICAL ENGINEERING
COLLEGE OF ENGINEERING
PRIVATE BAG 4800
CHRISTCHURCH 8140
NEW ZEALAND
Ph: +64 3 3642987
Fax: +64 3 364 2078

JOB No.

CONTRACT No.

AUTHORIZED BY

DATE

THIRD ANGLE PROJECTION
DO NOT SCALE FROM THIS DRAWING
IF IN DOUBT - ASK
DIMENSIONS ARE IN MILLIMETRES
DIMENSIONS ARE OF FINISHED PART
DO NOT PASS THIS DRAWING TO ANY THIRD PARTY WITHOUT AUTHORIZATION
DEBUR AND BREAK SHARP CORNERS

COMPONENT OR ASSEMBLY IS NOT TO BE MANUFACTURED UNLESS PROPERLY AUTHORIZED

Drawn By E. BARCLAY
Date Drawn FEB 2013
Checked By
Date Checked

Tolerances
0 ±0.25
0.0 ±0.13
0.00 ±0.05
Unless otherwise specified

Project: DROP TOWER
Product:
Materials: STEEL
Finish:
Heat Treatment:
Material Stock

Part TOP MOUNTING PLATE SUPPORT COLUMNS
Dwg No. 002
Part No.
SHEET 1 OF 1 A3
OEM No.

MODEL:G:\Masters 2.0\2 Experimental Testing\Test Rig Developement\CAD Files\Finished Design w Drawings\Top Mounting Plate

DRAWING: G:\Masters 2.0\2 Experimental Testing\Test Rig Developement\CAD Files\Finished Design w Drawings\Top Guide Rail Mount

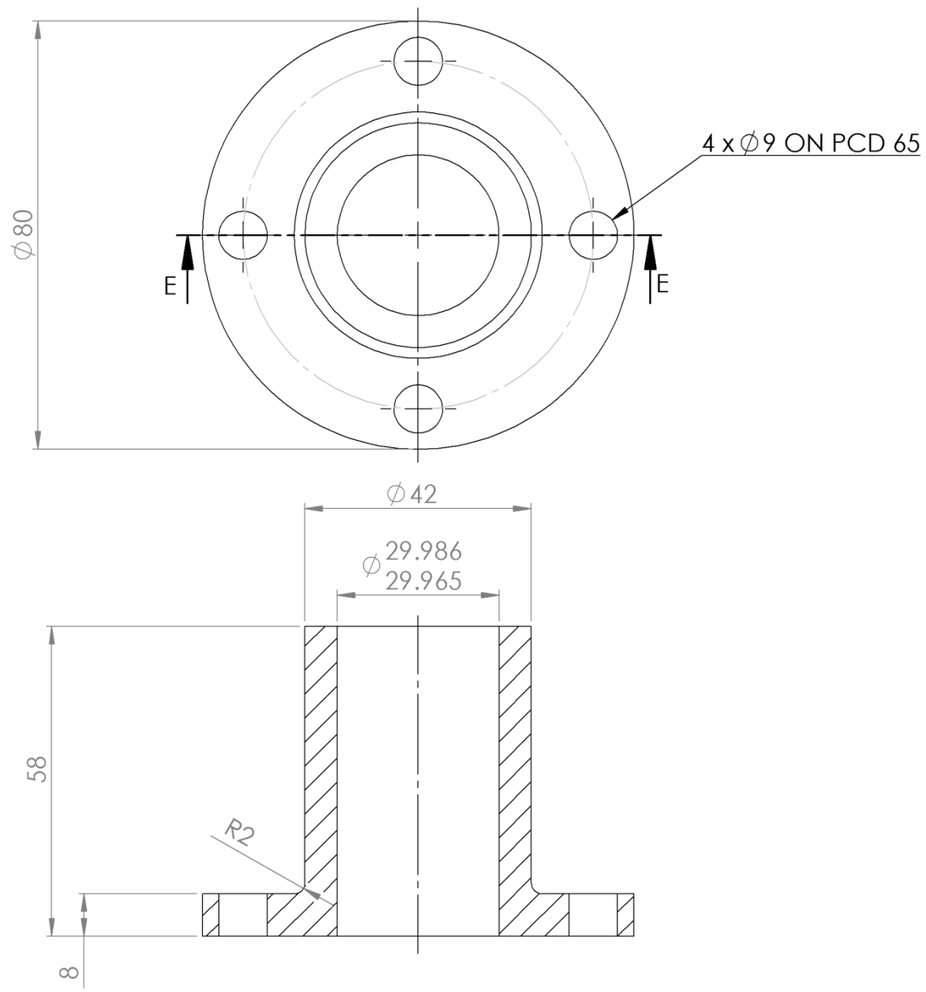

SECTION E:E

BASE GUIDE RAIL MOUNT **QUANTITY 2**

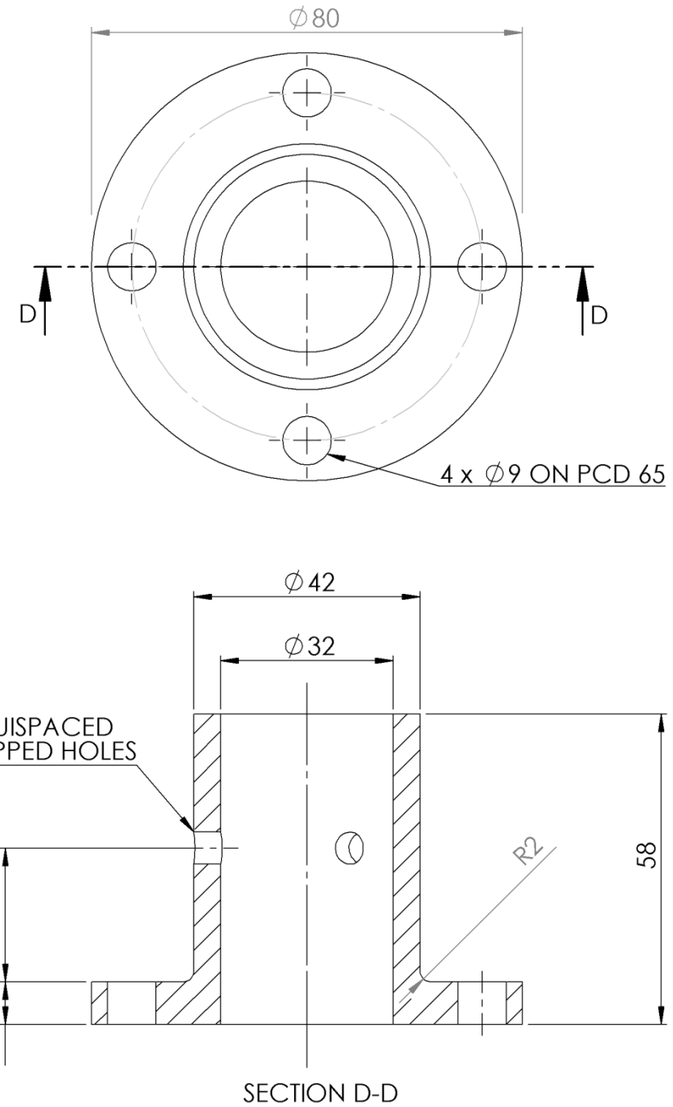

SECTION D-D

TOP GUIDE RAIL MOUNT **QUANTITY 2**

UNIVERSITY OF CANTERBURY
Te Whare Wānanga o Waitaha
CHRISTCHURCH NEW ZEALAND

ACOUSTICS RESEARCH GROUP
DEPT OF MECHANICAL ENGINEERING
COLLEGE OF ENGINEERING
PRIVATE BAG 4800
CHRISTCHURCH 8140
NEW ZEALAND
Ph: +64 3 3642987
Fax: +64 3 364 2078

JOB No.

CONTRACT No.

AUTHORIZED BY

DATE

THIRD ANGLE PROJECTION
DO NOT SCALE FROM THIS DRAWING
IF IN DOUBT - ASK
DIMENSIONS ARE IN MILLIMETRES
DIMENSIONS ARE OF FINISHED PART
DO NOT PASS THIS DRAWING TO ANY THIRD PARTY WITHOUT AUTHORIZATION
DEBUR AND BREAK SHARP CORNERS

COMPONENT OR ASSEMBLY IS NOT TO BE MANUFACTURED UNLESS PROPERLY AUTHORIZED

Drawn By E. BARCLAY
Date Drawn FEB 2012
Checked By
Date Checked

Tolerances
0 ±0.25
0.0 ±0.13
0.00 ±0.05
Unless otherwise specified

Project: DROP TOWER
Product:
Materials: STEEL
Finish:
Heat Treatment:
Material Stock

Part BASE GUIDE RAIL MOUNT
TOP GUIDE RAIL MOUNT
Dwg No. 003
Part No.
SHEET 1 OF 1 A3
OEM No.

MODEL:G:\Masters 2.0\2 Experimental Testing\Test Rig Developement\CAD Files\Finished Design w Drawings\Top Guide Rail Mount

DRAWING: G:\Masters 2.0\2 Experimental Testing\Test Rig Developement\CAD Files\Finished Design w Drawings\Drop Plate

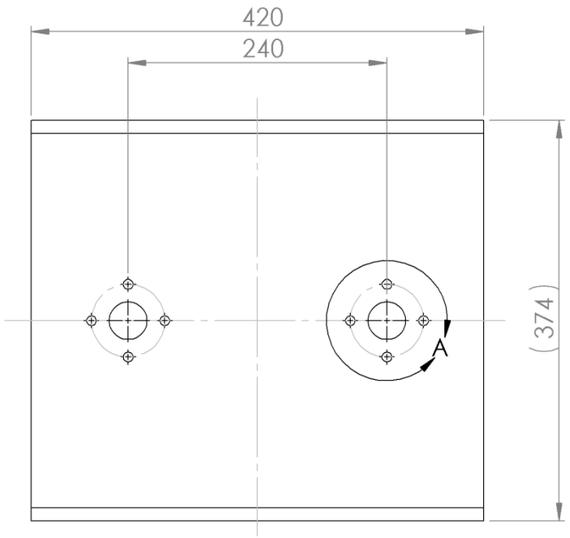

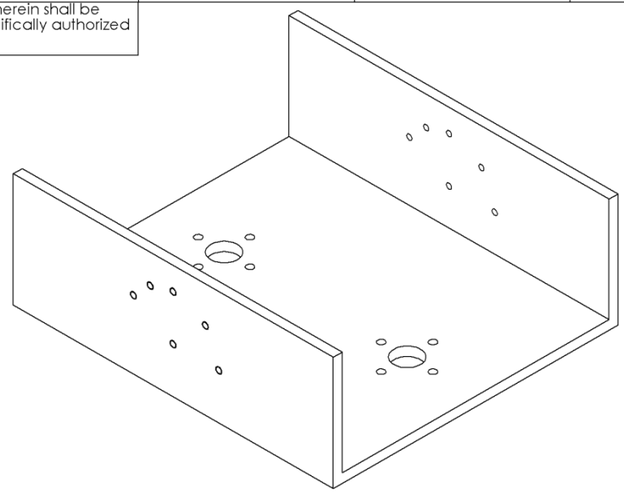

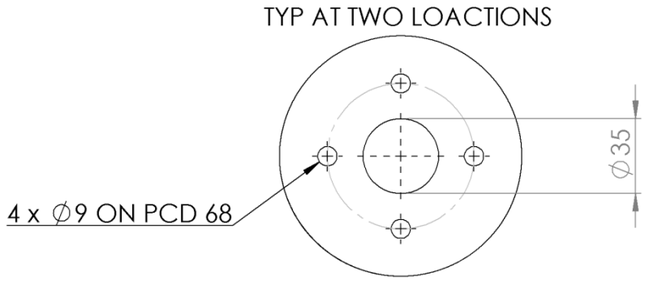

DETAIL A

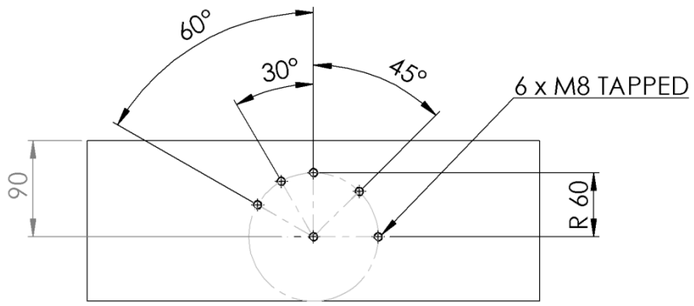

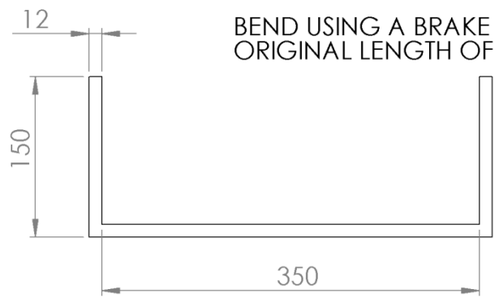

BEND USING A BRAKE PRESS
ORIGINAL LENGTH OF PLATE 675mm

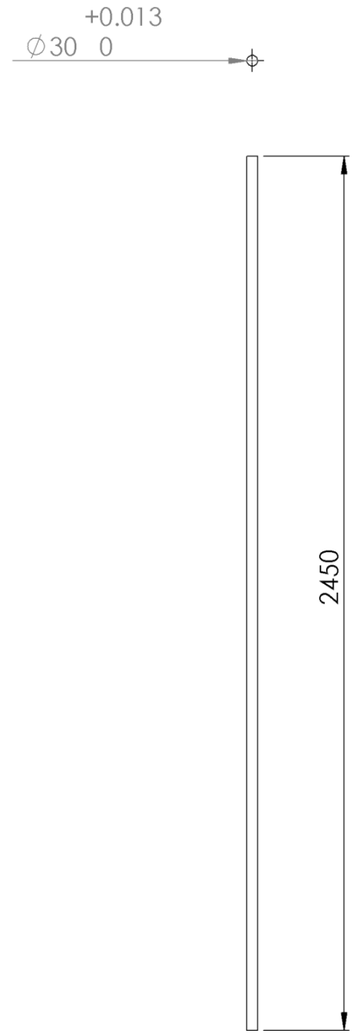

DROP PLATE

12 mm STEEL PLATE

HYDRAULIC RAM

GUIDE RAIL

QUANTITY 2

UNIVERSITY OF CANTERBURY
Te Whare Wānanga o Waitaha
CHRISTCHURCH NEW ZEALAND

ACOUSTICS RESEARCH GROUP
DEPT OF MECHANICAL ENGINEERING
COLLEGE OF ENGINEERING
PRIVATE BAG 4800
CHRISTCHURCH 8140
NEW ZEALAND
Ph: +64 3 3642987
Fax: +64 3 364 2078

JOB No.

CONTRACT No.

AUTHORIZED BY

DATE

THIRD ANGLE PROJECTION
DO NOT SCALE FROM THIS DRAWING
IF IN DOUBT - ASK
DIMENSIONS ARE IN MILLIMETRES
DIMENSIONS ARE OF FINISHED PART
DO NOT PASS THIS DRAWING TO ANY THIRD PARTY WITHOUT AUTHORIZATION
DEBUR AND BREAK SHARP CORNERS

COMPONENT OR ASSEMBLY IS NOT TO BE MANUFACTURED UNLESS PROPERLY AUTHORIZED

Drawn By E. BARCLAY
Date Drawn FEB 2013
Checked By
Date Checked

Tolerances
0 ±0.25 Unless
0.0 ±0.13 otherwise
0.00 ±0.05 specified

Project: DROP TOWER
Product:
Materials: STEEL
Finish:
Heat Treatment:
Material Stock

Part DROP PLATE GUIDE RAIL
Dwg No. 004
Part No.
SHEET 1 OF 1 A3
OEM No.

MODEL:G:\Masters 2.0\2 Experimental Testing\Test Rig Developement\CAD Files\Finished Design w Drawings\Drop Plate

DRAWING: G:\Masters 2.0\2 Experimental Testing\Test Rig Developement\CAD Files\Finished Design w Drawings\Bushing Housing

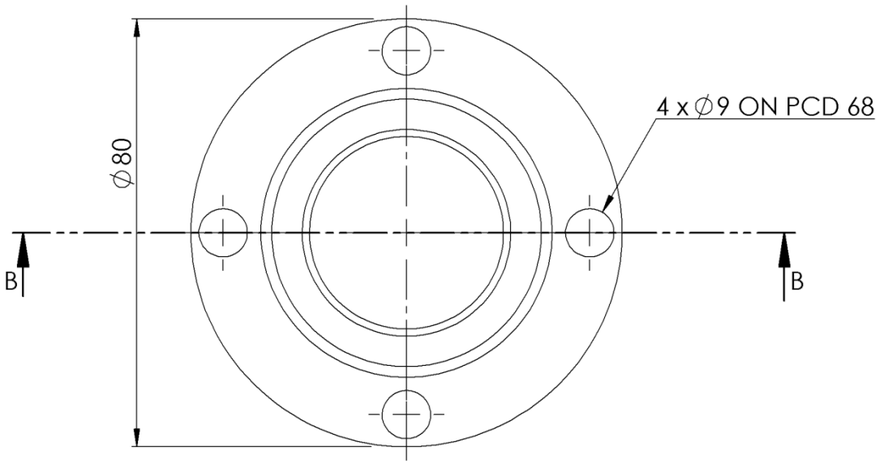

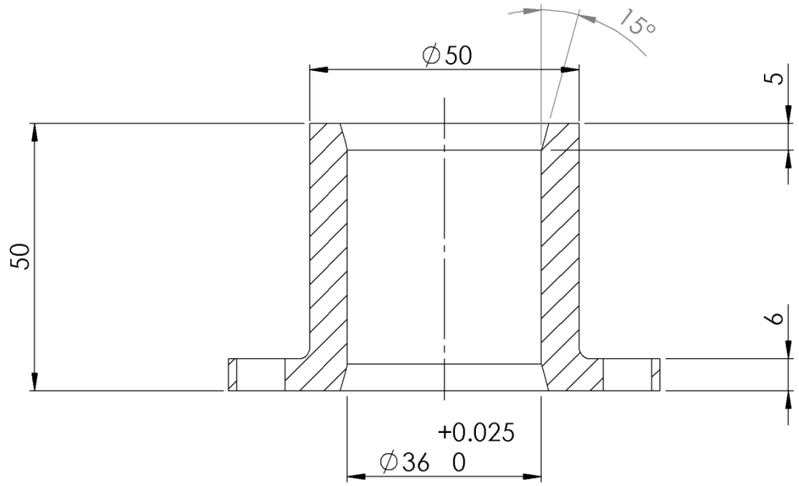

SECTION B-B

BUSHING HOUSING **QUANTITY 2**

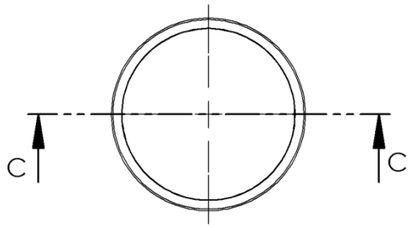

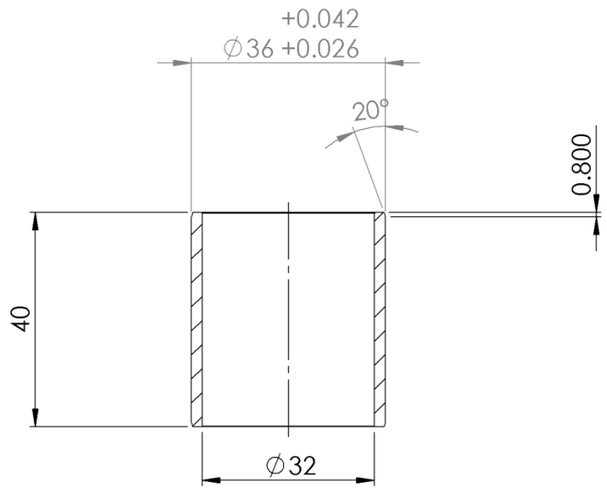

SECTION C-C

SKF BUSHING **QUANTITY 2**

UNIVERSITY OF CANTERBURY
Te Whare Wānanga o Waitaha
CHRISTCHURCH NEW ZEALAND

ACOUSTICS RESEARCH GROUP
DEPT OF MECHANICAL ENGINEERING
COLLEGE OF ENGINEERING
PRIVATE BAG 4800
CHRISTCHURCH 8140
NEW ZEALAND
Ph: +64 3 3642987
Fax: +64 3 364 2078

JOB No.

CONTRACT No.

AUTHORIZED BY

DATE

THIRD ANGLE PROJECTION
DO NOT SCALE FROM THIS DRAWING
IF IN DOUBT - ASK
DIMENSIONS ARE IN MILLIMETRES
DIMENSIONS ARE OF FINISHED PART
DO NOT PASS THIS DRAWING TO ANY THIRD PARTY WITHOUT AUTHORIZATION
DEBUR AND BREAK SHARP CORNERS

COMPONENT OR ASSEMBLY IS NOT TO BE MANUFACTURED UNLESS PROPERLY AUTHORIZED

Drawn By E. BARCLAY
Date Drawn FEB 2013
Checked By
Date Checked

Tolerances
0 ±0.25 Unless
0.0 ±0.13 otherwise
0.00 ±0.05 specified

Project: DROP TOWER
Product:
Materials: STEEL
Finish:
Heat Treatment:
Material Stock

Part BUSHING HOUSING
SKF BUSHING
Dwg No. 006
Part No.
SHEET 1 OF 1 A3
OEM No.

MODEL:G:\Masters 2.0\2 Experimental Testing\Test Rig Developement\CAD Files\Finished Design w Drawings\Bushing Housing

DRAWING: G:\Masters 2.0\2 Experimental Testing\Test Rig Developement\CAD Files\Finished Design w Drawings\Base Impact Plate

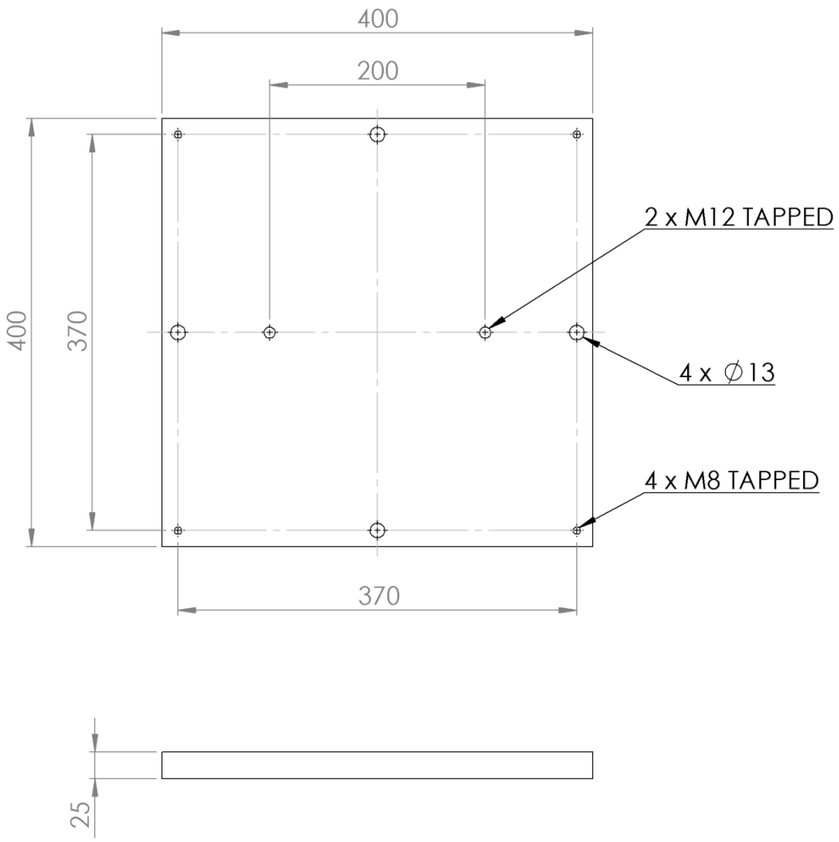

BASE IMPACT PLATE

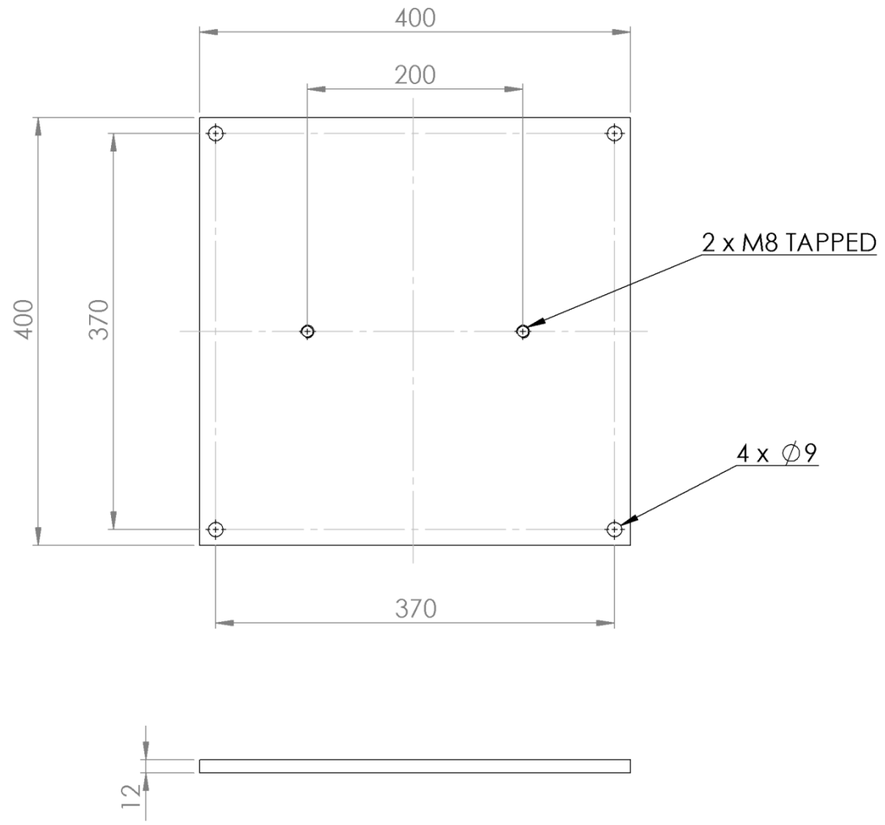

TOP IMPACT PLATE

SUGGESTED TO BE DRILLED TOGETHER TO GET GOOD ALLIGNMENT

UNIVERSITY OF CANTERBURY
Te Whare Wānanga o Waitaha
CHRISTCHURCH NEW ZEALAND

ACOUSTICS RESEARCH GROUP
DEPT OF MECHANICAL ENGINEERING
COLLEGE OF ENGINEERING
PRIVATE BAG 4800
CHRISTCHURCH 8140
NEW ZEALAND
Ph: +64 3 3642987
Fax: +64 3 364 2078

JOB No.

CONTRACT No.

AUTHORIZED BY

DATE

THIRD ANGLE PROJECTION
DO NOT SCALE FROM THIS DRAWING
IF IN DOUBT - ASK
DIMENSIONS ARE IN MILLIMETRES
DIMENSIONS ARE OF FINISHED PART
DO NOT PASS THIS DRAWING TO ANY THIRD PARTY WITHOUT AUTHORIZATION
DEBUR AND BREAK SHARP CORNERS

COMPONENT OR ASSEMBLY IS NOT TO BE MANUFACTURED UNLESS PROPERLY AUTHORIZED

Drawn By E BARCLAY
Date Drawn FEB 2013
Checked By
Date Checked

Tolerances
0 ±0.25
0.0 ±0.13
0.00 ±0.05
Unless otherwise specified

Project: DROP TOWER
Product:
Materials: STEEL
Finish:
Heat Treatment:
Material Stock

Part BASE IMPACT PLATE
TOP IMPACT PLATE
Dwg No. 005
Part No.
SHEET 1 OF 1 A3
OEM No.

MODEL:G:\Masters 2.0\2 Experimental Testing\Test Rig Developement\CAD Files\Finished Design w Drawings\Base Impact Plate

B Detailed Radio Finite Element Setup

This appendix describes the adaption and setup of Tait's handheld radio for use in drop-impact simulation. Explanation of how and why the geometry of the Tait handheld radio is modified are outlined. The materials and contact conditions are also presented and discussed.

B.1. Introduction

The level of detail present in the CAD geometry of Tait's handheld radio (Figure B.1) makes it impractical, in its current state, for use in finite element analysis. This appendix steps through the simplification of the radio as well as the setup of the initial finite element model, with explanation where necessary.

Figure B.1 - Tait handheld radio assembly before simplification

Before the Tait handheld radio was simulated, a simplified radio model (Figure B.2) was developed (Chapter 4). The investigation of the simplified radio provided valuable understanding about creating a dynamic finite element model as well as insight into the critical parameters required to generate an accurate model (and what can be excluded). Some of the key findings from the simplified radio simulation were:

- Mesh quality is very important for gathering reliable results (uniform, smooth transitions and appropriately sized)
- The smallest element defines the timestep and therefore the simulation solving time
- Material models and their associated parameters have a significant effect on the radio behaviour
- Contact behaviour between bodies must be representative of the physical product

Figure B.2 - Tait TP9400 handheld radio next to simplified handheld radio

B.2. Detailed Radio Assembly

The Tait radio (Figure B.1) is made of 5 subassemblies (Figure B.3): the front panel, chassis, MMI board, RF board and battery. Connections between parts are made via screws, solder (electrical components), clips (battery) and adhesives.

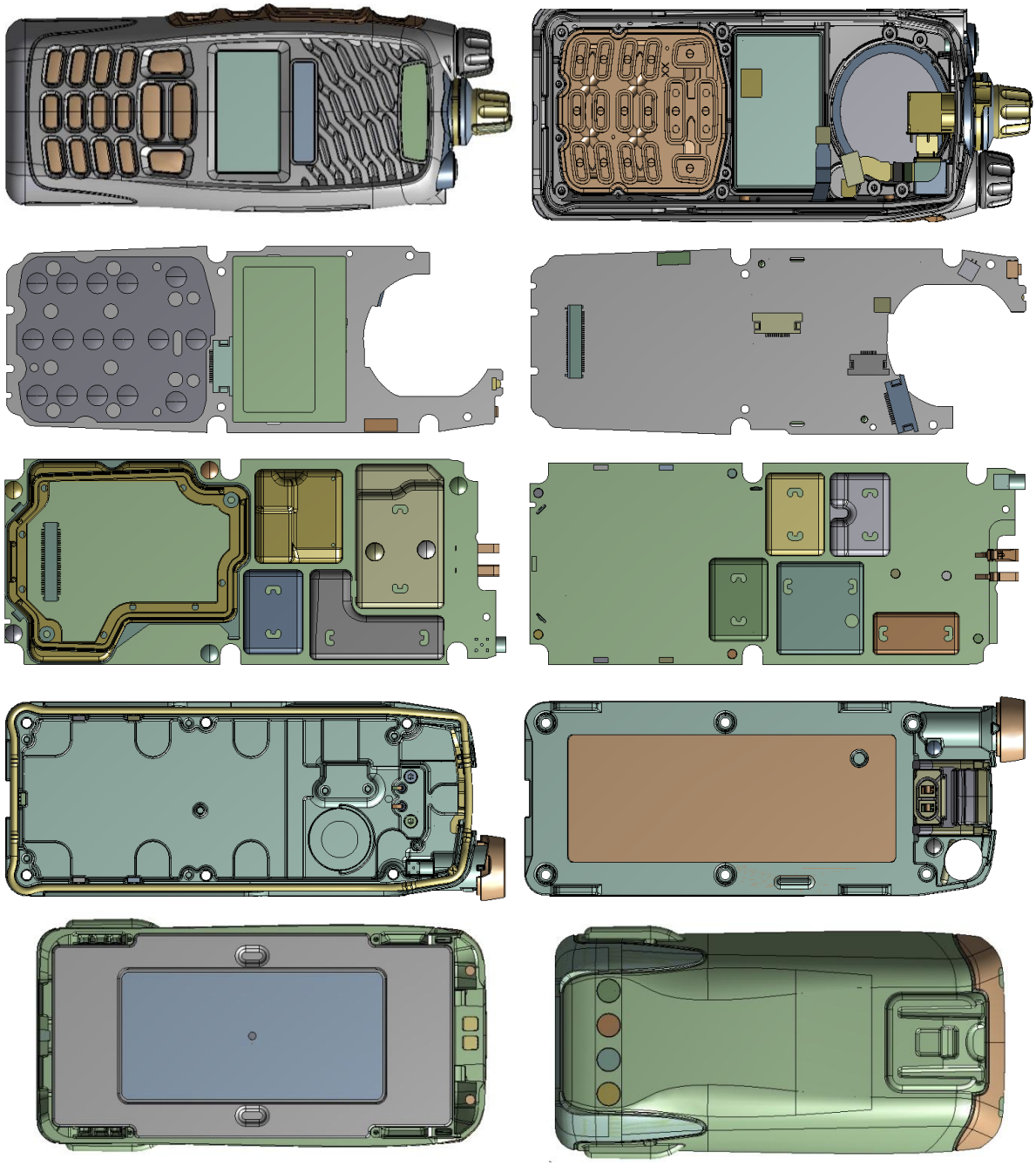

Figure B.3 - Subassemblies of Tait handheld radio, from top to bottom, front panel, MMI board, RF board, chassis, battery

B.3. Simplification of Geometry

The majority of parts present in the model require some level of modification to make for a more efficient simulation. The bulk of simplifications performed involve removing small features which have minor effects on the radio during impact, i.e. manufacturing stamps and filet radii. Some of the smaller parts have been removed altogether due to their assumed negligible effect on the global radio behaviour. All model simplifications are described in detail below.

B.3.1. Front panel subassembly

The front panel assembly (Figure B.4) is the largest and most complex subassembly of the handheld radio. The front panel assembly has the overall dimensions of 137 mm x 57 mm x 25 mm. The front panel assembly includes the front panel body, keypad, lens, push to talk buttons (side), emergency button (top), volume and channel knobs (top), various labels and stickers.

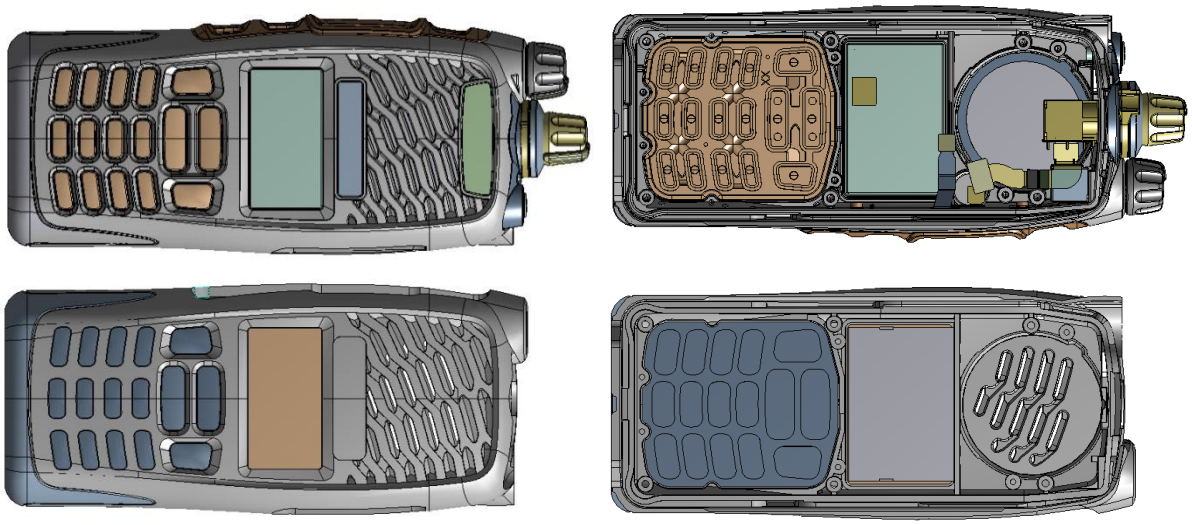

Figure B.4 - Front panel assembly before (top) and after (bottom) simplification

B.3.1.1. Front panel body

The main simplification steps involved removing small surface details on the front panel including filets, stamps and small recesses. The front panel (Figure B.5) is injection molded; in this case a two shot injection moulding process is used to make the part. The first injection of material is a hard Makroblend® plastic which makes up the majority of the part, the second injection was the softer Desmopan® 5377A which is overmolded at the base of the part (shown as blue in Figure B.5). The Desmopan® provides additional impact absorption so is an important inclusion in the finite element model. The CAD geometry was modelled as a single part so it became necessary to split into two separate bodies so that different material properties could be applied (Makroblend® and Desmopan®). A comparison between the front panel before and after the simplification is shown in Figure B.5.

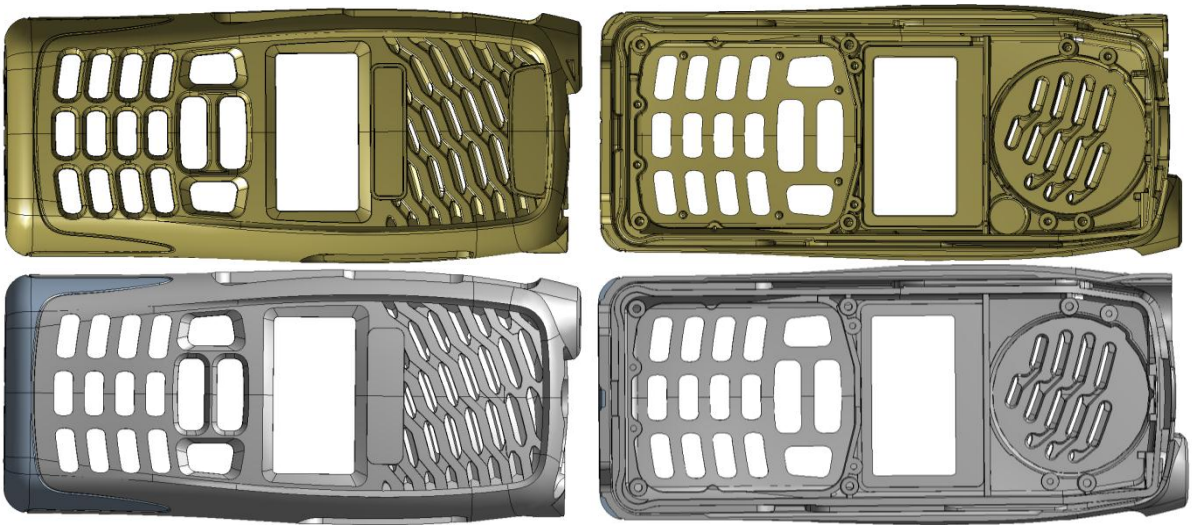

Figure B.5 - Front panel before (top) and after (bottom) simplification, the two different colours in the simplified part indicate two separate bodies

B.3.1.2. Keypad

The keypad (Figure B.6) was included in the finite element model as it absorbs energy during any front panel impact events. All fine details of the keypad were removed, predominantly on the rear face of the keypad which was modelled as a flat surface (Figure B.6).

Figure B.6 - Keypad before (left) and after (right) simplification

B.3.1.3. Accessory connection region

One side of the radio has a port where radio accessories attach (Figure B.7). There are a wide range of accessories that attach to the handheld radio. The large number of accessories makes it unreasonable to include each design in testing/simulation. The decision to remove accessories from the analysis was justified as the worst case side impact would likely occur when no accessory is attached as the accessory provides additional padding and rigidity to the assembly. With no accessory attached it means that there was a recess present on the front panel (Figure B.8). The cavity was simplified by removing of the screw boss, label recess and accessory connecting label (Figure B.8).

Figure B.7 - Tait radio assembly with (left) and without (right) accessory attached

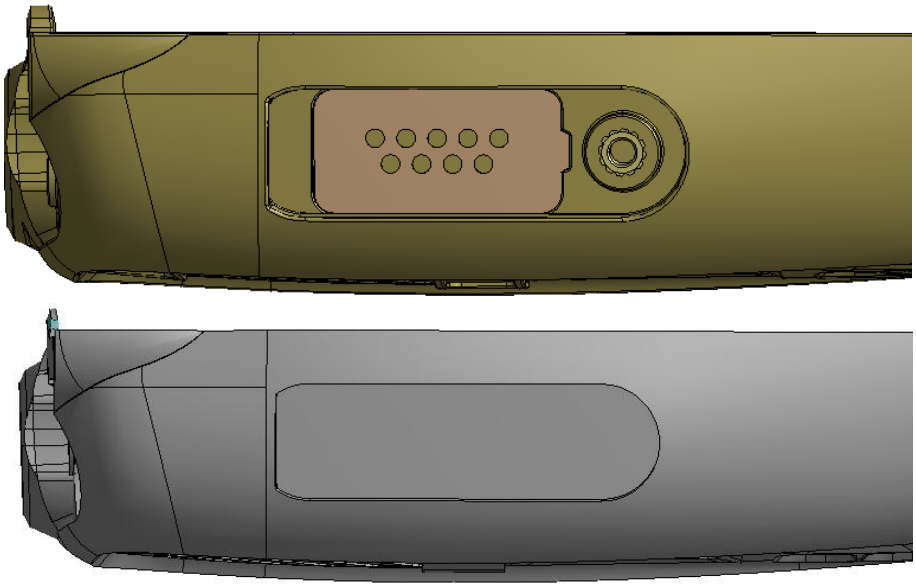

Figure B.8 - Accessory detail on front panel before (top) and after (bottom) simplification

B.3.1.4. PTT assembly

Buttons on the side of the radio (push to talk button and function buttons) form a reasonably complex subassembly (Figure B.9). For this project the main interest is in completing a model that represents the most severe loading upon the two circuit boards. This would likely occur during impact with the front and back faces, meaning that impact onto the side of the radio is not as important. The buttons and holding plate are removed to reduce complexity of the assembly, leaving

only a cavity in its place (Figure B.10). The cavity was simplified further by removal of its smaller features (Figure B.11).

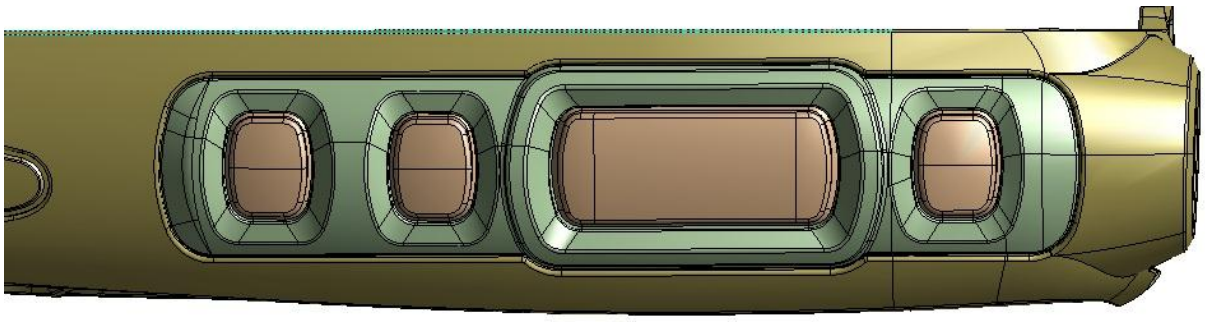

Figure B.9 - PPT region before any modification

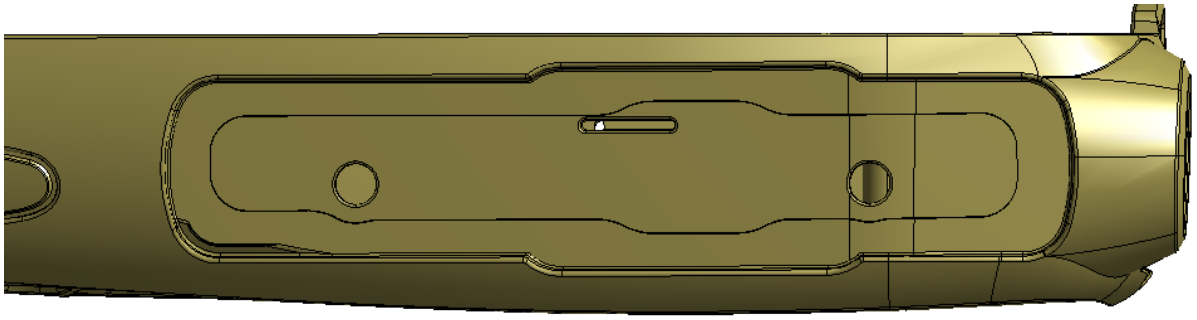

Figure B.10 - Front panel detail when PPT plate and keys disassembled

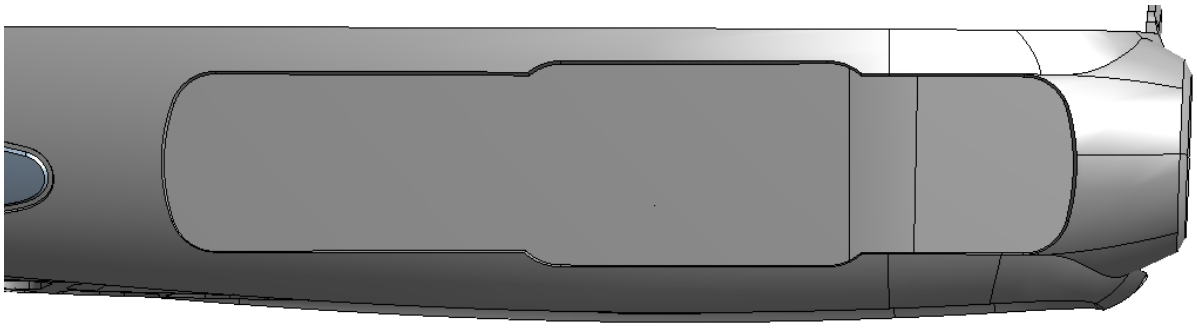

Figure B.11 - Front panel with simplified cavity

B.3.1.5. Lens

The lens was modified by removing the small filet radii (Figure B.12). The gap between the lens and front panel, present so that sealant could be inserted, was filled to ensure a face to face contact between the front panel and lens could be created (Figure B.13).

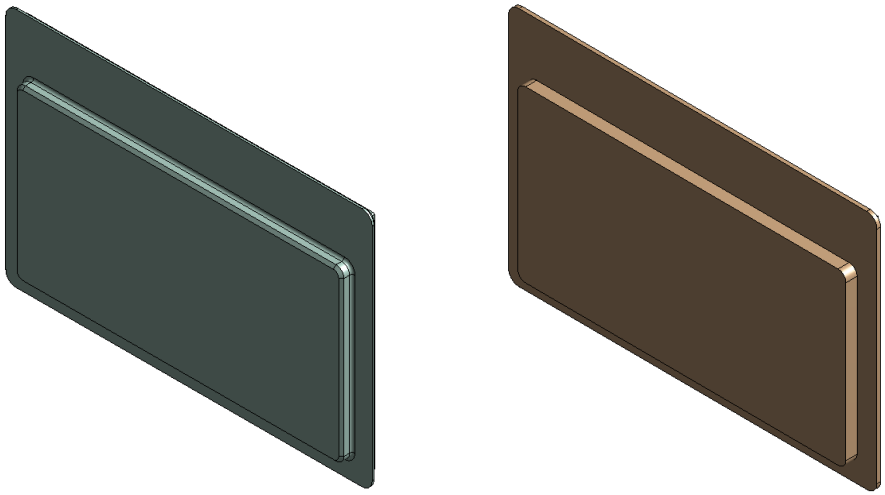

Figure B.12 - Front panel lens before (left) and after (right) simplification

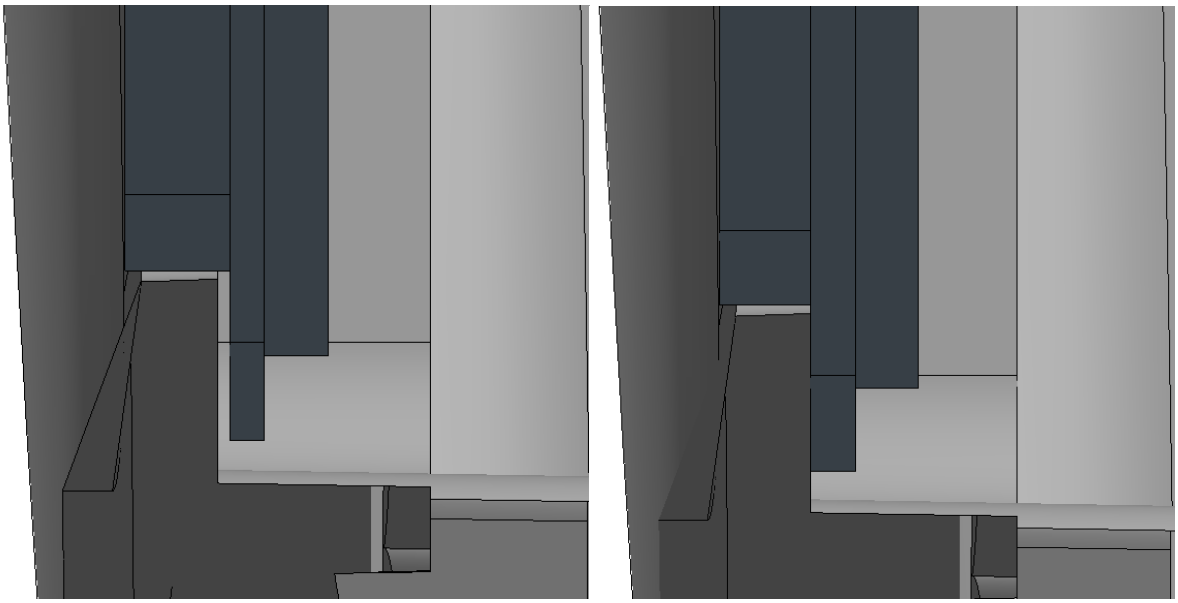

Figure B.13 - Sectioned view of lens (blue) interaction with front panel (grey) before (left) and after (right) gap has been closed to allow for a face to face contact condition. NB: the front face of the front panel and lens are on the far left side of each image

B.3.2. MMI PCB subassembly

Correctly simulating the behaviour of the circuit boards is critical as electrical failures are one of the most common issues resulting from an impact event. The small size of the board mounted components (Figure B.14) means it becomes unrealistic to include their detail in a system level impact simulation, because of the increased solver time. The removal of these components means that stress/strain acting on the solder ball connections cannot be studied, however the overall board

behaviour can still be observed which will indicate regions where component failure is possible (generally areas of high deformation/curvature).

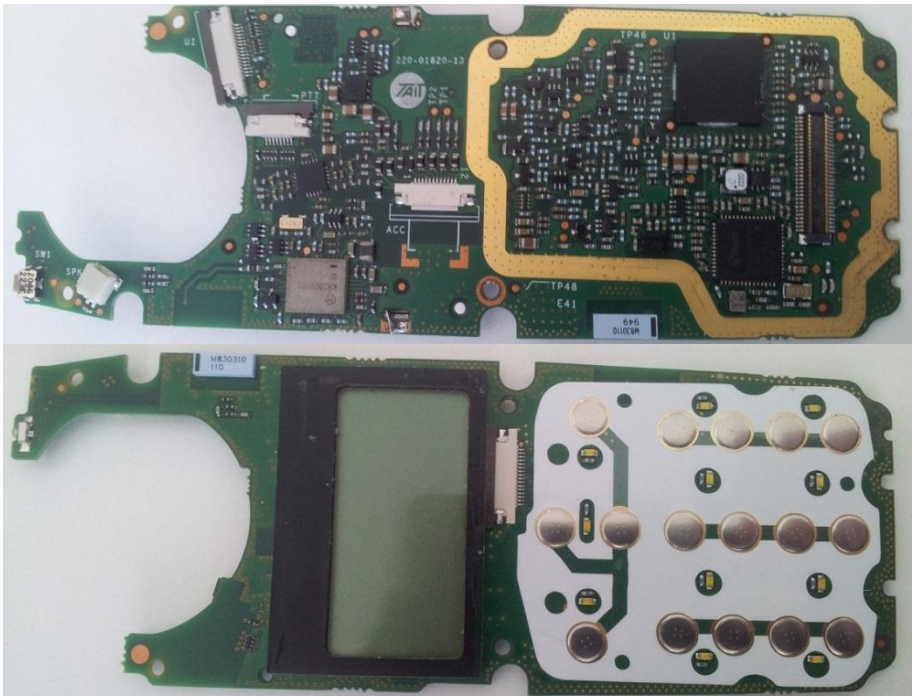

Figure B.14 - Physical MMI board showing small electrical components

The MMI PCB (Figure B.15) is located at the front of the radio. The front face of the board holds some of the key components for the radio user interface including the liquid crystal display (LCD) and the electrical buttons for the radio keypad. The MMI board is 120 mm x 45 mm x 1.21 mm (5.5 mm including the LCD). The board is constructed of layers of glass fibre reinforced (FR-4) and copper and uses surface mounting technology for placing the components on the board. The board assembly is attached to the front panel with 6 screws.

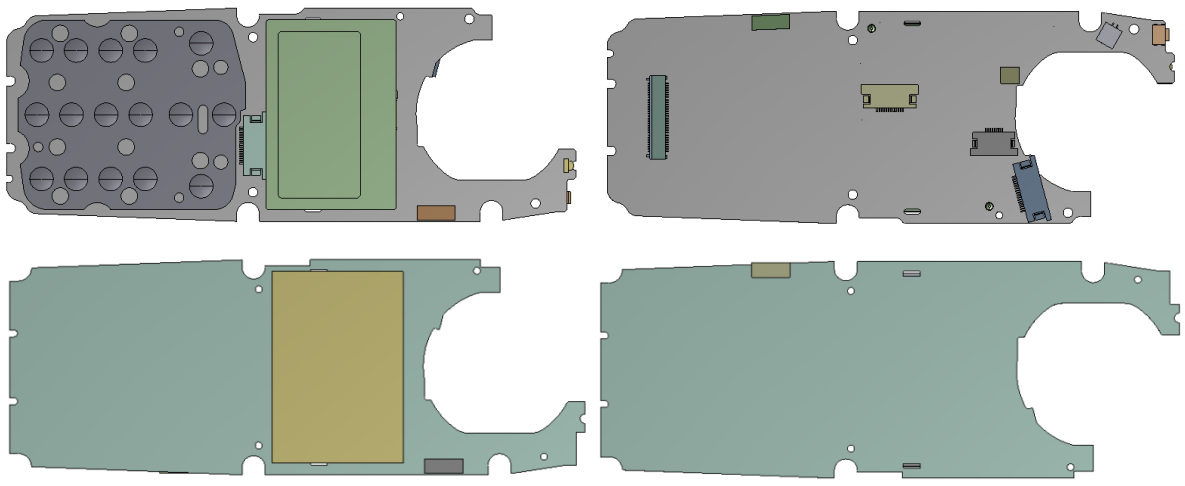

Figure B.15 - MMI board assembly before (top) and after (bottom) simplification

B.3.2.1. Small electrical components

All small electrical components (Figure B.14) were removed from the board (resistors/capacitors etc.). Large electrical components such as the processors and interface ports are also removed, these components do provide a certain level of rigidity to the board but due to their complex mounting structures (BGA's) they become difficult to include in that level of detail that would make their inclusion worthwhile.

B.3.2.2. Ceramic antenna

Two ceramic antennas (pale blue rectangular components shown in Figure B.16) have been included in the model as they are relatively large (8 mm x 3 mm x 1.3 mm) and have a simple geometry. The inclusion of these two parts into the model was to provide insight into the stresses experienced by smaller components during impact and a better understanding on how such components influence the behaviour of the board. The ceramic antennas are mounted onto the board by 6 solder pads which cover the majority of the mounting facing so a face to face bonding condition over the whole bottom face can be applied.

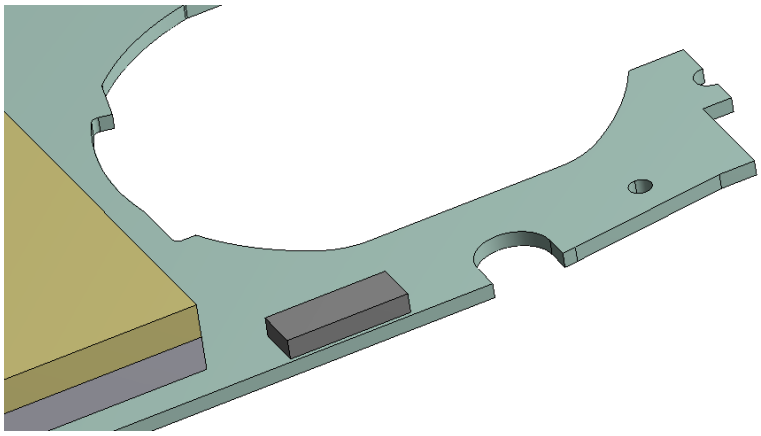

Figure B.16 - One of the two ceramic antennas included in the simplified radio

B.3.2.3. Liquid crystal display

The LCD is the largest component mounted to the MMI board and provides a large amount of mass and stiffness to the board. The size and simple dimensions of the LCD means its inclusion of this part should not have a significant effect on the solving time of the model. Internally, the LCD has a very complex construction, if this detail was included into the model it would lead to a high solver time. In place of a complex part it was assumed that the LCD was constructed of 50% polycarbonate and 50% glass (Figure B.17). The issue of simplifying the LCD means it may be difficult to apply material models/behaviours to the polycarbonate and glass that would accurately recreate the behaviour of the LCD assembly.

The LCD was assembled onto the MMI using two locator pins and two locator tabs which are bent through slots on the board and soldered in place (Figure B.18). The two locator pins were removed from the model as they do not provide significant constraint to the board/LCD. The sections where the LCD connection tabs protrude through were maintained but modified to create a face to face contact condition (Figure B.19).

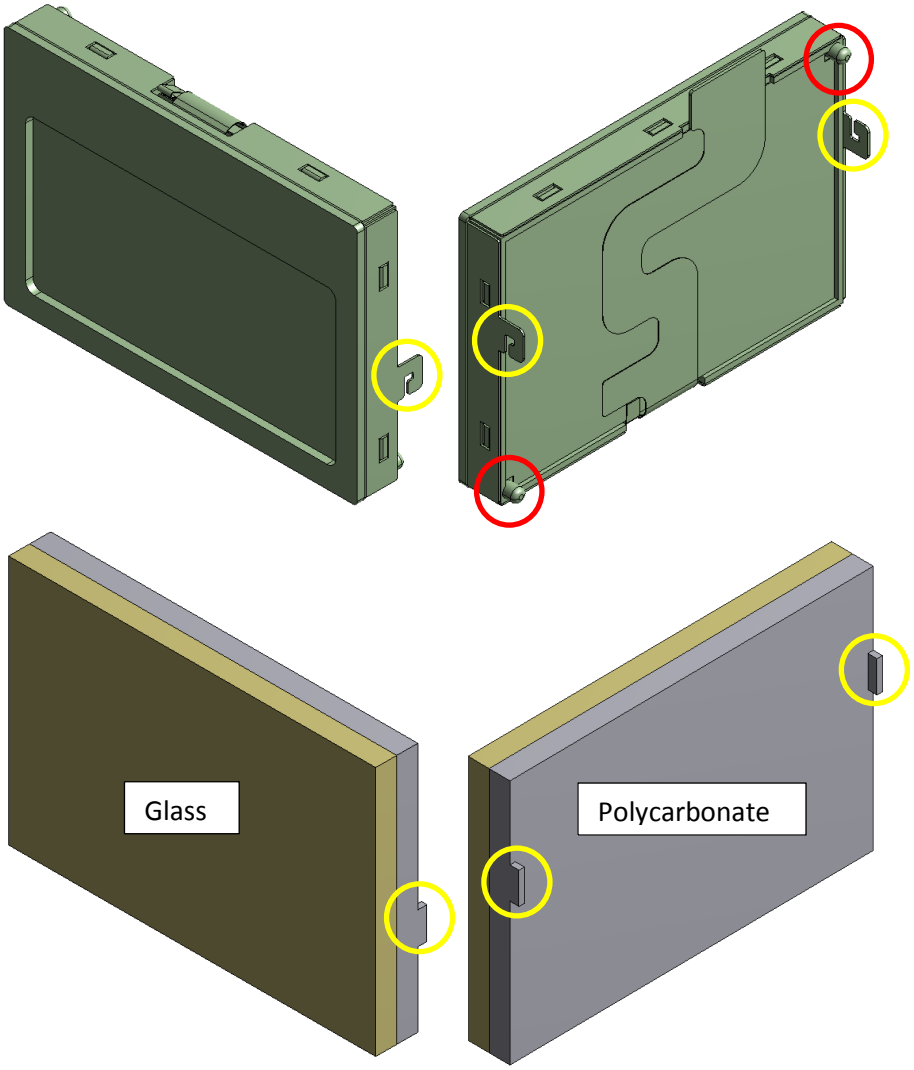

Figure B.17 - LCD before (top) and after (bottom) simplification, red - locating pin, yellow - solder tab connection

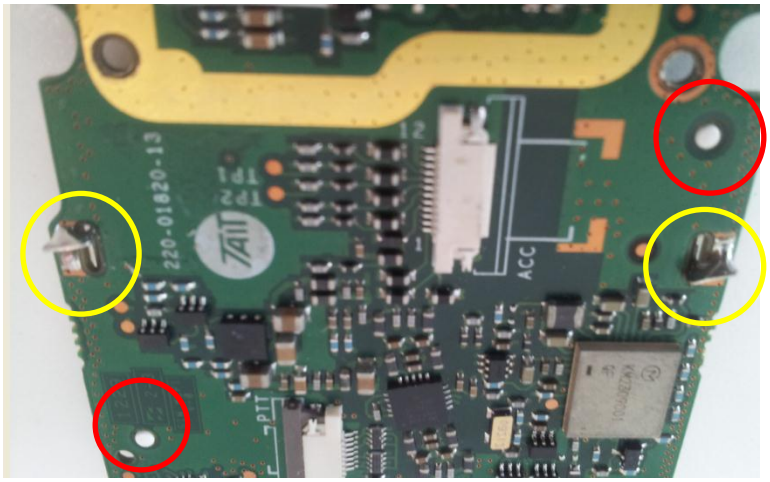

Figure B.18 - LCD screen connections to MMI board, red - locating pin, yellow - solder connection

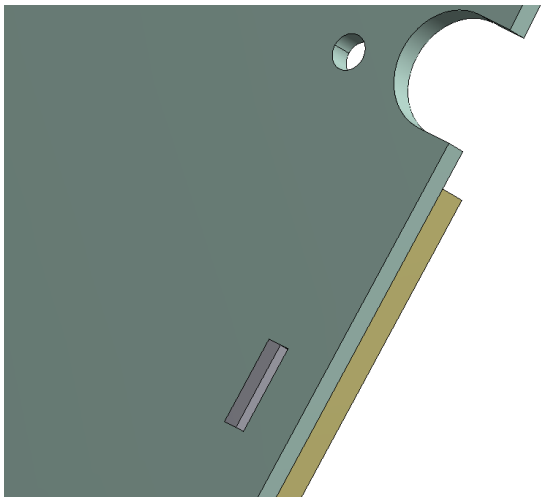

Figure B.19 - Geometry of LCD connection to MMI board

B.3.3. RF PCB subassembly

The RF board (Figure B.20) is the main circuit board, densely populated with processors and other large components. The RF board has the same material composition as the MMI board. In addition to the smaller electrical components and processors, the board also has 10 shields (9 tinplated steel and one elastomer) to protect components from radio frequency and electromagnetic interference (RF/EMI). The RF board has the dimensions 110 mm x 46.5 mm x 1.16 mm (10 mm if shields are included). The RF board is mounted to the chassis via 7 screws. The RF board after simplification is shown in Figure B.21

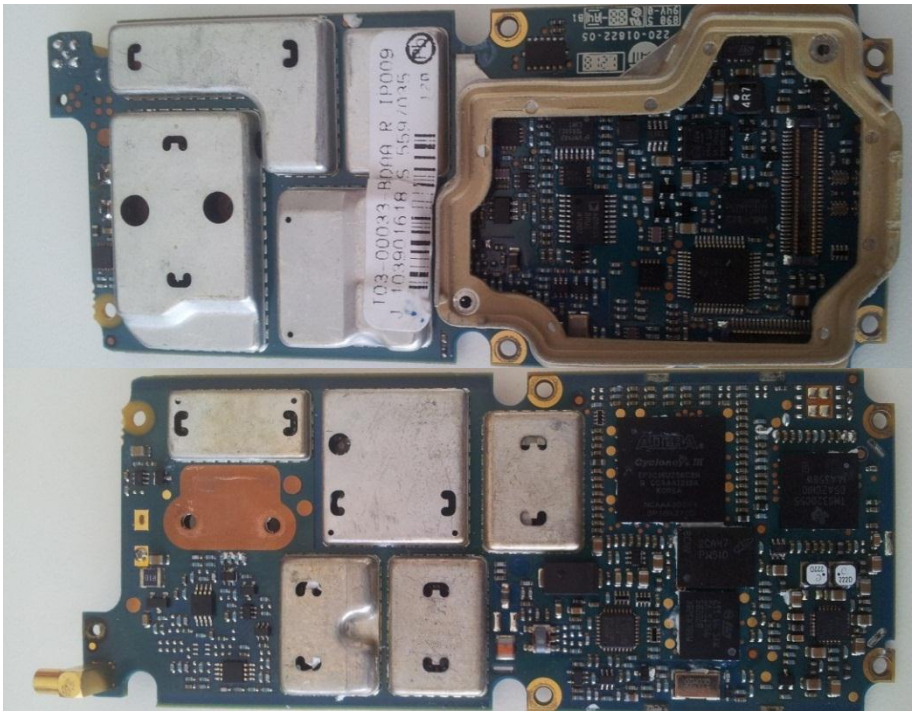

Figure B.20 - RF Board, Top – Front Face, Bottom – Rear Face

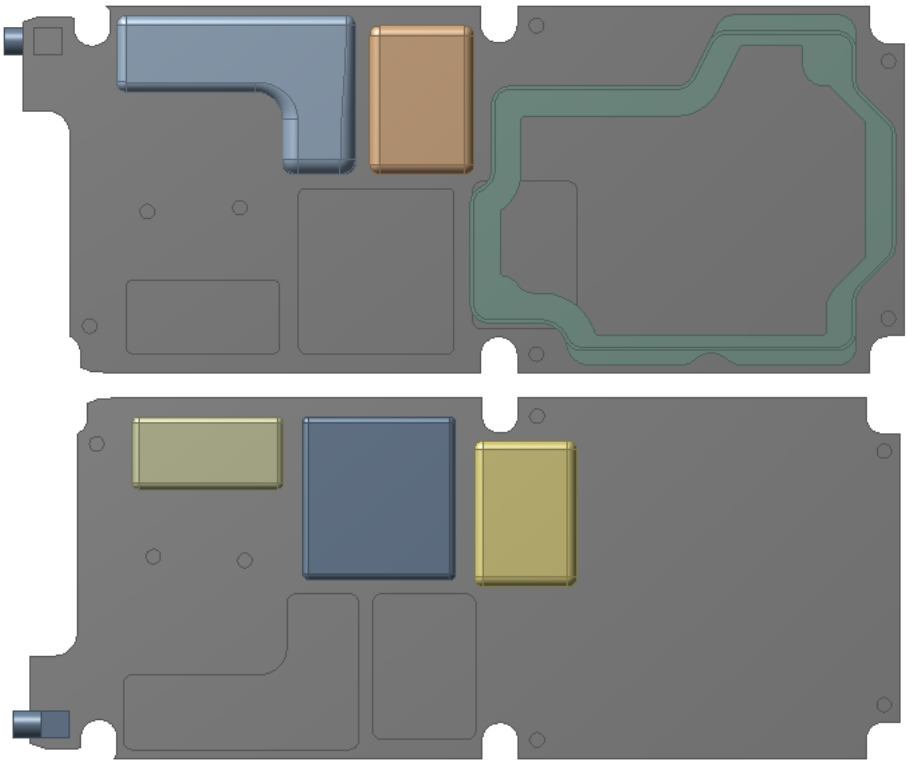

Figure B.21 - RF board after simplification process

B.3.3.1. Small electrical components

Small components such as the resistors and chips were removed from the RF board (Figure B.22). The smaller components have minimal effect on the behaviour of the board as they add little

stiffness or mass to the board, inclusion would increase the finite element solving time to an impractical level.

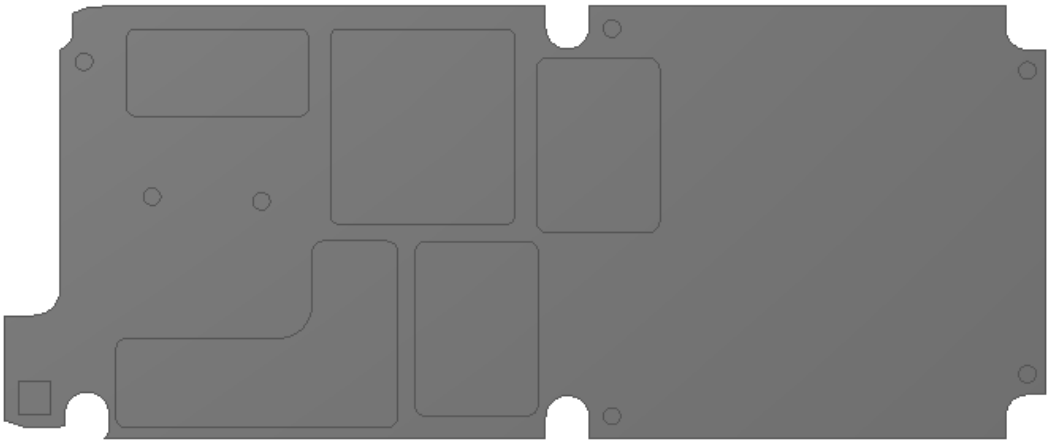

Figure B.22 - Bare RF board with smaller electrical components removed

B.3.3.2. Shielding – Cans

The shielding cans on the RF board provide components protection from electromagnetic and radio frequency interference. The can shields are made from tinplated steel. The thin nature and constant wall thickness of the shields encourages the use of shell elements instead of solid elements. Shell elements means larger elements can be used without any loss in accuracy. Punched holes were removed from the cans as they added unnecessary complexity to the model. The base of the cans have a slight kink in them where they attach to the PCB, this detail has been removed to reduce the mesh resolution (Figure B.23). It should be noted that this form of shielding is likely to be present in future board designs so the inclusion of such components in any finite element model is desirable.

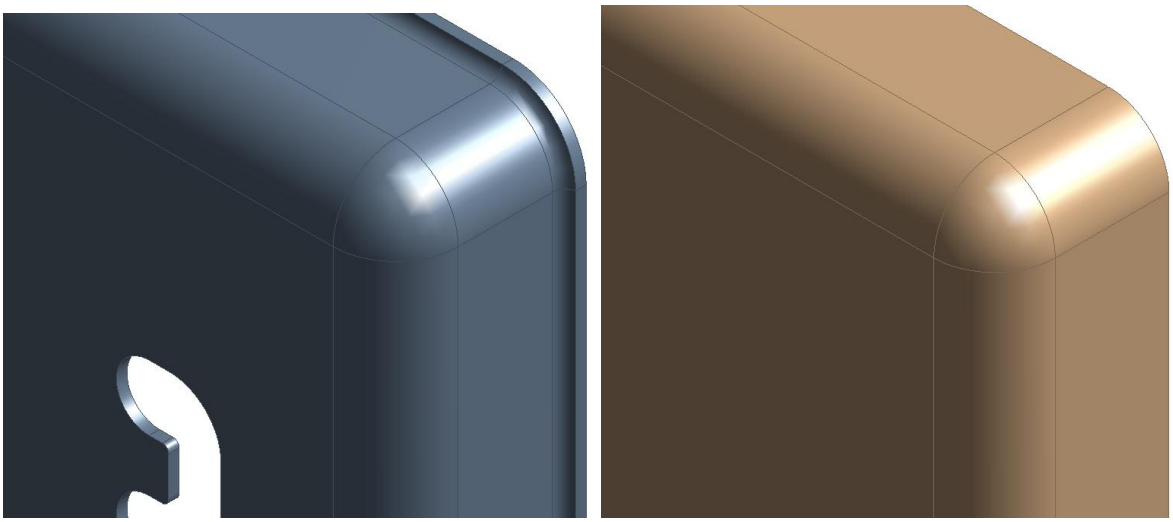

Figure B.23 - Shielding design before (left) and after (right) removal of pressed edging and punched holes

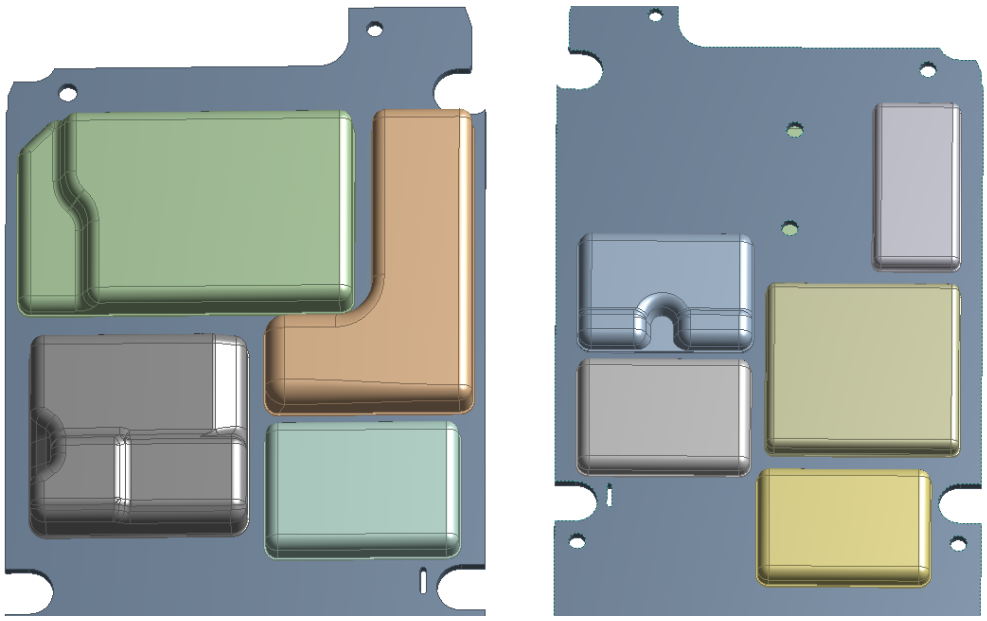

Figure B.24 - Can shields used in the finite element model

The more complex shields were removed from the RF board assembly (Figure B.25). This was done to improve on the solving time of the assembly. Enough shields were left on the board so that their influence could still be adequately observed.

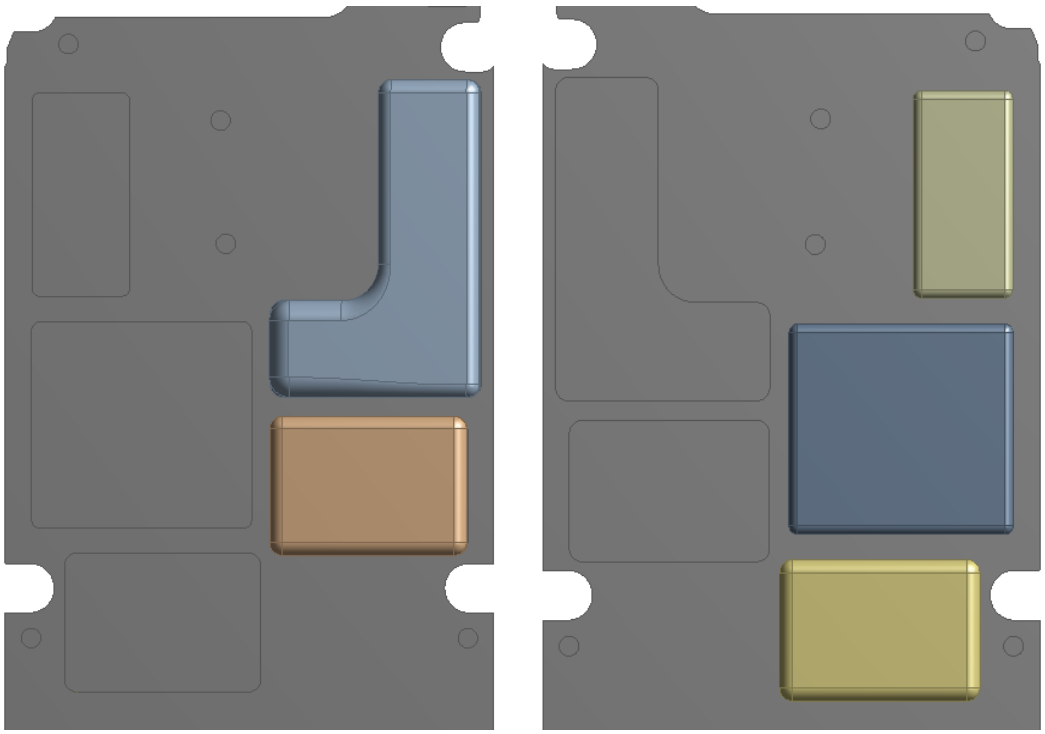

Figure B.25 - RF board with more complex shields removed from the assembly

B.3.3.3. Shielding – FIBS

A different type of shielding is also attached to the RF board (Figure B.26). This shield is constructed of two materials, a steel core over-molded with a conductive elastomer (Nolato Conductive Silicone Rubber 8630). The main purpose of this shield is to provide a common ground between the two circuit boards but it also provides some RF/EMI shielding. Both the MMI and RF boards are in contact with the elastomer, with the silicone being compressed approximately 0.3 mm to provide a complete seal. To simplify the model the FIBS shielding is modelled purely as an elastomer (Figure B.26), with each edge in contact with the board having the same thickness as the physical product. The central region, not in contact with the boards, has been thickened so that the overall stiffness of the shield is more representative of the metal cored physical product.

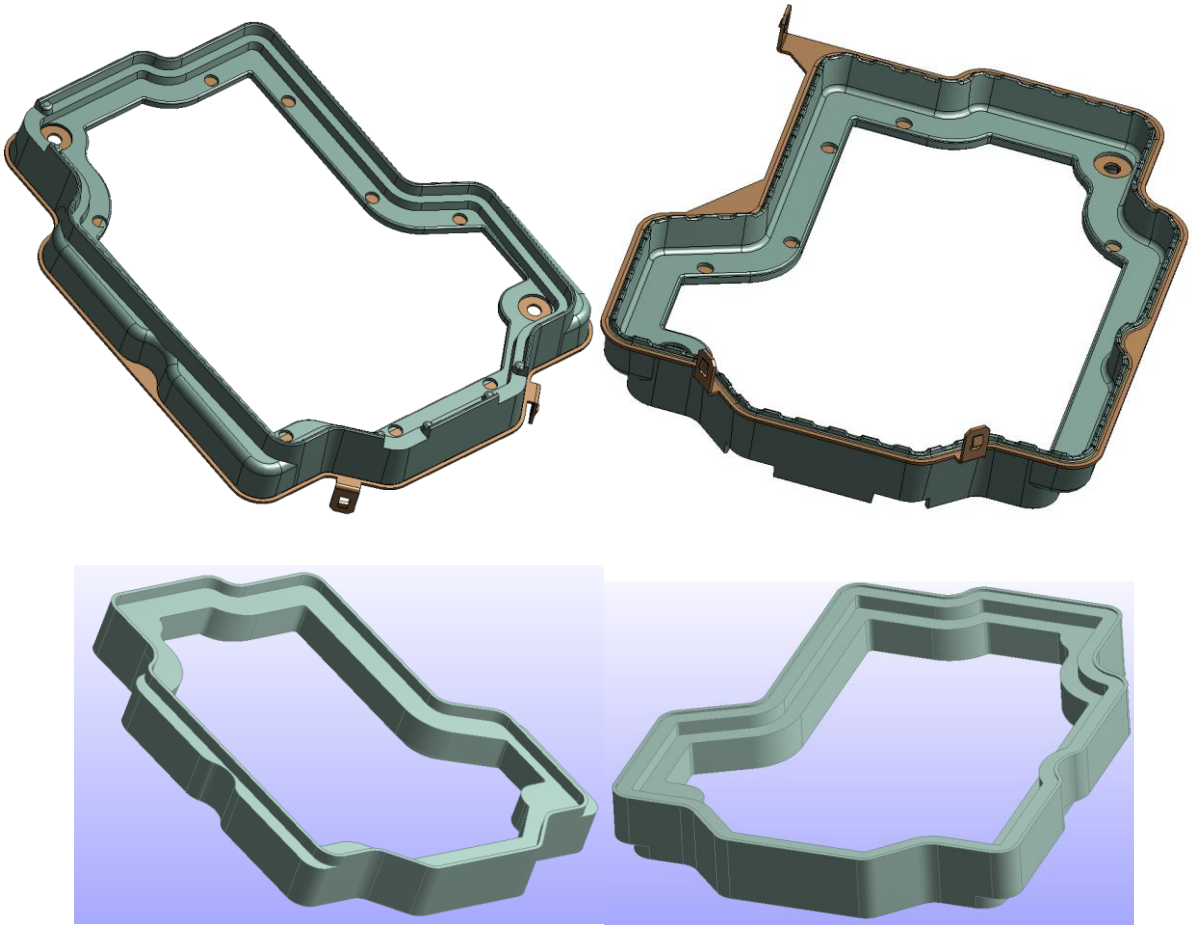

Figure B.26 - Depiction of FIBS shielding, top before simplification, bottom simplified version to be used in impact simulation

B.3.3.4. Antenna connection

The antenna connection (Figure B.27) provides a connection between the antenna and the RF board, this makes its inclusion in the model necessary as it will limit the deformation of the board. Small details were removed from the connector (Figure B.28).

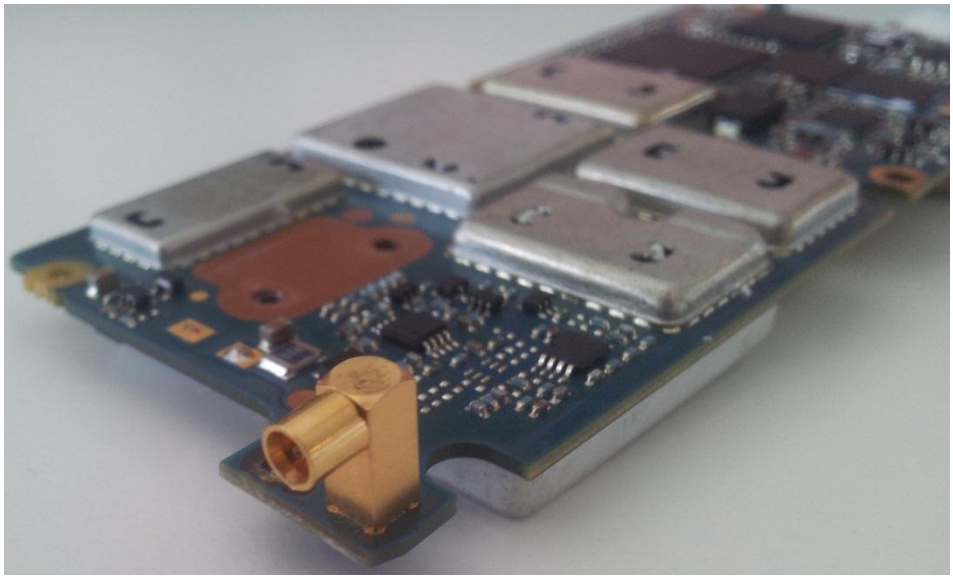

Figure B.27 - Antenna connection (foreground)

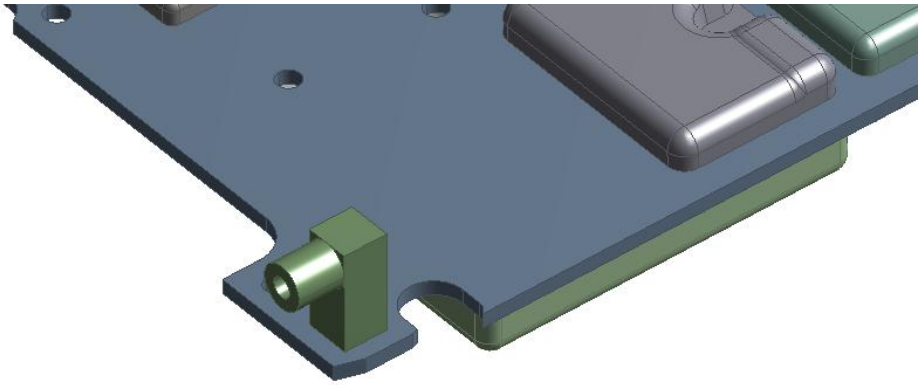

Figure B.28 - Simplified antenna connection

B.3.4. Chassis subassembly

The chassis adds rigidity to the handheld radio assembly due to its size and aluminium construction and a mounting structure for the heavily populated RF board. It attaches onto the back side of the front panel with 6 screws. The rear panel attaches to the back side of the chassis and is used to hold the battery in place. The chassis assembly is 137 x 54 x 14 mm (nominal wall thickness is approximately 1.5 mm).

B.3.4.1. Chassis body

The chassis body is die cast using aluminium alloy AlSi12Cu. Small level changes, stamped part descriptors, location tabs and filet radii were removed from the geometry. The hole used for venting/pressure relief was also removed. The end result of the simplification process is shown in Figure B.30.

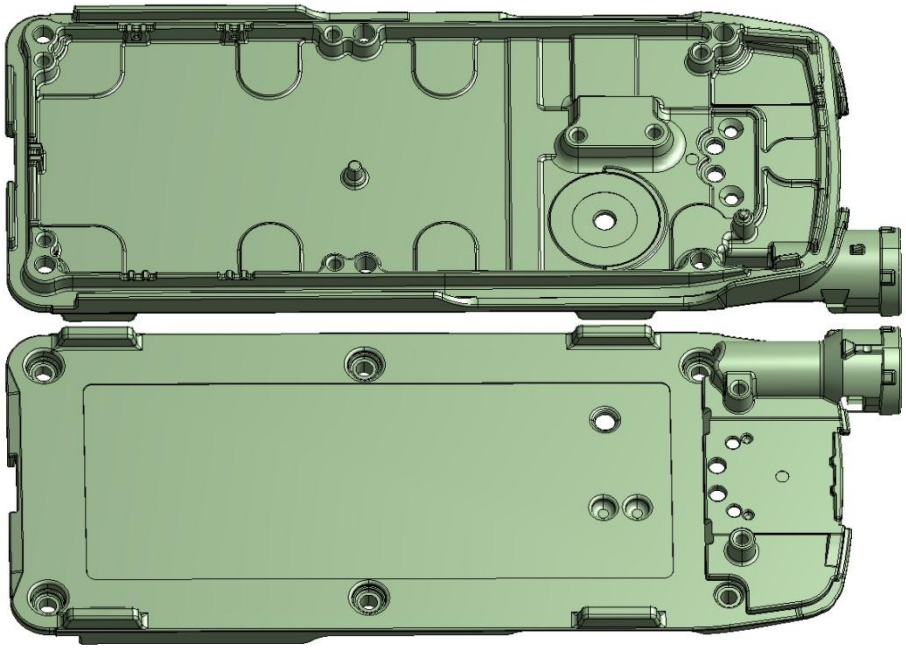

Figure B.29 - TPD chassis prior to CAD model simplification

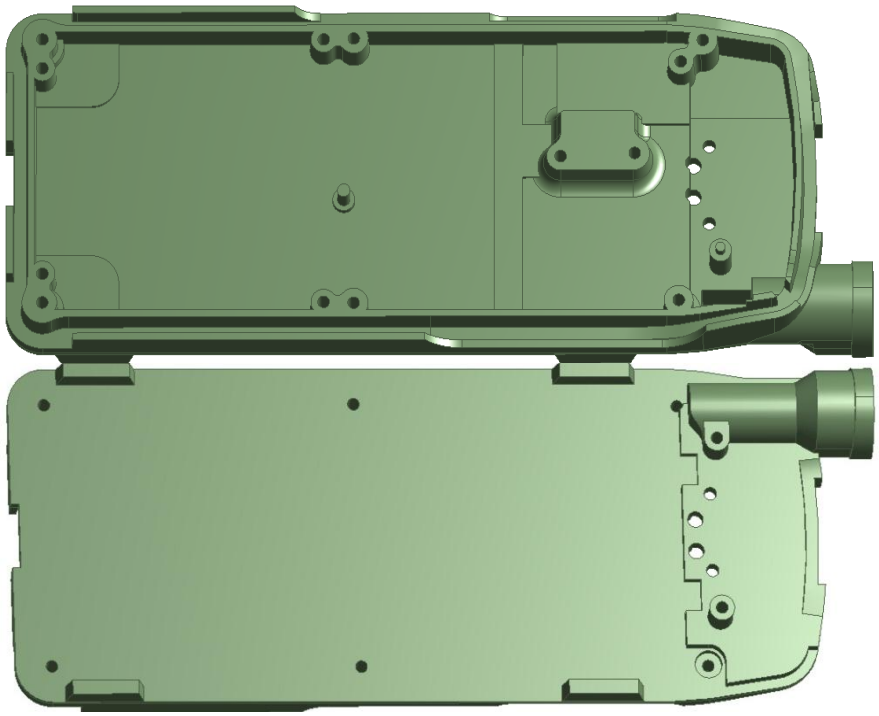

Figure B.30 - Simplified Chassis Model

B.3.4.2. Rear panel

The rear panel (Figure B.31) attaches to the back side of the chassis using two screws. The main purpose of the rear panel is to hold the battery in place while still making it easy to remove so that the battery can be swapped out when it loses its charge. The rear panel is a relatively complex part that uses three springs to control the clipping mechanism. The rear panel was simplified to create a fixed clip design (Figure B.32), the modifications had the battery in place the same way as the final

design but does not allow for the clip to move to release the battery. The design used in the finite element model is shown in Figure B.31.

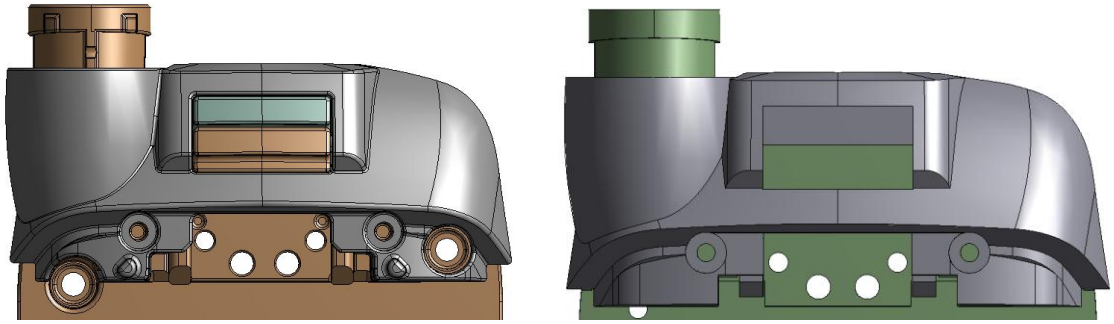

Figure B.31 - Rear panel before (left) and after (right) simplification

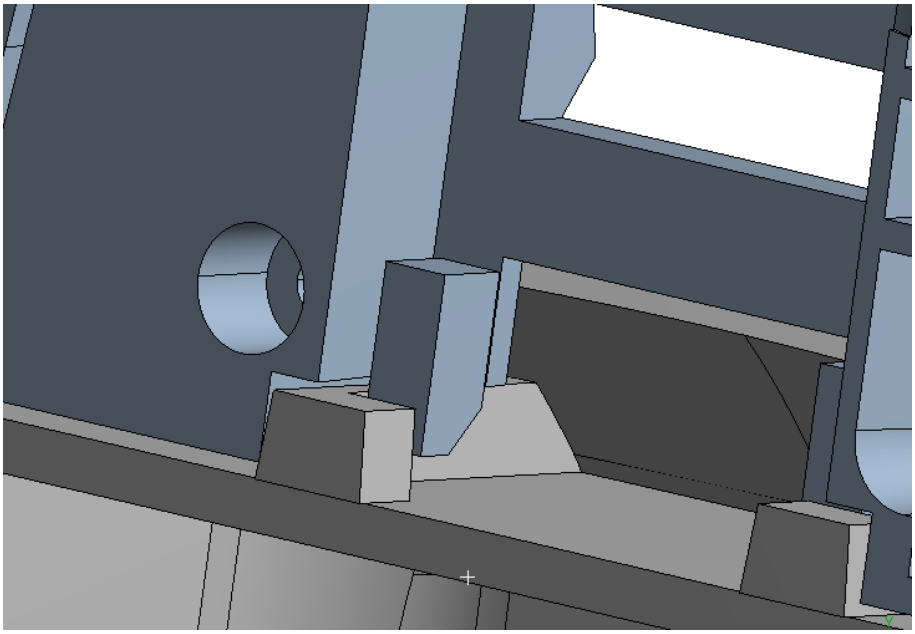

Figure B.32 - Rear panel (blue) constraining the movement of the battery case (grey)

B.3.4.3. Seal

The seal (Figure B.33) is positioned in a channel running around the perimeter of the chassis and creates a seal between the front panel and chassis, protecting the internal radio components from water and other contaminants. The seal was modified to remove interferences with the chassis and front panel (necessary to compresses the seal to ensure a complete seal is achieved). The interferences were cut away from the seal as finite element analysis does not deal with such phenomena well. The location tabs positioned at intervals along the seal were also removed (Figure B.33).

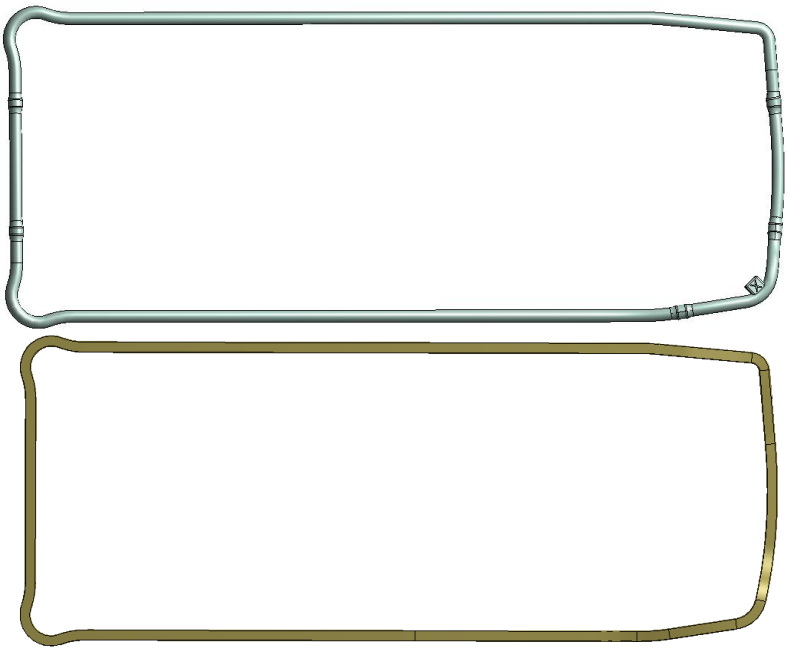

Figure B.33 - Comparison between the main seal before (top) and after (bottom) simplification

B.3.5. Battery subassembly

The battery subassembly (Figure B.34) is constructed of an outer housing which holds 6 AA batteries, connection circuitry and insulation between the batteries. The battery housing is constructed of two parts which are ultrasonically welded together. The battery subassembly has the overall dimensions of 118 x 30 x 21 mm.

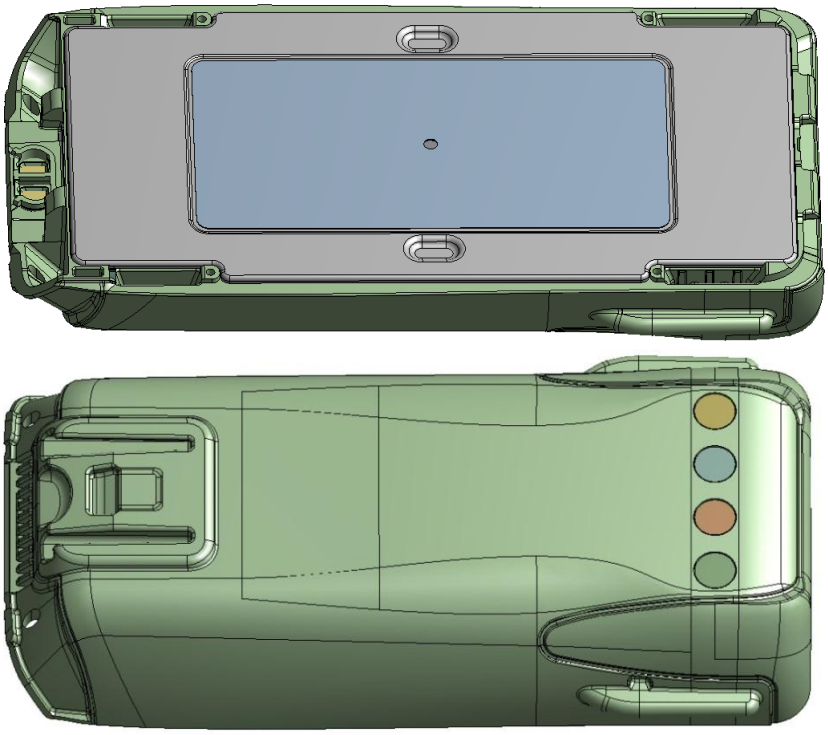

Figure B.34 - Battery assembly before simplification

B.3.5.1. Battery housing

The battery case (Figure B.35) and the battery lid (Figure B.36) are ultrasonically welded together to form the battery housing. The battery case is predominantly made from Makroblend® 3103 but has the softer Desmopan® over-moulding on the corners, added by way of a secondary injection shot during the moulding process. The battery lid is made of an impact modified PC.

The belt clip attachment was removed from the battery case. Fins on the side of the battery case used to guide the battery into a charging dock were removed. The four brass charging contacts were also excluded from the model. The sticker recess and vent hole features were removed from the battery lid. The battery lid was widened to ensure that face to face contact between it and the battery case could be achieved (the gap would normally be closed during the welding process). The final simplification of the battery case and lid is shown in Figure B.35 and Figure B.36 respectively.

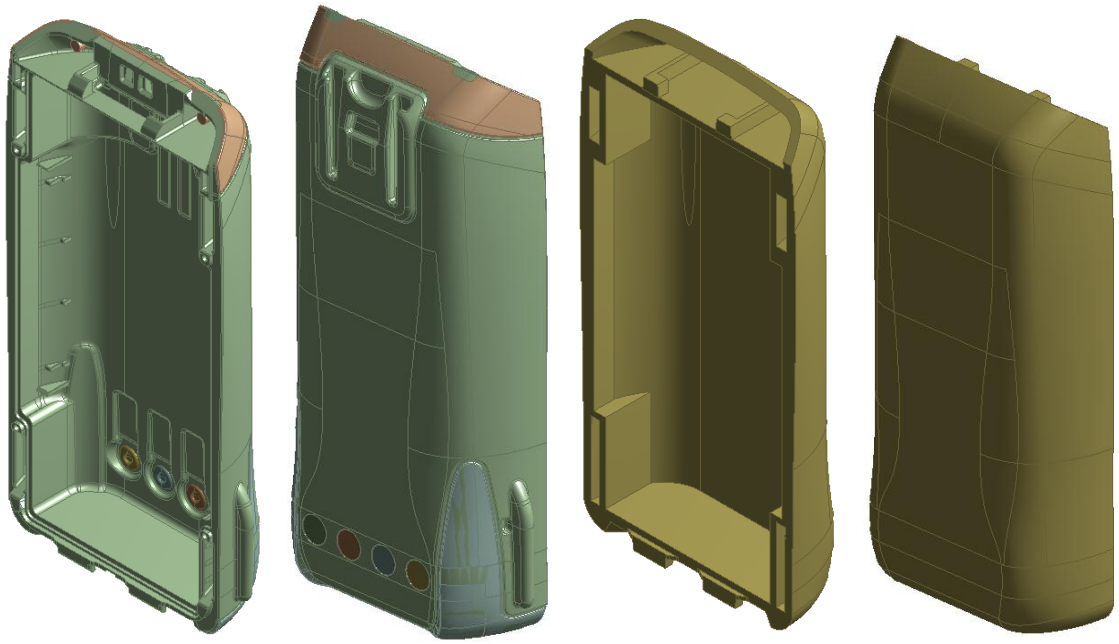

Figure B.35 - Battery casing before and after simplification

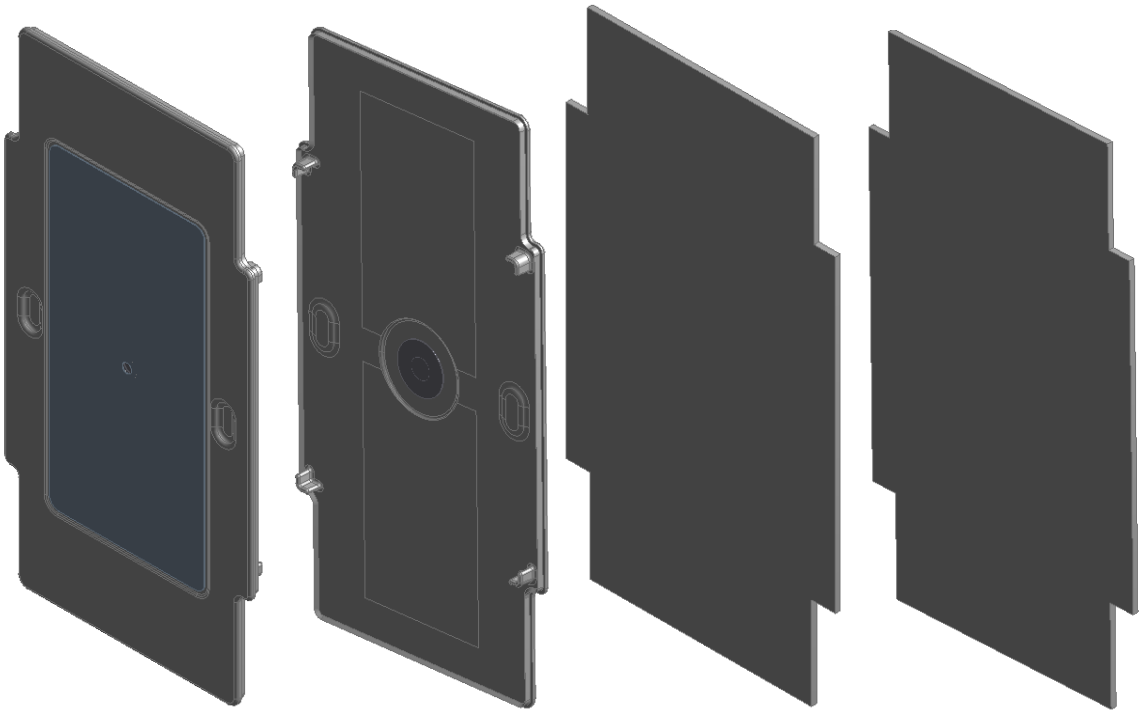

Figure B.36 - Battery lid before (left) and after (right) simplification

B.3.5.2. Battery internals

There are two battery packs that are paired with the handheld radio, one uses AA batteries and the other prismatic Li-ion batteries. The AA batteries are included in this model as it they are the heaviest of the two battery assemblies, meaning higher inertial forces. The AA battery pack consists of an array of 6 AA batteries. The batteries are held in place onto the base of the battery case using Super-X adhesive.

The AA batteries were modelled as solid cylinders, with appropriate density and stiffness applied. The bottom of the batteries are bonded to the battery pack via an elastomer sheet, the top of the batteries are not in contact with the battery lid. All the battery insulators, circuitry and other connections were removed from the assembly as the thin nature of these parts would not contribute to the structural integrity of the battery.

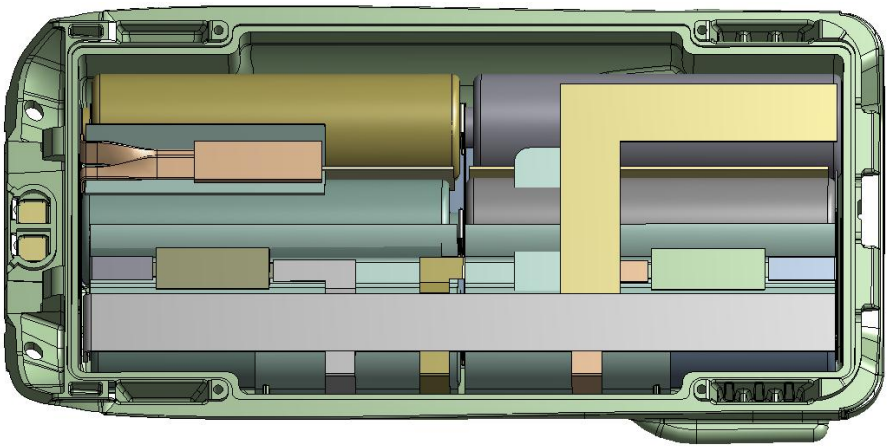

Figure B.37 - Battery internal assembly before simplification

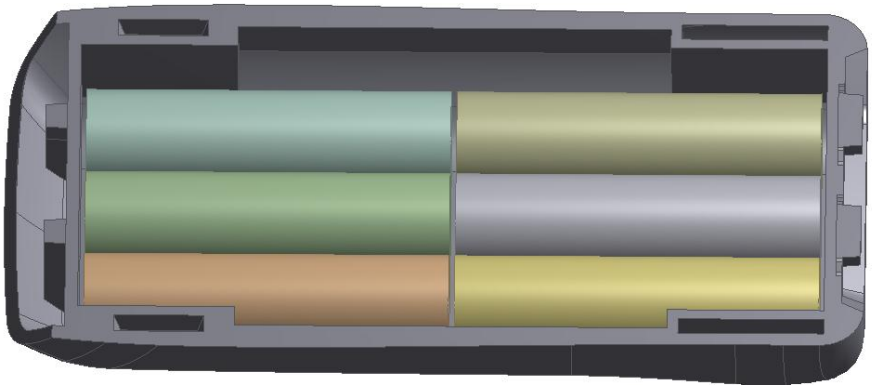

Figure B.38 - Battery internals after simplification

B.3.6. Final assembly

The final simplified version of Tait's handheld radio is shown in Figure B.39. Any parts removed from the radio assembly for the simulation model were also removed from the physical radio for the validation experimental drop tests.

Figure B.39 - Final render of detailed radio after simplification process for finite element analysis

Parts have been modified in a way that their external shape may have changed, it was therefore important to check that part interactions observed in the physical assembly were maintained. An interference defection algorithm was run in the CAD program (Creo 2.0 Parametric). Interference between some parts were detected, these were modified to remove any observed interferences. Other parts were changed in such a way that they were no longer in contact with parts they were previously, again these parts were altered to ensure realistic contact interactions. Hole diameters were changed so that they were the same at all locations (Figure B.27), this meant face to face and edge to edge contact conditions could be applied at any screw/hole location.

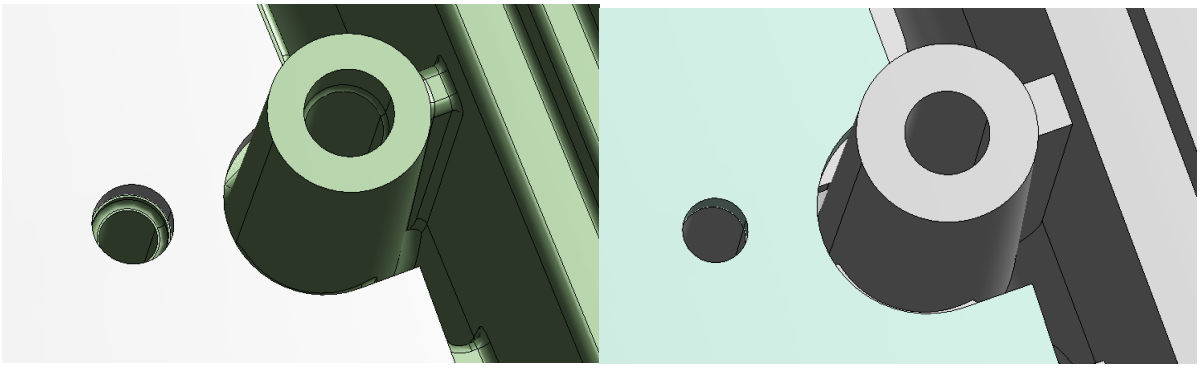

Figure B.40 - Holes size before (left) and after (right) modification to make equal diameter

There was some concern that the modification of parts would affect their behaviour due to changes in volume/mass. The change in volumes during the simplification process was found to be negligible, for example the front panel before simplification had a volume of 34.66 cm^3 and after the simplification process it was 35.63 cm^3, a difference of around 3%. If the weight of the individual parts was overly critical to the simulation results then the density used in the material model could be altered to get better agreement between the physical and virtual products, in this case this was deemed unnecessary. The thickness of parts was also not altered greatly during the simplification process meaning part stiffness's were also unaffected.

B.4. Material Properties

The majority of materials used in the finite element model relied on information given by the various material suppliers. The supplier information commonly included density, shrink rates/percentages, and tensile/flexural information such as yields, strains, strengths and moduli. The material model used for all parts in the finite element model was a linear elastic model which requires a Young's modulus, Poisson's ratio and material density. Some of the data sheets provided by suppliers included both tensile and flexural modulus information, due to the likely loading experienced by the parts the flexural modulus was selected over the tensile modulus.

The front panel is made from Makroblend® UT250 [44] which consists of a blend of polycarbonate (PC) and polyester (PET). This particular blend has been developed for impact resilience and has good impact properties, toughness, reduced susceptibly to stress cracking, is easily injectable, has good chemical resistance and a low moisture uptake. The material behaviour is considered linear elastic with the Young's modulus assumed to be the same as its flexural modulus.

The battery case was made of Makrolon 310 MAS157 [45] which is a polycarbonate based product. It is a general purpose grade polycarbonate that has high viscosity.

Both the front panel and battery cover both have a secondary material modelled using a secondary material shot in the injection moulding process. The areas where this second shot applied were on the corner on the parts where impact is more likely to occur. The material used is Desmopan 5377A [46] which is a Thermoplastic Polyurethane Elastomer (TPU). Shore A hardness data is provided in place of tensile/flexure data so the method detailed by Kunz et al. [37] is used to find it's Young's modulus. A Poisson's ratio of 0.49 is assumed due to its rubber like deformation behaviour.

The battery lid is ultrasonically welded onto the battery case. The lid is made of a polycarbonate RTP399 X 62313B [47] which was developed for better impact properties.

The chassis is made of Al12SiCU [48] (commonly called LM20 in the UK and A413 in the USA) and manufactured using die casting techniques. Again, like the front panel both flexural and tensile moduli were quoted with the flexural modulus used in the finite element model.

The softer materials like the keypad, seal and front panel/battery over-moluding do not provide tensile or flexural moduli, instead Shore A hardness test data is provided. Kunz et al. [37] details a way of converting Shore A hardness information to Young's modulus using the following equation:

$$E = \frac{1-\mu^2}{2 \cdot R \cdot C_3} \cdot \frac{C_1 + C_2 \cdot Sh_A}{100 - Sh_a} \cdot (2.6 - 0.02 \cdot Sh_A) \quad \textbf{(B.1)}$$

where E is the Young's modulus, μ is Poisson's ratio, Sh_a is the measured Shore A Hardness, R = 0.395 mm, C_1 = 0.549 N , C_2 = 0.07516 N, and C_3 = 0.025 mm. This method can only be applied to materials that have a Shore A hardness in the range between 30 and 95, all the used materials fell within this range.

Unlike the other parts the MMI and RF boards do not have material property data provided by the suppliers. Fortunately during the tuning of the simplified radio impact hammer tests their material properties were generated (Section 4.14).

The AA batteries included in the model use a density calculated by the weight of a normal AA battery and the volume of the batteries in the finite element model. The Young's modulus for the batteries was assumed the same as steel, 200 GPa.

The other parts in the finite element model have data provided from the material suppliers. All material values are summarised in the table below (Table B.1), bold properties are those used in the finite element model.

Table B.1 - Summary of material properties used for handheld radio

Part	***Material***	***Property***	***Value***	
Front Panel	Makroblend® UT250	Density	**1210**	kgm^{-3}
		Tensile modulus	1.1	GPa
		Yield stress	55	MPa
		Yield strain	5	%

Part	*Material*	*Property*	*Value*	
Front Panel		Flexural modulus	**2.3**	GPa
		Flexural stress at 5% strain	88	MPa
Battery Case	Makrolon 3103 MAS157	Density	**1190**	kgm^{-3}
		Tensile modulus	2.35	GPa
		Yield stress	65	MPa
		Yield strain	6.3	%
		Flexural modulus	2.3	GPa
		Flexural strength	**98**	MPa
Over-moulding (Front Panel and Battery Cover)	Desmopan 5377A	Density	**1140**	kgm^{-3}
		Shore A hardness	77	
		Ultimate tensile strength	26	MPa
		Elongation at break	740	%
		Young's modulus*	**11.1**	MPa
Battery Lid	PC Impact Modified RTP 399 X 62313B	Density	**1190**	kgm^{-3}
		Tensile strength	54	MPa
		Tensile modulus	2.07	GPa
		Flexural strength	86	MPa
		Flexural modulus	**2.206**	GPa
Chassis	LM20/AlSi12Cu/A413	Density	**2650**	kgm^{-3}
		Tensile strength	290	MPa
		Yield strength	130	MPa
		Yield strain	3.5	%
		Young's modulus	**71**	GPa
Keypad	Silicone KE-961T-U [38]	Density	**1170**	kgm^{-3}
		Shore A hardness	62	
		Tensile strength	9.7	MPa
		Elongation at break	310	%
		Young's modulus*	**7.08**	MPa
Lens	PMMA [39]	Density	**1190**	kgm^{-3}
		Tensile strength	71.7	MPa
		Tensile strain	4	%
		Flexural strength	120	MPa
		Flexural modulus	**3.1**	GPa
Rear Panel	Glass Reinforced Nylon TDS Grilon® BG-50 [40]	Density	**1580**	kgm^{-3}
		Tensile strength	165	MPa
		Elongation at break	6	%

Part	*Material*	*Property*	*Value*	
Rear Panel		Tensile modulus	**11.5**	GPa
Seal	Liquid Silicone Rubber	Density	**1143**	kgm^{-3}
	XIAMETER®RBL-2004-40	Shore A hardness	44	
	[41]	Tensile strength	8.7	MPa
		Elongation at break	742	%
		Young's modulus*	**4.2**	MPa
RF/MMI Board	Glass Fibre Reinforce	Density	**3090**	kgm^{-3}
		Young's modulus**	**13.69**	GPa
FIBS Shield	Conductive Silicone	Density	**1900**	kgm^{-3}
	Nolato Silicone 8630 [42]	Shore A hardness	75	
		Tensile strength	1.5	MPa
		Elongation at break	90	%
		Compression modulus 10% ε	9.2	MPa
		Compression modulus 20% ε	9.8	MPa
		Young's modulus*	**10.3**	MPa
AA Battery	Lithium Ion	Density	**4200**	kgm^{-3}
		Young's modulus	**20**	GPa
Super-X adhesive	Super X No.8008 – black [43]	Density	**1270**	kgm^{-3}
		Tensile shear adhesive strength	4	MPa
		Shore A hardness	43	
		Elongation at break	200	%
		Young's modulus*	**4.38**	MPa
Impact plate		Density	**7850**	kgm^{-3}
		Young's modulus***	**12.15**	GPa

* Calculated using "Calculation of Young's Modulus using Shore A Hardness"(B.1), [37]
** Calculated using design optimisation, (Section 4.14)
*** Calculated using design study, (Section 4.18)

B.5. Contacts and Connections

The handheld radio is held together via screws, adhesives and clips. Table B.2 summarises the part to part interactions and examples of the different contact conditions are presented in Figure B.41 through to Figure B.44. In absence of screws from the model a face to face bonded contact condition of the vacant screw holes was used (Figure B.42). The use of a frictional contact condition over frictionless is discussed Section 4.8.

The shields were modelled as shell elements, it was found that there was difficulty in creating a bonded connection to the solid elements of the RF board as they were too dissimilar (solid to shell

elements and edge to face connection types). The RF board was therefore also modelled as a shell element. The RF board had its face split such that it matched the shape of the shields it was connecting to (Figure B.25). A mesh to mesh bonded contact condition was used between the RF board and the shields by selecting the complimentary edges. The RF board was bonded to the chassis using a face to face contact condition at the screw locations. In place of holes at the screw locations the areas were instead filled and had their face split so that a bonded contact area of the correct diameter could be applied, this was done as it was found that an edge to edge contact condition did not work within the explicit dynamics environment.

Table B.2 - Summary of part contacts and interactions

Part 1	***Part 2***	***Contact Condition***	***Example***
Front Panel (body)	MMI Board (body)	Frictional	Figure B.41
Front Panel (screw face)	MMI Board (screw face)	Bonded	Figure B.42
Front Panel	Glass LCD	Frictional	Figure B.41
Front Panel	Seal	Frictional	Figure B.41
Front Panel	Front Panel Over-moulding	Bonded	Figure B.43
Front Panel (body)	Chassis (body)	Frictional	Figure B.41
Front Pane (screw face)	Chassis (screw face)	Bonded	Figure B.42
Front Panel	Lens	Frictional	Figure B.41
Front Panel	Lens	Bonded	Figure B.43
Lens	Glass LCD	Frictional	Figure B.41
MMI Board	Ceramic Antenna (x2)	Bonded	Figure B.43
MMI Board	Keypad	Frictional	Figure B.41
MMI Board	FIBS Shield	Frictional	Figure B.41
Glass LCD	PC LCD	Bonded	Figure B.43
Seal	Chassis	Frictional	Figure B.41
AA Battery (x6)	Battery Foam	Bonded	Figure B.43
AA Battery (x6)	Battery Case	Bonded	Figure B.43
Chassis (body)	Rear Panel (body)	Frictional	Figure B.41
Chassis (screw faces)	Rear Panel (screw faces)	Bonded	Figure B.42
Front Panel	Rear Panel	Frictional	Figure B.41
MMI Board (body)	PC LCD (body)	Frictional	Figure B.41
MMI Board (tab faces)	PC LCD(tab faces)	Bonded	Figure B.42
Antenna	Chassis	Frictional	Figure B.41
Chassis (body)	RF Board (body)	Frictional	Figure B.41
Chassis (screw faces)	RF Board (screw faces)	Bonded	Figure B.42

Part 1	*Part 2*	*Contact Condition*	*Example*
Battery Case	Rear Panel	Frictional	Figure B.41
Battery Lid	Chassis	Frictional	Figure B.41
Battery Lid	Battery Case	Bonded	Figure B.43
Antenna	RF Board	Bonded	Figure B.43
RF Board	Can Shields	Bonded (Mesh – Mesh)	Figure B.44

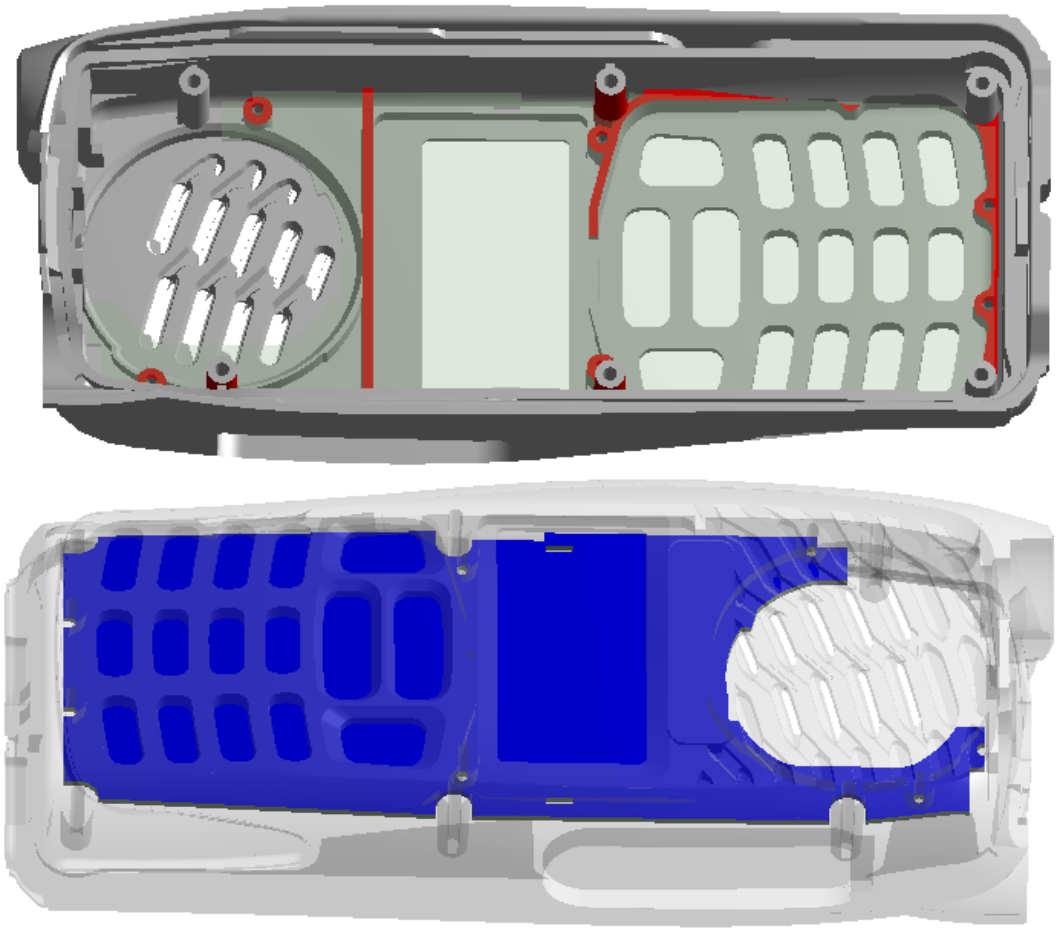

Figure B.41 - Frictionless contact interaction between front panel (red) and MMI board (blue)

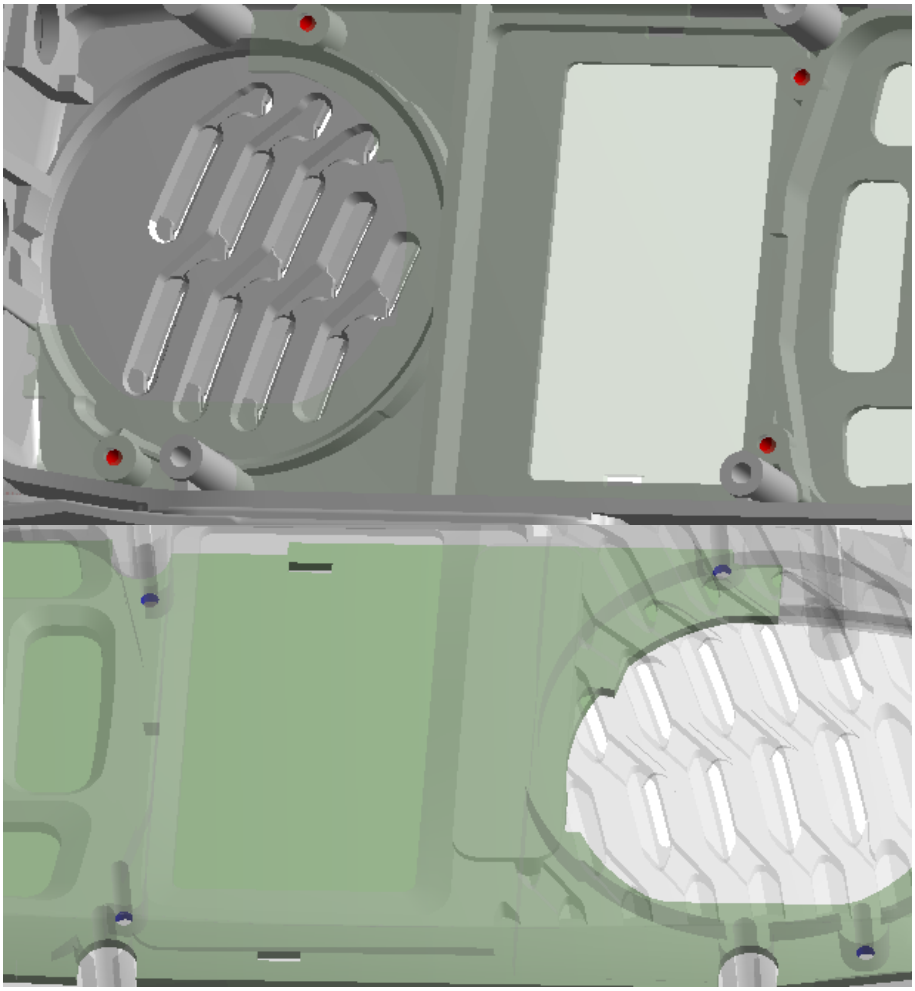

Figure B.42 - Face - face screw connection between front panel (red) and MMI board (blue)

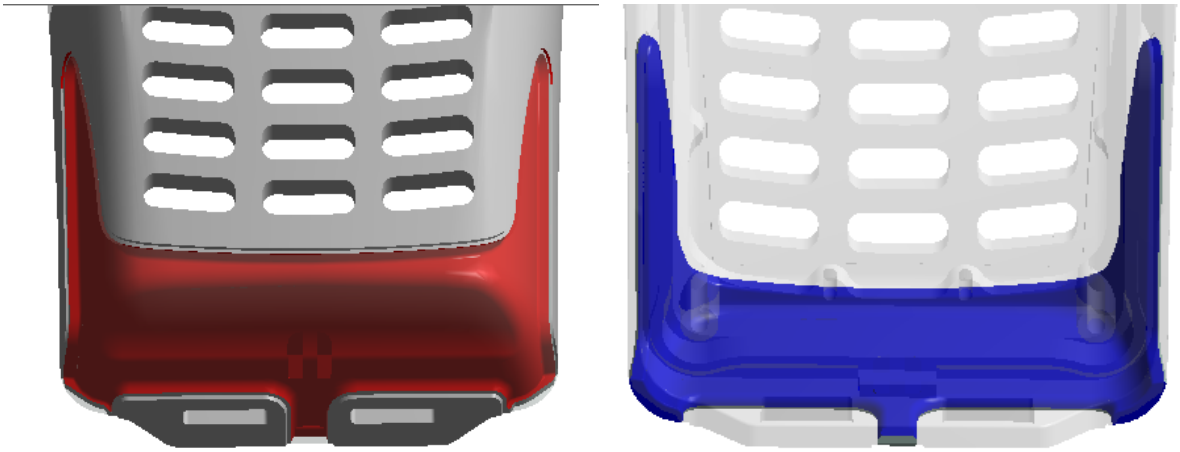

Figure B.43 - Face to face bonded condition between front panel (red) and front panel over-moulding (blue)

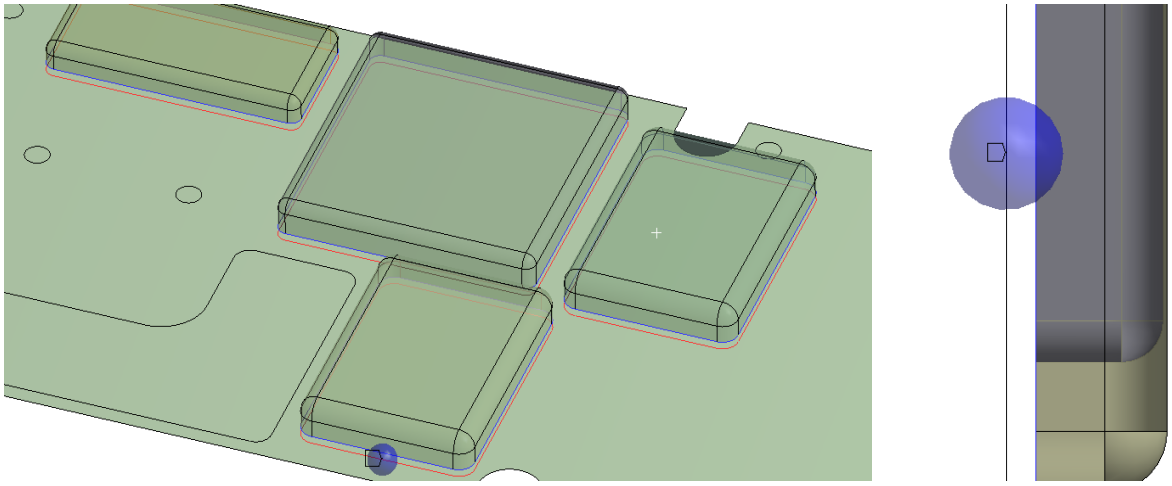

Figure B.44 - Mesh to mesh contact condition between RF board (red) and shielding cans (red), blue sphere indicating contact tolerance (necessary for surface to surface body contacts)

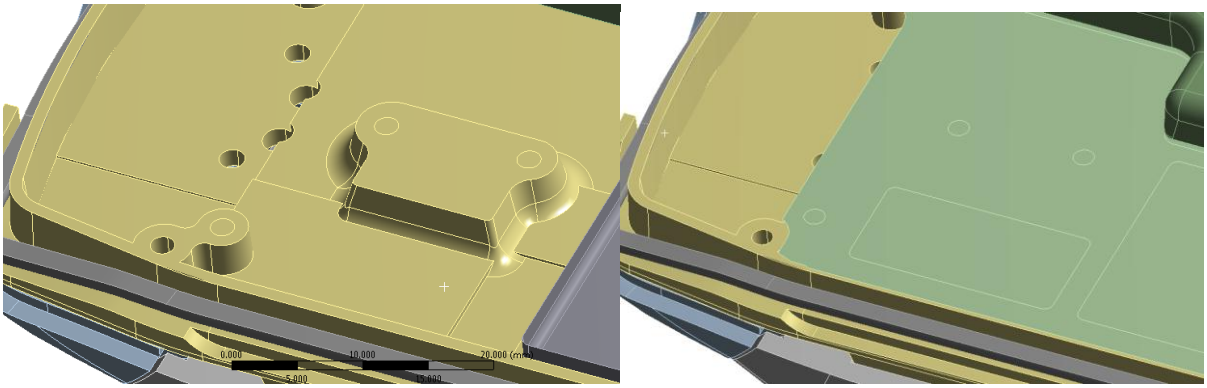

Figure B.45 - Setup of chassis and RF board to be able to apply a face to face contact condition at screw locations

B.6. Discussion on Detailed Radio Geometric Setup

All modifications to the geometry were completed and the contact conditions set to match the physical assembly as best as possible. The current model was meshed, initial conditions, boundary conditions and analysis setting applied according to the simulation was to be investigated.

The simplification of parts helped in eliminating unnecessary complexity from the model. The simplification process relied on identifying geometric features, finding the feature in the CAD environment and suppressing the feature. It was found that for parts with less detail it was easier to remove the unnecessary features. Complex parts such as the front panel and chassis which had over a thousand features were more difficult to simplify as some were linked to other features, making it difficult to supress without errors in the part. If more time was available, it would be better to remodel the parts from scratch so that any complexity was not present in the first place.

References

1. E.H. Wong, S.K.W.S., V.P.W. Shim, *A review of board level solder joints for mobile applications.* Microelectronics Reliability, 2008. **28**: p. 1747-1758.
2. Schueneman, H.H. *Package Engineering, Design and Testing: A step by step approach for protection of fragile products*. Westpak Inc. 1-50.
3. Herber H Schueneman, M.E. *Package Drop Testing: The do's and don'ts of package impact performance tests*. Westpak Inc. 1-30.
4. Pal Khangaldy, H.S. *Design Parameters for Deformable Cushion Systems*. Westpak Inc. 1-17.
5. (IEC), I.E.C., *IEC 60068-2-32*, in *Part 2: Test - Test Ed: Free fall*1990.
6. Yi-Shao Lai, P.-F.Y., Chang-Lin Yeh, *Experimental studies of board-level reliability of chip-scale packages subjected to JEDEC drop test condition.* Microelectronics Reliability, 2006. **46**: p. 645-650.
7. (JEDEC), J.E.D.E.C., *JESD22-B110A - Subassembly Mechanical Shock* 2009. p. 9.
8. (JEDEC), J.E.D.E.C., *JESD22-B111 - Board Level Drop Test Method of Components for Handheld Electronic Products*, 2003. p. 16.
9. Hum Shen Ng, T.Y.T., Jing-en Luan, *Design for Standard Impact Pulses of Drop Tester using Dynamic Simulation*, in *Electronics Packaging Conference*2004, IEEE. p. 793-799.
10. A F Askari Farahani, M.A.-B., A Dasgupta, *Shock and Dynamic Loading in Partable Electronic Assemblies: Experimental Results.* Journal of Electronic Packaging, 2011. **133**: p. 041010-1 - 041010-10.
11. C Y Zhou, T.X.Y., R S W Lee, *Drop/impact tests and analysis of typical portable electronic devices.* International Journal of Mechanical Sciences, 2007. **50**: p. 905-917.
12. Shia-Chung Chen, H.-L.W., Lei-Ti Huang, Ying-Chieh Wang, *Drop Test System with Orientation Repeatabilty for 3C Products*, in *33rd Annual Conference of the IEEE Industrial Electronics Society (IECON)*2007, IEEE: Taipei, Taiwan. p. 2910-2915.
13. Lim C.T., L.Y.J., *Investigating of Drop Impact of Portable Electronic Products*, in *Electronic Components and Technology Conference*2002. p. 1270-1274.
14. Victor Phyau Wui Shim, C.T.L., *Impact drop tester for portable consumer products*, U.S. Patent, Editor 2003.
15. Tan L.B., A.C.W., Lim C.T., Tan V.B.C., Zhang X, *Modal and Impact Analysis of Modern Portable Electronic Products*, in *Electronic Components and Technology Conference*2005, IEEE. p. 645-653.
16. Ong Y.C., S.V.P.W., Chai T.C., Lim C.T., *Comparison of Mechanical Response of PCBs Subjected to Product-Level and Board-Level Drop Impact Tests*, in *Electronics Packaging Technology Conference*2003, IEEE. p. 223-227.
17. Suresh Goyal, E.K.B., *Methods for Realistic Drop-Testing.* The International Journal of Microcircuits and Electronics Packaging, 2000. **23**(1): p. 45-52.
18. Da Yu, J.B.K., Seungbae Park, John Lee, *Dynamic responses of PCB under product-level free drop impact.* Microelectronics Reliability, 2010. **50**: p. 1028-1038.
19. America, D.o.D.-U.S.o., *Environmental Engineering Considerations and Laboratory Tests*, in *MIL-STD-810G*2008. p. 804.
20. H. Hashamdar, Z.I., M. Jameel, *Finite element analysis of nonlinear structures with Newmark method.* International Journal of the Physical Sciences, 2011. **6**: p. 1395-1403.
21. Inc, A., *Appendix G. Explicit Dynamics Theory Guide*, 2012.
22. Dowling, N.E., *Mechanical Behaviour of Materials - Engineering Methods for Deformation, Fracture, and Fatigue*. 3 ed: Pearson Hill.
23. ANSYS, *Lecture 7 - Explicit Meshing*, in *Explicit STR*2012: ANSYS.com.
24. ANSYS, *Meshing User's Guide*, in *Release 14.5*, ANSYS Inc.: http://www.ansys.com. p. 124.

25. Jason Wu, G.S., Chao-pin Yeh, Karl Wyatt, *Drop/Impact Simulation and Test of Telecommunication Products*, in *InterSociety Conference on Thermal Phenomena*1998.
26. Zhu, L., *Modeling Technique for Reliability Assesment of Portable Electronic Product Subjected to Drop Impact Loads*, in *Electronic Components and Technology Conference*2003. p. 100-104.
27. Constance Ziemian, M.S., Sophia Ziemian *Anisotropic Mechanical Properties of ABS Parts Fabricated by Fused Deposition Modelling*. 2012.
28. Robin Alastair Amy, G.S.A., Guy Richardson, *Accuracy of simplified printed circuit board finite element models.* Microelectronics Reliability, 2010. **50**: p. 86-97.
29. ANSYS, *Mechanical Users Guide*, in *Release 14.5*, ANSYS Inc.: http://www.ansys.com. p. 157.
30. Ted Diehl, D.C., Ben Nagaraj, *Applications of DSP to Explicit Dynamic FEA simulations of elastically-dominated impact problems.* Shock and Vibration, 2000. **7**(3/2000): p. 167-177.
31. ANSYS, *Mechanical Users Guide*, in *Release 14.5*, ANSYS Inc.: http://www.ansys.com. p. 1596.
32. ANSYS, *Mechanical Users Guide*, in *Release 14.5*, ANSYS Inc.: http://www.ansys.com. p. 1600.
33. O.C. Zienkiewicz, R.L.T., *The finite element method*. Vol. Volume 1.
34. Burton A.J., *Explicit, Large Strain, Dynamic Finite Element Analysis with Applications to Human Body Impact Problems*, 1996, University of Wales.
35. Bonet J., M.H., Hassan O., *An averaged nodal deformation gradient linear tetrahedral element for large strain explicit dynamics applications.* Communications in Numerical Methods in Engineering, 2001. **17**: p. 551-561.
36. Puso M.A., S.J., *A stabilized nodally integrated tetrahedral.* International Journal for Numerical Methods in Engineering, 2006. **67**: p. 841-867.
37. Johannes Kunz, M.S. *Determining the Modulus of Elasticity in Compresssion via the Shore A Hardness*. 2006.
38. Shin-Etsu, *Silicone Rubber - Performance Test Results*, S.-E. Silicone, Editor 2004: http://www.silicone.jp/e/catalog/pdf/rubber_et.pdf.
39. Sumipex, *Sumipex MH Data Sheet*, 2013: http://plastics.ides.com/datasheet/e46779/sumipex-mh.
40. EMS-Grivory, *Grilon BG-50 Glass Reinforced Nylon (Conditioned)*, 2013: www.matweb.com.
41. Corning, D., *Xiameter RBL-2004-40 Liquid Silicone Rubber*, 2011: https://www.xiameter.com/EN/Products/Pages/ProductDetail.aspx?pid=04088663&lir=X7767.
42. Karin Sundberg, M.M., *Product Data Sheet - Nolato Conductive Silicone Rubber 8630*, N. Silikonteknik, Editor 2012.
43. Cemedine, *Super-X Series*, 2013: http://www.cemedine.co.jp/e/product/super_x.html.
44. AG, B.M.S., *Makroblend Product Range - Typical Values*, 2006: www.plastics.bayer.de.
45. AG, B.M., *Makrolon Product Range - Typical Values*, 2005: www.plastics.bayer.de.
46. AG, B.M.S., *Desmopan 5377A ISO Datasheet*, 2004: www.bayermaterialscience.com.
47. RTP, *Product Data Sheet and General Processing Conditions RTP 399 X 623131 B*, 2006.
48. NADC, *Alloy Data: Aluminum Die Casting Alloys*, 1997: http://www.krdiecasting.com/pdf/Sect3.pdf.